UNIVERSITY OF SOUTHAMPTON

FACULTY OF NATURAL AND ENVIRONMENTAL SCIENCES

SCHOOL OF OCEAN AND EARTH SCIENCES

IMPACT OF SUBSURFACE FLUID FLOW ON SEDIMENT ACOUSTIC PROPERTIES, IMPLICATIONS FOR CARBON CAPTURE AND STORAGE

---

by

Melis CEVATOGLU

Thesis for the degree of Doctor of Philosophy

August 3, 2015

UNIVERSITY OF SOUTHAMPTON

ABSTRACT

FACULTY OF NATURAL AND ENVIRONMENTAL SCIENCES
SCHOOL OF OCEAN AND EARTH SCIENCES

Doctor of Philosophy

IMPACT OF SUBSURFACE FLUID FLOW ON SEDIMENT ACOUSTIC PROPERTIES, IMPLICATIONS FOR CARBON CAPTURE AND STORAGE

by Melis CEVATOGLU

Geological Carbon Capture and Storage (CCS) is a promising climate change mitigation technology, which allows the reduction of anthropogenic carbon dioxide (CO_2) emissions into the atmosphere. Although CCS is considered to have a significant potential in tackling climate change, several uncertainties remain, including the efficiency and permanency of carbon sequestration, and notably risks of CO_2 leakage from the storage reservoir. A better understanding of fluid flow activity within the sedimentary overburden and the identification of the best monitoring techniques are crucial for increasing societal confidence in sequestration.

This thesis reports findings from two different offshore CCS projects: a controlled sub-seabed CO_2 release experiment completed in Ardmucknish Bay, Oban (*Quantifying and Monitoring Potential Ecosystem Impacts of Geological Carbon Storage*, QICS), and a multidisciplinary research project conducted in the vicinity of Sleipner CCS site, in the Central North Sea (*Sub-seabed CO_2 Storage: Impact on Marine Ecosytems*, ECO_2).

During the QICS project, a borehole was drilled from land, allowing 37 days of CO_2 release in unconsolidated marine sediments. Analysis of the time-lapse high-resolution seismic reflection data reveals development of acoustic anomalies within the overburden and water column, caused by CO_2 fluxing in the vicinity of the injection site. The impacts of CO_2 injection on sediment acoustic properties are investigated, where changes in seismic reflectivity, seismic attenuation, acoustic impedance and P-wave seismic velocity are detected on high-resolution seismic reflection data. CO_2 migration within the overburden is interpreted to be controlled by sediment stratigraphy and injection rate/total injected volume throughout the gas release, and by the sediment stratigraphic geometry post-release. Seismic quantification of the gaseous CO_2 indicates that most of the injected CO_2 is trapped below a stratigraphic boundary, located at 4 m depth below the seafloor, or dissolved, throughout the gas release. These observations are in agreement with seabed gas flux measurements by passive hydroacoustics and water column bubble sampling, which suggest that only 15% of the injected CO_2 emerges at the seabed, towards the end of gas release.

Within the scope of the ECO_2 project, increased fluid flow activity is detected along, and in the vicinity of a seabed fracture, the Hugin Fracture. Although there is no evidence of anthropogenic CO_2 leakage in the Central North Sea from the current dataset, biogenic and thermogenic gas leakage at the Hugin Fracture suggest a well-established hydraulic and structural connection. The origin of the Hugin Fracture is proposed to be controlled by an E-W transtensional stress regime, and differential compaction above a buried tunnel valley system.

CONTENTS

Abstract iii

Table of Contents v

List of Figures ix

List of Tables xv

Declaration of Authorship xvii

Abbreviations xix

Acknowledgements xxiii

Chapter 1 General Introduction 1

1.1 Global warming 1

1.2 Carbon Capture and Storage 3

1.2.1 Definition and different types 3

1.2.2 Leakage from offshore geological storage sites and monitoring 5

1.3 The QICS project – Ardmucknish Bay, Oban 7

1.4 The ECO_2 project – Sleipner CCS site, North Sea 8

1.5 Research questions 12

1.6 Thesis structure 12

Chapter 2 Gas migration pathways, controlling mechanisms and changes in sediment acoustic properties observed in a controlled sub-seabed CO_2 release experiment 15

Abstract 15

2.1 Introduction 16

2.2 The QICS experiment 17

2.2.1 Subsurface structure of the QICS site 19

2.3 Materials and methods 22

2.3.1 Multibeam bathymetry and 2D seismic reflection data acquisition and processing 22
2.3.2 Reflection coefficient and seismic attenuation calculation 23
2.4 Results and analysis 28
2.4.1 Subsurface seismic stratigraphy 28
2.4.2 Temporal and spatial evolution of CO_2-related acoustic anomalies 28
2.4.3 Impacts on sediment acoustic properties 37
2.4.3.1 Reflection coefficient 37
2.4.3.2 Attenuation 46
2.5 Discussion 53
2.5.1 Mechanisms controlling CO_2 migration 54
2.5.2 Improvements in CO_2 detection within the subsurface 56
2.6 Conclusion 57

Chapter 3 Analysis of the post-release seismic reflection data from Ardmucknish Bay, Oban 59

Abstract 59
3.1 Introduction 60
3.2 Results 62
3.2.1 Spatial distribution of acoustic anomalies 62
3.2.2 Reflection coefficient calculation 68
3.2.3 Seismic attenuation 70
3.3 Discussion 75
3.4 Conclusion 78

Chapter 4 Quantification of CO_2 in gassy marine sediments and acoustic impedance inversion 79

Abstract 79
4.1 Introduction 80
4.2 Methods 82

4.2.1 Thickness analysis above Horizon 2 and variations in seismic P-wave velocity 82
4.2.2 CO_2 quantification above Horizon 2 85
4.2.3 Acoustic impedance inversion 87
4.2.3.1 Genetic algorithms 87
4.2.3.2 Seismic reflection data processing flow 91
4.2.3.3 Consolidation correction 92
4.3 Results 95
4.3.1 Thickness analysis above Horizon 2 and seismic P-wave velocity variations 95
4.3.2 CO_2 quantification above Horizon 2 100
4.3.3 Acoustic impedance inversion 108
4.4 Discussion 112
4.4.1 Discussion of results 112
4.4.1.1 Isopach maps, P-wave velocity and CO_2 volume *in situ* above Horizon 2 112
4.4.1.2 Acoustic impedance inversion 114
4.4.2 Source of errors in gas quantification 114
4.5 Conclusion 118

Chapter 5 Near-surface fluid flow activity in the vicinity of Sleipner Carbon Capture and Storage site in the Central North Sea 121

Abstract 121
5.1 Introduction 122
5.2 Overview of Sleipner Carbon Capture and Storage 124
5.2.1 The Utsira Sand Storage Reservoir, its caprock and the underlying units 125
5.2.2 The current state of the injected CO_2 130
5.2.3 Fluid flow activity within the overburden above the Utsira Sand Reservoir 134
5.3 Data acquisition and processing 139

5.3.1 High-resolution 2D seismic reflection data acquisition and processing 142
5.3.2 Side-scan sonar and multibeam bathymetry data acquisition and processing 146
5.3.3 Autosub 6000 images and HyBIS video surveying 147
5.3.4 Sediment vibrocore operations 149
5.3.5 Water column geochemistry 153
5.4 Results 154
5.4.1 Greater Sleipner Area 154
5.4.2 CO_2 Plume Area and South of the Plume Area 156
5.4.3 Middle Area 156
5.4.4 Hugin Fracture Area 158
5.4.4.1 Surface 158
5.4.4.2 Subsurface 166
5.4.4.3 Vibrocore data analysis 176
5.5 Discussion 182
5.6 Conclusion 186

Chapter 6 Synthesis and Future Work 189

6.1 Synthesis and implications 189
6.2 Future Work 199

Appendices 201

Appendix A 203
Appendix B 217
Appendix C 219
Appendix D 223

Bibliography 227

LIST OF FIGURES

CHAPTER 1

Figure 1.1 Anthropogenic greenhouse gas emissions between 1970 and 2010 2

Figure 1.2 Overview of geological CO_2 sequestration options 5

Figure 1.3 Potential CO_2 leakage scenarios associated with offshore geological storage 7

Figure 1.4 Location of the QICS and Sleipner CO_2 injection sites 10

CHAPTER 2

Figure 2.1 Schematic overview of CO_2 release experiment, changes in total gas injection flux and timing of 2D seismic reflection surveys 18

Figure 2.2 Detailed stratigraphy and grain-size distribution of sediments within Core 6 21

Figure 2.3 Detailed location map of the experiment site and 2D seismic reflection profiles within Ardmucknish Bay 26

Figure 2.4 Time-lapse 2D seismic reflection data illustrating CO_2 migration within unconsolidated sediments around the diffuser, Ardmucknish Bay 30

Figure 2.5 Pockmarks and water column bubbles imaged on the multibeam bathymetry data at Day 34 32

Figure 2.6 Spatial distribution of CO_2-related high reflectivity anomalies for Horizon 2 and seismic chimneys within the overburden 33

Figure 2.7 Seismic wiggle traces from outside the chimney area for all days of 2D seismic surveying in Ardmucknish Bay 35

Figure 2.8 Schematic diagram summarising stages of gas migration revealed by the repeated 2D seismic reflection surveys 36

Figure 2.9 Temporal variation in the reflection coefficient of Horizon 2 40

Figure 2.10 Temporal variation in reflection coefficient of the seabed 42

Figure 2.11 Changes in Horizon 2 reflection coefficients between Chirp surveys 44

Figure 2.12 Comparison of synthetic and real seismograms for different days during the release experiment 48
Figure 2.13 The temporal variation of Q during the QICS experiment 49
Figure 2.14 Temporal and spatial variation of the seismic amplitude spectrum of Chirp data 52
Figure 2.15 Changes in the reflection coefficient of Horizon 2, quality factor above and below Horizon 2, and cumulative amount of CO_2 injected during the experiment 55

CHAPTER 3

Figure 3.1 Position of the post-release seismic reflection data 61
Figure 3.2 Stratigraphic horizons and enhanced reflectivity imaged on a seismic line (NS3_2) from the post-release seismic reflection dataset 64
Figure 3.3 Stratigraphic horizons and enhanced reflectivity imaged on a seismic line (NS4x_1) from the post-release seismic reflection dataset 65
Figure 3.4 Stratigraphic horizons and enhanced reflectivity imaged on a seismic line (Perp3_2) from the post-release seismic reflection dataset 66
Figure 3.5 Location of the high reflectivity acoustic anomalies imaged along Horizon 2 from the syn-release and post-release seismic reflection datasets 67
Figure 3.6 Horizon 2 polarity reversal imaged on the post-release seismic reflection dataset 69
Figure 3.7 Horizon 2 reflection coefficient maps from the syn-release and post-release seismic reflection datasets 71
Figure 3.8 The seabed reflection coefficient maps from the syn-release and post-release seismic reflection datasets 72
Figure 3.9 Q values above and below Horizon 2 from the post-release seismic reflection dataset, within and outside of the circular area 74
Figure 3.10 Summary of the changes in the acoustic properties of sediments during and after CO_2 injection in Ardmucknish Bay, and cumulative CO_2 injected during the QICS experiment 76

CHAPTER 4

Figure 4.1 Method used in thickness analysis for the seabed-Horizon 2 interval in Ardmucknish Bay seismic reflection data 83
Figure 4.2 Results from MSCL measurements along Core 6 84
Figure 4.3 Flow chart illustrating the process of a genetic algorithm used in acoustic impedance inversion 89
Figure 4.4 Location of Core 6 and a pre-release boomer seismic reflection profile acquired in Ardmucknish Bay 90
Figure 4.5 Evolution of residuals for varying values of input parameters during acoustic impedance inversion of a pre-release boomer trace 91
Figure 4.6 Generation of consolidation correction for Ardmucknish Bay sediments 94
Figure 4.7 Isopach maps of the seabed-Horizon 2 interval from seismic reflection data acquired in Ardmucknish Bay 97
Figure 4.8 Change in thickness of seabed-Horizon 2 interval between syn-/post-release and Day minus 2 seismic reflection data 98
Figure 4.9 Seismic P-wave velocity above Horizon 2 calculated for syn- and post-release seismic reflection surveys 99
Figure 4.10 CO_2 content above Horizon 2 within the combined chimney area..... 103
Figure 4.11 CO_2 volume above Horizon 2 within the combined chimney area..... 105
Figure 4.12 Variation in CO_2 volume above Horizon 2 during injection 107
Figure 4.13 Evolution of acoustic impedance inversion of a single seismic (Chirp) reflection trace acquired at Day 12 110
Figure 4.14 Acoustic impedance inversion of the pre-release boomer and syn-release Chirp seismic reflection datasets 111
Figure 4.15 The relationship between the CO_2 volume *in situ* above Horizon 2, seabed leakage and cumulative CO_2 input 113

CHAPTER 5

Figure 5.1 Map of the *JC077* cruise track lines 123

Figure 5.2 Distribution of the Utsira Sand in the North Sea and block diagram summarizing geological carbon sequestration in Sleipner 125
Figure 5.3 The major geological domains in the Norwegian North Sea..... 126
Figure 5.4 Seismic reflection data illustrating Utsira Sand, its caprock and the underlying units in the Sleipner area 128
Figure 5.5 The lithostratigraphic chart of the North Sea..... 130
Figure 5.6 3D time-lapse seismic imaging of the Sleipner CO_2 plume. 133
Figure 5.7 Bright spots and three different types of seismic chimneys identified on the 3D seismic reflection data in Sleipner, prior to CO_2 injection .. 135
Figure 5.8 An example of a seismic section from North Sea, illustrating buried tunnel valleys 137
Figure 5.9 Multibeam, Chirp and side-scan sonar track lines (with Autosub 6000 flying altitude at 12 m) 140
Figure 5.10 Multibeam, Chirp and side-scan sonar track lines (with Autosub 6000 flying altitude at 3 m)..... 141
Figure 5.11 The seismic source used during Autosub 6000 seismic reflection data acquisition in the Central North Sea 143
Figure 5.12 Seismic reflection (Chirp) data processing steps for a random seismic line (M62) acquired during the *JC077* cruise with Edgetech 2200-M Modular Sonar System mounted on Autosub 6000 144
Figure 5.13 Track lines of the TOPAS sub-bottom seismic reflection profiles..... 145
Figure 5.14 Maps showing the survey track lines for HyBIS dives..... 148
Figure 5.15 Maps showing the vibrocore locations 151
Figure 5.16 Multibeam bathymetry data acquired during the *JC077* cruise in the Central North Sea..... 154
Figure 5.17 Dissolved CH_4 concentrations from CTD samples in the Central North Sea..... 155
Figure 5.18 Side-scan mosaics from the CO_2 Plume Area (M65), and South of the Plume Area (M59) 157
Figure 5.19 Side-scan mosaic of the Middle Area (M60) 158
Figure 5.20 Side-scan mosaic of the overall Hugin Fracture Area 160
Figure 5.21 Hugin Fracture surface fault geometry 161
Figure 5.22 Enlarged side-scan sonar images of the Hugin Fracture 162

Figure 5.23 Multibeam bathymetry data superimposed on the side-scan mosaic of the Hugin Fracture Area 163
Figure 5.24 Austosub 6000 pictures acquired within the Hugin Fracture Area..... 164
Figure 5.25 Results from Eh sensor mounted on Autosub 6000 during the *JC077* cruise 165
Figure 5.26 TOPAS seismic reflection data analysis 168
Figure 5.27 Seismic reflection (Chirp) data analysis 169
Figure 5.28 The spatial extent of the Hugin Fracture improved after seismic data analysis..... 170
Figure 5.29 Acoustic amplitude anomalies from TOPAS seismic reflection data... 172
Figure 5.30 Acoustic amplitude anomalies from seismic reflection (Chirp) data within the overburden 173
Figure 5.31 Acoustic amplitude anomalies from seismic reflection (Chirp) data within the overburden and water column 174
Figure 5.32 RMS seismic amplitude anomalies from Chirp and TOPAS seismic reflection data within the Hugin Fracture Area 175
Figure 5.33 Location of the vibrocores recovered during the *JC077* cruise in the Hugin Fracture Area..... 177
Figure 5.34 Pore water analysis for VC 01 and VC 08..... 178
Figure 5.35 MSCL measurements down VC 06 180
Figure 5.36 MSCL measurements down VC 21 181
Figure 5.37 Time slices from the 3D seismic reflection data over the Quaternary sediment package in the Central North Sea 186

CHAPTER 6

Figure 6.1 Summary of the change in sediment acoustic properties in Ardmucknish Bay..... 191
Figure 6.2 Cartoon illustrating the fate of the injected gaseous CO_2 in Ardmucknish Bay..... 194
Figure 6.3 Relationship between the CO_2 injection rate and seabed leakage in Ardmucknish Bay 198

LIST OF TABLES

CHAPTER 1

Table 1.1 Source of data acquired as part of the QICS and ECO_2 projects 11

CHAPTER 2

Table 2.1 Description of the 2D seismic reflection datasets collected during the QICS experiment in Ardmucknish Bay and associated CO_2 injection rates 19

Table 2.2 Seismo-stratigraphic horizons imaged on the 2D seismic reflection data, Ardmucknish Bay 22

Table 2.3 2D seismic reflection and multibeam bathymetry data acquisition parameters 27

Table 2.4 Mean reflection coefficient for the seabed and Horizon 2 observed on different days relative to the area affected by seismic chimneys on Day 12 for Day 12 and Day 13, and on Day 34 for Day 34 45

Table 2.5 Variation of the Quality factor above and below Horizon 2 observed on different survey days, within and outside the chimney area 50

CHAPTER 3

Table 3.1 Summary of the 2D seismic reflection datasets acquired as part of the QICS experiment in Ardmucknish Bay (pre-, syn- and post-release) and associated CO_2 injection rates 62

Table 3.2 Mean reflection coefficients calculated for the seabed and Horizon 2 from the pre-, syn- and post-release seismic reflection datasets 70

Table 3.3 Variation of the Quality factor above and below Horizon 2 calculated from the pre-, syn- and post-release seismic reflection datasets 73

CHAPTER 4

Table 4.1 Scientific literature for remote free gas quantification in marine sediments 81

Table 4.2 Key properties of sediments used in this study to derive a consolidation trend for glacio-marine sediments located beneath Horizon 2 93

Table 4.3 Mean and minimum seismic P-wave velocities above Horizon 2 on pre-, syn- and post-release seismic reflection datasets 100

Table 4.4 Values of parameters used in Anderson and Hampton compressible fluid model to calculate CO_2 content above Horizon 2 101

Table 4.5 Variation of CO_2 content above Horizon 2 within a circular area around the diffuser 102

Table 4.6 Total CO_2 volume within the combined chimney area above Horizon 2 106

Table 4.7 Total CO_2 volume within the combined chimney area above Horizon 2, corrected for compression 107

Table 4.8 Effect of thickness estimate errors on seismic velocity and CO_2 volume 115

CHAPTER 5

Table 5.1 Summary of Autosub 6000 missions 139

Table 5.2 List of HyBIS dives and summary data 149

Table 5.3 Vibrocores recovered during the *JC077* cruise and related informations 152

Table 5.4 Summary of seismic reflectors and sediment packages imaged on the seismic reflection data 167

Declaration of Authorship

I, Melis Cevatoglu, declare that this thesis titled, *"Impact of subsurface fluid flow on sediment acoustic properties, implications for Carbon Capture and Storage"* and the work presented in it are my own. I confirm that:

1. This work was done wholly or mainly while in candidature for a research degree at this university;
2. Where any part of this thesis has previously been submitted for a degree or any other qualification at this University or any other institution, this has been clearly stated;
3. Where I have consulted the published work of others, this is always clearly attributed;
4. Where I have quoted from the work of others, the source is always given. With the exception of such quotations, this thesis is entirely my own work;
5. I have acknowledged all main sources of help;
6. Where the thesis is based on work done by myself jointly with others, I have made clear exactly what was done by others and what I have contributed myself;
7. I am the lead author and co-author of these following publications:
    - Blackford, J., Bull, J.M., Cevatoglu, M., Connelly, D., Hauton, C., James, R.H., Lichtschlag, A., Stahl, H., Widdcombie, S., Wright, I.C., 2015. Marine baseline and monitoring strategies for carbon dioxide capture and storage (CCS). *International Journal of Greenhouse Gas Control* 38, 221-229.
    - Blackford, J., Stahl, H., Bull, J.M., Berges, B.J.P., Cevatoglu, M., Lichtschlag, A., Connelly, D., James, R.H., Kita, J., Long, D., Naylor, M., Shitashima, K., Smith, D., Taylor, P., Wright, I., Akhurst, M., Chen, B., Gernon, T.M., Hauton, C., Hayashi, M., Kaieda, H., Leighton, T.G., Sato, T., Sayer, M.D.J., Suzumura, M., Tait, K., Vardy, M.E., White, P.R., Widdicombe, S., 2014. Detection and impacts of leakage from sub-seafloor deep geological carbon dioxide storage. *Nature Climate Change* 4(11), 1011-1016.
    - Cevatoglu, M., Bull, J.M., Vardy, M.E., Gernon, T.M., Wright, I.C., Long, D., 2015. Gas migration pathways, controlling mechanisms and

changes in sediment acoustic properties observed in a controlled sub-seabed CO_2 release experiment. *International Journal of Greenhouse Gas Control* 38, 26-43.

Signed: _____

Date: _____

Abbreviations

a_0	Bubble radius
A	Seismic amplitude
Ag	Silver
AgCl	Silver chloride
AI	Acoustic impedance
ATP	Attenuation trend plot
AUV	Autonomous underwater vehicle
AVO	Amplitude versus offset
BGS	British Geological Survey
BOSCORF	British Ocean Sediment Core Facility
BP	Before present
BSR	Bottom simulating reflector
°C	Celcius (degree)
cm^3	Cubic centimetre
CCS	Carbon Capture and Storage
CH_4	Methane
Cl	Chloride
CO_2	Carbon dioxide
CTD	Conductivity temperature depth
dB	Decibel
dm^3	Cubic decimetre
E	East
ECO_2	Sub-seabed CO_2 Storage: Impact on Marine Ecosystems
Eh	Redox potential
E(m)	Residual seismic amplitude between the field and synthetic seismic reflection data
f	Frequency
F-gas	Fluorinated gas

FP7	The seventh framework for research and technological development
g	Gravitational constant
G	Sediment shear modulus
GHG	Greenhouse gas emissions
GPa	Gigapascal
G_R	Spherical divergence
Gt	Gigatonne
h	Height
HISAS	Synthetic aperture sonar
H_2S	Hydrogen sulphide
HyBIS	Hydraulic Benthic Interactive Sampler
Hz	Hertz
IEA	International Energy Agency
IPCC	International Panel on Climate Change
J	Joule
JC077	James Cook 077 cruise
jsf	Edgetech 2200-M Modular Sonar System data format
K	Sediment bulk modulus
Ka	Kiloyear
KCl	Potassium chloride
K_{com}	Sediment composite bulk modulus
K_{dr}, R_R	Deeper reflector reflection coefficient
K_f	Sediment frame modulus
K_g	Bulk modulus of gas
kHz	Kilohertz
K_m	Sediment mineral modulus
KPa	Kilopascal
K_{sf}, R_S	Seabed reflection coefficient
K_w	Bulk modulus of water

K'_w	Bulk modulus of water modified by free gas
LEFM	Linear elastic fracture mechanics theory
L(m)	Likelihood of a model
Ma	Million years
mmol	Millimol
M-pixel	Mega pixel
ms	Millisecond
MSCL	Multi sensor core logger
Mt	Million tonne
n	Sediment fractional porosity
N	North
NE	North-east
NERC	The National Environment Research Council
n_g	Gas content
n'_g	Fraction of pore space occupied by gas
N_2O	Nitrous oxide
NOCS	National Oceanography Centre Southampton
NW	North-west
ORP	Oxidation reduction potential
OSPAR	The Convention for the Protection of the Marine Environment of the North-East Atlantic
P	Pressure
pCO_2	CO_2 concentration
pH	Power of Hydrogen
PPD	Posteriori probability density function
ppm	Parts per million
P-wave	Compressional seismic wave
RC	Reflection coefficient
RMS	Root mean square
ROV	Robotic underwater vehicle

S	South
SE	South-east
SO_2	Sulphur dioxide
SSP	Spectral Signature Plot
STP	Standard temperature and pressure
SW	South-west
t	Time
T	Temperature
TVG	Time varying gain
TWT	Two-way travel time
UK	United Kingdom
USBL	Ultra short baseline positioning system
USGS	United States Geological Survey
Q	Seismic quality factor
QICS	Quantifying and Monitoring Potential Ecosystem Impacts of Geological Carbon Storage
V_p	Seismic velocity
VC	Vibrocore
V_{gas}	Volume of gas
V_s	Volume of gas at standard temperature and pressure
W	West
α	Seismic attenuation
γ	Ratio of specific heats of gas
ΔRC	Difference in reflection coefficient
Δt	Difference in two-way travel time
μs	Microsecond
μm	Micrometre
ρ_s	Sediment bulk density
Φ	Logarithmic grain size scale representing grain diameter

Acknowledgments

My main supervisor ***Jonathan Bull***, I am extremely grateful to you, at first for giving me the opportunity to do this PhD, but also for your continuous encouragement, support, and invaluable feedback. During these four years, I have learned a lot from you, scientifically but also personally. Thank you for always pushing me further, you helped me to cross my own boundaries. My other supervisors ***Ian Wright*** and ***Tom Gernon***, thank you for your continuous support and guidance during my PhD. My panel chair ***Tim Henstock***, thank you for your valuable guidance.

Mark Vardy, it would not be possible to complete this PhD without your immense support and guidance. You always inspired and encouraged me, even when I was not seeing the light at the end of the tunnel. Thank you for everything. ***John Davis***, I express my grateful thanks to you, for your immense help up in Oban, without forgetting Bangladesh. Our fieldtrips together were always a pleasure.

Anja Reitz and ***Klauss Wallmann***, thank you for great coordination and management during the ECO_2 project. I am also very grateful to the ***ECO_2*** project for funding (EU Framework 7) my PhD thesis. ***Doug Connelly***, ***Tim Le Bas***, ***Steve McPhail*** and the ***JC077 crew***, thank you for all your support during the JC077 cruise.

Henrik Stahl, the QICS project would not be that successful without your immense help. ***Jerry Blackford***, thank you for your excellent coordination during the QICS project. Thank you to ***SAMS*** for providing excellent work environment during the QICS project. ***Crew of Seol Mara***, thank you for your support for the data acquisition in Oban.

Katsia Pabortsava and ***Konstantionos Kouvaris***, it is simply impossible for me to thank you in just few lines. What I can only say is that I have a real sister and brother since September 2011. Thank you very much for every moment together, and all your support. Maybe you are not anymore in 54, but always in my heart. Special thanks to ***Ilse Bloom*** and ***Andrew Said***. You both are very precious gifts to me in my life. ***Anna Lichtschlag*** and ***Gaye Bayrakçı***, you both deserve a big thank you, mostly for making me smile and believe in myself all this time. ***Aude Mazuel***. Soulmate. We have started a story back in 2008 and we continue. We will continue. Thank you very much for everything.

To my family and friends in Turkey

Benim canım annem ***Serpil Cevatoğlu*** ve babam ***Kazım Cevatoğlu***. Sizin kızınız olmaktan her zaman gurur duydum. Bana bu 4 senede verdiğiniz sonsuz destek ve sevgi için çok teşekkür ederim. Siz olmasaydınız, asla olmazdı. Kardeşim ***Oytun Mataracı***, abim ***Murat Karagözoğlu*** ve ablam ***Mine Brooks***, herşey icin çok teşekkür ederim, sizleri çok seviyorum. ***Balki***, sen hep benimlesin. ***Melahat Ibrahimoğlu***, ***Nizar Cevatoğlu*** ve ***Cevat Cevatoğlu***, kalbimdeki yeriniz çok büyük…

GRADUATE SCHOOL OF THE NATIONAL OCEANOGRAPHY CENTRE, SOUTHAMPTON

This PhD thesis by

Melis Cevatoglu

has been produced under supervision of the following persons

Supervisors

Prof. Jonathan M. Bull

Prof. Ian C. Wright

Dr. Tom Gernon

Chair of the Advisory Panel:

Prof. Tim Henstock

Chapter 1

General Introduction

1.1 Global warming

The mean Earth's land and ocean surface temperature has been shown to have increased by c. 0.85 °C since the early-twentieth century, resulting in a global sea level rise of 0.19 m, significant ice sheet melting, i.e., a decrease in the mean Arctic sea-ice extent by 4% per decade, as well as ocean acidification (IPCC, 2014). The most recent Intergovernmental Panel on Climate Change (IPCC) synthesis report clearly underlines that the increase in the anthropogenic greenhouse gas emissions since the industrial revolution, including carbon dioxide (CO_2), methane (CH_4) and nitrous oxide (N_2O), is the predominant cause of the observed global warming (IPCC, 2014). CO_2 emissions from fossil fuel combustion and other industrial processes are estimated to be responsible for more than half of the enhanced greenhouse gas emissions since the mid-twentieth century (IPCC, 2005; Meinshausen et al., 2009; IPCC, 2014) (Fig. 1.1). Direct measurements of atmospheric CO_2 concentrations at Mauna Loa Observatory (Hawaii), show a continuous CO_2 increase since 1958, with CO_2 being 400 ppm at present, considerably higher than pre-industrial levels c. 280 ppm (Bala, 2013).

To avoid dangerous anthropogenic interference with the climate system, a substantial and sustained reduction in greenhouse gas emissions, notably that of CO_2, is required, implying a need for climate mitigation technologies (Den Elzen and Meinshausen, 2006; IPCC, 2014). Many strategies have been proposed to address the need to reduce anthropogenic CO_2 emissions, including transition from fossil fuel combustion to alternative energy sources, enhancement of biological natural sources, and Carbon Capture and Storage (CCS) (Canadell and Raupach, 2008; Luderer et al., 2014). Considering that current renewable energy sources provide less than 20% of the world energy, it becomes clear that the continued usage of fossil fuels is inevitable, at

least in the near-medium term (Chu and Majumdar, 2012). Recent studies indicate that the potential contribution of the nuclear energy to climate change mitigation is relatively minor, c. 6% of the total energy demand (Moriarty and Honnery, 2012). The International Energy Agency (IEA) states that CCS is a promising climate mitigation technology, as it could achieve 14% reduction in the cumulative global greenhouse gas emissions by 2050, while securing reliable energy supply from fossil fuel combustion (IEA, 2013). Similarly, CCS can contribute one-sixth of the CO_2 emission reductions by 2050 (IEA, 2013), and might allow stabilization of CO_2 concentrations around 450 ppm by 2100 (IPCC, 2014).

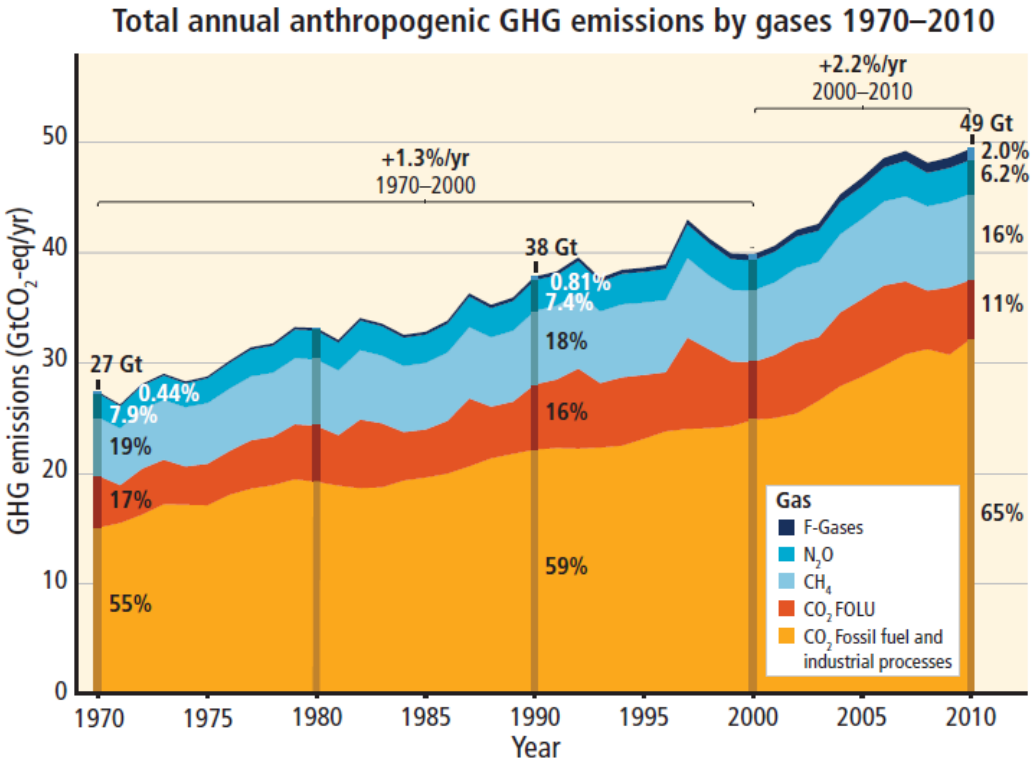

Figure 1.1 *Anthropogenic greenhouse gas emissions between 1970 and 2010 (IPCC, 2014). This figure illustrates increased greenhouse gas emission since the mid-twentieth century, with fluorinated gases (F-gases), CH_4, N_2O, and CO_2 from forestry and other land use, as well as fossil fuel and industrial processes.*

This thesis present findings on two different offshore CCS projects: "Quantifying and Monitoring Potential Ecosystem Impacts of Geological Carbon Storage" (QICS project, Ardmucknish Bay, Oban, see Section 1.3) and "Sub-seabed CO_2 Storage: Impact on Marine Ecosytems" (ECO_2 project, Sleipner CCS site, Central North Sea, see Section 1.4), to achieve the main objectives described in Section 1.5.

Table 1.1 summarizes various datasets acquired as part of the QICS and ECO_2 projects, and which were used in this thesis.

1.2 Carbon Capture and Storage

1.2.1 Definition and different types

CCS is a climate mitigation technology, comprising capturing CO_2 from industrial plants and fossil fuel generated power stations, transporting it to a storage location, and sequestering it over geological timescales, either onshore or offshore. To date, three storage options have been proposed: geological storage, ocean storage, and mineral storage (IPCC, 2005).

Geological storage assembles pre-existing technologies used by the oil and gas industry, and involves storing CO_2 in depleted oil and gas reservoirs, saline aquifers, unmineable coal beds, or using it in enhanced oil recovery (Fig. 1.2). The global storage capacity of depleted oil and gas reservoirs and saline aquifers is predicted to be several gigatonnes (Gt) of CO_2, likely sufficient to host several decades of anthropogenic CO_2 emissions, thus significantly contributing to climate change mitigation efforts (Bickle, 2009). According to the Global Carbon Capture and Storage Institute (2015), there are 22 large-scale industrial geological storage projects worldwide, with an annual storage capacity of 40 million tonnes (Mt) of CO_2 (13 operational and 9 under construction), as well as 33 large-scale projects at different stage of development, as of May 2015.

Following the injection of CO_2 in a supercritical state, various trapping mechanisms are proposed to occur within the subsurface, including physical trapping (structural and stratigraphic trapping), solubility trapping, residual (capillary) trapping, and mineral trapping, each of which contributing to increase geological CO_2 storage security (Gunter et al., 2004; Suekane et al., 2008; Matter and Kelemen, 2009). Physical trapping is estimated to be the most dominant trapping mechanism in the early stages of CO_2 sequestration, where the upward migration of CO_2 is inhibited by low-permeability caprock or other structural and stratigraphic features, reducing the risk of CO_2 leakage into the overlying layers (Yang et al., 2010; Furre and Eiken, 2014). Solubility trapping involves the dissolution of CO_2 into the brine and its subsequent sinking within the reservoir, which results in the injected CO_2 remaining permanently trapped within the storage reservoir, without any risks of leakage into the overlying sediments, or the

atmosphere, in the long-term (Bolster, 2014). The efficiency of solubility trapping depends on various factors, including pressure and temperature conditions within the storage reservoir, as well as composition of the *in situ* brine (Bradshaw et al., 2007). The trapping of CO_2 through capillary forces within the pore space, residual trapping, is proposed to be an efficient trapping mechanism in the early stages of CO_2 injection (IPCC, 2005; Burnside and Naylor, 2014). It is noteworthy that residual trapping controls the ultimate extent of CO_2 migration within a storage reservoir (Niu et al., 2014). Mineral trapping, which has a dominant CO_2 immobilization potential in long-term, defines the incorporation of the injected CO_2 into minerals, caused by chemical precipitation (Klein et al., 2013). Natural analogues for mineral trapping have been documented in several studies, emphasizing the viability and efficiency of mineral trapping during geologic sequestration (Liu et al., 2011; Lu et al., 2011).

Oceans, the largest natural sink for anthropogenic CO_2 on Earth, have already taken up to almost half of the global CO_2 emissions over the last 200 years (Doney et al., 2009; Pandolfi et al., 2011). This has so far resulted in a pH decrease of about 0.1 unit for the surface waters since the preindustrial era, i.e., from 8.2 to 8.1, altering seawater geochemistry and biogeochemical cycles (Caldeira and Wickett, 2005; Feely et al., 2009). Relying on oceans CO_2 storage capacity, another form of carbon sequestration was first proposed in 1970's, which involves direct CO_2 injection into deep oceans, i.e., beyond 3000 m depth (Marchetti, 1977). However, current studies underline inherent risks associated with ocean CO_2 storage, including large perturbations to seawater geochemistry and resulting impacts on deep sea ecosystems (Barry et al., 2004; Kurihara et al., 2004). Thus, in 2007, the most comprehensive legal framework governing the marine environment, the OSPAR convention, prohibited direct discharge of CO_2 into deep oceans (OSPAR Decision 2007/1) (Chow, 2014).

Mineral storage, or mineral carbonation, consists of converting the anthropogenic CO_2 into solid inorganic carbonates via chemical reactions (Zevenhoven et al., 2011; Gislason and Oelkers, 2014). Mineral carbonation can be realized either *in situ*, i.e., within geological formations, or *ex situ*, i.e., within chemical processing plants. Mineral storage provides thermodynamically stable products, thus it is considered the most effective and permanent climate mitigation strategy, ruling out CO_2 leakage (Brent et al., 2012; Azdarpour et al., 2014). While geological carbon sequestration is considered the best option for large CO_2 emitters, mineral storage is

suggested to be an efficient mitigation strategy for small to medium scale industry, where total CO_2 emissions can be reduced on the order of 10-15% (Sanna et al., 2014). Mineral storage is also proposed to be an alternative climate change mitigation strategy for some countries, where geological CO_2 storage is limited or unviable (Koljonen et al., 2004).

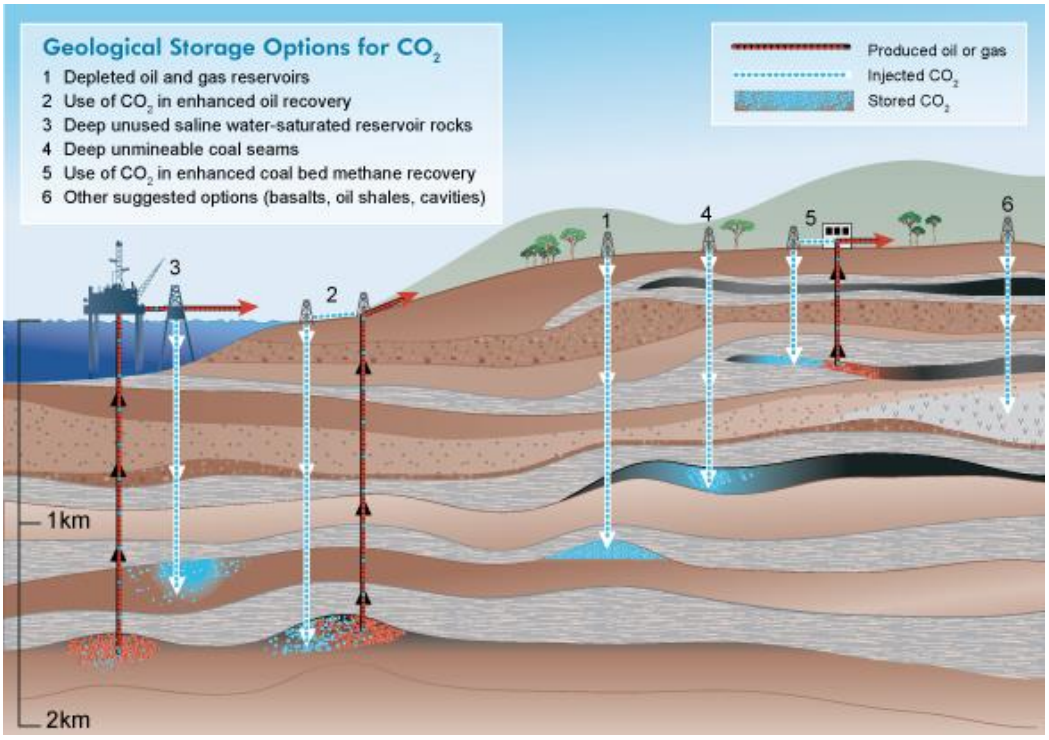

Figure 1.2 *Overview of geological CO_2 sequestration options (IPCC, 2005). CO_2 can be stored onshore or offshore, in depleted oil and gas reservoirs, saline aquifers, unmineable coal beds, or can be used in enhanced oil recovery.*

1.2.2 Leakage from offshore geological storage sites and monitoring

Although there is a scientific consensus that geological CO_2 storage can significantly contribute to climate change mitigation efforts, anthropogenic CO_2 leakage from the storage reservoir into the overlying water column, and ultimately the atmosphere, is undoubtedly a potential risk factor, calling into question the permanency and efficiency of geologic sequestration. According to IPCC projections, the stored CO_2 will certainly remain trapped over 100 years within the storage reservoir, and will likely be retained over 1000 years (IPCC, 2005). However, these projections are very site specific and should be evaluated critically. Many studies underline the likelihood of an

unpredictable CO_2 leakage from the storage reservoir, mainly due to hydraulic fracturing, reactivation of pre-existing faults, weakening of the caprock integrity, seismicity, as well as through operational or abandoned wells, in the vicinity of the CO_2 injection site (Nicoll, 2012; Blackford et al., 2013; Verdon et al., 2013; Miocic et al., 2014) (Fig. 1.3). If leakage were to occur, the released CO_2 could have unwanted impacts on the natural environment, adversely affecting climate change mitigation efforts (Bachu and Celia, 2009). In addition, CO_2 leakage from the storage reservoir can trigger the displacement of *in situ* CH_4 to the overlying layers, whose global warming potential is 25 times more than that of CO_2 (Damen et al., 2006).

Overall, it has been concluded that risks related to potential CO_2 leakage can be significantly reduced by appropriate storage site selection, followed by multidisciplinary long-term monitoring, and implementation of a comprehensive regulatory framework, as well as development of remediation techniques in the event of leakage (IPCC, 2005). The integration of various monitoring techniques with different spatial and temporal resolution can greatly enhance the detection of CO_2 leakage from the storage reservoir, notably in the early stages. Numerous monitoring techniques have been deployed at on-going and planned offshore storage sites including: 3D time-lapse seismic reflection, gravity and controlled-source electromagnetic surveys (Chadwick et al., 2005; Nooner et al., 2007; Arts et al., 2008; Chadwick et al., 2008; Chadwick et al., 2010; Alnes et al., 2011; Eiken et al., 2011; Boait et al., 2012; Hansen et al., 2013; Al Hseinat and Hübscher, 2014; Chadwick et al., 2014; Furre and Eiken, 2014; Grude et al., 2014; Park et al., 2014; White and Williams, 2014; Ghosh et al., 2015), side-scan sonar and multibeam bathymetry seabed imaging (Chadwick and Eiken, 2013; Heap et al., 2014), and wellhead pressure measurements (Chadwick et al., 2012).

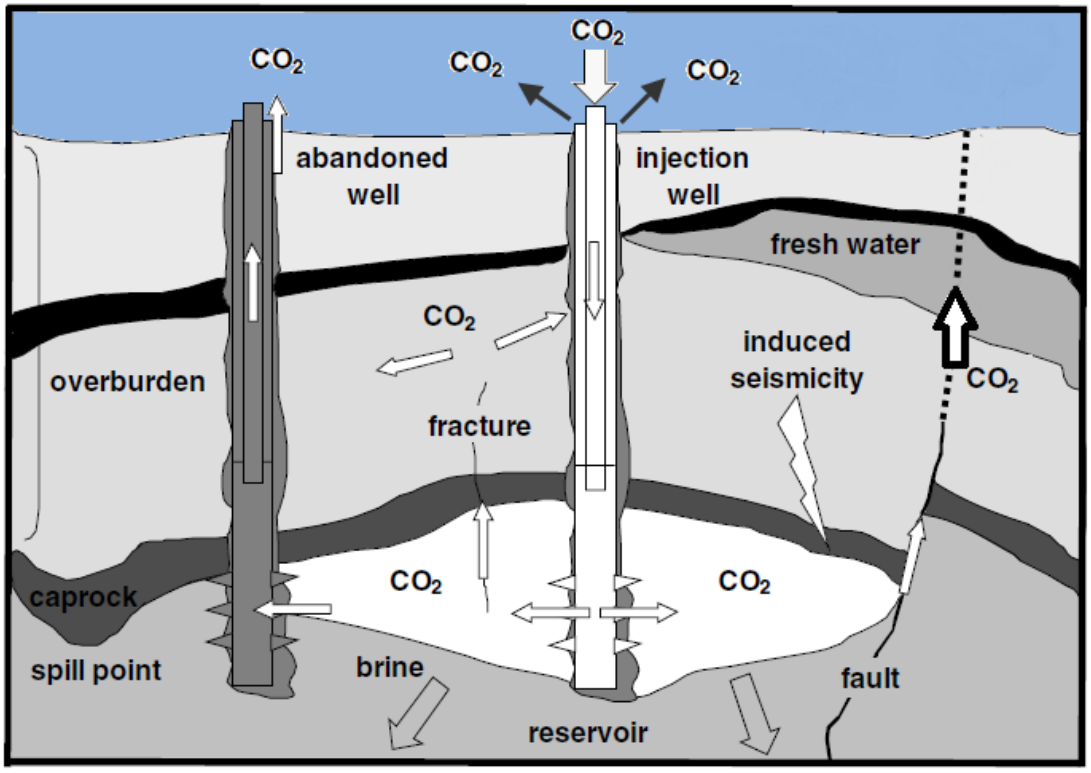

Figure 1.3 *Potential CO_2 leakage scenarios associated with offshore geological storage (modified after Damen et al. (2006)). The injected CO_2 might leak through fractures, existing wells or by means of a caprock failure.*

1.3 The QICS project - Ardmucknish Bay, Oban

A major component of the work presented in this thesis (Chapters 2, 3 and 4) was completed as part of the QICS project. QICS is a research project funded by the Natural Environmental Research Council (NERC, UK), with support from the Scottish Government. The project consortium is composed of UK research institutes and universities, as well as a Japanese research consortium, and a comprehensive advisory committee. The project started in June 2010, and was completed in June 2014.

The QICS experiment is the first controlled CO_2 release investigating the detectability and environmental impacts of leakage from geological storage sites (Blackford et al., 2014; Taylor et al., 2015). By means of a borehole drilled from land, 350 m offshore and at 12 m water depth, 4.2 tonnes of CO_2 were injected into the unconsolidated marine sediments at 12 m depth beneath the seabed in Ardmucknish Bay, Oban (Blackford et al., 2014; Cevatoglu et al., 2015) (Fig. 1.4). The CO_2 flow rate

was increased from 10 kgs/day to 210 kgs/day over 37 days of injection (from 17/05/2012 until 23/06/2012) (Blackford et al., 2014; Cevatoglu et al., 2015).

The temporal and spatial migration of CO_2, as well as its physical, geochemical and biological impacts, were continuously monitored during the controlled release experiment, using various multidisciplinary monitoring techniques, both in the vicinity of the injection and at control sites (Blackford et al., 2014). Baseline surveys were completed before the CO_2 injection, allowing to improve our understanding of the subsurface geology and the surrounding environment. Post-release surveys were crucial in determining the response of the system to the cessation of CO_2 injection, notably the time required for the site to restore back to equilibrium conditions. Gas flux calculations from passive hydroacoustics and water column bubble sampling indicated that 15% of the injected CO_2 was leaking at the seabed at Day 34, suggesting that the remaining CO_2 was either confined within the overburden at this time, in free gas or dissolved phases, or leaking at the seabed in dissolved phase (Blackford et al., 2014; Bergès et al., 2015).

In this thesis, we report and discuss the results from the analysis of the high-resolution 2D seismic reflection data (Table 1.1) acquired pre-release (2 days before injection), syn-release (6 days during injection), and post-release (nearly 2 years after injection), in the vicinity of the CO_2 injection site (Fig. 1.4; see Chapters 2, 3 and 4 for more details).

1.4 The ECO_2 project - Sleipner CCS site, North Sea

The second major component of the work presented in this thesis (Chapter 5) was completed as part of the ECO_2 project. The ECO_2 project is a large scale international research project, funded by the European Commission FP7 work program, and coordinated by GEOMAR. The main objectives of the ECO_2 project are to evaluate the likelihood and risks of leakage associated with sub-seabed CO_2 storage, as well as consequent environmental risks. The ECO_2 consortium involves 27 partners in total, with 24 research institutes, one independent foundation (Det Norske Veritas), and two industrial partners, including Statoil AS and Grupa Lotos. The project started in May 2011, and finished in April 2015.

The main study sites of the ECO_2 project involve operational and potential CO_2 storage sites including Sleipner (North Sea), Snohvit (Barents Sea), B3 field (Polish Baltic Sea), as well as natural CO_2 seep sites including Panarea (Tyrrhenian Sea), Jan Mayen vent fields (North Atlantic), Salt Dome Juist (North Sea), and Southern Okinawa Trough (SW of Japan). To date, 23 research cruises have been completed in these areas, using multidisciplinary monitoring and sampling techniques.

In this thesis, we report and discuss the results from the analysis of a multidisciplinary dataset (Table 1.1) acquired during the James Cook 077 (*JC077*) cruise, between 2^{nd}-28^{th} of September 2012, in the vicinity of Sleipner CCS site in the Central North Sea (Fig. 1.4; see Chapter 5 for more details). To achieve the main objectives set in Section 1.5, ten sciences missions were completed during the *JC077* cruise, using various instruments mounted on an autonomous underwater vehicle (Autosub 6000). Instruments included an Edgetech 2200-M Modular Sonar System (High-resolution seismic reflection (Chirp) and side scan sonar surveys), a 5M pixel colour camera, as well geochemical sensors (Table 1.1). In addition, a shipboard multibeam system (EM 710) was used for bathymetry and backscatter data acquisition. Seabed video surveying was completed using a robotic underwater vehicle (HyBIS). Sediment and water column samples were collected using British Geological Survey (BGS) 6 m seabed vibrocorer and a CTD rosette, respectively (Table 1.1). EK60 echosounder profiling was also used throughout the *JC077* cruise.

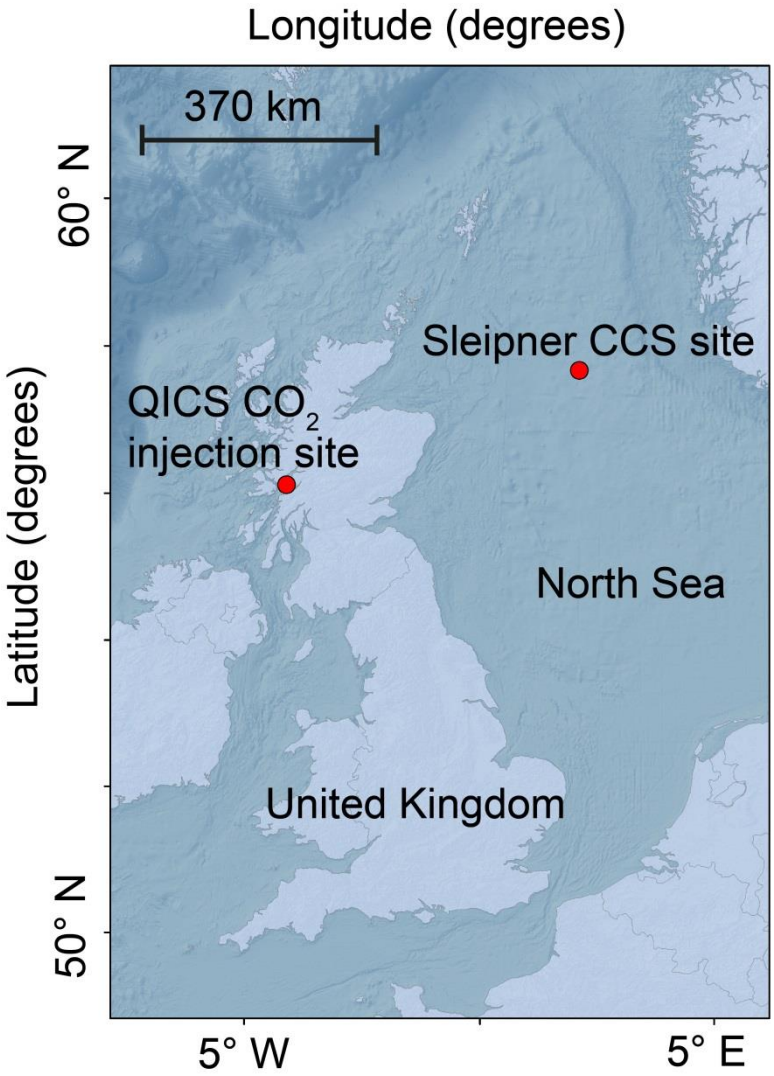

Figure 1.4 *Location of the QICS and Sleipner CO_2 injection sites. CO_2 was injected over 37 days in Ardmucknish Bay, Oban, during the QICS project. Sleipner Carbon Capture and Storage site has been operational since 1996, with 1 Mt of CO_2 annually injected into a saline aquifer in the Central North Sea. The JC077 cruise was completed in the vicinity of Sleipner CCS site.*

Project	Time	Data type	Thesis Chapter
QICS Experiment, Ardmucknish Bay	Pre-release 30/08/2010 - 16/05/2012	**Seismic reflection (Chirp)**	**2, 3, 4**
		Seismic reflection (boomer)	**4**
		Multibeam bathymetry	-
		Sediment coring	**2, 4**
		Water column profiling and sampling	-
		Benthic chambers	-
		Passive acoustics	-
	Syn-release 17/05/2012 - 23/06/2012	**Seismic reflection (Chirp)**	**2, 3, 4**
		Seismic reflection (boomer)	**2, 3, 4**
		Multibeam bathymetry	**2**
		Sediment coring	-
		Water column profiling and sampling	-
		Benthic chambers	-
		Time-lapse photography	-
		Passive acoustics	**4**
		Atmospheric CO_2 sensor	-
	Post-release 24/06/2012 - 24/04/2014	**Seismic reflection (Chirp)**	**3, 4**
		Sediment coring	-
		Water column profiling and sampling	-
		Benthic chambers	-
		Time-lapse photography	-
		Passive acoustics	-
ECO_2, Sleipner, JC077 cruise	02/09/2012 - 28/09/2012	**Autosub 6000 seismic reflection (Chirp)**	**5**
		Autosub 6000 side scan	**5**
		Autosub 6000 camera	**5**
		Autosub 600 Eh sensor	**5**
		Autosub 600 pH, pCO_2 and ORP sensors	-
		EM710 multibeam bathymetry	**5**
		CTD water column profiling	**5**
		Sediment vibrocoring	**5**
		HyBIS video surveying	**5**
		HyBIS sediment sampling	-
		EK60 echosounder	-

Table 1.1 *Source of data acquired as part of the QICS and ECO_2 projects. Data used in this thesis are highlighted in bold.*

1.5 Research questions

The key research questions addressed in this thesis are as follows:

- What are the impacts of free gas on sediment acoustic properties and how these are related to the injection rate/total injected volume?
- What are the main mechanisms controlling gas migration within the subsurface?
- What are the best monitoring technologies to detect free gas within the overburden and leakage into the overlying water column?
- How can we quantify free gas within the subsurface?

1.6 Thesis structure

Chapter 2 investigates acoustic evidence of CO_2 fluxing within the overburden and the overlying water column, as well as the temporal and spatial evolution of the CO_2-related acoustic anomalies, from 2D time-lapse high-resolution seismic reflection data (QICS). The impact of CO_2 injection on sediment acoustic properties, including seismic reflectivity and attenuation, as well as mechanisms controlling CO_2 migration, are investigated.

Chapter 3 investigates potential acoustic evidences of CO_2 on the post-release high-resolution 2D seismic reflection data (QICS). The impacts of CO_2 injection on sediment acoustic properties are analysed, and the results are compared to the observations from the pre-release and syn-release seismic reflection datasets. The mechanisms controlling CO_2 migration within the overburden are investigated after the cessation of CO_2 injection.

Chapter 4 presents a methodology to quantify gaseous CO_2 within the overburden, at the QICS site. Temporal thickness variations of the same stratigraphic unit are used to constrain seismic P-wave velocity changes from high-resolution seismic reflection data. These seismic P-wave velocities are then used together with a rock physics model to get the *in situ* gas content/volume within the overburden. In addition, acoustic impedance inversion of the seismic reflection data is performed, to quantitatively assess the impact of CO_2 injection on the acoustic impedance of the key stratigraphic boundaries.

Chapter 5 presents the multidisciplinary dataset acquired during the *JC077* cruise, in the vicinity of Sleipner CCS site, to investigate the fluid activity within the shallow overburden and the overlying water column in the Central North Sea (ECO_2). This dataset is also used to improve our understanding of the surrounding geology around the Sleipner CCS site, and its control on the fluid flow activity, with specific attention to a seabed fracture (Hugin Fracture), previously discovered 25 km N of the Sleipner CCS site (Landschulze and Pedersen, 2013b; Pedersen et al., 2013).

Finally, **Chapter 6** synthesizes the major findings of the present work, and outlines some directions for future work.

Chapter 2

Gas migration pathways, controlling mechanisms and changes in sediment acoustic properties observed in a controlled sub-seabed CO_2 release experiment

The following chapter is published: Cevatoglu, M., Bull, J.M., Vardy, M.E., Gernon, T.M., Wright, I.C., Long, D., 2015. Gas migration pathways, controlling mechanisms and changes in sediment acoustic properties observed in a controlled sub-seabed CO_2 release experiment. *International Journal of Greenhouse Gas Control* 38, 26-43, doi: 10.1016/j.ijggc.2015.03.005.

Abstract

Carbon Capture and Storage (CCS) is a key technology to potentially mitigate global warming by reducing carbon dioxide (CO_2) emissions from industrial facilities and power generation that escape into the atmosphere. To broaden the usage of geological storage as a viable climate mitigation option, it is vital to understand CO_2 behaviour after its injection within a storage reservoir, including its potential migration through overlying sediments, as well as biogeochemical and ecological impacts in the event of leakage.

The impacts of a CO_2 release were investigated by a controlled release experiment that injected CO_2 at a known flux into shallow, unconsolidated marine sediments for 37 days. Repeated high-resolution 2D seismic reflection surveying, both pre-release and syn-release, allows the detection of CO_2-related anomalies, including: seismic chimneys; enhanced reflectors within the subsurface; and bubbles within the water column. In addition, reflection coefficient and seismic attenuation values calculated for each repeat survey, allow the impact of CO_2 flux on sediment acoustic properties to be comparatively monitored throughout the gas release. CO_2 migration is interpreted as being predominantly controlled by sediment stratigraphy in the early stages of the experiment. However, either the increasing flow rate, or the total injected

volume become the dominant factors determining CO_2 migration later in the experiment.

2.1 Introduction

CCS is considered a promising technology to mitigate anthropogenically driven climate change which would enable the continued use of fossil fuels, while contributing on the order of 15-50% of the total climate change mitigation effort until 2100 (Katzer et al., 2007). CCS involves capturing CO_2 from industrial facilities and energy-related sources, transporting it to a storage location, and sequestering it over geologic timescales, with the aim of avoiding its release into the atmosphere. Geological storage is considered the most viable given the overall available storage capacity (at least 2000 gigatonnes (Gt) of CO_2), and the maturity of current technologies within use by the oil industry (IPCC, 2005; Celia and Nordbotten, 2009; Pires et al., 2011).

Associated with the growing interest in CCS as an effective climate mitigation technology, there is an emerging public debate concerning the associated operational and *in situ* risks of leakage. Various factors leading to leakage can be identified within the surface and subsurface. Failure of injection facilities, including pipelines and wellheads on the surface, as well as injection wells within the subsurface, are operational risks. Inadequately completed abandoned wells, insufficient/incomplete top seals or existing faults can cause the ascent of resident fluids (Lackner and Brennan, 2009; Upham and Roberts, 2011). The increase in the subsurface pressure may lead to undesirable geomechanical and hydrodynamical effects, potentially opening pre-existing fractures and/or initiating new fracturing, as well as triggering seismicity in some cases (Bachu, 2008). Such CO_2 leakage could have significant damaging effects to the local environment, with elevated CO_2 levels known to be toxic to ecosystems, as well as contamination of surface waters, decrease in pH and resulting ocean acidification, all being possible outcomes in the medium to long term (Benson et al., 2002; Damen et al., 2006). CO_2 leakage causes an additional carbon input into the atmosphere, and therefore represents a loss of value, or even calling into question CCS operations. Impurities, including H_2S and SO_2, that may be present in leaking CO_2, also have significant environmental impacts (West et al., 2005).

Large-scale implementation of CCS as a viable climate mitigation option requires a much improved understanding of the fate of the injected CO_2 in the subsurface, including its migration, and subsequent potential impacts on the marine environment. The goal of the controlled CO_2 release experiment, Quantifying and Monitoring Potential Ecosystem Impacts of Geological Carbon Storage (QICS), conducted in Ardmucknish Bay Oban, Scotland (Fig. 2.1a), was to simulate leakage into the near-surface from geological storage sites, and thus improve our understanding of the behaviour of the injected CO_2 in the subsurface, critical injection rates leading to leakage, amount of leakage, and resulting physical, geochemical, and environmental impacts (Blackford et al., 2014). This paper focuses specifically on the analysis of high-resolution near-surface 2D Chirp and boomer seismic reflection data, together with multibeam bathymetry imagery, acquired before, and during CO_2 release. These data allow an understanding of the CO_2 migration within the subsurface and into the overlying water column, as well as impacts of CO_2 injection on sediment acoustic properties, namely reflectivity and seismic attenuation.

2.2 The QICS experiment

As part of the QICS experiment, a narrow borehole terminating in unconsolidated, shallow marine sediments was drilled from land in Ardmucknish Bay Oban, during February 2012 (Fig. 2.1a). At the end of the borehole, a 5 m long well screen was installed at a depth of 12 m below the seabed to operate as a diffuser, allowing controlled CO_2 release into sediments from the 17th of May 2012 until the 23rd of June 2012 (Table 2.1). Details of the drilling operation, and controls on the sub-sea location of the pipeline are given in Taylor et al. (2015). CO_2 injection rate was increased up to 210 kgs/day from the beginning of the QICS experiment (17/05/2012, Day 0) until Day 37 (23/06/2012) (Fig. 2.1b). The total amount of CO_2 injected during the 37-day release was c. 4200 kgs (Taylor et al., 2015).

Numerous monitoring strategies were deployed to track the injected CO_2, detect leakage from the subsurface into the overlying water column, and potentially ultimately into the atmosphere. The period after the cessation of CO_2 injection was also investigated to see if and how the system stabilised post-release, and how these related/differed from the initial conditions. A comprehensive dataset, consisting of multibeam bathymetry, 2D seismic reflection, passive hydroacoustics (Bergès et al.,

2015), geochemistry, microbiology, macroecology, camera and video surveys, were acquired covering pre-release, syn-release, and the recovery period stages (up to 90 days after cessation of injection), to evaluate the interaction of injected CO_2 with the marine environment. In this paper, we report the results of repeated 2D seismic reflection profiling that was used to determine the spatial and temporal propagation mechanisms of the gaseous CO_2 and assess its role in changing sediment acoustic properties.

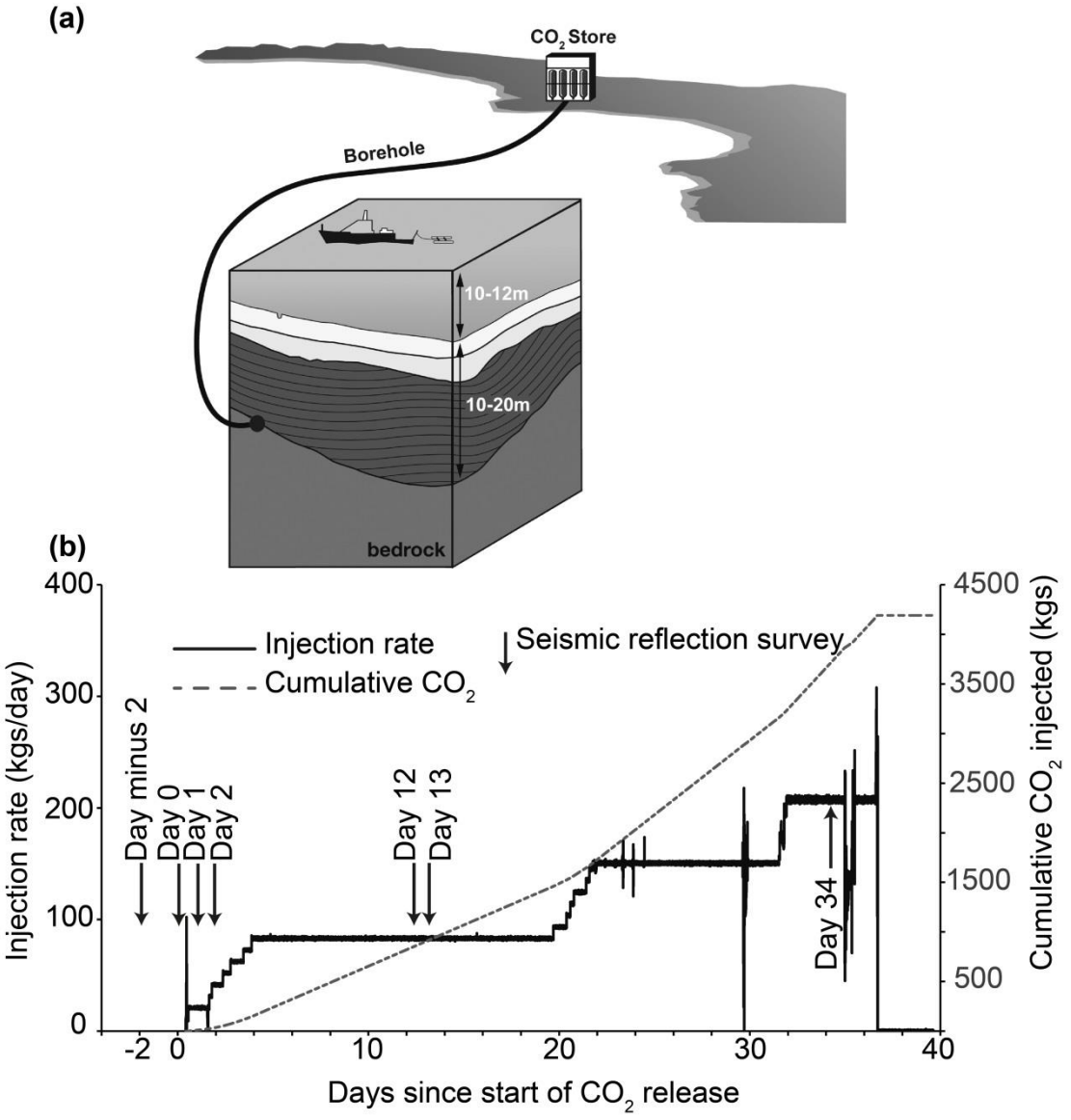

Figure 2.1 *Schematic overview of CO_2 release experiment, changes in total gas injection flux and timing of 2D seismic reflection surveys.* ***(a)*** *A stainless steel lined borehole was connected to a controlled CO_2 supply located onshore, with a 5 m long diffuser located 12 m below the sea floor. The diffuser (black dot) was located at the*

interface between bedrock and layered glacio-marine sedimentary sequence, which is overlain by an unlayered sequence. Observations were conducted using in situ, boat towed and diver deployed instrumentation; this paper focusses on the analysis of repeated 2D seismic reflection surveys. ***(b)*** *Gas injection flux during the experiment and the dates at which 2D seismic reflection surveys were completed pre-release and during the CO_2 release (black arrows; see also Table 2.1).*

Days	Description	Seismic source	CO_2 injection rate (kgs/day)
15/05/2012	pre-release (Day minus 2)	Chirp	none
17/05/2012	1st day of release (Day 0)	Chirp	20
18/05/2012	2nd day of release (Day 1)	Chirp	20
19/05/2012	3rd day of release (Day 2)	Chirp	45
29/05/2012	12 days after release (Day 12)	Chirp	85
30/05/2012	13 days after release (Day 13)	Chirp	85
20/06/2012	34 days after release (Day 34)	Boomer	210

Table 2.1 *Description of the 2D seismic reflection datasets collected during the QICS experiment in Ardmucknish Bay and associated CO_2 injection rates.*

2.2.1 Subsurface structure of the QICS site

The QICS site was selected as being suitable for the controlled CO_2 release for several reasons, including: proximity to an onshore drill site; having bedrock that was conducive to drilling; and having a suitable sequence and thickness of sediments above bedrock offshore for the drill pipe to terminate within. High-resolution 2D seismic imaging and sediment coring show that the site comprises up to 20 m of sediment overlying glacial till/bedrock, under 10-12 m depth of water, within 350 m range of a drill site, on the northern shoreline of Ardmucknish Bay (Taylor et al., 2015). The pre-release boomer data suggest that it is possible to distinguish between the glacial till and bedrock without drilling so that an undisturbed location with minimal till coverage was selected for the gas delivery borehole (Taylor et al., 2015). Multibeam bathymetry data collected before the experiment showed a featureless seabed with water depths ranging from 5 m to 30 m with no evidence of pockmarks.

Analysis of sediment cores (including Core 6) collected 200 m S of the CO_2 injection site (Figs. 2.2 and 2.3a), shows that the surficial sediments comprised a c. 1.5 m thick layer of coarse to very coarse sand and gravel, overlying a c. 2 m thick fine

sand layer (see Taylor et al. (2015) for a detailed description of the regional stratigraphy). Underlying the fine sand layer is a laminated mud, with the interface appearing as a sharp decrease in grain size (Fig. 2.2), c. 3-4 m below the seabed. Regional 2D seismic reflection data suggest that this lower sediment unit is c. 15 m thick in total (Fig. 2.4). In this study the boundary between the near-surface coarse sand and gravel, and fine sand is defined as Horizon 1, and the boundary between the fine sand and the underlying laminated mud as Horizon 2 (Table 2.2). Taylor et al. (2015) map Horizon 2 as the top of an extensive, highly layered seismic facies (SSS II) interpreted as being glacio-marine deposition, while the fine sand corresponds to their facies SSS III, which is one of several stacked, erosional, acoustically transparent, fluvial units.

This stratigraphy is in agreement with 2D seismic data collected previously in Loch Etive (Fig. 2.3a), located 6 km N of Oban, showing two seismic sequences separated by a distinct reflector "E1" with modern fluvial sediments, less than 5 m thick, overlying 10-50 m thick glacio-marine sediments (Howe et al., 2002; Nørgaard-Pedersen et al., 2006). The unconformity "E1" corresponds to the erosional surface Horizon 2 in our study, and represents an abrupt change in the sedimentary regime in Ardmucknish Bay from glacially influenced conditions (Younger Dryas; 12.9-11.7 Ka BP) with silty-muddy sediments to overlying coarser-grained sandy-silty fluvial sediments deposited during the Holocene (Fig. 2.2).

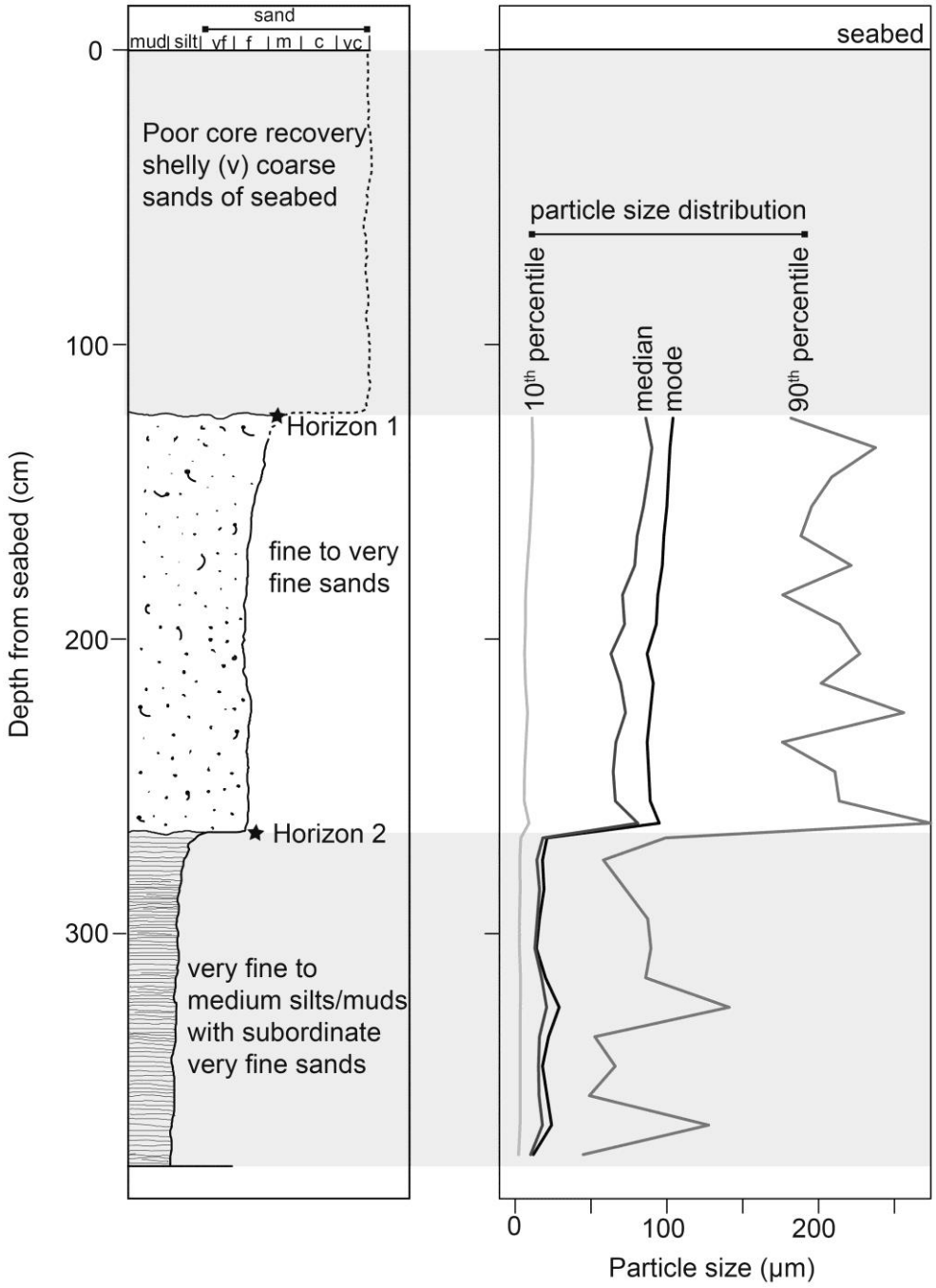

Figure 2.2 *Detailed stratigraphy and grain-size distribution of sediments within Core 6 (position shown in Fig. 2.3a). The seabed is composed of coarse-grained shelly sediments which were only partially recovered. The positions of stratigraphic boundaries that are linked to seismic horizons Horizon 1 and Horizon 2 are shown. Previous studies date Horizon 2 to be of early Holocene age (Howe et al., 2002).*

Horizon	Depth	Description
Seabed	0 m	High amplitude and continuous, undulating seismic reflector overlying reflection free unit.
Horizon 1	~-1.5 m	Sub-parallel to seabed, separating two reflection free units.
Horizon 2	~-3/-4 m	Continuous reflector with significant topography which erosionally truncates the underlying unit. Separates reflection free unit above from underlying unit with regularly spaced sub-parallel reflections.
Base of the layered sequence	~-15/-16 m	Undulating reflector with high seismic amplitude overlying a zone with chaotic reflectivity. Marks base of unit with simple sub-parallel reflectors. Seismic imaging is limited beneath this reflector.

Table 2.2 *Seismo-stratigraphic horizons imaged on the 2D seismic reflection data, Ardmucknish Bay. Depths are those observed at the diffuser location. From previous studies, Horizon 2 was dated to early Holocene (Howe et al., 2002), and corresponds to the boundary between modern fluvial sandy sediments above, and to glacio-marine finer-grained sediments below. See main text for more details.*

2.3 Materials and methods

2.3.1 Multibeam bathymetry and 2D seismic reflection data acquisition and processing

Seven high-resolution 2D seismic reflection surveys (176 Chirp and 18 boomer profiles, totalling 65 km of data) were acquired in Ardmucknish Bay covering both pre-release and CO_2-release stages (Fig. 2.3; Table 2.1). Line spacing ranged from 5 m to 15 m, with closer spacing around the diffuser, while the length of the 2D seismic reflection profiles varied between 250 m and 400 m (Fig. 2.3). Multibeam bathymetry data were acquired using a Kongsberg EM 2040-07 echosounder, and tidally corrected. Technical details of the 2D seismic reflection and multibeam bathymetry surveys are summarized in Table 2.3.

Chirp transducers and a boomer plate were both mounted on catamarans towed behind the survey vessel, and all 2D seismic reflection data were corrected for layback

(Table 2.1). Boomer data were band-pass filtered within the frequency range 200-500-4000-6000 Hz. The seismic processing flow applied to the Chirp data included correlation with the source sweep (Quinn et al., 1998), Ormsby band-pass filtering, 3-trace mixing, true amplitude recovery correction and instantaneous amplitude correction. There is no migration applied to the 2D seismic data. Where Chirp data were used for physical property determination, only correlation was applied; no further processing was undertaken. Finally, tidal corrections were applied to the Chirp and boomer data using the pre-release tidally-corrected swath bathymetry mosaic.

It is worth noting that the water and target depths investigated in this study, c. 10-12 m and less than 15 m, respectively, are significantly shallower than that typically investigated by the oil and gas industry. The frequency range of the high-resolution 2D seismic systems (1.5-13.0 kHz for Chirp and 0.5-4.0 kHz for boomer) results in an improved vertical seismic resolution of tens of cm compared to a few metres for typical industry seismic data. However, the data presented here consist of a repeat set of 2D seismic reflection profiles, which has inherent limitations in terms of tow depth, tidal state, navigation and tow speed repeatability, as well as wavefield sampling (and therefore imaging) when compared to the 3D marine surveying, typical of industry surveys. Readers are advised to bear in mind these differences in seismic source and acquisition methodology when comparing the presented results with previously published seismic time-lapse studies of CCS sites (Arts et al., 2008; Chadwick et al., 2010).

2.3.2 Reflection coefficient and seismic attenuation calculation

Gas within pore space will change the bulk acoustic properties of marine sediments. In this paper two attributes of the 2D seismic reflection data, and their spatial and temporal variation, were determined: the reflection coefficient of the seabed and subsurface horizons; and acoustic attenuation of near-surface sediments. These data are then used to infer variations in the spatial distribution and flux of CO_2.

Following previous work (Anstey, 1977; Warner, 1990; Spence et al., 1995; Bull et al., 1998), the reflection coefficient of the seabed (K_{sf}) and a deeper reflector (K_{dr}) can be calculated from Eqs. 1 and 2:

$$K_{sf} = \frac{TWT(m)}{TWT(p)} \times \frac{A(m)}{A(p)} \quad (1)$$

$$K_{dr} = K_{sf} \times \frac{TWT(dr)}{TWT(p)} \times \frac{A(dr)}{A(p)} \quad (2)$$

where, *A(p)*, *A(m)* and *A(dr)* represent the seismic amplitudes of the primary seabed reflector, the first multiple of seabed reflector and deeper reflector respectively, while *TWT(p)*, *TWT(m)* and *TWT(dr)* are the corresponding two-way travel times.

These relationships inherently include a correction for geometrical spreading, which is proportional to the ratio of *TWT(m)/TWT(p)* in Eq. 1, and *TWT(dr)/TWT(p)* in Eq. 2. Since the application of complex seismic processing algorithms (such as deconvolution) often results in alteration of reflection amplitudes, the 2D seismic data used in the reflection coefficient analysis were simply correlated with the source sweep in Chirp data, and band-pass filtered, in the case of boomer data, with no further processing in either. After correlation, a time gate of 1 ms was chosen to analyse amplitude values associated with the seabed and subsurface horizons. It should be noted that the analysis of reflection coefficient is based on the ratio of amplitudes. Therefore, the changes in the raw amplitudes of the whole traces on different survey days due to changes in seismic source and/or survey conditions do not affect our calculations.

The spectral-ratio technique has previously been used to determine the seismic quality factor (*Q*), which is inversely proportional to seismic attenuation (α) (Williams et al., 2002; Schock, 2004; Pinson et al., 2008). By combining this technique with a statistically robust regression, it is possible to calculate *Q* with an associated confidence interval for the uppermost 30 m of marine sediments (Pinson et al., 2008) (Eq. 3):

$$ln\frac{|A_R(f)|}{|A_S(f)|} = ln\frac{|G_R \times (1 - R_S^2) \times R_R|}{|R_S|} - \frac{\pi \times f \times \Delta t_R(f)}{Q(f)} \quad (3)$$

where $A_S(f)$ and $A_R(f)$ indicate amplitudes of the seabed reflection and horizon of interest beneath the seabed at the frequency *f*. G_R, R_S and R_R correspond to spherical

divergence between the seabed and the horizon of interest, reflection coefficient of the seabed, and the horizon of interest, respectively. Finally, $\Delta t_R(f)$ is the two-way travel time between the seabed and the horizon of interest.

Under the condition of sampling two sub-horizontal reflections, G_R can be considered to be constant from trace to trace, and also frequency independent. In addition, the target reflection is required to be shallower than the first seabed multiple to avoid delayed energy contaminating the spectra. The effect of noise and local inhomogeneities can be overcome by using multiple traces, which produces a more accurate Q estimation, but under these conditions we have to assume that R_S and R_R are laterally consistent. After selecting suitable traces that clearly image the seabed and the seismic horizon of interest, 2D seismic data were subjected to a sequence of 1 kHz wide zero-phase Ormsby band-pass filters, where the central frequency incremented by 0.25 kHz steps, and reflection amplitudes were extracted for each frequency window. After the application of the spectral-ratio technique to the selected traces, two plots were generated. The spectral signature plot (SSP), which shows the variation of $ln\ (|A_R|/|A_S|)$ and $ln\ (Noise/|A_S|)$ with frequency, which was used to identify the uncontaminated frequency band containing the attenuation trend, in a way that the selected band contains signal above the background noise, and has a good match between the mean and median values. The average Q of a sediment package was then calculated by plotting the attenuation trend plot (ATP), showing the variation of $-ln\ |(A_R(f)/A_S(f))|$ with $\pi f \Delta t_R(f)$ in Eq. 3. By means of using simple least-square regression, Q values are first estimated with 95% confidence interval, and then by fitting the best iteratively reweighted robust least-squares regression curve to the current data points, a robust Q value is calculated. The analysed 2D seismic data had only minimal processing applied (correlation with source sweep), as further processing would modify the spectral content of the data, and therefore invalidate the Q calculation. Similarly to reflection coefficient calculation, Q estimates are based on the ratio of the relevant horizon amplitudes, thus excluding the absolute changes in the raw amplitudes on different survey days.

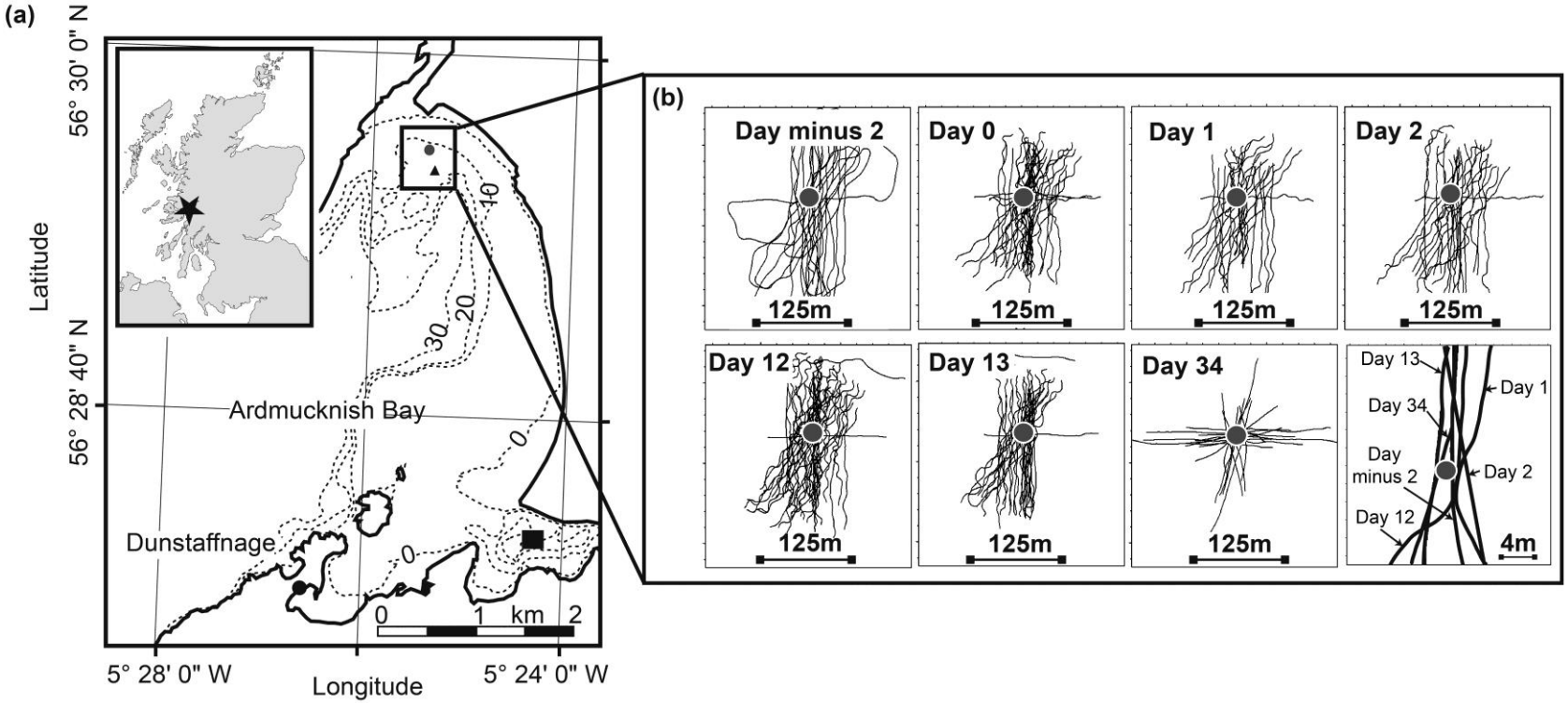

Figure 2.3 *Detailed location map of the experiment site and 2D seismic reflection profiles within Ardmucknish Bay.* ***(a)*** *Diffuser (dark gray dot) and position of Core 6 (black triangle), superimposed on the bathymetry data (10 m contours). Entrance to Loch Etive is indicated by the black rectangle.* ***(b)*** *Location maps of 2D seismic profiles acquired on different days; Chirp data were acquired on Day minus 2 to Day 13; while boomer data were acquired on Day 34. The bottom right box illustrates track lines of the seismic data illustrated in Fig. 2.4a-f. The diffuser is indicated by the dark gray dot in each case.*

	Seismic Reflection		Multibeam Bathymetry	
Seismic Source	Geoacoustics GeoChirp	Applied Acoustics Boomer	Operating frequency	400 kHz
Trace spacing	0.3 m	0.35 m	Pulse length	50 μs
Seismic Source	4 transducers array, 1.5-13 kHz, 32ms, sine squared 8^{th} sweep (Gutowski et al., 2002)	Boomer plate operating at 200 J	Swath width	280° (400 beams x 0.7°)
Hydrophone	1 m long, single channel, towed behind the survey vessel	10 m long, single channel, towed behind the survey vessel	Theoretical Resolution	4 cm
Pulse rate	0.25 Hz	3 Hz		
Trace length	200 ms	250 ms		
Surveyed area	600 m x 400 m	400 m x 500 m		
Line orientation	NS, EW, NE-SW	EW, NE-SW, NW-SE		
Survey Vessel	*R/V Seol Mara*	*R/V White Ribbon*		

Table 2.3 *2D seismic reflection and multibeam bathymetry data acquisition parameters. See Supplementary material (Appendix A) for more detail about Chirp and boomer seismic survey geometries.*

2.4 Results and analysis

2.4.1 Subsurface seismic stratigraphy

Four horizons were identified around the CO_2 injection area in Ardmucknish Bay from Chirp and boomer 2D seismic reflection profiles (see also Section 2.2.1). The topmost horizon is the seabed, which is a high amplitude slightly undulating reflector, with depth increasing up to c. 15 m with distance from the shore (Figs. 2.2 and 2.4). The second horizon, referred to as Horizon 1, is sub-parallel to the seabed, c. 2 ms (around 1.5 m) below it (Figs. 2.2 and 2.4). The next horizon, Horizon 2, c. 3-4 m below the seabed, defines the base of an acoustically transparent, reflection-free deposit, and represents the boundary between this unit and the underlying stratified sedimentary sequence (Figs. 2.2 and 2.4). Horizon 2 is a characteristic unconformity, easily traced throughout the 2D seismic dataset, has significant topography, deepening significantly to the W-SW, and erosionally truncates the underlying sequence. The layered sequence beneath Horizon 2 is a thick (up to 40 m) stratigraphic facies, containing regularly spaced sub-parallel reflections (Figs. 2.2 and 2.4). The deepest horizon detected on the 2D seismic data corresponds to the base of the layered sedimentary infill (Fig. 2.4). The base of the layered sedimentary infill is a chaotic seismic horizon with high amplitude seismic reflections, and has a highly undulating surface, deepening significantly in the SE while truncating Horizon 2 in the W-SW. The properties of these four key seismic horizons are summarised in Table 2.2.

Recent work on the depositional history of the Scottish west coast fjords since the last glaciation has revealed the presence of diamict (Mcintyre and Howe, 2010), which likely corresponds to the stratigraphic unit below the base of the layered sedimentary infill in this 2D seismic dataset. Thus, we interpret the base of the layered sedimentary infill as being the top of a thin glacial till unit overlying bedrock.

2.4.2 Temporal and spatial evolution of CO_2-related acoustic anomalies

The 2D seismic reflection data were also interpreted for evidence of gas in the water column and sediment, including: acoustic turbidity; gas blanking; bright spots; reflector terminations; and polarity reversals. The aim of the interpretation was to

understand the temporal development of CO_2 migration pathways in the subsurface and overlying water column. Acquisition of pre-release 2D seismic reflection data was crucial for determining the baseline subsurface reflectivity, allowing comparison with 2D seismic data acquired during CO_2 injection. As a result, many CO_2-related temporal reflectivity changes were observed on the Chirp and boomer 2D seismic profiles (Fig. 2.4).

Analysis of the pre-release 2D seismic data (Day minus 2) reveals no direct indicators of gas within the subsurface around the CO_2 injection site (Fig. 2.4a). Over the first two days of release, Day 0 and Day 1, where the CO_2 injection rate/total injected volume was relatively small (Table 2.1), there is an increase in the reflectivity of Horizon 2, compared to pre-release data (Fig. 2.4b). With the increase of CO_2 injection rate/total injected volume (Table 2.1), 2D seismic data show localised, well-defined, low amplitude, vertical transparent zones up to 8 m in width, rising from the diffuser up to Horizon 2, as well as the formation of small scale pockmarks (4.5 m wide, 60 cm deep) on the seabed (Fig. 2.4c).

With an increased amount of CO_2 injected into the subsurface, by Day 12 and Day 13, Horizon 2 displays enhanced reflectivity and up-warped geometry, but the vertical transparent zones and associated reflector terminations remain confined within the layered sequence below Horizon 2 (Fig. 2.4d and 2.4e). However, water column anomalies are also widely observed on the 2D seismic data (Fig. 2.4e).

Boomer data collected later in the release period, Day 34, reveal many CO_2 related features, including: enhanced reflectivity for Horizon 2; columnar zones of low and chaotic seismic reflectivity; and water column anomalies (Fig. 2.4f). Most importantly, following the significant increase in the CO_2 injection rate/total injected volume at Day 34 (Table 2.1), these vertical acoustic disturbance columns, which were previously confined within the layered sedimentary sequence below Horizon 2, now reach the seabed, leading to CO_2 leakage directly into water column (Fig. 2.4f).

Multibeam bathymetry data collected on Day 34 clearly image both pockmarks on the seabed and the column of gas within the water column (Blackford et al., 2014) (Fig. 2.5). The position of the pockmarks and water column bubbles are all observed up to c. 15 m W of the diffuser (Fig. 2.5). The height of the gas streams above the seabed varies over the area: bubbles in the immediate vicinity of the diffuser were imaged to

rise up to c. 8 m above the seabed, whereas more distal bubbles are observed to rise up to c. 2 m above the seabed (Fig. 2.5).

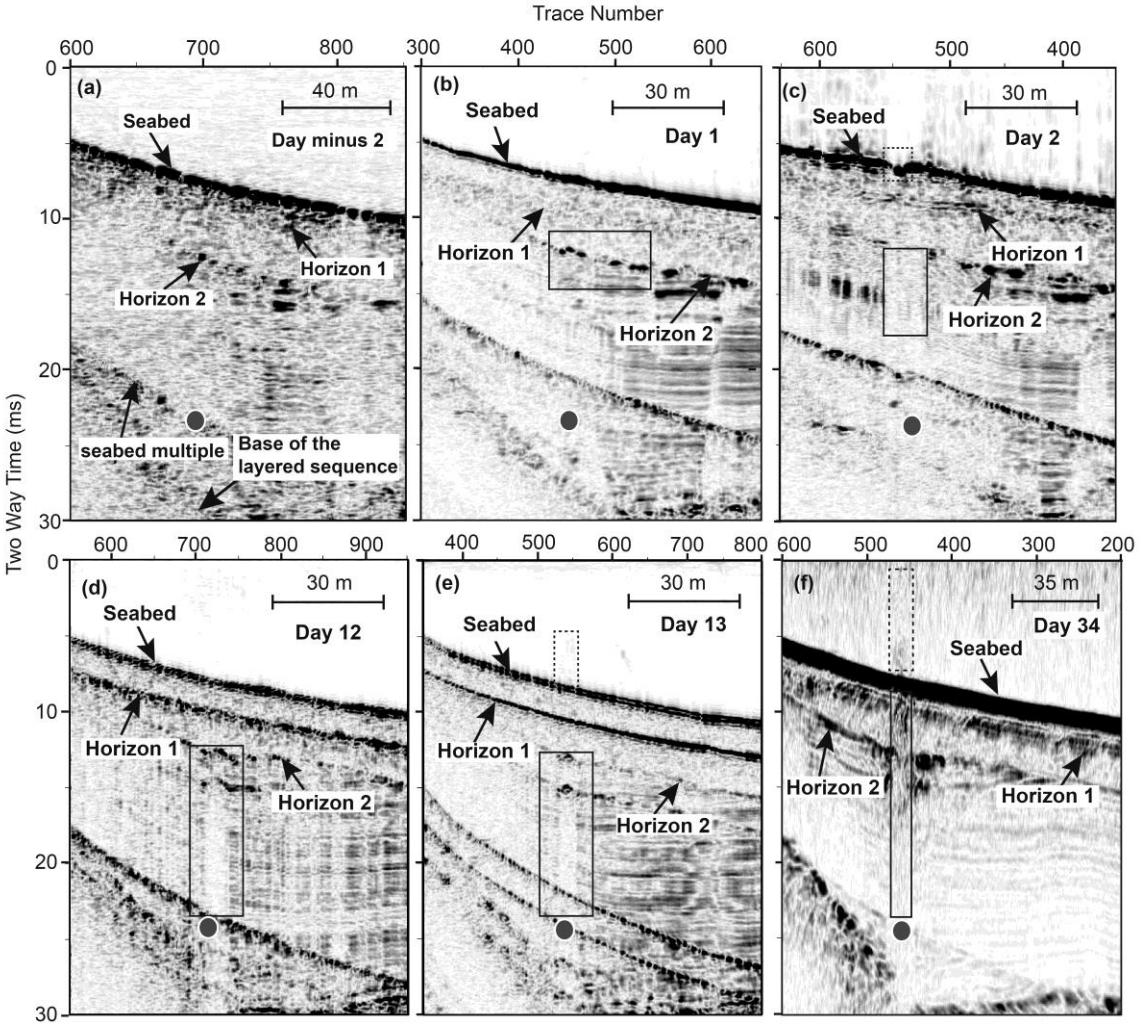

Figure 2.4 *Time-lapse 2D seismic reflection data illustrating CO_2 migration within unconsolidated sediments around the diffuser, Ardmucknish Bay. The position of each seismic profile is given in Fig. 2.3b.* ***(a)*** *Pre-release Chirp data. There is no evidence for gas on the seismic data before CO_2 injection. Sandy-silty fluvial sediments are located above Horizon 2, and silty-muddy glacio-marine sediments are located below Horizon 2.* ***(b)*** *Day 1 Chirp data. Following gas release, the reflectivity of Horizon 2 has slightly increased (black rectangle).* ***(c)*** *Day 2 Chirp data. CO_2 injection has caused acoustic blanking within sediments (black rectangle), as well as formation of pockmark on the seabed (black dashed rectangle) due to upward migration of CO_2 from the diffuser. There is no clear acoustic evidence of gas between Horizon 2 and the seabed.* ***(d)*** *Day 12 Chirp data. Seismic chimneys (black rectangle) below Horizon 2*

are interpreted to be caused by the acoustic impedance contrast in the presence of gas. The topmost part of the chimneys shows increase in the reflectivity. No gas was observed between Horizon 2 and the seabed on the 2D seismic data. ***(e)*** *Day 13 Chirp data. Seismic chimneys detected (black rectangle) within the muddy sediments, below Horizon 2. Enhanced reflectors correspond to the topmost part of the chimneys. Bubbles imaged within the water column (black dashed rectangle).* ***(f)*** *Day 34 boomer data. Seismic chimneys (black rectangle) have reached the seabed, without being trapped by Horizon 2. Leakage of CO_2 from the seabed, indicated by the water column acoustic anomalies (dashed black rectangle). The diffuser at 12 m depth below the seabed is indicated by dark gray dot on each figure. The seabed multiple and base of the layered sequence are also indicated by black arrows. Seabed depths vary slightly between the days due to small change in location.*

Enhanced seismic reflectivity has been shown in various geological settings to be associated with the typical seismic response of sediments containing shallow gas (Petersen et al., 2010; Rajan et al., 2012; Zhang et al., 2012; Yoo et al., 2013). These high seismic amplitudes are caused by the large acoustic impedance contrast between gas-charged and gas-free sediments. Vertical transparent acoustic disturbance zones (Days 2-13), or chaotic and relatively low amplitude internal reflections (Day 34), detected on the 2D seismic data, will henceforth be referred to as seismic chimneys. Seismic chimneys are the acoustic evidence of focused fluid flow pathways, and found commonly associated with upward hydrocarbon migration from source rocks to the reservoir, and between reservoirs at different depths (Meldahl et al., 2001; Løseth et al., 2009; Baristeas et al., 2012). Enhanced reflectors at the crest of seismic chimneys detected at Day 12 and Day 13 (Fig. 2.4d and 2.4e) have previously been well-documented in seismic reflection data, and represent the acoustic impedance contrast in the presence of free-gas within the overburden (Tomasini et al., 2010; Sun et al., 2012). The slightly up-warped internal reflections found within the topmost part of seismic chimneys at Day 12 and Day 13 are possibly related to the sediment deformation caused by the buoyancy of moving gases in the early stages of chimney formation (Cathles et al., 2010; Plaza-Faverola et al., 2011), as free-gas within the sediment pore space would normally cause down-warping associated with the decrease in the seismic velocity. Due to the imperfect spatial repeatability of the 2D seismic lines (Fig. 2.4), as well as the

lack of imaging of individual reflectors within the seismic chimneys, we do not observe the impacts of velocity push-down within the seismic data.

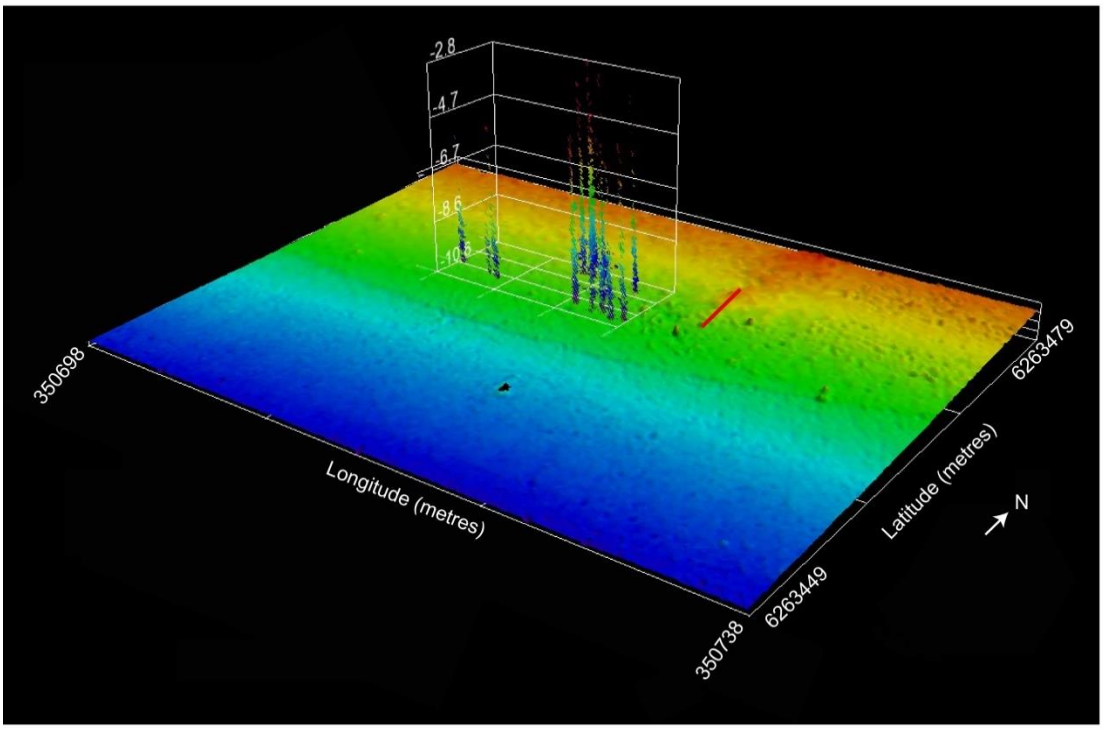

Figure 2.5 *Pockmarks and water column bubbles imaged on the multibeam bathymetry data at Day 34. The location of the gas streams and pockmarks are within the area of chimneys detected on the boomer data. Pockmarks are visible as circular depressions on the seabed S and W of the end of the diffuser (position at depth shown by red line). Many of the pockmarks have gas streams emerging from them, with the height of the bubble streams varying, perhaps reflecting the relative flux emerging from each pockmark.*

High reflectivity anomalies for Horizon 2, as well as the spatial extent of the seismic chimneys detected on the Chirp and boomer datasets were mapped (Fig. 2.6a and 2.6b). In the early stages of the experiment, most of the high reflectivity anomalies are clustered c. 30 m W of the diffuser (Fig. 2.6a), whereas, in the latter stages, these anomalies are detected over a wider area c. 30 m either side of the diffuser (Fig. 2.6b). Contrary to the increase in the spatial extent of high reflectivity anomalies with time, the area covered by seismic chimneys decreases significantly in the latter stages of the experiment, from 65x40 m on Days 12 and 13, to 20x20 m on Day 34, suggesting a more localized focussed flow at depth above the diffuser at Day 34 (Fig. 2.6). Fig. 2.6c-d represents the subsurface horizons and associated chimneys within the black boxes on

Fig. 2.6a-b. Analysis of the occurrence of seismic chimneys reveals that their number increased proportionally with CO_2 injection rate/total injected volume, with no chimneys on Day 0 and Day 1, a small number of chimneys detected at Day 2, and a significant increase in the number of chimneys at Day 12 onwards (Fig. 2.6c and 2.6d; Table 2.1).

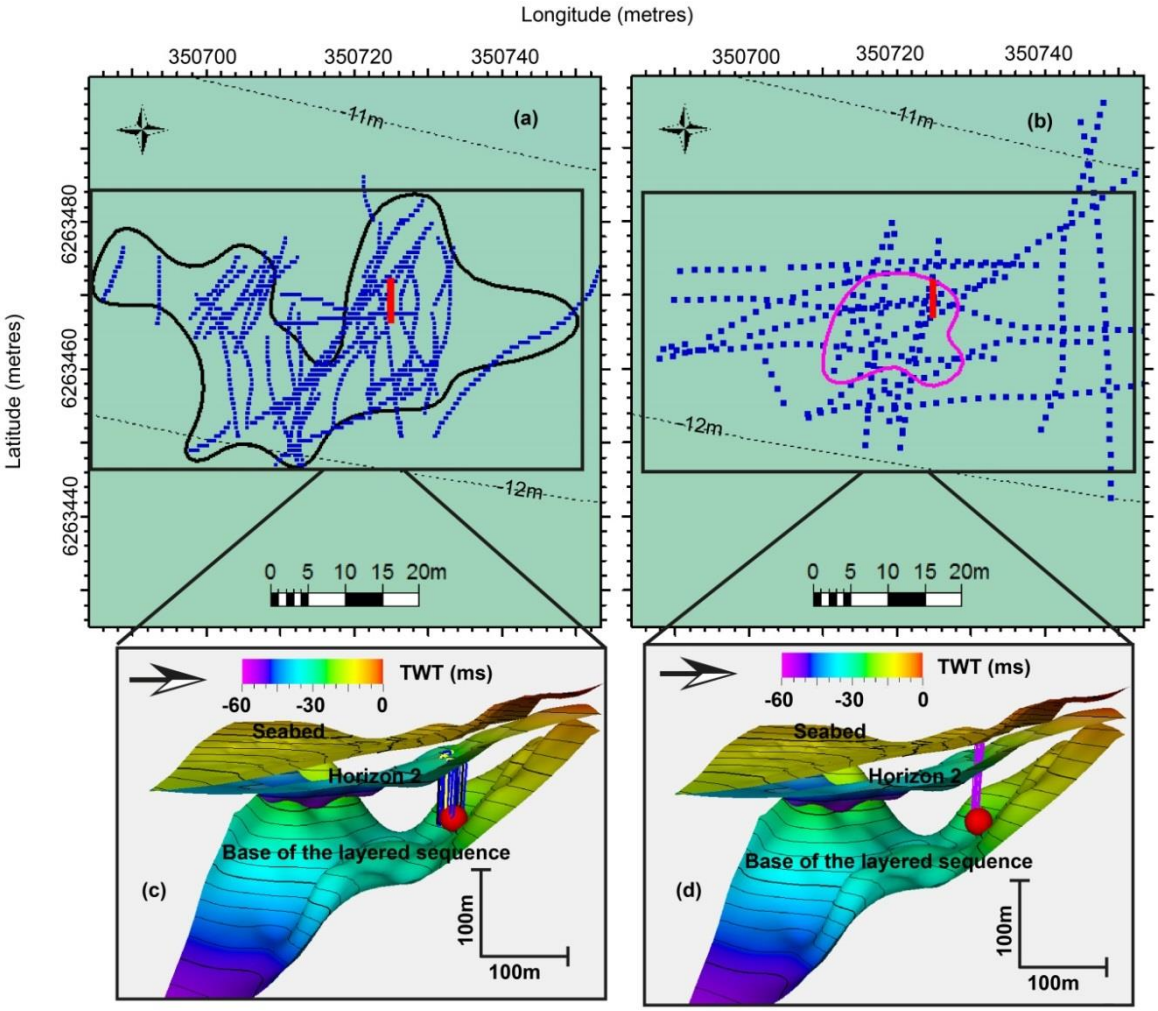

Figure 2.6 *Spatial distribution of CO_2-related high reflectivity anomalies for Horizon 2 and seismic chimneys within the overburden.* ***(a)*** *Spatial extent of high reflectivity anomalies (blue dots) and seismic chimneys (black polygon) detected on the Chirp dataset, from Day 0 to Day 13. Most of the high amplitude anomalies are up to c. 30 m W of the diffuser (red line).* ***(b)*** *Spatial extent of high reflectivity anomalies (blue dots) and seismic chimneys (pink polygon) detected on the boomer dataset, Day 34. There is an increase in the overall extent of high amplitude anomalies, up to c. 30 m each side of the diffuser (red line). However, note the significant decrease in the area affected by chimneys at Day 34.* ***(c)*** *3D image of the key seismic horizons (Seabed,*

Horizon 2, and Base of the layered sequence) and Chirp chimneys (Day 2 chimneys (black polygons), Day 12 chimneys (blue polygons) and Day 13 chimneys (yellow polygons)). From Day 0 to Day 13, seismic chimneys reach Horizon 2. ***(d)*** *3D image of the key seismic horizons (Seabed, Horizon 2, and Base of the layered sequence) and boomer chimneys (purple polygons). At Day 34, seismic chimneys are no longer restricted by Horizon 2: they reach the seabed and* CO_2 *is released into the water column.*

The seismic response of different horizons (seabed, Horizon 1 and Horizon 2) outside the chimney area is illustrated in Fig. 2.7. The seismic traces from different survey days on Fig. 2.7 are chosen to be approximately at the same location within an area not affected by gas flux. The amplitudes are normalised by their seabed multiple, and 7-trace mixing is applied. Slight changes in the seismic amplitudes of the key horizons on different days are probably related to the small variation of the spatial location of these traces; however, the seismic response remains coherent overall.

The temporal propagation of gas is illustrated by the schematic diagram shown in Fig. 2.8. In the very early stages of the experiment, at Day 0 and Day 1, CO_2 migrated within the lower layered mud sequence, and reached Horizon 2, revealed by an increase in acoustic impedance contrast between gas-free and gassy sediments (Fig. 2.8a). Isolated bubble streams were also detected in the water column at this stage, showing that the injected CO_2 travelled above Horizon 2, despite the lack of clear acoustic evidence within the acoustically transparent sandy unit (Fig. 2.8a). On Day 2, a few seismic chimneys were formed within the muddy sediments, rising from the diffuser to Horizon 2, allowing the rapid upward transport of CO_2 to Horizon 2 (Fig. 2.8b). Pockmarks were imaged on the seabed, which were seen by divers to be emitting isolated bubble streams (Fig. 2.8b). On Day 12 and Day 13, many seismic chimneys were imaged, rising from the diffuser to Horizon 2. Gas had spread along the base of the overlying sand layers, as revealed by the high reflectivity of Horizon 2, and is consistent with this horizon inhibiting/slowing gas migration upward into the overlying sediments (Fig. 2.8c). More bubbles were observed within the water column on the 2D seismic reflection data, although no significant acoustic anomalies were detected above Horizon 2 at this stage (Fig. 2.8c). Eventually, on Day 34, seismic chimneys were imaged from the diffuser to seabed, leading to many more bubbles imaged on the 2D

seismic reflection and multibeam bathymetry data, as well as being observed by divers (Fig. 2.8d).

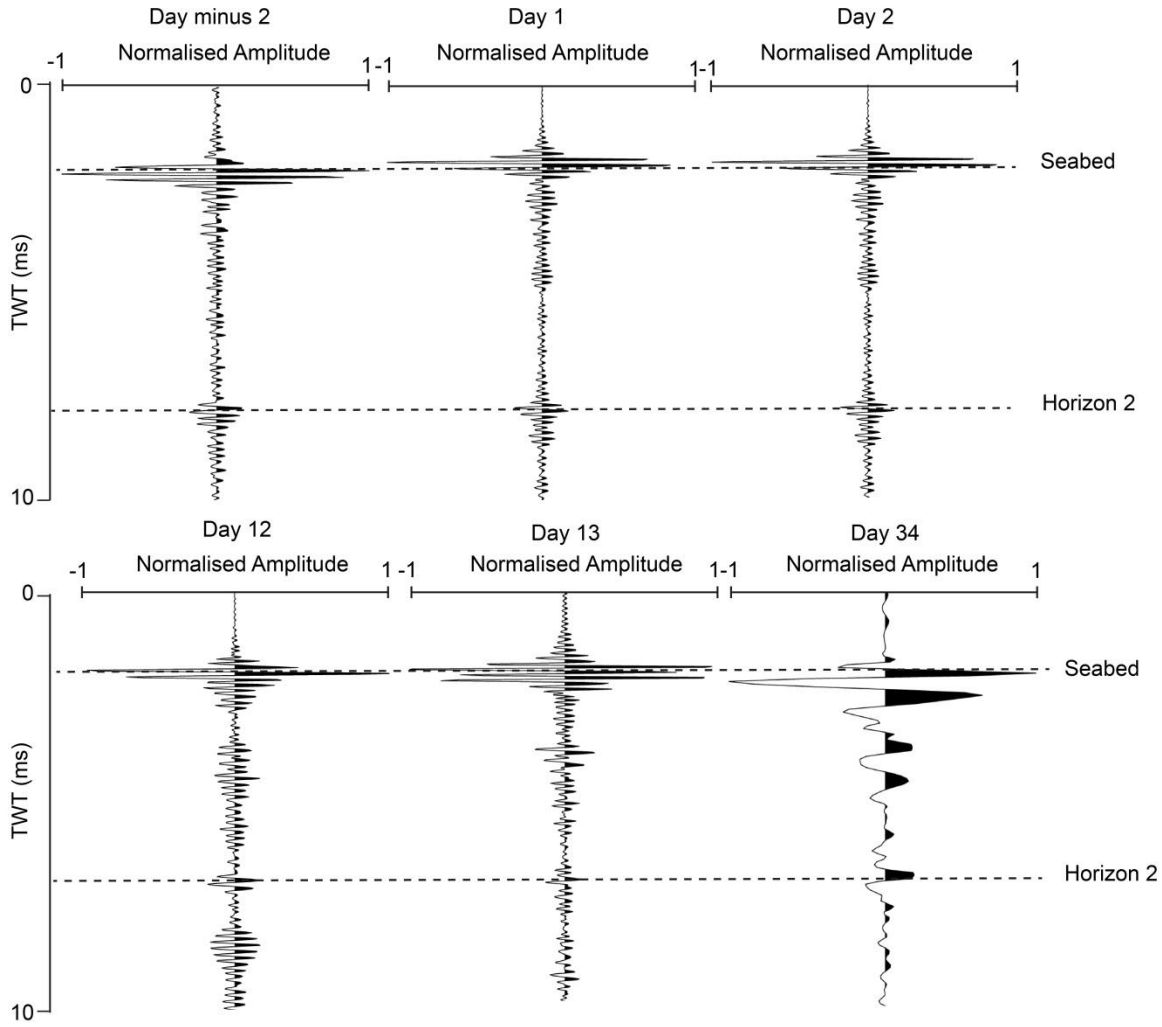

Figure 2.7 *Seismic wiggle traces from outside the chimney area for all days of 2D seismic surveying in Ardmucknish Bay. The seismic traces are normalized by their seabed multiple and 7-trace mixing is applied. The comparison of different days of seismic data within the non-gassy sediments clearly illustrates the coherency of the seismic response outside the chimney area. Small changes in the horizon amplitudes are probably related to the small variations in the spatial location, errors inherent in the repeatability of 2D seismic surveying. Note that the polarity of Horizon 2 is consistently positive outside the chimney area.*

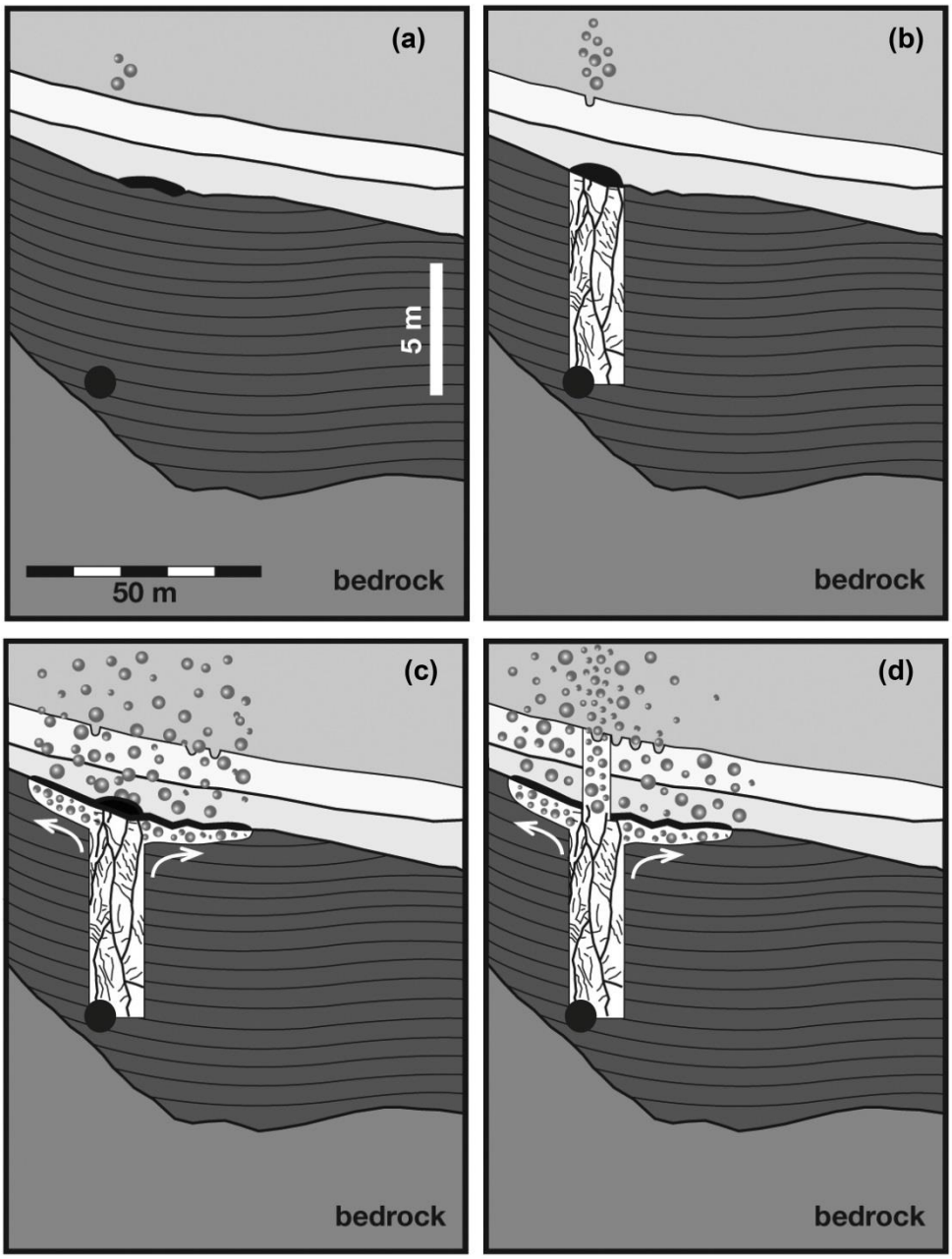

Figure 2.8 *Schematic diagram summarising stages of gas migration revealed by the repeated 2D seismic reflection surveys.* ***(a)*** *Within 24 h gas bubbles were visible in the water column, Horizon 2 has increased reflectivity, but no significant anomalies were detected above Horizon 2.* ***(b)*** *A connected series of fractures allowed propagation of gas through the mud layer which was imaged as chimney structures at Day 2. Formation of pockmarks on the seabed, as well as bubbles detected within the water column. No gas imaged in the overlying sand.* ***(c)*** *With continued gas release, at Day 12 and Day 13, gas spread along the base of the overlying sand layers, as revealed by high reflectivity of Horizon 2. Chimneys below Horizon 2 are frequently imaged, but there is*

no clear acoustic evidence of gas above Horizon 2. ***(d)*** *Eventually the overlying sand layer was also fractured and chimney structures are imaged from the diffuser (black dot) up to the seabed at Day 34. Gas bubbles were imaged on 2D seismic reflection profiles in the water column, as well as on the multibeam bathymetry data (Fig. 2.5). The overall area affected by chimneys is smaller; however, the spatial extent of high reflectivity anomalies for Horizon 2 is larger compared to previous days (Fig. 2.6a-b).*

2.4.3 Impacts on sediment acoustic properties

2.4.3.1 Reflection coefficient

Detailed analysis of the 2D seismic reflection data reveals a polarity reversal for Horizon 2 within the chimney area (Fig. 2.9a), compared to its former signature and that of the seabed (Fig. 2.7). This is consistent with a reduction in acoustic impedance due to the presence of CO_2 in the pore space. Temporal variation of seismic reflectivity following CO_2 injection was evaluated by determining the reflection coefficients of the seabed and Horizon 2. The pre-release (Day minus 2) seismic reflection dataset allowed a baseline to be determined (Figs. 2.9b and 2.10a). For seismic surveys completed during gas release, the reflection coefficient for the seabed and Horizon 2 were calculated for data affected by prominent CO_2 chimneys, as well as for data without evidence of seismic chimneys (Figs. 2.9c-e and 2.10b-e).

In the pre-release Chirp data, there is no significant spatial variation in the reflection coefficient of Horizon 2 in the study area (Fig. 2.9b); the mean reflection coefficient for Horizon 2 is +0.04 (±0.01) (Table 2.4). However, Horizon 2 reflection coefficient values from Day 12 and Day 13 2D seismic reflection data, show a significant decrease, within the area affected by chimneys, mainly to the W of the diffuser (Fig. 2.9c and 2.9d; Table 2.4). The mean reflection coefficient is initially +0.11 (±0.05) outside the chimney, and reduces to -0.12 (±0.1) and -0.10 (±0.08) within the chimney area for Days 12 and 13 (Table 2.4). The E and S of the diffuser area show significant reflectivity variation between Day 12 and Day 13 (Fig. 2.9c and 2.9d). At Day 34, there is a significant reduction in the reflection coefficient of Horizon 2 within the chimney area, as well as an increase in the spatial extent of the area affected by high reflectivity (Fig. 2.9e). The mean reflection coefficient for Horizon 2 on Day 34 within the chimney is -0.11 (±0.04) and +0.05 (±0.03) outside the chimney area, with an overall reduction in Horizon 2 reflection coefficient by -0.16 within the chimney at this

time (Table 2.4). At Day 34, the spatial distribution of Horizon 2 reflectivity variations within the chimney area is more uniform (Fig. 2.9e), compared to the uneven spatial distribution of the reflectivity anomalies observed at Day 12 and Day 13 within the seismic chimney (Fig. 2.9c and 2.9d).

The seabed reflection coefficient map from pre-release Chirp data shows that there is no significant spatial variation (Fig. 2.10a; Table 2.4). Days 12 and 13 show a general increase in seabed reflectivity compared to the pre-release data (Fig. 2.10b and 2.10c; Table 2.4). By combining the seabed reflection coefficient values from Days 12 and 13, the difference in the reflection coefficient of the seabed (ΔRC) between Day minus 2 and Days 12-13 (combined anomaly) can be determined (Fig. 2.10d). The combined anomaly shows the overall area with increased reflectivity for the seabed, and this correlates closely with the position of the subsurface chimneys (Fig. 2.10d). The seabed reflectivity on Day 34 also shows an increase within the area affected by chimneys, extending to the N of the survey area (Fig. 2.10e; Table 2.4). In summary, the temporal changes in seabed reflectivity between Day 12 and Day 34 were found to be within, and in the immediate vicinity of, the area affected by seismic chimneys at depth (Fig. 2.10b-e).

To better evaluate the variation in the reflectivity of Horizon 2 due to CO_2 injection, the difference in the reflection coefficient of Horizon 2 (ΔRC) between pre-release and syn-release data was also investigated (Fig. 2.11). From the analysis of the difference in the reflection coefficient of Horizon 2 (ΔRC) between Day minus 2 and Day 12 (Day 12-Day minus 2), a significant decrease in the reflection coefficient of Horizon 2 is observed within the seismic chimney area, mainly to the W of the diffuser (Fig. 2.11a). Similarly, the reduction in the reflection coefficient of Horizon 2 within the chimney area is remarkable between Day minus 2 and Day 13 (Day 13-Day minus 2) (Fig. 2.11b). By combining the reflection coefficient values calculated for Horizon 2 from Day 12 and Day 13 within and outside the chimney area (combined anomaly), the overall area with decreased reflection coefficient of Horizon 2 can be identified (Fig. 2.11c). Finally, the difference in the reflection coefficient of Horizon 2 (ΔRC) between the pre-release data and combined anomaly is calculated (Fig. 2.11d). All of these maps (Fig. 2.11) clearly show isolated patches of reflectivity anomalies with significant reductions in the reflection coefficient within the area of seismic chimneys. To the NW of the area, the change in the reflection coefficient appears to be consistent between

Day 12 and Day 13 (Fig. 2.11a and 2.11b). The variations in the Horizon 2 reflectivity between Day 12 and Day 13 occur mostly to the E and S of the diffuser (Fig. 2.11a and 2.11b). It is worth noting that Figs. 2.9-2.11 focus on the area affected by seismic chimneys at depth. Changes in the reflectivity within the entire survey area covered by all seismic lines are given in the Supplementary material (Appendix A), but are minor in comparison to those in the vicinity of the seismic chimneys.

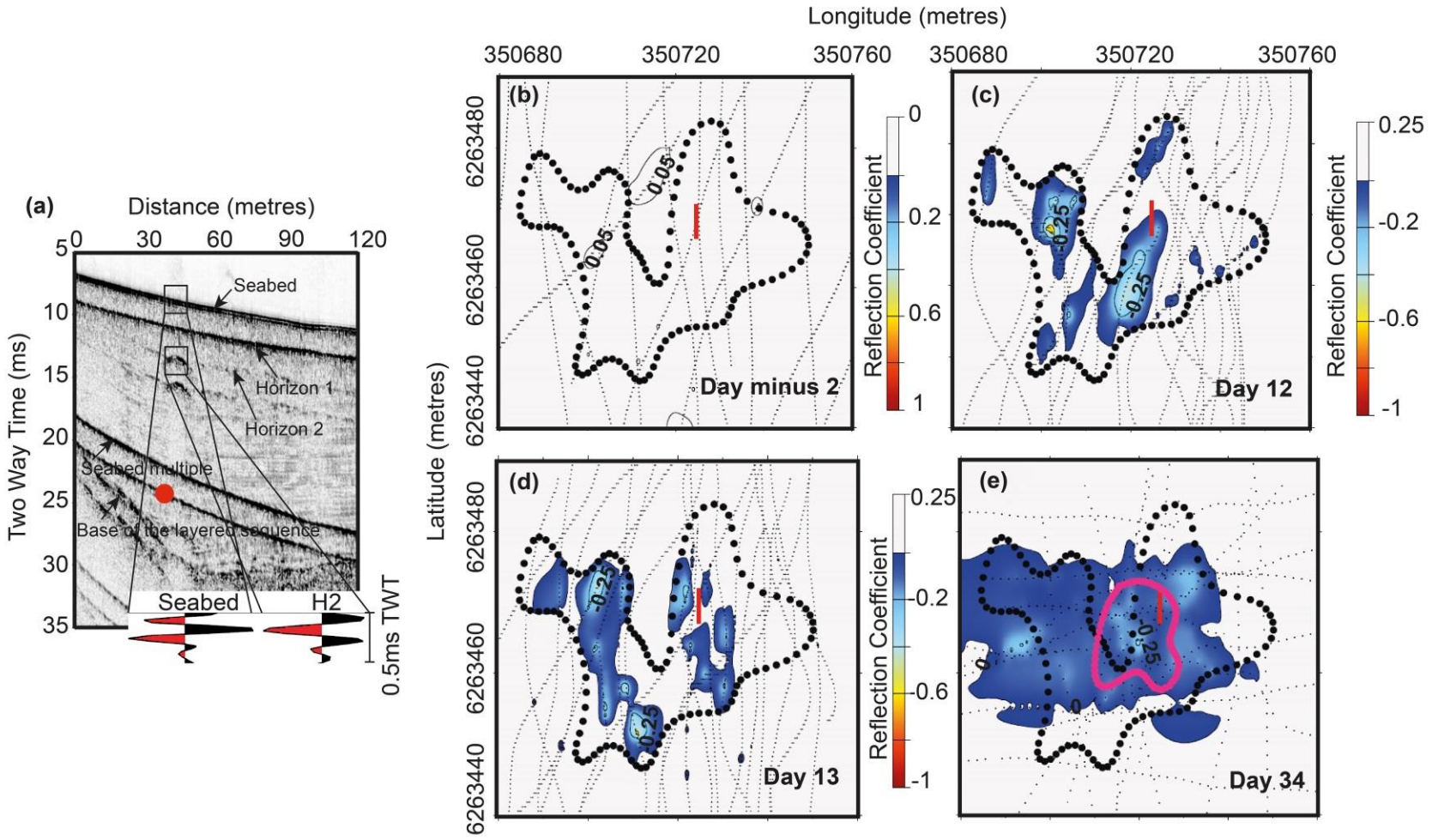

Figure 2.9 *Temporal variation in the reflection coefficient of Horizon 2.* ***(a)*** *2D seismic profile acquired on Day 12 and inset showing polarity reversal on Horizon 2 due to the presence of CO_2 within the chimney. The seabed has a positive polarity and Horizon 2 has a negative*

polarity; diffuser indicated by red dot. Horizon 1 is also indicated. ***(b)*** *The reflection coefficient map prior to CO_2 injection (Day minus 2), showing no significant spatial reflection coefficient anomaly in the area. The outline of the seismic chimney which later developed on Day 12 is indicated by the black dotted polygon.* ***(c)*** *The reflection coefficient map at Day 12. Due to gas injection, significant reflection coefficient reduction for Horizon 2 occurs within the chimney, mostly to the W of the diffuser (red line).* ***(d)*** *The reflection coefficient map at Day 13. There is an obvious decrease in the reflection coefficient within the chimney, to the W of the diffuser.* ***(e)*** *The reflection coefficient map for Horizon 2 at Day 34. Significant reflection coefficient reduction is observed within and outside the seismic chimney area (pink polygon) at Day 34. 2D seismic line locations are shown by the black dashed lines. Mean values of reflection coefficients within and outside the area affected by chimneys are shown in Table 2.4.*

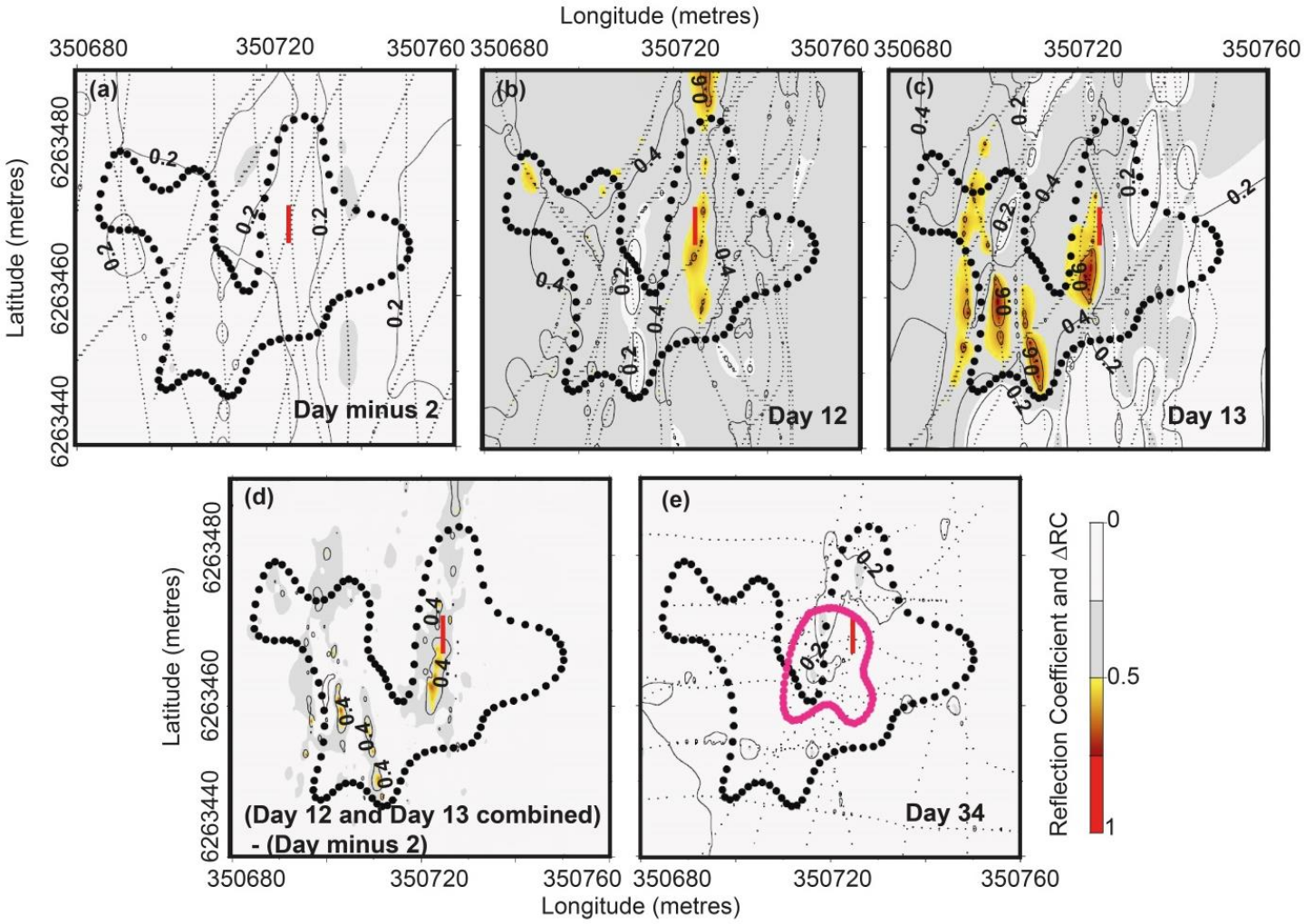

Figure 2.10 *Temporal variation in reflection coefficient of the seabed.* ***(a)*** *The reflection coefficient map prior to CO_2 injection (Day*

minus 2). There is no significant variation in the seabed reflectivity. The chimney which later developed on Day 12 is indicated by the black polygon. ***(b)*** *The reflection coefficient map for Day 12. The seabed reflectivity is uniform on either side of the chimney, with the exception of small areas of increased reflectivity at the close proximity of the diffuser (red line), as well as to the W.* ***(c)*** *The reflection coefficient map at Day 13. Large variation in the seabed reflectivity is observed within the chimney area, as well as outside the chimney.* ***(d)*** *The difference in the seabed reflection coefficient (ΔRC), using pre-release and during injection 2D seismic reflection data. The largest difference in the reflection coefficient (ΔRC) is spatially correlated with the seabed reflectivity anomalies determined for Day 12 and Day 13.* ***(e)*** *The reflection coefficient map at Day 34. The seabed reflectivity shows an increase within the seismic chimney (pink polygon), extending outside of the chimney, to further N within the study area. Mean values of reflection coefficients within and outside the area affected by chimneys are shown in Table 2.4.*

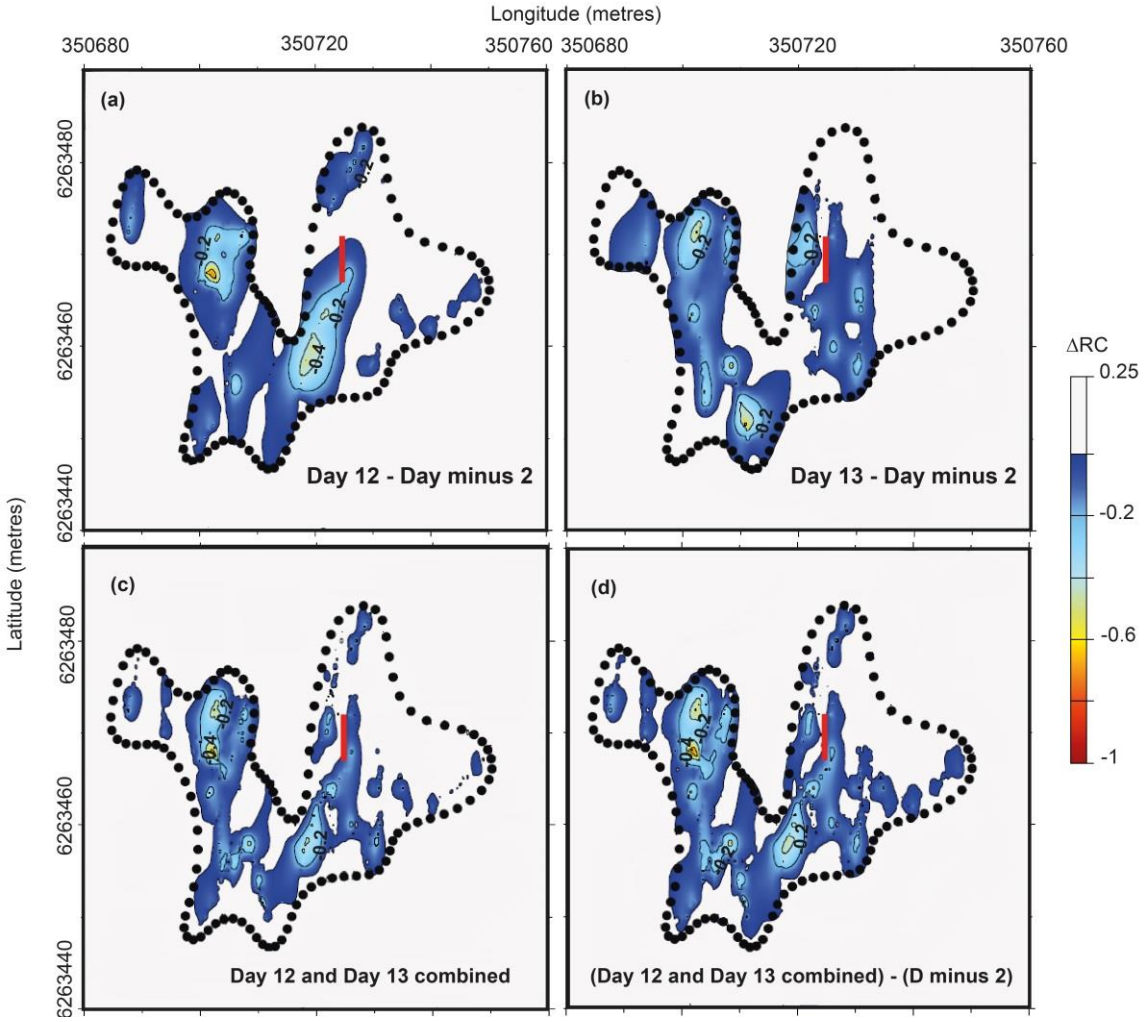

Figure 2.11 *Changes in Horizon 2 reflection coefficients (ΔRC) between Chirp surveys.* ***(a)*** *The difference in the reflection coefficient (ΔRC) between pre-release and Day 12 2D seismic reflection data, showing a significant reduction in the reflectivity of Horizon 2 within the chimney area (black polygon).* ***(b)*** *The difference in the reflection coefficient (ΔRC) between pre-release 2D seismic data and Day 13 2D seismic reflection data, revealing the decrease in reflection coefficient of Horizon 2 within the seismic chimney.* ***(c)*** *Combined reflection coefficient values for Horizon 2 within the chimney area, using reflectivity values calculated from Day 12 and Day 13.* ***(d)*** *The difference in the reflection coefficient (ΔRC) between the combined reflection coefficient anomaly and the pre-release 2D seismic reflection dataset, illustrating the overall difference in Horizon 2 reflectivity due to CO_2 injection. The diffuser is indicated by the red line.*

Days	Seabed mean reflection coefficient		Horizon 2 mean reflection coefficient	
	Inside Chimney	*Outside Chimney*	*Inside Chimney*	*Outside Chimney*
Day minus 2	0.21 (+/-0.03)	0.21 (+/-0.03)	0.04 (+/-0.01)	0.04 (+/-0.01)
Day 12	0.38 (+/-0.09)	0.37 (+/-0.07)	-0.12 (+/-0.10)	0.11 (+/-0.05)
Day 13	0.39 (+/-0.12)	0.27 (+/-0.14)	-0.10 (+/-0.08)	0.11 (+/-0.05)
Day 34	0.18 (+/-0.03)	0.15 (+/-0.03)	-0.11 (+/-0.04)	0.05 (+/-0.03)

Table 2.4 *Mean reflection coefficient for the seabed and Horizon 2 observed on different days relative to the area affected by seismic chimneys on Day 12 for Day 12 and Day 13, and on Day 34 for Day 34. Note that there is no significant variation in the mean reflection coefficient prior to gas release (Day minus 2) across the area. Gas release increases the reflectivity of the seabed, but also causes a polarity reversal on Horizon 2 within the area affected by chimneys at depth. The larger standard deviations for Horizon 2 reflectivities at Day 12 and Day 13 inside the chimney area are possibly related to the uneven gas distribution within the chimney.*

The significant decrease in the reflection coefficient of Horizon 2 within the chimney area at Day 12 and Day 13 (Table 2.4), is interpreted to result from CO_2 injection deeper within the sediments, where upward migrating free gas is likely to cause a significant acoustic impedance contrast between gassy and gas-free sediments (Fig. 2.9c and 2.9d). The reduction in the reflection coefficient of Horizon 2, both within and outside the seismic chimney area at Day 34, is interpreted to be caused by free gas within the overburden, and the spatial extent of the area with decreased reflection coefficient (Fig. 2.9e) is consistent with the area of enhanced acoustic impedance contrast mapped from the boomer dataset (Fig. 2.6b). Further, the CO_2 distribution within the chimney area is uneven at Day 12 and Day 13, emphasising the temporal variation of preferential gas migration pathways within the subsurface at this time (Figs. 2.9c-d and 2.11a-d). The experimental simulation of the migration of free gas within porous sediments (Chadwick, pers. comm.) has shown that free gas migrates upwards through alternating pathways within the overburden, confirming the patchy distribution of a network of acoustic anomalies within the overall chimney area, detected in this study (Figs. 2.9c-d and 2.11a-d).

The increase in the seabed reflectivity from Day 12 onwards is most likely caused by free gas within the pore space of sediments just beneath the seabed (Fig.

2.10b-e). It is interesting to note that these seabed changes occur further N than the changes at depth, which might be related to the presence of shallow lateral conduits moving the gas up-dip (Fig. 2.10b-e). Previous studies have shown that change in the acoustic impedance is controlled by the distribution of free gas within the overburden, where thin gas-charged layers might lead to normal polarity, as the individual reflections of gas are indistinguishable, where the thickness of the gassy layer is less than one-eighth of the predominant wave-length (Widess, 1973; Geletti and Busetti, 2011; Ker et al., 2014). For this study, the thickness of the gassy layer should be equal or less than 1.25 cm to cause such effect, which is believed to be highly unlikely. Additionally, these seabed reflection coefficient anomalies are not randomly located within the overburden: they are spatially correlated with the Horizon 2 reflection coefficient anomalies (Figs. 2.9c-d and 2.10b-d), proving that despite the lack of clear acoustic evidence of free gas between Horizon 2 and the seabed, free gas migrated through sediments above Horizon 2 at this time. The spatial extent of the seabed reflectivity changes on Day 34 corresponds to the area with gas streams and pockmarks imaged on the multibeam bathymetry (Figs. 2.5 and 2.10e).

Synthetic seismograms produced using a temporally varying reflectivity model of the subsurface, and realistic source signatures, can be used together to validate our interpretation of changing acoustic properties during gas propagation. Reflectivities derived for the seabed and Horizon 2 (Table 2.4) on different days were convolved with Chirp or boomer source signatures to produce synthetic seismograms that could be compared with real data. This comparison was done for the same small area outside (Fig. 2.12a) and inside the chimney (Fig. 2.12b) areas, which was sampled on all 2D seismic reflection surveys. Care was taken so that the synthetic and real data were processed using identical simple processing schemes. There is a good agreement between the synthetic and real data for each survey day (Fig. 2.12), including the development of negative polarity reflections on Horizon 2 (Fig. 2.12b, Days 12-34), confirming the robustness of changes in reflection coefficient given in Table 2.4.

2.4.3.2 Attenuation

The spectral-ratio technique described in Section 2.3.2 was applied to the 2D seismic reflection data to determine temporal and spatial variations in the *Q* values (Fig. 2.13; Table 2.5). The analysis focussed largely on the near-surface sediments between

the seabed and Horizon 2, where the technique could be straightforwardly applied. It was more difficult to derive *Q* values for sediments below Horizon 2 due to the interference of the seabed multiple. To increase robustness of the results, Q_{mean} for a specific sediment package was calculated, averaging individual *Q* estimates from adjacent 2D seismic lines acquired on the same day.

Analysis of the Chirp data prior to release (Day minus 2) shows distinct values of *Q* above and below Horizon 2 throughout the survey area, ranging between 83-114 above Horizon 2 (Q_{mean}=98), and 190-212 below Horizon 2 (Q_{mean}=198; Fig. 2.13a and 2.13d; Table 2.5). At Day 12 when the *Q* analysis was repeated in the zone of seismic chimneys, *Q* was significantly reduced (43%) for sediments above Horizon 2 compared to the pre-release values (*Q* range 55.2-56.1; Q_{mean}=55.6; Fig. 2.13b; Table 2.5). A very similar reduction (42%) in *Q* for sediments above Horizon 2 in the chimney zone was also observed for Day 34 (Q_{mean}=56.6; Fig. 2.13c; Table 2.5). On Day 34, *Q* for sediments between Horizon 2 and the base of the layered sedimentary infill was 21% lower than the pre-release values, although this estimate is affected by large error bars (Q_{mean}=157; Fig. 2.13e; Table 2.5).

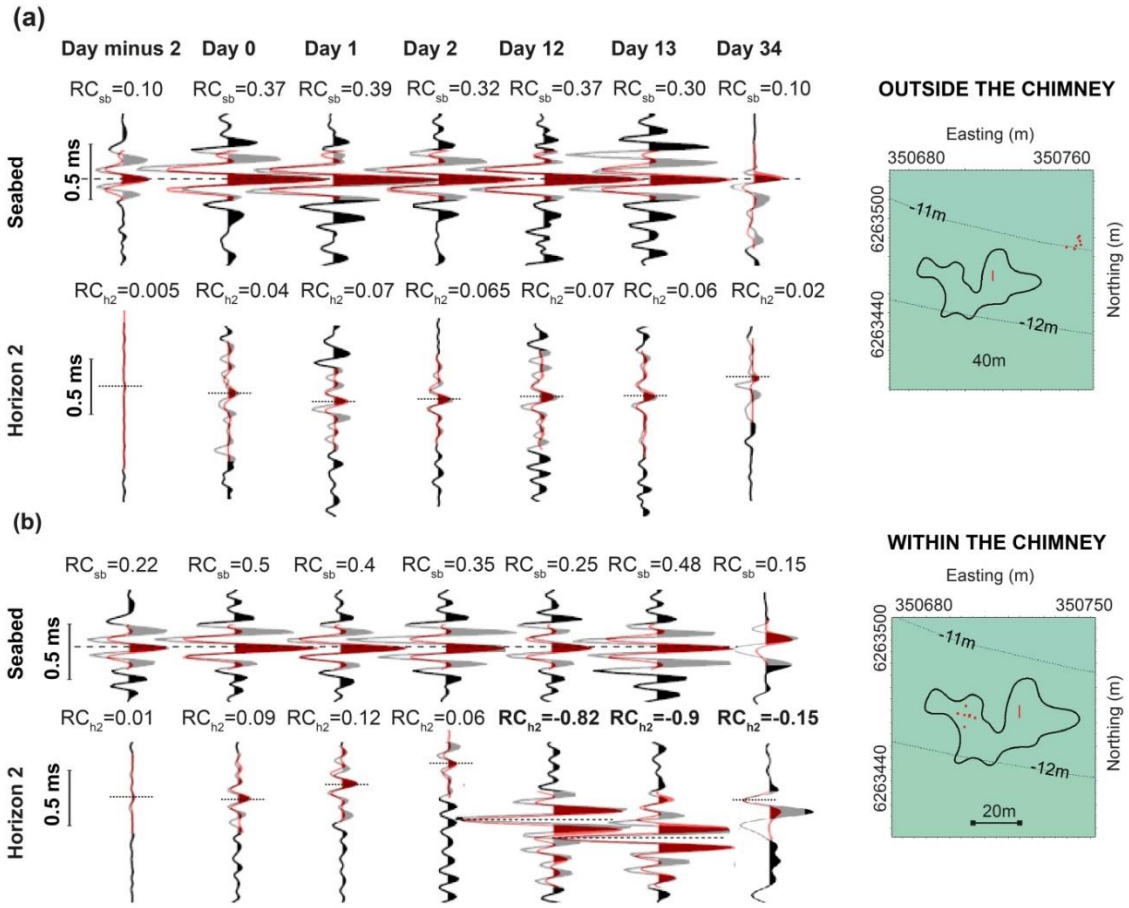

Figure 2.12 *Comparison of synthetic and real seismograms for different days during the release experiment.* ***(a)*** *Outside of area affected by seismic chimneys on Day 12.* ***(b)*** *Inside of area affected by seismic chimneys on Day 12. Note the good agreement between the real and synthetic data including where Horizon 2 becomes negative polarity due to the presence of gas within the chimney area. See main text for explanation of generation of synthetic seismograms. Real data and synthetic data are shown by the black and red wiggle traces, respectively. Location of the real wiggle traces (red dots) and the reflection coefficient values for the seabed (RC_{sb}) and Horizon 2 (RC_{h2}) used to produce synthetic seismograms are also shown. All wiggle traces are normalised.*

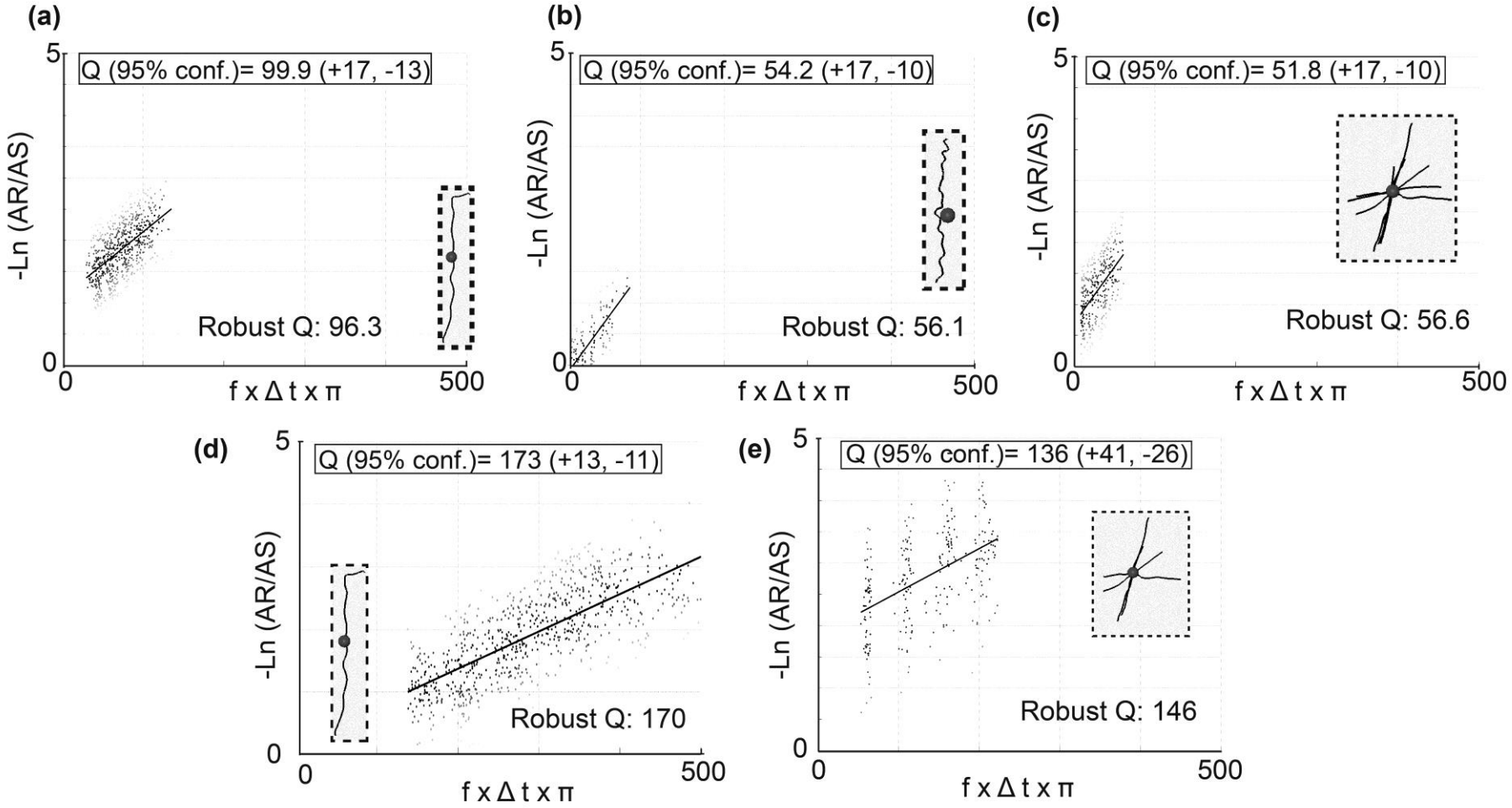

Figure 2.13 *The temporal variation of Q during the QICS experiment.* ***(a)*** *Q above Horizon 2 prior to CO_2 release. Q is 96.3 above Horizon 2.* ***(b)*** *Q above Horizon 2 at Day 12. There is a significant decrease in Q above Horizon 2, in the order of 43% (from Q_{mean}=98 at Day minus 2 to*

Q=56.1 at Day 12). ***(c)*** *Q above Horizon 2 at Day 34. Q above Horizon 2 has decreased by 42% (from* Q_{mean}*=98 at Day minus 2 to Q=56.6 at Day 34).* ***(d)*** *Q between the seabed and the base of the layered sequence at Day minus 2. Knowing the depth between surfaces, Q between Horizon 2 and the base of the layered sequence was inferred as 192 at Day minus 2.* ***(e)*** *Q between seabed and the base of the layered sedimentary infill at Day 34. Q between Horizon 2 and the base of the layered sequence was inferred as 157, suggesting a decrease by 21% below Horizon 2 at Day 34. Note the larger error bars for this calculation. 2D seismic lines used in Q analysis are given inset, indicated by black lines, as well as the diffuser (the dark gray dot).*

Days	Q_{mean} (inside the chimney)		Q_{mean} (outside the chimney)
	Above Horizon 2	*Below Horizon 2*	*Above Horizon 2*
Day minus 2	98 (+15/-10)	198 (+13/-11)	103 (+12/-9.4)
Day 12	56.1 (+17/-10)	no robust values	108 (+25/-10)
Day 34	56.6 (+17/-10)	157 (+27/-19)	no robust values

Table 2.5 *Variation of the Quality factor (*Q_{mean}*) above and below Horizon 2 observed on different survey days, within and outside the chimney area. The change in* Q_{mean} *on Day minus 2, within and outside the chimney area, above and below Horizon 2, is consistent with the change in grain size from sandy to muddy sediments. Injection of gas decreases* Q_{mean} *throughout the sediment column above the diffuser, within the chimney area. Note that* Q_{mean} *measurements above Horizon 2 outside the chimney area are similar to pre-release values. Note also that* Q_{mean} *values below Horizon 2 within the chimney are associated with larger errors.*

The amplitude spectrum of high frequency 2D seismic reflection data can be affected by the presence of gas, as gas bubbles can resonate at certain frequencies, scattering the incident sound energy. This was demonstrated by comparing the amplitude spectrum of Chirp data acquired on different days for the seabed-Horizon 2 interval, both in areas affected by seismic chimneys and those that are not (Fig. 2.14). The spectral content of the 2D seismic data outside the chimney area is quite similar throughout the survey, with the dominant frequency at -30 dB being 7270 (±65) Hz between Day 0 and Day 13 (Fig. 2.14a and 2.14c). However, for 2D seismic data within the seismic chimney zone, the dominant frequency at -30 dB is 7260 (±60) Hz at Day 0 and Day 1, reducing to 7190 (±30) Hz at Day 2, 7065 (±80) Hz at Day 12, and 6695 (±80) Hz at Day 13 (Fig. 2.14b and 2.14c). This suggests that the higher frequency

components of the seismic data are more attenuated than the low frequency components from Day 2 onwards within the seismic chimney area, leading to a dominant frequency shift towards lower frequencies (Fig. 2.14c).

A close relationship between *Q* and mean-grain size (Φ) of sediments has been previously reported (Shumway, 1960; Hamilton, 1972; Guigné et al., 1989; Pinson et al., 2008). *Q* values less than 75 are attributed to granular, sandy and coarse silty sediments (Φ < 6), while *Q* values larger than 75 are associated with finer silts and clay-dominated sediments (Φ > 6) that deform as a coherent matrix rather than a granular medium. *Q* analysis from pre-release 2D seismic data is consistent with previous core grain-size analysis in Ardmucknish Bay (Fig. 2.2), where sediments above Horizon 2 (Fig. 2.13a) are coarser-grained silty-sands (Q_{mean}=98; Table 2.5), and sediments underlying Horizon 2 (Fig. 2.13d) are finer-grained muddy sediments with a high clay content (Q_{mean}=198; Table 2.5). Although a Q_{mean}=98 is indicative of some finer fraction content above Horizon 2, the contrast with a Q_{mean}=198 below Horizon 2 is indicative of a significant contrast in grain size distribution between these two facies.

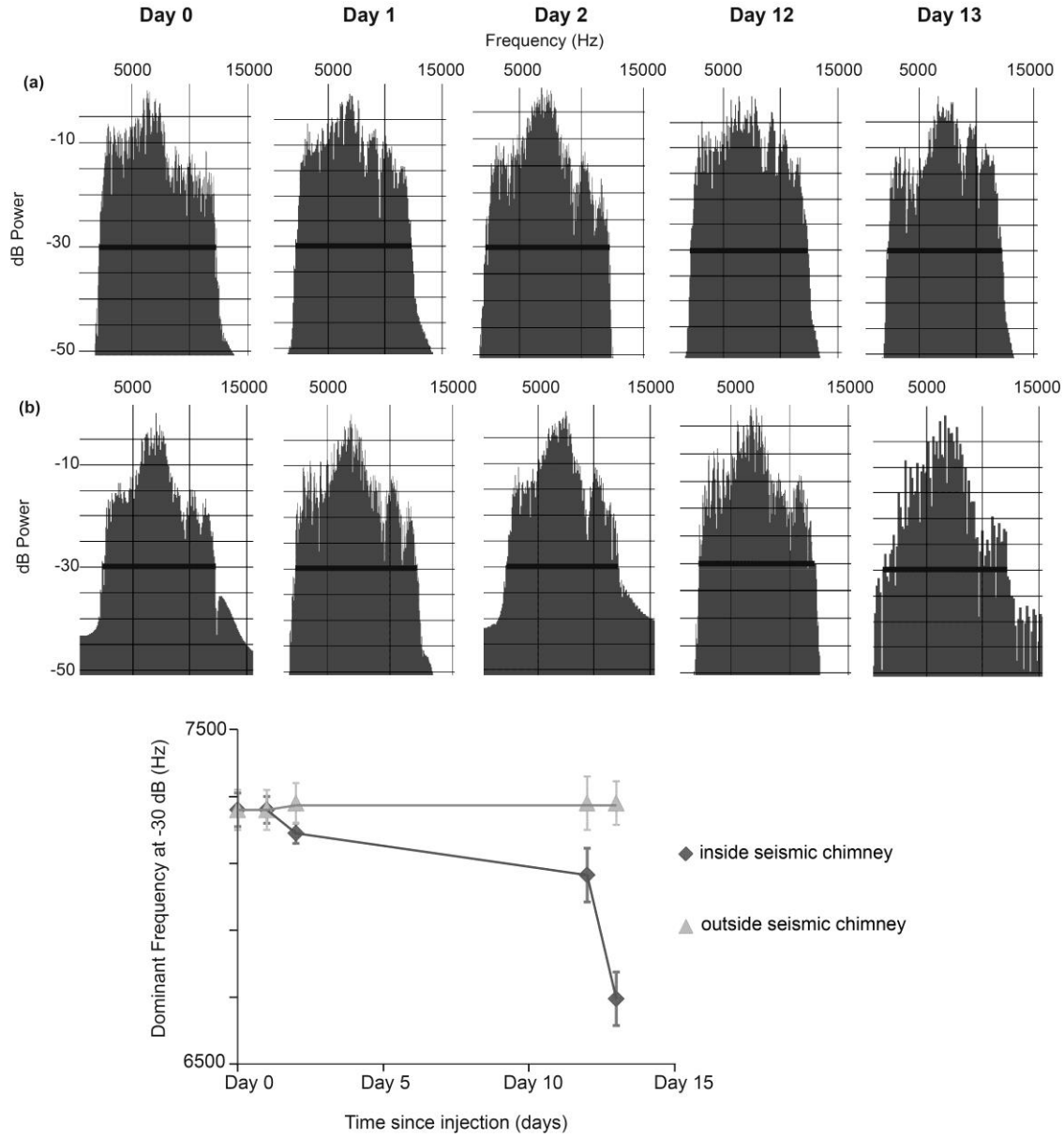

Figure 2.14 *Temporal and spatial variation of the seismic amplitude spectrum of Chirp data.* ***(a)*** *Amplitude spectrum of the seismic data outside the chimney area (developed on Day 12) for the seismic traces shown at Fig. 2.12a. The dominant frequency at -30 dB is 7270 (+/−65) Hz for Days 0-13.* ***(b)*** *Amplitude spectrum of the 2D seismic data within the chimney area for the seismic traces shown at Fig. 2.12b. The dominant frequency at -30 dB is 7260 (+/−60) Hz at Day 0 and Day 1, and reduces to 7190 (+/−30) Hz at Day 2, 7065 (+/−80) Hz at Day 12, and 6695 (+/−80) Hz at Day 13, revealing the increased attenuation of high frequencies in the presence of free gas.* ***(c)*** *The temporal variation of the dominant frequency of the 2D seismic data (at -30 dB) outside and inside of the area affected by chimneys.*

The seismic quality factor (or attenuation) has been shown to be useful in determining the presence of free gas within sediments, as well as providing more quantitative estimates including gas saturation (Hamilton, 1972; White, 1975; Mavko and Nur, 1979; Winkler and Nur, 1979; Carcione and Picotti, 2006; Rossi et al., 2007; Morgan et al., 2012). Seismic quality factors are observed to decrease (i.e., increased levels of attenuation) in response to relatively low level of free gas (< 20%) within the pore space (Morgan et al., 2012). The presence of gas within the pore space dramatically alters the mesoscopic fluid flow (Johnson et al., 2002; Quintal et al., 2011), which has a major influence on the attenuation of seismic waves (Müller et al., 2010). The decrease of the seismic quality factor above Horizon 2, on the order of 42-43% (Fig. 2.13b and 2.13c; Table 2.5) is interpreted as being the result of free gas within the upper acoustically transparent unit, for the period Days 12-34. Similarly, the decrease in *Q* below Horizon 2 at Day 34 is probably caused by upward migrating CO_2 within the seismic chimneys (Fig. 2.13e; Table 2.5). The consistency of observed *Q* values for the period Days 12-34 (Fig. 2.13b and 2.13c; Table 2.5) probably indicates that the gas saturation above Horizon 2 remained approximately constant.

The low-frequency-shift of the recorded spectrum has also been observed in other studies, where the low velocity gas charged sediments have been interpreted to cause increased attenuation of high-frequencies (Quan and Harris, 1997; Tréhu and Flueh, 2001; Rossi et al., 2007). The frequency-dependant decrease in seismic amplitudes detected from Day 2 onwards within the seismic chimney zone is thus interpreted to be due to CO_2 fluxing through the sediments, and causing changes in the sediment acoustic properties (Fig. 2.14a-c).

2.5 Discussion

Our experiment has shown that 2D seismic reflection surveying can indicate probable gas migration pathways in shallow marine sediments, and associated changes in acoustic properties. The temporal variation in sediment acoustic properties and correlation with the cumulative injected CO_2 are summarised in Fig. 2.15. Here, we discuss possible mechanisms controlling CO_2 migration, before emphasizing the importance of reflection coefficient and attenuation analysis from 2D seismic reflection data for improving free gas detection within near-surface sediments.

2.5.1 Mechanisms controlling CO_2 migration

Bubble growth within unconsolidated soft sediments emphasizes grain-size control on gas invasion. Mechanical response of sediments to rising bubbles differs significantly, with coarse-grained sandy sediments favouring capillary invasion and fluidisation, while fracturing dominates in fine-grained media (Boudreau et al., 2005; Best et al., 2006; Jain and Juanes, 2009). In coarse-grained sandy sediments, rising bubbles percolate into the inter-granular pore space leading to sediment fluidisation, whereas in fine-grained muddy sediments, grains are forced apart by migrating bubbles, leading to the initiation and propagation of a fracture. Although perceived pliability of muddy sediments counteracts their elastic behaviour in response to rising bubbles, the eccentric oblate spheroid shape of bubbles microscopically imaged within muddy sediments (Barry et al., 2010), can only be explained if the mechanical response of these sediments follows Linear elastic fracture mechanics theory (LEFM) (Best et al., 1994; Anderson et al., 1998a; Johnson et al., 2002; Barry et al., 2010; Katsman et al., 2013). Additionally, buoyancy-driven hydro-fracturing occurs as a response to the relative motion of fluids against solids, including magma intrusion, migration of hydrocarbons, and metamorphic water through porous media (Lister, 1990; Dahm, 2000; Menand and Tait, 2002; Nunn and Meulbroek, 2002; Levine et al., 2009; Fall et al., 2012). During laboratory experiments, recorded bubble internal pressure suggests a cyclicity, with increasing pressures related to gas injection, and pressure decrease due to sediment fracturing (Johnson et al., 2002).

Based on previous research on gas migration mechanisms within unconsolidated sediments, as well as analysis of temporal and spatial evolution of the acoustic anomalies from our 2D seismic dataset, we interpret that CO_2 migration is predominantly controlled by the grain-size of the surrounding sediments in the initial period of the release, whereas in the later stages, the CO_2 injection rate or total volume injected probably become the dominant factors (Fig. 2.8). In the early phases, up to Day 13, seismic chimneys detected below Horizon 2 are interpreted as inter-connected micro-scale fractures within the muddy sediments (Fig. 2.8b and 2.8c). The change in the grain-size from silty-clayey sediments below Horizon 2 to sandy-silty sediments above it possibly caused a change in the CO_2 migration pattern, from fracture-dominated regime to capillary invasion and fluidisation. Seismic chimneys reaching the

seabed on Day 34 (Table 2.1) are interpreted to demonstrate that either CO_2 injection rate or the total volume injected become the dominant factors controlling CO_2 migration later in the experiment (Fig. 2.8d). CO_2 transport occurs by vertical channelling from the diffuser up to seabed in spite of grain-size differences within the travelled media. As there is no seismic data collected between Day 13 and Day 34, it is not possible to determine the critical injection rate/total volume needed to move from stratigraphic control on CO_2 migration. However, the injection rate at Day 34 (210 kgs/day) or the total volume injected by Day 34 (3600 kgs) is proposed as possible upper limits (Table 2.1).

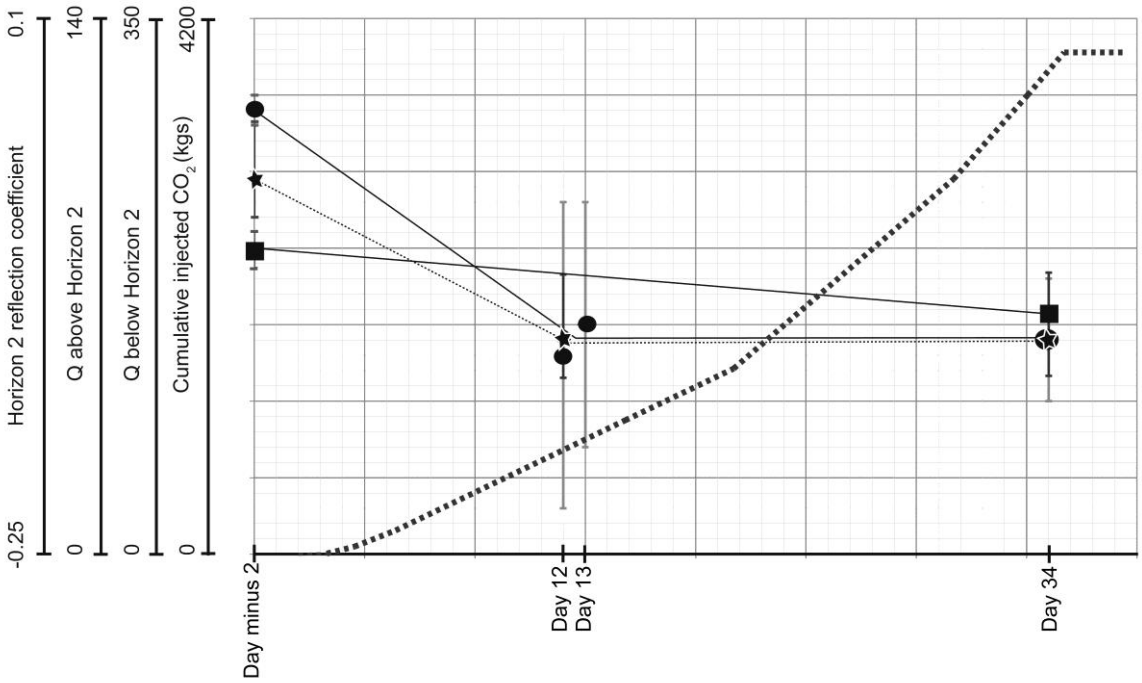

Figure 2.15 *Changes in the reflection coefficient of Horizon 2, quality factor (Q) above and below Horizon 2, and cumulative amount of CO_2 injected during the experiment. Sampling points are indicated as circles (Horizon 2 reflection coefficient), stars (Q above Horizon 2), and squares (Q below Horizon 2). Due to increasing CO_2 within the overburden, the reflection coefficient for Horizon 2 decreases, while attenuation increases above and below Horizon 2. The cumulative amount of injected CO_2 is indicated by bold dashed line.*

2.5.2 Improvements in CO_2 detection within the subsurface

It is crucial to note that, unlike fracture identification, capillary invasion of CO_2 above Horizon 2 is not seismically resolvable as a distinct and continuous change in the seismic reflection amplitudes, despite the high-resolution (i.e., centimetre scale) of our seismic reflection dataset (Fig. 2.8). This observation is fundamental for CCS operations where time-lapse 3D seismic reflection data, with significantly lower vertical resolution compared to the 2D seismic dataset used in this study, is commonly used to track and assure safe storage of CO_2 within the reservoir. In the case of Sleipner CCS site, where CO_2 has been injected into the Utsira Formation since 1996, at a rate of 1 Mt/year, time-lapse seismic surveys demonstrate that the injected CO_2 is securely confined within the Utsira Formation, as there is no contrast of acoustic impedance imaged above the topmost layer of the Utsira Sand (Arts et al., 2008; Chadwick et al., 2010). Our study clearly demonstrates that free gas can be present within the overburden without presenting a classical seismic reflection indicator, i.e., continuous high-amplitude, polarity-reversed reflection. However, the analysis of reflection coefficient for the seabed and increased seismic attenuation between the seabed and Horizon 2 are supportive of the presence of free gas above Horizon 2.

Risk assessment and storage verification rely on high-resolution seismic imaging of the shallow overburden, as well as traditional, lower-frequency imaging at reservoir depths. Our results indicate that the traditional qualitative interpretive approach based on the mapping of high-amplitude, polarity-reversed reflections may not be sufficient to reliably track the upward migration of free gas in the event of leakage, and the interpretations can be significantly improved and validated by the analysis of reflection coefficient and seismic attenuation calculations.

2.6 Conclusion

In this first controlled CO_2 release experiment, where CO_2 was injected into unconsolidated, shallow marine sediments over 37 days, repeated 2D seismic reflection surveys imaged the propagation of gas through the subsurface and into the water column. Analysis of the 2D seismic reflection data, acquired pre-release and syn-release, led to the following conclusions:

- Local stratigraphy influenced CO_2 migration in subsurface sediments around the diffuser, and comprised c. 1.5 m thick layer of coarse-sand and gravel, above a c. 2 m thick fine-sand layer. These two acoustically transparent units overlie a c. 15 m layered muddy sequence with sub-parallel reflections (Fig. 2.4; Table 2.2). The boundary between this mud sequence and the overlying fine-sand forms a characteristic erosional unconformity (Horizon 2).

- This erosional unconformity, Horizon 2, was found to partially trap the injected CO_2 in the early stages of the experiment, revealed by enhanced reflectivity and seismic chimneys imaged beneath the unconformity (Fig. 2.8a-c). Following an increase in the amount of injected CO_2 later on in the experiment (Table 2.1), seismic chimneys previously confined within the layered sequence reached the seabed, leading to CO_2 leakage into the water column (Fig. 2.8d). We argue that in the early stages of the experiment, up to Day 13, capillary invasion and fluidisation were the main mechanisms allowing CO_2 migration above Horizon 2 within sandy sediments, while fracture initiation and propagation facilitated gas migration in the lower fine-grained sediment. Unconformity Horizon 2 trapped the majority of the gas until either increases in gas pressure or increases in the total volume of CO_2 led to seismic chimneys reaching the seabed, overriding stratigraphic control.

- Following CO_2 injection, changes in the reflection coefficient of the seabed and Horizon 2, as well as seismic attenuation within the near-surface sediments were identified (Tables 2.4 and 2.5). The reflection coefficient of Horizon 2 decreased and became negative polarity within the seismic chimney area (Fig. 2.15; Table 2.4). The seismic quality factor, *Q*, decreased during the release by 42-43% above Horizon 2, and 21% below Horizon 2 within the chimney area. The

variations in the reflection coefficient and *Q* identified from 2D seismic reflection data demonstrate that we can efficiently track CO_2 propagation by its impact on sediment acoustic properties.

- The assessment of the changes in the reflection coefficient and seismic attenuation from the seismic reflection data is complementary to traditional seismic interpretation, enhancing and validating CO_2 detection within the subsurface, and allowing a better understanding of the impact of CO_2 on sediment acoustic properties. On-going work is focused on improving estimates of gas content within the sediment pore space by the inversion of the reflection coefficient and attenuation values, together with an appropriate rock physics model which describes accurately the physical properties of surrounding sediments, and gas distribution within the pore space.

Acknowledgments

We acknowledge funding from NERC (NE/H013962/1), the Scottish government and the European Union. We thank the crew of research vessels *Seol Mara* and *White Ribbon*, John Davis for technical assistance with geophysical data acquisition, Alice Tan for sediment analysis, and Craig Wallace of Kongsberg Ltd. for provision and processing of the multibeam data. The *White Ribbon* surveys were funded by the BGS Maremap project.

Chapter 3

Analysis of the post-release seismic reflection data from Ardmucknish Bay, Oban

Abstract

During the QICS experiment, 4.2 tonnes of CO_2 were injected into unconsolidated shallow marine sediments in Ardmucknish Bay over 37 days. Nearly two years after the cessation of injection, the University of Southampton acquired further 2D high-resolution seismic reflection data to evaluate the response of the overburden to the end of CO_2 injection.

Analysis of the post-release seismic reflection data reveals the presence of gaseous CO_2 within the subsurface, located immediately beneath an erosional unconformity Horizon 2. There is no significant evidence of acoustic anomalies detected elsewhere, as confirmed by the analysis of seabed reflection coefficients and seismic attenuation. The spatial distribution of CO_2-related acoustic anomalies indicates a preferential clustering within a circular area, located up-dip of the diffuser, emphasizing the strong control of the subsurface stratigraphic geometry on CO_2 migration, after the cessation of injection. The lack of acoustic anomalies above Horizon 2 on the post-release seismic reflection data, compared to the syn-release seismic reflection datasets, is possibly related to post-release continued CO_2 leakage into the overlying water column and/or dissolution.

3.1 Introduction

Seismic reflection data have been shown to be a powerful geophysical tool for detecting acoustic changes caused by the presence of free gas within the overburden and water column. Free gas within the overburden causes a decrease in the acoustic impedance compared to the surrounding sediments, resulting in enhanced reflectivity, acoustic blanking and polarity reversal (Rajan et al., 2012; Sarkar et al., 2012; Zhang et al., 2012; Ker et al., 2014).

As part of the QICS experiment, during which 4.2 tonnes of CO_2 were injected into the sub-seabed over 37 days in Ardmucknish Bay, the University of Southampton acquired 176 2D high-resolution seismic reflection (Chirp) profiles from Day minus 2 to Day 13 (see Chapter 2, Table 2.1), covering both pre-release and syn-release stages of CO_2. These data, together with 18 boomer lines acquired by the British Geological Survey (BGS) at Day 34, have extensively been studied to detect acoustic changes related to CO_2 fluxing within the overburden and water column, as well as to improve our understanding of various mechanisms controlling CO_2 migration (Blackford et al., 2014; Cevatoglu et al., 2015). As a result, CO_2 was found to significantly change the acoustic properties of sediments, including seismic reflectivity and attenuation (Cevatoglu et al., 2015). In addition, CO_2 migration was found to be controlled by the surrounding stratigraphy, injection rate, and total injected volume (Cevatoglu et al., 2015). Gas flux calculations from passive hydroacoustics and water column bubble sampling showed that 15% of the injected CO_2 was leaking at the seabed at Day 34, indicating that the remaining CO_2 was either confined within the overburden (gaseous or dissolved phase) at this time, or leaking in dissolved phase at the seabed (Blackford et al., 2014; Bergès et al., 2015).

Following the cessation of CO_2 injection in Ardmucknish Bay, The University of Southampton acquired 45 2D high-resolution seismic reflection (Chirp) profiles during 23-24 April 2014 (Days 706 and 707), in the vicinity of the CO_2 injection site and southwards (Fig. 3.1; Table 3.1). The main objective of this post-release seismic reflection survey was to assess the prolonged response of the overburden to the cessation of CO_2 injection in the vicinity of the injection site. The specific aims were (1) to determine whether the injected CO_2 was still present within the overburden and overlying water column, and if so (2) to determine the spatial distribution of CO_2 and

impact on sediment acoustic properties. The results from the analysis of the post-release data are then compared to the observations from pre-release and syn-release seismic reflection surveys. Further, the seismic reflection data acquired south of the injection site (Fig. 3.1) will be used in the future as a pre-release seismic reflection dataset, for a potential research project, QICS 2. In this chapter, we will focus analysis on the post-release seismic reflection data acquired in the vicinity of the sub-seafloor diffuser (Fig. 3.1).

The methodology used in the analysis of the post-release seismic reflection (Chirp) data is identical to that of pre-release and syn-release seismic reflection (Chirp) datasets (see Chapter 2, Section 2.3 Materials and Methods) (Cevatoglu et al., 2015). Thus, in this chapter we move directly into results, followed by discussion and conclusions.

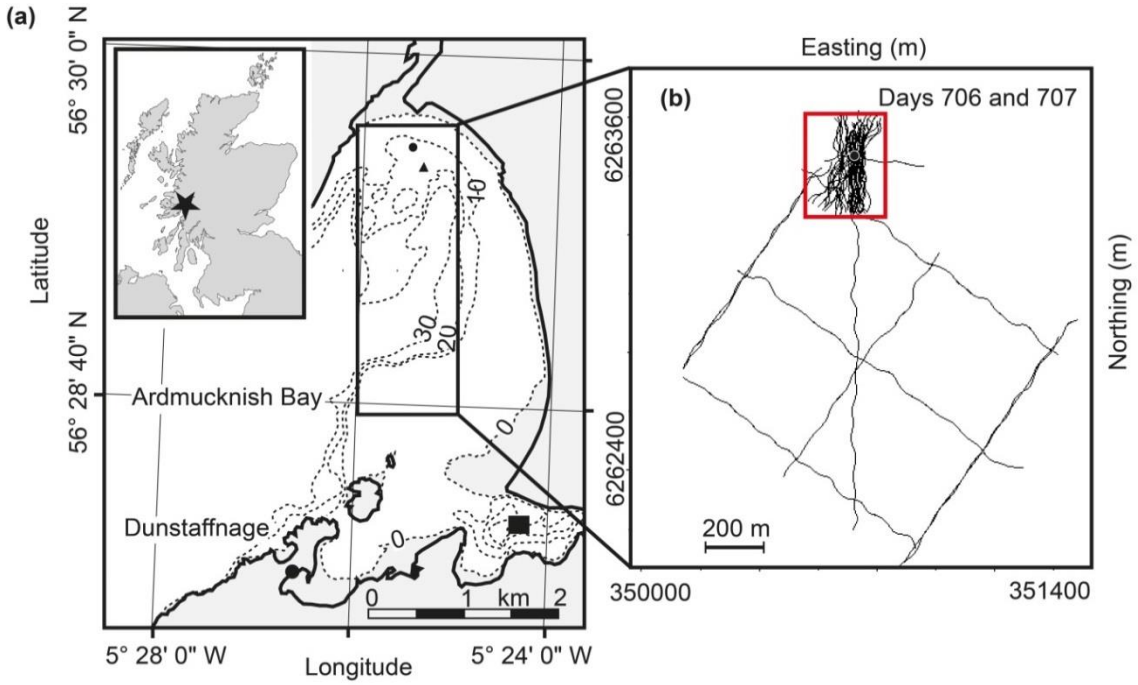

Figure 3.1 *Position of the post-release seismic reflection data (Days 706 and 707).* ***(a)*** *Location map of Ardmucknish Bay, Oban.* ***(b)*** *45 2D high-resolution seismic reflection (Chirp) profiles were acquired in the vicinity of the injection site (black dot) and an area to the south. The seismic reflection profiles cover an area of 1.4 km x 1.2 km. Track lines are indicated as solid black lines. In this chapter, we focus on the post-release seismic reflection data acquired in the vicinity of the diffuser (red rectangle).*

Days	Description	Seismic source	CO_2 injection rate (kgs/day)
15/05/2012	pre-release (Day minus 2)	Chirp	none
17/05/2012	1st day of release (Day 0)	Chirp	20
18/05/2012	2nd day of release (Day 1)	Chirp	20
19/05/2012	3rd day of release (Day 2)	Chirp	45
29/05/2012	12 days after release (Day 12)	Chirp	85
30/05/2012	13 days after release (Day 13)	Chirp	85
20/06/2012	34 days after release (Day 34)	Boomer	210
23/04/2014	706 days after release (Day 706)	Chirp	none
24/04/2014	707 days after release (Day 707)	Chirp	none

Table 3.1 *Summary of the 2D seismic reflection datasets acquired as part of the QICS experiment in Ardmucknish Bay (pre-, syn- and post-release) and associated CO_2 injection rates.*

3.2 Results

3.2.1 Spatial distribution of acoustic anomalies

The post-release seismic reflection data were analysed to detect seismic amplitude anomalies within the overburden and overlying water column. As a result, Horizon 2 (see Chapter 2 for a detailed analysis of the seismic stratigraphy, Fig. 2.2 and Table 2.2) was found to show enhanced reflectivity, compared to the pre-release 2D seismic reflection dataset; whereas there is no evidence of seismic amplitude anomalies above and below Horizon 2 within the overburden on Days 706 and 707 seismic reflection data (Figs. 3.2-3.4). In addition, there are no acoustic anomalies detected within the water column in the vicinity of the diffuser from the latest seismic reflection data (Figs. 3.2-3.4). It is interesting to note the lack of seismic chimneys on the post-release seismic reflection data (Figs. 3.2-3.4), which were previously detected between the diffuser-Horizon 2 interval from the Chirp dataset (Day 2 to Day 13), and the diffuser-seabed interval from the boomer dataset (Day 34) (See Chapter 2, Figs. 2.4 and 2.6).

Following the identification of the high reflectivity acoustic anomalies along Horizon 2 from the post-release seismic reflection data, the spatial distribution of these enhanced reflectivities were mapped (Fig. 3.5a). These acoustic anomalies were mostly found to cluster NW of the diffuser (Fig. 3.5a). The comparison of the spatial location of high reflectivity anomalies along Horizon 2, between post-release and syn-release

seismic reflection datasets, indicates a temporal variation in the location of these acoustic anomalies, from being up to c. 30 m W of the diffuser (up to Day 13) and up to c. 30 m each side of the diffuser (Day 34) to a NW up-dip migration on Days 706 and 707 (Fig. 3.5).

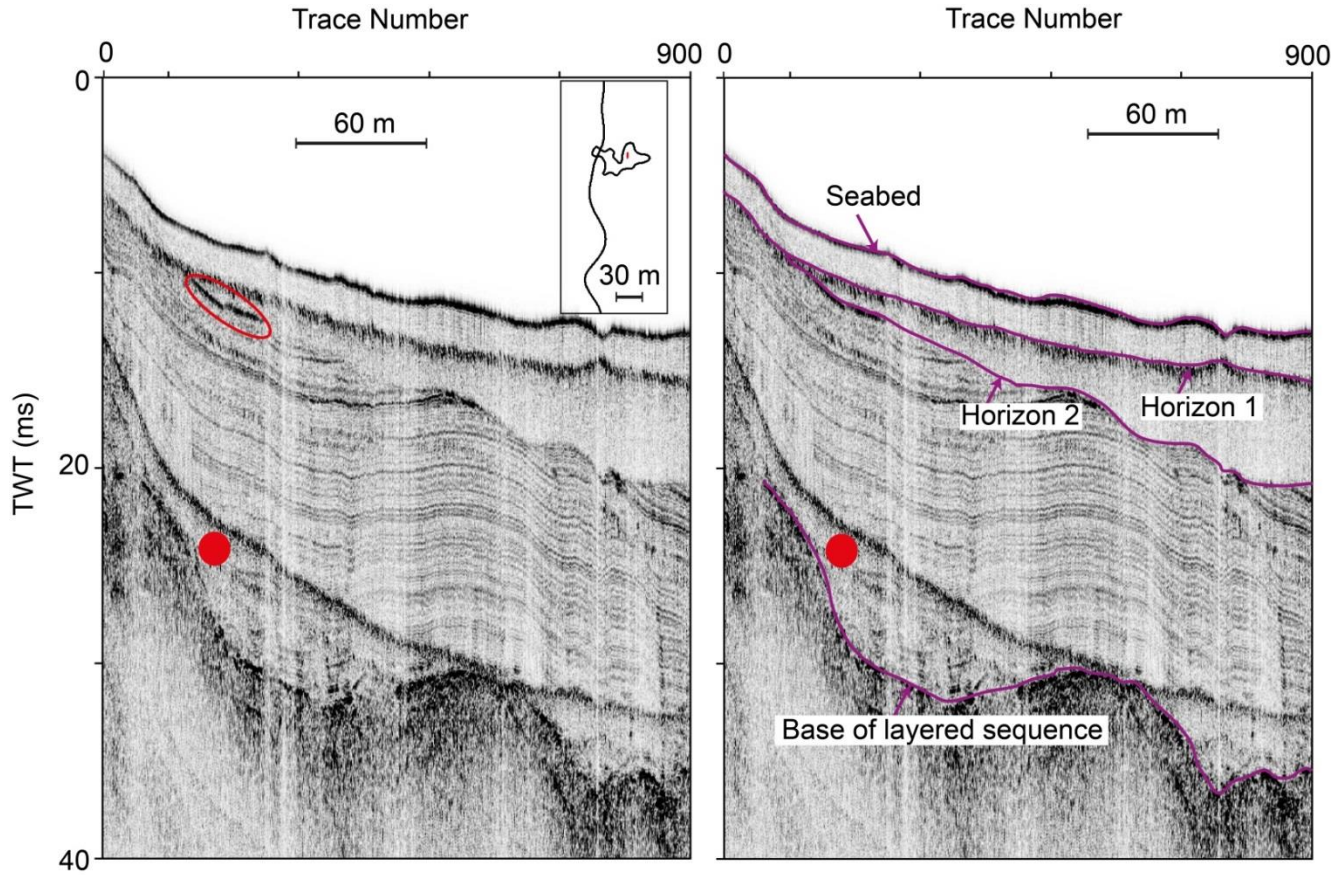

Figure 3.2 *Stratigraphic horizons and enhanced reflectivity imaged on a seismic line (NS3_2) from the post-release seismic reflection dataset. The enhanced reflectivity along Horizon 2 is highlighted by the red polygon. The diffuser is also shown by the red dot on the seismic reflection data. The seabed, Horizon 1, Horizon 2 and the base of the layered sequence are highlighted by solid purple lines. Inset shows position of the seismic reflection profile relative to Day 12 chimney position and diffuser.*

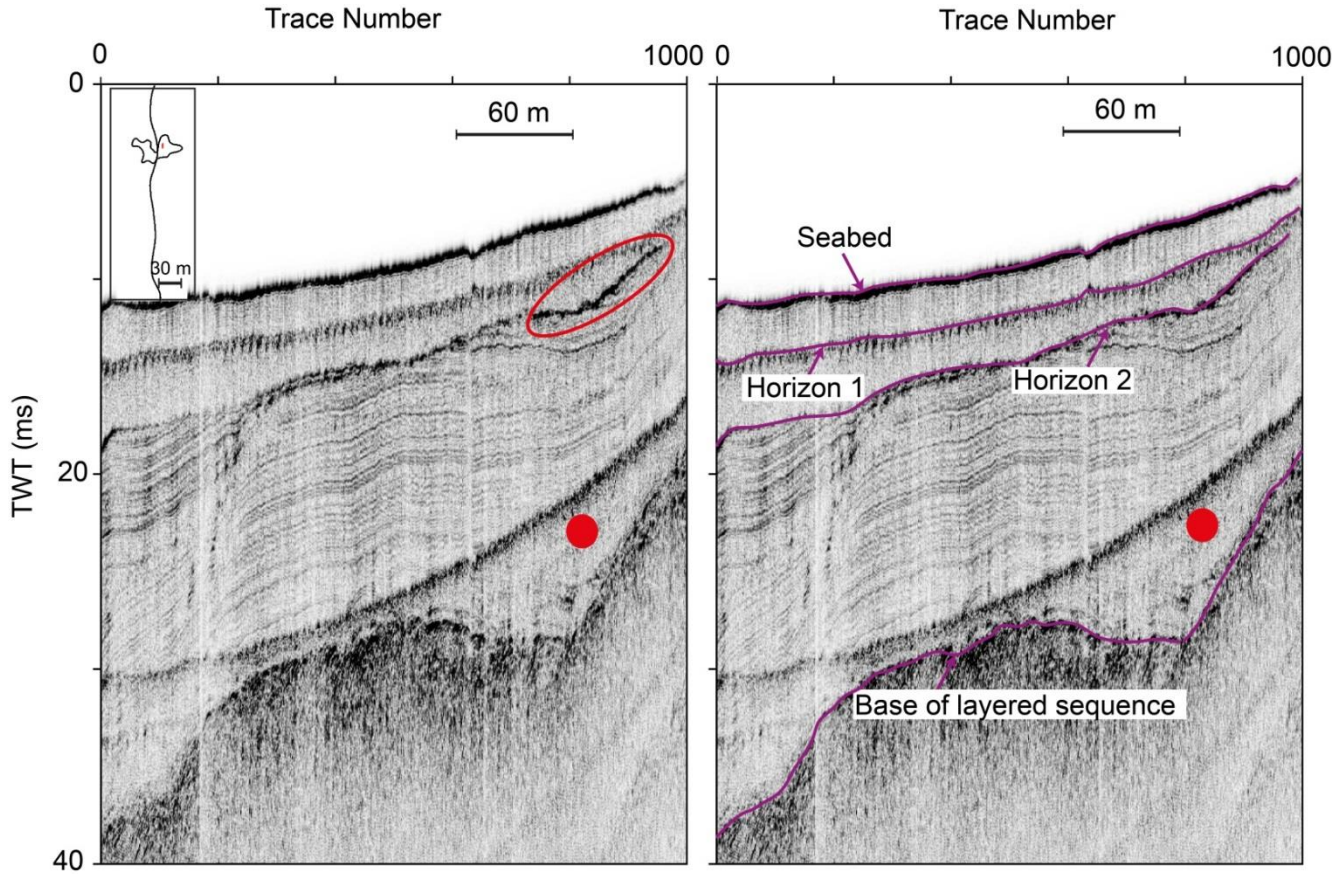

Figure 3.3 *Stratigraphic horizons and enhanced reflectivity imaged on a seismic line (NS4x_1) from the post-release seismic reflection dataset. The enhanced reflectivity along Horizon 2 is highlighted by the red polygon. The diffuser is also shown by the red dot on the seismic reflection data. The seabed, Horizon 1, Horizon 2 and the base of the layered sequence are highlighted by solid purple lines. Inset shows position of the seismic reflection profile relative to Day 12 chimney position and diffuser.*

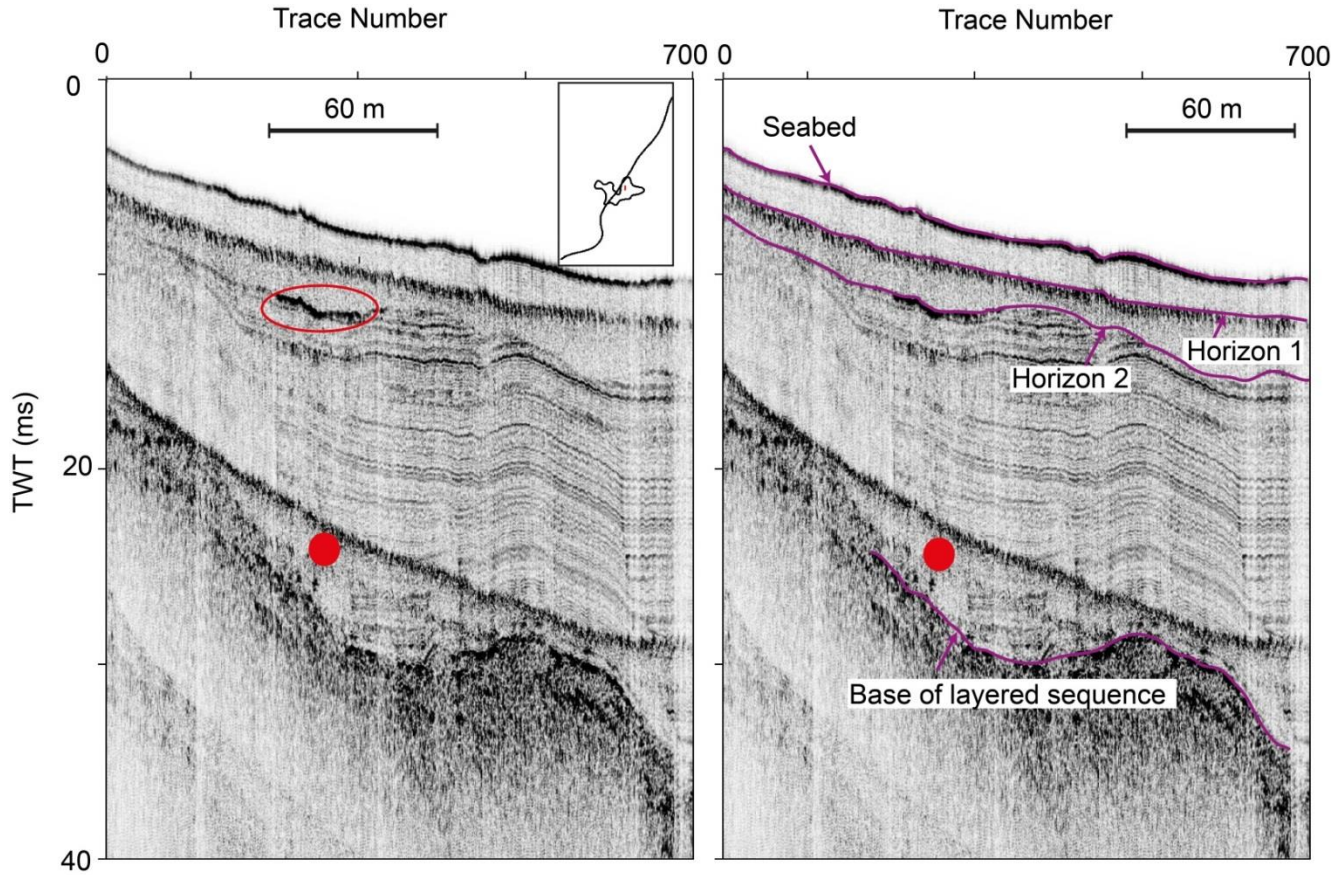

Figure 3.4 *Stratigraphic horizons and enhanced reflectivity imaged on a seismic line (Perp3_2) from the post-release seismic reflection dataset. The enhanced reflectivity along Horizon 2 is highlighted by the red polygon. The diffuser is also shown by the red dot on the seismic reflection data. The seabed, Horizon 1, Horizon 2 and the base of the layered sequence are highlighted by solid purple lines. Inset shows position of the seismic reflection profile relative to Day 12 chimney position and diffuser.*

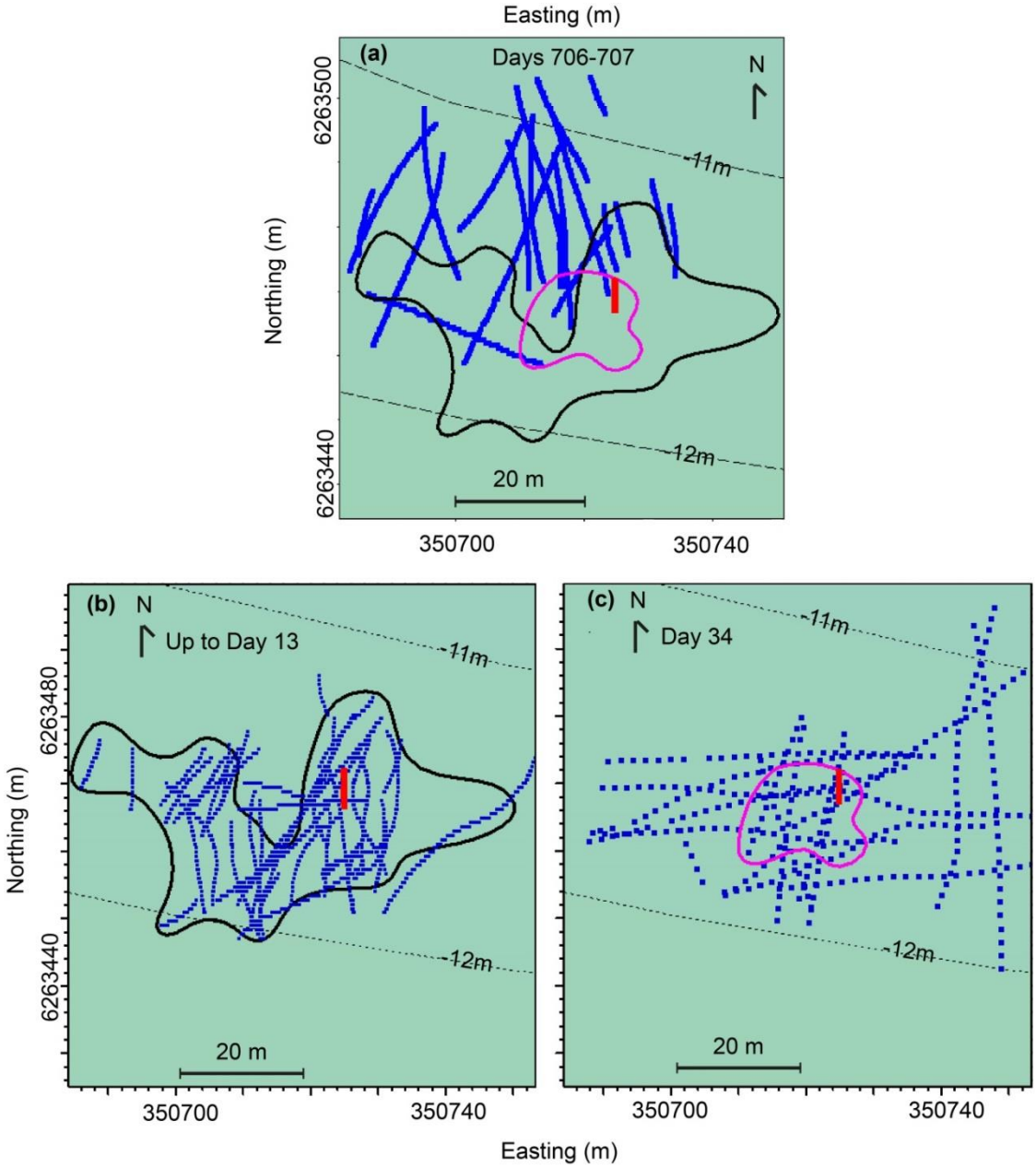

Figure 3.5 *Location of the high reflectivity acoustic anomalies imaged along Horizon 2 from the syn-release and post-release seismic reflection datasets.* ***(a)*** *High reflectivity anomalies along Horizon 2 from the post-release seismic dataset (Days 706 and 707).* ***(b)*** *High reflectivity anomalies along Horizon 2 from the syn-release Chirp dataset (up to Day 13).* ***(c)*** *High reflectivity anomalies along Horizon 2 from the syn-release boomer dataset (Day 34). The diffuser is indicated by the red line, and seismic amplitude anomalies are indicated by blue dots on each case. The black polygon is the spatial extent of the subsurface chimneys detected on Chirp data (up to Day 13), and the pink polygon is the spatial extent of the chimneys from boomer data (Day 34).*

3.2.2 Reflection coefficient calculation

Analysis of the post-release seismic reflection data reveals a polarity reversal for Horizon 2, compared to its former signature and that of the seabed (Fig. 3.6; see also Chapter 2, Figs. 2.7 and 2.12). This observation led to the analysis of reflection coefficient for Horizon 2 and for the seabed from the post-release seismic dataset (Figs. 3.7a and 3.8a; Table 3.2), using the equations (1) and (2) given in Chapter 2 (Section 2.3.2 Reflection coefficient and seismic attenuation calculation).

The reflection coefficient map for Horizon 2 shows a largely circular area (diameter of c. 40 m) with decreased reflection coefficient values, located to the NW of the diffuser (Fig. 3.7a). The spatial extent of this circular area with decreased reflection coefficient values correlates partly with the location of subsurface chimneys detected from Day 12 to Day 34 (Fig. 3.7b-d). However, the decreased reflection coefficient values for Horizon 2 observed at Days 706 and 707 are predominantly located up-dip of the diffuser (Fig. 3.7a). The mean reflection coefficient for Horizon 2 inside the circular area is -0.07 (+/-0.03), and 0.06 (+/-0.03) outside the circular area, on the post-release seismic reflection dataset (Table 3.2). The mean reflection coefficient for Horizon 2, within the circular area on seismic reflection data for Days 706-707, is larger compared to the reflection coefficient values calculated within the chimney area from Day 12 to Day 34, yet smaller compared to the pre-release Horizon 2 reflection coefficient values (Table 3.2). In addition, the mean reflection coefficient value for Horizon 2 outside the circular area on Days 706-707, is similar to the Horizon 2 reflectivity values calculated from Day minus 2 to Day 34 outside the chimney area (Table 3.2).

The post-release seabed reflection coefficient map shows no significant anomalies within the overall survey area, compared to the larger seabed reflection coefficient anomalies previously detected on the syn-release seismic reflection datasets (Fig. 3.8). Nevertheless, a few small areas with increased reflectivity were detected on the post-release seismic reflection data, mainly located to the NW of the diffuser (Fig. 3.8a). The spatial extent of these small areas with increased seabed reflectivity correlates with the area where Horizon 2 reflectivity anomalies were previously identified in the post-release seismic reflection dataset (Figs. 3.7a and 3.8a). The mean reflection coefficient for the seabed inside the circular area is 0.32 (+/-0.09), and 0.30

(+/-0.08) outside the circular area, revealing the consistency of the seabed reflectivity values either side of the circular area on Days 706 and 707 (Table 3.2).

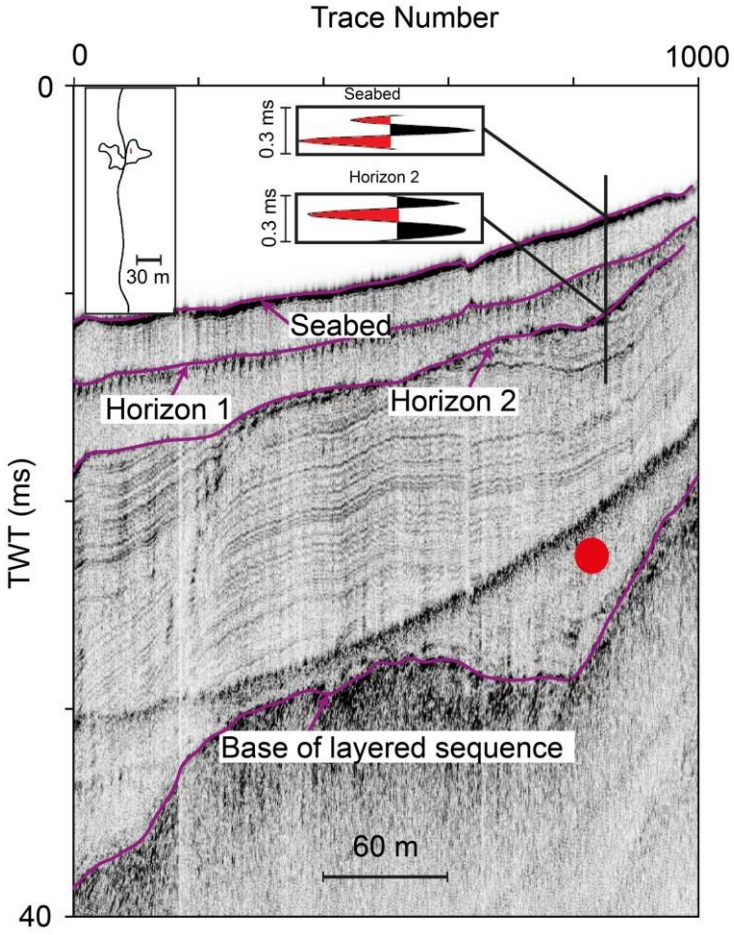

Figure 3.6 *Horizon 2 polarity reversal imaged on the post-release seismic reflection dataset (location given in inset). The seabed has a positive polarity while Horizon 2 has a negative polarity. The diffuser is indicated by the red dot.*

Days	Seabed mean reflection coefficient		Horizon 2 mean reflection coefficient	
	Inside Chimney	*Outside Chimney*	*Inside Chimney*	*Outside Chimney*
Day minus 2	0.21 (+/-0.03)	0.21 (+/-0.03)	0.04 (+/-0.01)	0.04 (+/-0.01)
Day 12	0.38 (+/-0.09)	0.37 (+/-0.07)	-0.12 (+/-0.10)	0.11 (+/-0.05)
Day 13	0.39 (+/-0.12)	0.27 (+/-0.14)	-0.10 (+/-0.08)	0.11 (+/-0.05)
Day 34	0.18 (+/-0.03)	0.15 (+/-0.03)	-0.11 (+/-0.04)	0.05 (+/-0.03)
	Inside Circle	*Outside Circle*	*Inside Circle*	*Outside Circle*
Days 706 and 707	0.32 (+/-0.09)	0.30 (+/-0.08)	-0.07 (+/-0.03)	0.06 (+/-0.03)

Table 3.2 *Mean reflection coefficients calculated for the seabed and Horizon 2 from the pre-, syn- and post-release seismic reflection datasets. Horizon 2 reflection coefficient values on Days 706 and 707 within the circular area are larger than the reflection coefficient values from Day 12 to Day 34. The seabed reflectivity on Days 706 and 707 is quite uniform either side of the circular area.*

3.2.3 Seismic attenuation

The spectral-ratio technique described in Chapter 2 (Section 2.3.2 Reflection coefficient and seismic attenuation calculation) was used to calculate the seismic attenuation (inverse of the Quality Factor *Q*) above, and below Horizon 2, from the post-release seismic reflection data. Similar to the observations from the pre-release and syn-release seismic reflection datasets, the seismic attenuation calculation below Horizon 2 was more difficult due to the interference of the seabed multiple.

From the post-release seismic reflection dataset, *Q* above Horizon 2 is between 94.5-99.3 within the circular area, and between 90.2-95.2 outside the circular area, with Q_{mean} being 94.8 (+14/-11) within the overall survey area above Horizon 2 (Fig. 3.9a-d; Table 3.3). These *Q* values above Horizon 2 are similar to the pre-release *Q* values (Fig. 3.9a-d; Table 3.3). In addition, the Q_{mean} above Horizon 2 on Days 706 and 707 is larger compared to the Q_{mean} calculated for Days 12 and 34 above Horizon 2 (Table 3.3). Q_{mean} below Horizon 2 is 205 (+17/-15) outside the circular area on the post-release seismic reflection data (Fig. 3.9e; Table 3.3). This *Q* estimate below Horizon 2 is similar to the pre-release *Q* values (Table 3.3). No robust *Q* values were determined within the circular area below Horizon 2 from the post-release seismic reflection data.

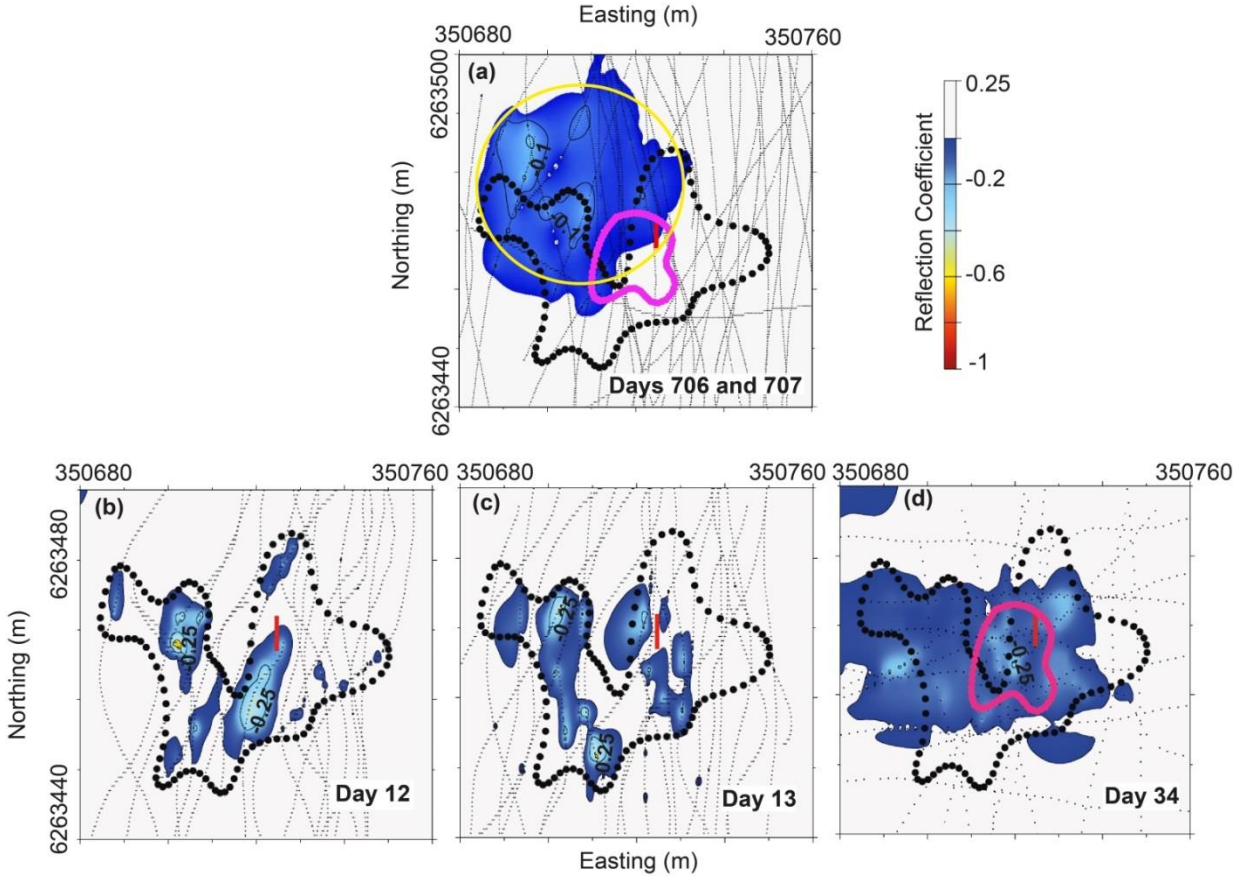

Figure 3.7 *Horizon 2 reflection coefficient maps from the syn-release and post-release seismic reflection datasets.* ***(a)*** *Horizon 2 reflection coefficient map from post-release seismic reflection data. There is a decrease in Horizon 2 reflection coefficient values located mostly to the NW of the diffuser, within a circle of radius of 20 m (yellow circle).* ***(b), (c)*** *and* ***(d)*** *Horizon 2 reflection coefficient maps from the syn-release seismic reflection data (Day 12 to Day 34, see Cevatoglu et al. (2015)).*

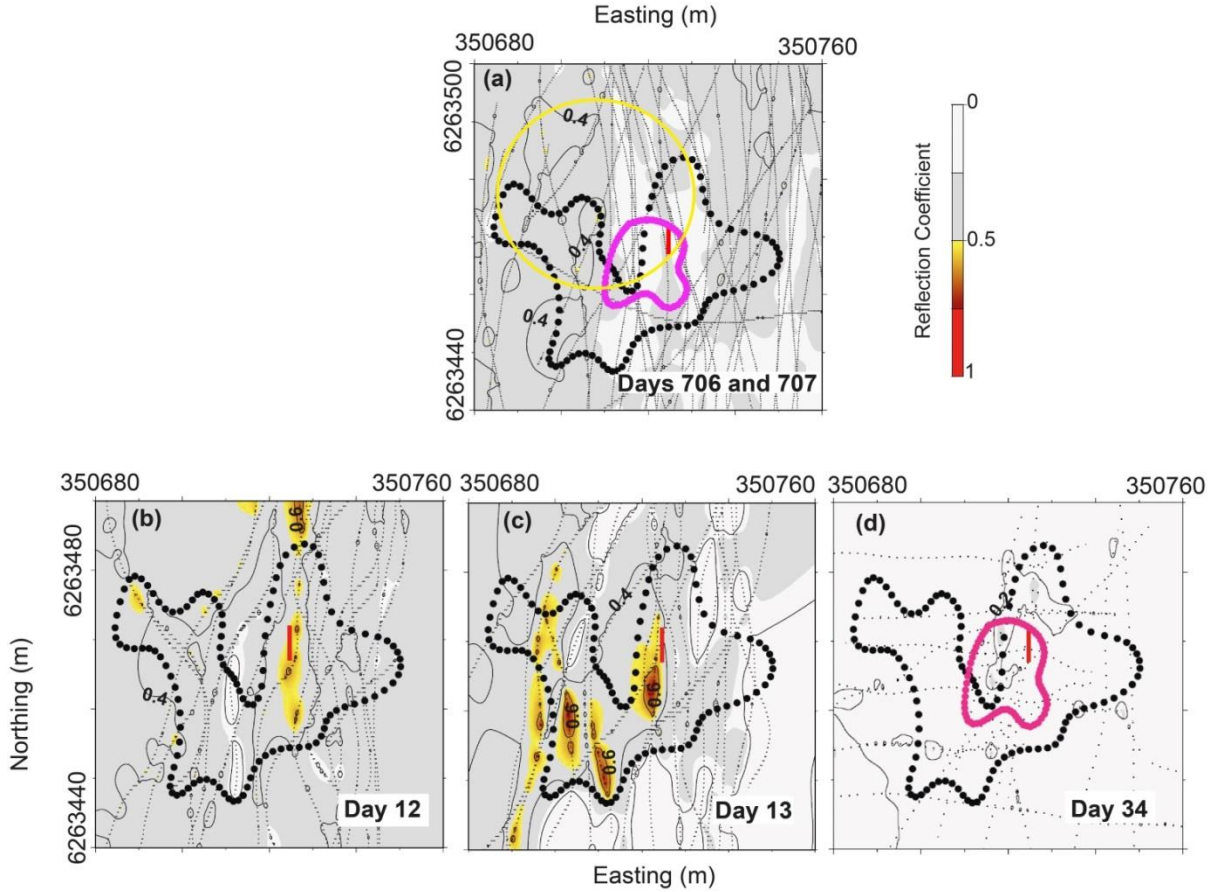

Figure 3.8 *The seabed reflection coefficient maps from the syn-release and post-release seismic reflection datasets.* ***(a)*** *The seabed reflection coefficient map from post-release seismic reflection data. There are no significant seabed reflectivity anomalies compared to the larger seabed reflection coefficient anomalies detected on Days 12 and 13 seismic reflection datasets. Very small areas of increased seabed reflectivity are*

found within the circular area (yellow circle). ***(b), (c)*** *and* ***(d)*** *The seabed reflection coefficient maps from the syn-release seismic reflection data (Day 12 to Day 34, see Cevatoglu et al. (2015)).*

Days	Q_{mean} (inside the chimney)		Q_{mean} (outside the chimney)
	Above Horizon 2	*Below Horizon 2*	*Above Horizon 2*
Day minus 2	98 (+15/-10)	198 (+13/-11)	103 (+12/-9.4)
Day 12	56.1 (+17/-10)	no robust values	108 (+25/-10)
Day 34	56.6 (+17/-10)	157 (+27/-19)	no robust values

	Q_{mean} (inside circle)		Q_{mean} (outside circle)	
	Above Horizon 2	*Below Horizon 2*	*Above Horizon 2*	*Below Horizon 2*
Days 706 and 707	97 (+13/-10)	no robust values	92.7 (+15/-13)	205 (+17/-15)

Table 3.3 *Variation of the Quality factor (Q_{mean}) above and below Horizon 2 calculated from the pre-, syn- and post-release seismic reflection datasets. Q_{mean} above Horizon 2 on the post-release seismic data, within and outside the circular area, are similar to the pre-release values. Q_{mean} below Horizon 2 from the post-release seismic reflection data outside the circular area is also similar to pre-release values. Note that there are no robust Q values for below Horizon 2 within the circular area.*

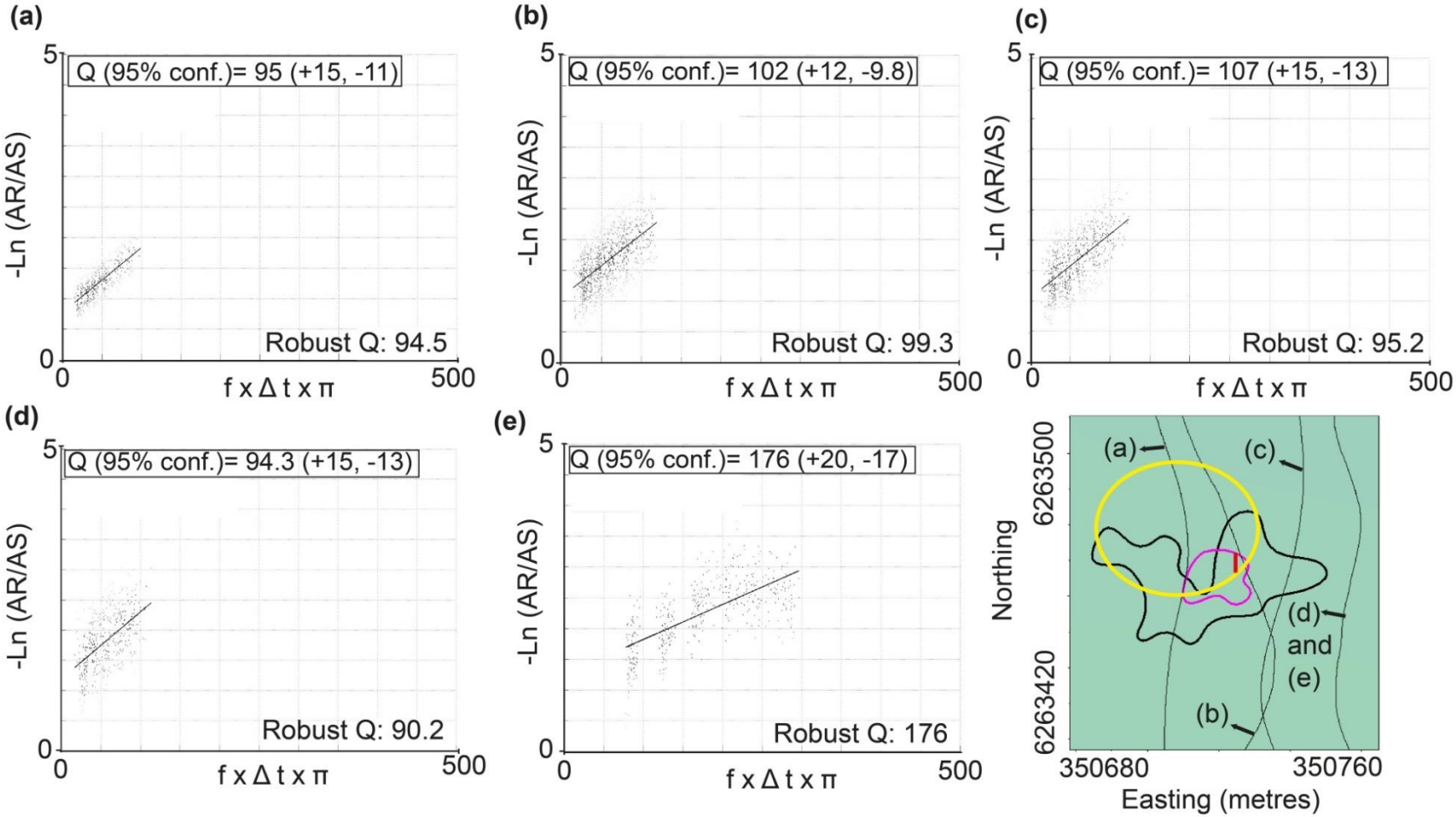

Figure 3.9 *Q values above and below Horizon 2 from the post-release seismic reflection dataset (Days 706 and 707), within and outside of the circular area.* ***(a)*** *Q above Horizon 2 from a seismic line (NS4_1) within the circular area. Q is 94.5 above Horizon 2.* ***(b)*** *Q above Horizon 2*

from a seismic line (NS4x_2) within the circular area. Q is 99.3 above Horizon 2. ***(c)*** *Q above Horizon 2 from a seismic line (NS10_2) outside the circular area. Q is 95.2 above Horizon 2.* ***(d)*** *Q above Horizon 2 from a seismic line (NS12) outside the circular area. Q is 90.2 above Horizon 2.* ***(e)*** *Q between the seabed and the base of the layered sequence from a seismic line (NS12) outside the circular area. Q is inferred as 205 below Horizon 2. The location of the seismic lines (black lines) used in the Q analysis, as well as the spatial extent of the circular area (yellow circle) are given in inset. The spatial location of the Chirp and boomer chimneys detected previously from the syn-release seismic reflection datasets are also shown as black and pink polygons respectively. The diffuser is indicated by the solid red line.*

3.3 Discussion

Analysis of the post-release seismic reflection data clearly demonstrates that the gaseous CO_2 is still present within the overburden, almost 2 years after injection, as indicated by the high-reflectivity acoustic anomalies and polarity reversal imaged along Horizon 2, as well as Horizon 2 reflection coefficient anomalies (Figs. 3.2-3.7a, 3.10; Table 3.2). None of these acoustic anomalies were detected on the pre-release seismic reflection data, indicating that these acoustic changes are due to the gas remaining within the overburden, after the cessation of CO_2 injection (Figs. 3.2-3.7a, 3.10; Table 3.2; see also Cevatoglu et al. (2015)). Previous studies have shown that free gas within the overburden causes enhanced reflectivity and polarity reversal in the seismic reflection data, as well as reflection coefficient anomalies, due to the increase in acoustic impedance contrast in the presence of gas (Plaza-Faverola et al., 2012; Bünz et al., 2014; Minshull et al., 2014; Tóth et al., 2014a; Cevatoglu et al., 2015).

Traditional qualitative analysis of the post-release seismic reflection data shows that these CO_2-related acoustic anomalies are only located along Horizon 2, i.e., no clear evidence of acoustic anomalies detected above or below Horizon 2 within the overburden and water column (Figs. 3.2-3.4). The analysis of the reflection coefficients for Horizon 2 shows a circular area with reflectivity anomalies, located to the NW of the diffuser, in agreement with the presence of gaseous CO_2 immediately beneath this unconformity (Figs. 3.7a and 3.10; Table 3.2). It is noteworthy that the change in Horizon 2 mean reflection coefficient is smaller between the pre-release and post-release seismic reflection data, compared to between the pre-release and syn-release

datasets (notably at Day 12 and Day 13) (Table 3.2). This observation most likely suggests causality between the amount CO_2 immediately beneath Horizon 2 and the magnitude of reflection coefficient. Further, there are no significant reflectivity anomalies detected in seabed reflection coefficients, with the exception of a very few localized areas with increased reflectivity, in agreement with the gaseous CO_2 being predominantly confined immediately beneath Horizon 2 on Days 706 and 707 (Figs. 3.8a and 3.10; Table 3.2). *Q* values outside the circular area from the post-release seismic reflection dataset are similar to those calculated from the pre-release seismic reflection data, consistent with the lack of acoustic anomalies above and below Horizon 2 on Days 706 and 707 (Figs. 3.9 and 3.10; Table 3.3). Q values above Horizon 2 within the circular area are similar to the pre-release Q values, indicating lack of gaseous CO_2 above Horizon 2 on Days 706 and 707 (Figs. 3.9 and 3.10; Table 3.3).

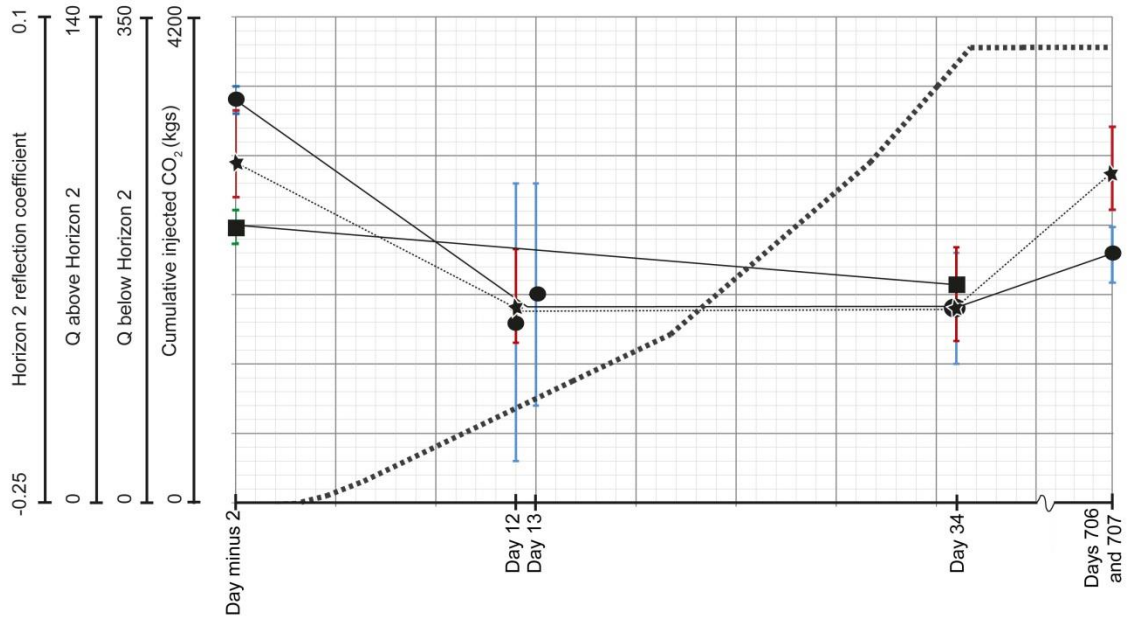

Figure 3.10 *Summary of the changes in the acoustic properties of sediments during and after CO_2 injection in Ardmucknish Bay, and cumulative CO_2 injected during the QICS experiment. Sampling points are indicated as circles (Horizon 2 reflection coefficient), stars (Q_{mean} above Horizon 2), and squares (Q_{mean} below Horizon 2). Data are summarized in Table 3.2 and Table 3.3.*

The spatial extent of the CO_2-related acoustic anomalies shows a preferential clustering within a circular area of 40 m diameter, mostly located up-dip of the diffuser (Figs. 3.2-3.5a). This spatial distribution clearly demonstrates the control of the

subsurface geometry, i.e., up-dipping strata, on CO_2 migration in Ardmuknish Bay, after the cessation of gas injection. The dip of Horizon 2 in the vicinity of the injection site is 3.5° (Figs. 3.2-3.4). It is interesting to note that even a very small dip can control CO_2 migration pattern within the subsurface. Up-dip gas migration has been shown in previous studies, where the up-dipping strata facilitates the buoyancy-driven migration of fluids (Bangs et al., 2011; Bünz et al., 2012; Brothers et al., 2014; Sha et al., 2015). This mechanism might be similar to the preferential migration of fluids along discontinuities within the overburden, i.e., permeable faults and seismic chimneys, where the fluids are channelled within the subsurface towards a dominant direction (Sassen et al., 2001; Annunziatellis et al., 2008; Rajan et al., 2012; Yang and Davies, 2013).

Finally, an important question derives from the analysis of the post-release seismic reflection data: what happened to gas above Horizon 2, which was detected on seabed reflection coefficient maps and seismic attenuation calculations between Day 12 to Day 34 (Cevatoglu et al., 2015). Among various alternatives considered, the most likely explanation is the combination of CO_2 leakage into the water column from Day 34 onwards, as well as the dissolution of the CO_2 within the sediment pore space.

3.4 Conclusion

Post-release seismic reflection (Chirp) data were acquired in Ardmucknish Bay, to assess the recovery response of the overburden. Analysis of this seismic reflection dataset reveals enhanced reflectivity and polarity reversal along Horizon 2, as well as reflection coefficient anomalies along the same horizon, implying the trapping of the gaseous CO_2 immediately beneath Horizon 2. There is no other significant evidence of acoustic anomalies within the subsurface or the overlying water column. High-reflectivity anomalies are shown to cluster within a circle of 40 m diameter, located up-dip of the diffuser, suggesting the strong control of the subsurface geometry on CO_2 migration. A very small dip, of c. 3.5°, is found to significantly control CO_2 migration within the overburden, after the cessation of injection. The lack of gaseous CO_2 above Horizon 2 can be interpreted as the consequence of post-release continued leakage into the water column and/or dissolution.

It is important to note that, approximately 2 years after the cessation of injection, CO_2 is still present within the overburden in a gaseous form in Ardmucknish Bay. This result is crucial for ongoing and planned CCS projects, emphasizing that sub-seabed geological storage contributes to the atmospheric CO_2 mitigation effort, even after the cessation of injection. However, risk assessments for geological carbon sequestration should also consider that, if the reservoir leaks into the overburden, the gaseous CO_2 could migrate within the subsurface after the cessation of injection. This migration is controlled, and even facilitated, by the subsurface geometry, underlining the importance of site selection for CCS operations.

Chapter 4

Quantification of CO_2 in gassy marine sediments and acoustic impedance inversion

Abstract

As part of the QICS experiment, 4.2 tonnes of CO_2 were injected over 37 days into the unconsolidated marine sediments in Ardmucknish Bay, Oban. During the syn-release period, CO_2 migration was controlled by sediment stratigraphy and injection rate/total injected volume, leading to gas leakage at the seabed. Following the cessation of injection, the gaseous CO_2 was found to be largely trapped below a stratigraphic boundary (Horizon 2), located at c. 4 m depth below the seafloor.

Here we first determine the *in situ* CO_2 content/volume above Horizon 2, using apparent temporal thickness changes of the seabed-Horizon 2 interval on seismic reflection data, combined with the Anderson and Hampton compressible fluid model. Further, we investigate the change in acoustic impedance along Horizon 2, by performing acoustic impedance inversion of seismic reflection data. The maximum CO_2 volume above Horizon 2 is detected at Day 12, c. 320 dm^3. The total CO_2 volume *in situ* was found to increase up to Day 12 with the increasing injection rate/total injected volume, and then decreased, which is interpreted as being due to increased CO_2 leakage at the seabed. The largest decrease in acoustic impedance along Horizon 2 is c. 3000 m/s g/cm^3 at Day 12, which reduces the impedance below that of the water column, possibly suggesting a significant free gas saturation.

In future work, acoustic impedance variations along Horizon 2 will be used to determine the *in situ* CO_2 content immediately beneath Horizon 2. Further, the quantification of dissolved gas within the overburden from geochemistry data will allow the investigation of the accuracy of CO_2 volume estimation from seismic reflection data.

4.1 Introduction

Sub-seabed gas flow is a common geological process that modifies the acoustic and mechanical properties of sediments, thus resulting in significant seismic amplitude, velocity and attenuation anomalies. Although many studies report the widespread occurrence of free gas within the overburden, relatively little attempt has been made to determine the *in situ* gas saturation in shallow marine sediments (Andreassen et al., 1997; Best et al., 2004). Quantification of free gas within the shallow subsurface is important for resource exploration and carbon sequestration, as well as geohazard assessment (Robb et al., 2007; Morgan et al., 2012).

Seismic reflection methods have been the most widely used approach to quantify free gas in sediments, combined with rock physics modelling. Using simple travel time inversion and interval velocity analysis, several authors determined the *in situ* gas saturation for marine sediments (Table 4.1). For instance, Tóth et al. (2014b) used average interval seismic velocities from multichannel seismic reflection data (frequency range between 200-600 Hz), together with the Anderson and Hampton geoacoustics model (Anderson and Hampton, 1980b), to estimate free gas content in Baltic Sea sediments. Their results indicate that even a very small amount of free gas in sediment pore space, c. 0.046% of the total sediment volume, drastically reduces seismic P-wave velocities, c. of 500 m/s reduction. Further, effective medium modelling was used to determine free gas saturation in Blake Ridge sediments, together with interval velocity changes, showing c. 1-2% gas saturation, assuming uniform saturation (Ecker et al., 2000). The Biot-Geertsma-Smit rock physics equations (Tinivella, 1999) were applied to seismic velocities derived from travel-time inversion (airgun data), where a gas saturation of 4% of the total sediment volume was calculated for South Shetland Margin sediments, considering patchy saturation (Tinivella et al., 2002). By combining an effective medium approach, described in detail in Leighton (2007a), with seismic velocities derived from apparent travel time changes, Leighton and Robb (2008) remotely calculated bubble void fractions from high-resolution seismic reflection (Chirp) data, for Northern Ireland offshore sediments, getting values of <0.01%.

Apart from simple travel time inversion or interval velocity analysis, other authors used more complex approaches to determine the *in situ* gas saturation from

acoustic methods (Table 4.1). For instance, Anderson and Hampton geoacoustics model (Anderson and Hampton, 1980a, b) was used to determine bubble size distribution and gas porosities for attenuation coefficient peaks, measured during an acoustic monitoring experiment in tidally-affected Dibden Bay, for seismic frequencies ranging between 600-3000 Hz (Best et al., 2004). Further, the amplitude-versus-offset (AVO) modelling of a bottom simulating reflector (BSR), combined with the Gregory (1977) rock physics empirical relationships, were used to determine free gas saturation from multichannel airgun seismic reflection data, acquired in offshore Oregon and the Beaufort Sea (Andreassen et al., 1997). Qian et al. (2014) determined free gas saturation within fine-grained sediments of the South China Sea, c. 0.2-10% gas saturation within sediment pore space, using AVO modelling from multichannel seismic reflection data (central frequency 70 Hz), and effective medium theory. In addition, a genetic algorithm was used to invert a P-wave seismic attenuation model to estimate free gas content in Finneidfjord and Blake Ridge sediments, using multichannel airgun (frequency range between 40-500 Hz) and single channel seismic reflection data, respectively (Morgan et al., 2012). Ghosh et al. (2015) used pressure-dependant differential effective medium theory (Ghosh and Sen, 2012) to relate post-stack acoustic impedance inversion results of seismic reflection data to gas content for Sleipner CCS site, where they determine CO_2 saturation between 20-80% of the pore space, depending on the saturation model.

Authors	Method	Rock physics model/ equations
Toth et al. (2014)	Interval velocity analysis	Anderson and Hampton (1980b)
Ecker et al. (2000)	Interval velocity analysis	Effective medium theory (Dvorkin et al., 1999)
Tinivella et al. (2002)	Travel time inversion	Biot-Geertsma-Smith equations (Tinivella, 1999)
Leighton and Robb (2008)	Travel time inversion	Effective medium theory (Leighton, 2007)
Best et al. (2004)	Seismic attenuation modelling	Anderson and Hampton (1980a, b)
Andreassen et al. (1997)	AVO	Gregory (1977)
Qian et al. (2014)	AVO	Effective medium theory (Dvorkin et al., 1999; Ecker et al., 2000)
Morgan et al. (2012)	Seismic attenuation inversion	Carcione and Picotti (2006) attenuation model
Ghosh et al. (2015)	Acoustic impedance inversion	Differential effective medium theory Ghosh and Sen (2012)

Table 4.1 *Scientific literature for remote free gas quantification in marine sediments.*

A controlled CO_2 injection experiment was completed in Ardmucknish Bay, where 4.2 tonnes of CO_2 were injected into unconsolidated marine sediments over 37 days (see Chapter 2). High-resolution seismic reflection (Chirp and boomer) data acquired syn-release showed several acoustic anomalies within the overburden and water column, caused by CO_2 fluxing (see Chapter 2). Analysis of post-release seismic reflection (Chirp) data indicated that gaseous CO_2 was largely trapped below a stratigraphic boundary (Horizon 2) within the overburden, located at c. 4 m depth below the seafloor (see Chapter 3). CO_2 migration was found to be controlled by sediment stratigraphy in the early stages of the QICS experiment, where sediment fracturing occurred below Horizon 2, and capillary invasion and fluidisation occurred above Horizon 2. In the late stages of the QICS experiment, the CO_2 injection rate/total injected volume overrode the stratigraphic control on gas migration (see Chapter 2). Following the cessation of injection, CO_2 migrated up-dip along Horizon 2, revealing the stratigraphic geometry control on gas migration (see Chapter 3).

Here, our objectives are (1) to compare the amount of injected CO_2 during the QICS experiment with gaseous CO_2 trapped above Horizon 2 and, (2) to quantify the acoustic impedance variation along Horizon 2 during the QICS experiment. To quantify the amount of CO_2 above Horizon 2, we completed thickness analysis of the seabed-Horizon 2 stratigraphic boundaries from pre-, syn- and post-release seismic reflection datasets acquired in Ardmucknish Bay. Temporal thickness variations are then used to estimate seismic velocity changes above Horizon 2, followed by quantification of free gas *in situ*, using the Anderson and Hampton geoacoustics model. To achieve our second objective, we completed acoustic impedance inversion of pre- and syn- release seismic reflection datasets.

4.2 Methods

4.2.1 Thickness analysis above Horizon 2 and variations in seismic P-wave velocity

To assess temporal thickness variations of the seabed-Horizon 2 interval, seismic wavelets corresponding to the horizons of interest (seabed and Horizon 2) were systematically picked on pre-, syn- and post-release seismic reflection datasets (from Day minus 2 to Days 706-707; see Chapter 3, Table 3.1 for more details on seismic

datasets acquired as part of the QICS experiment). Although the phase of the Chirp and boomer source wavelets are different (zero phase for Chirp, and minimum phase for boomer), thickness analysis is not affected by the difference in source wavelet, as care was taken to ensure that picking was consistent for horizons of interest, for any given seismic dataset (Fig. 4.1).

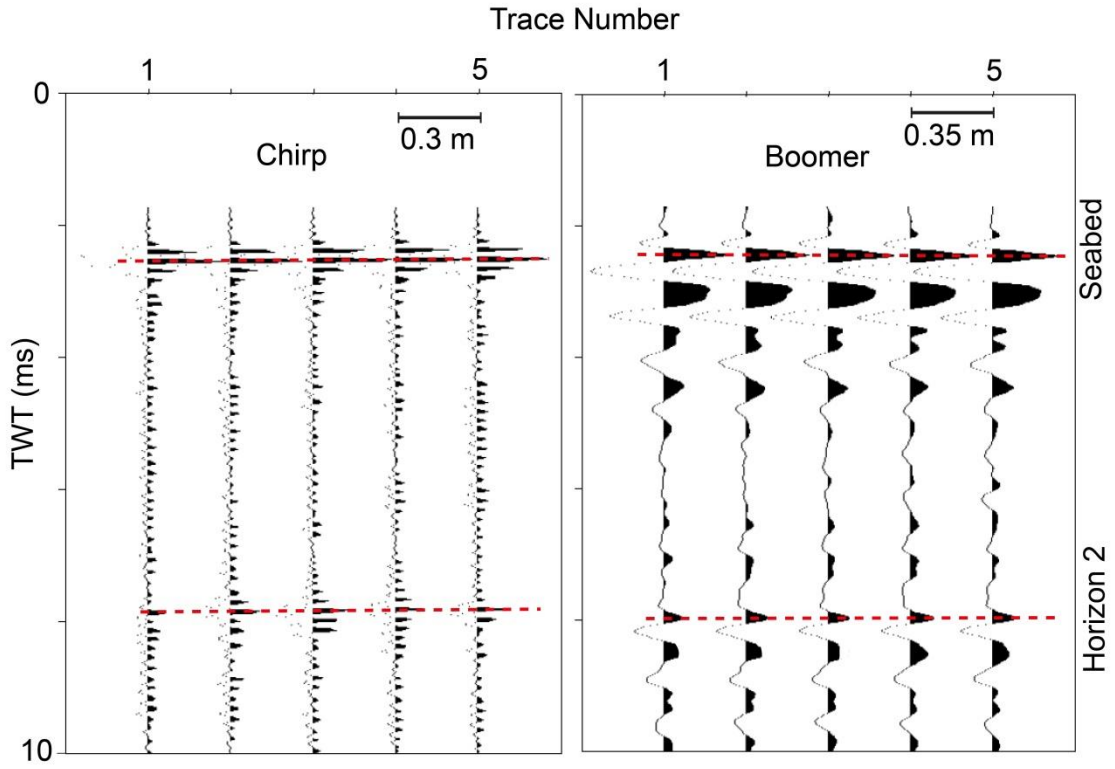

Figure 4.1 *Method used in thickness analysis for the seabed-Horizon 2 interval in Ardmucknish Bay seismic reflection data. Red dashed line indicates picks for seabed and Horizon 2 on two different seismic reflection dataset (Chirp data is from Day 2 and Boomer data is from Day 34).*

Two different sets of isopach maps were produced, showing: (1) the thickness of seabed-Horizon 2 interval on each day of seismic reflection data acquisition (from Day minus 2 to Days 706-707) and, (2) difference in thickness of seabed-Horizon 2 interval between the day of interest and the pre-release seismic reflection data. Isopach maps cover an area located in the vicinity of the CO_2 injection diffuser, as previous studies showed that CO_2 had only migrated above Horizon 2 in the immediate vicinity of the injection site (Cevatoglu et al., 2015).

Assuming that thickness variations between any given day and the pre-release seismic reflection data are only related to seismic P-wave velocity changes in the presence of CO_2 above Horizon 2, i.e., excluding any possibility for expansion in sediment volume caused by CO_2 injection, the relationship between the pre-release seismic P-wave velocity (V_{p1}) and syn- or post-release velocity (V_{p2}) can be expressed as follows (Eq. 1):

$$V_{p1}\, t_1 = V_{p2}\, t_2 \quad (1)$$

where V_{p1} and V_{p2} correspond to seismic P-wave velocity above Horizon 2 before and during/post CO_2 injection (in m/s), respectively, and t_1 and t_2 are the corresponding travel times (in one-way time, ms).

MSCL measurements were completed on Core 6 (Jacobs, 2010) which was recovered pre-release in Ardmucknish Bay (Fig. 4.2; see also Chapter 2, Figs. 2.2 and 2.3). The average seismic velocity before injection, above Horizon 2, is V_{p1}=1575 m/s, calculated from MSCL measurements on Core 6 (Fig. 4.2).

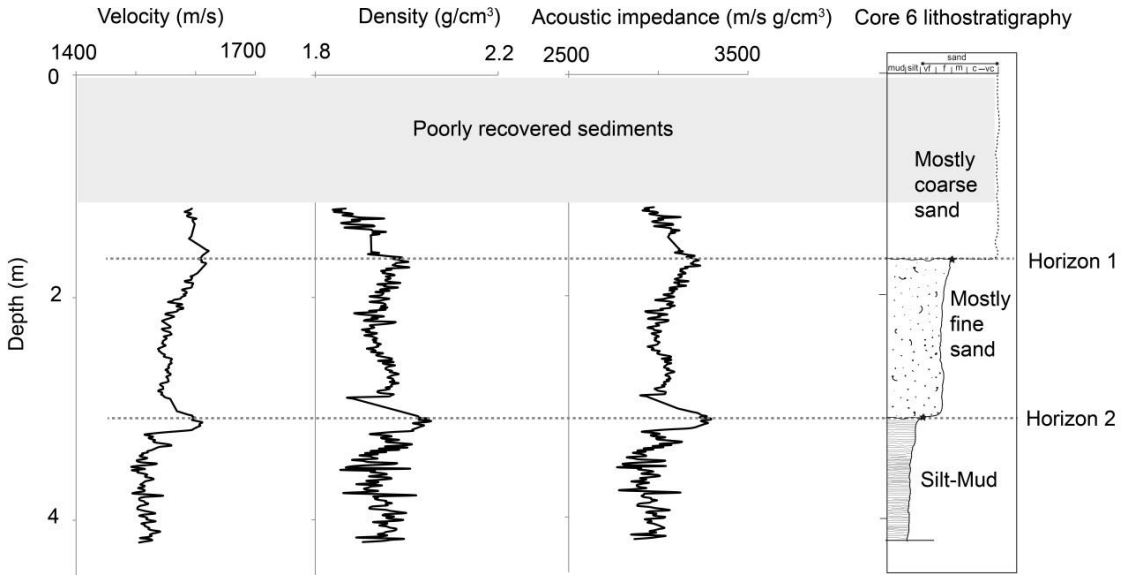

Figure 4.2 *Results from MSCL measurements along Core 6. Seismic velocity and density data were used to calculate the acoustic impedance variation which is used later in this chapter. Core 6 lithostratigraphy is also given.*

4.2.2 CO_2 quantification above Horizon 2

To relate changes in seismic P-wave velocity to CO_2 content above Horizon 2, we use the Anderson and Hampton compressible fluid model (Anderson and Hampton, 1980b). The Anderson and Hampton model has been frequently used to determine the effect of *in situ* fluids on sediment acoustic properties (Wilkens and Richardson, 1998; Best et al., 2004; Tóth et al., 2014b). The Anderson and Hampton model was chosen in this thesis to estimate *in situ* CO_2 saturation for several reasons. It is a simple model, assuming that free gas is uniformly distributed within sediment pore space, which in turns makes the calculations easier compared to considering patchy saturation, e.g., White's patchy saturation model (White, 1975). The Anderson and Hampton model assumes a homogenous and isotropic medium containing Type III bubbles within sediment pore space (bubble size larger than sediment pore size), which displace sediment grains and deform the sediment matrix (Anderson et al., 1998b). These assumptions exclude the natural variability in sediment mineralogy, grain contact, pore size/shape and bubble size/shape, in contrast to more complex rock physics models, which take into account these variations (Hashin and Shtrikman, 1963; Hornby et al., 1994; Mavko et al., 2009; Ba et al., 2013; Sain et al., 2014). Finally, all the input parameters required to estimate *in situ* CO_2 content are easily accessible from the scientific literature (based on laboratory experiments and the lithology identified in Core 6).

Assuming a homogenous and isotropic medium, the seismic P-wave velocity can be determined by solving the wave equation (Eq. 2) (Telford et al., 1990; Slawinski, 2003). Eq. 2 shows that the seismic P-wave velocity is determined by the elastic properties of a medium through which it propagates (Eq. 2):

$$V_p = \sqrt{\frac{K + 4/3G}{\rho_s}} \qquad (2)$$

where V_p is the seismic velocity, K is the sediment bulk modulus, G is the sediment shear modulus and ρ_s is the sediment bulk density.

Anderson and Hampton (1980b) suggest that, in the presence of free gas in sediment pore space, the bulk modulus of the sediment is modified (K_{com}) compared to gas-free sediment, where the gas only changes the compressibility of interstitial water; however, it does not have any effect on the sediment mineral modulus (K_m), frame modulus (K_f) or shear modulus (G) (Eq. 3). P-wave velocity modified by gas (V_p) is calculated by using the elastic properties of sediments (K_{com} and G), as well as sediment bulk density (ρ_s), for seismic frequencies below the bubble resonance frequency (Anderson and Hampton, 1980b) (Eq. 3):

$$V_p = \sqrt{\frac{K_{com} + 4/3G}{\rho_s}} \qquad (3)$$

The composite bulk modulus (K_{com}) is calculated using Gassmann (1951) fluid substitution equations (Eqs. 4, 5 and 6) by Anderson and Hampton (1980b):

$$K_{comp} = K_m \frac{K_f + Q'}{K_m + Q'} \qquad (4)$$

$$Q' = K'_w \frac{K_m - K_f}{n\,(K_m - K'_w)} \qquad (5)$$

$$K'_w = \frac{K_w K_g}{n'_g K_w + (1 - n'_g) K_g} \qquad (6)$$

where K_w is the bulk modulus of water, K'_w is the bulk modulus of water modified by free gas within pore space, K_g is the bulk modulus of gas, n is the sediment fractional porosity, and n'_g is the fraction of pore space occupied by gas.

Under adiabatic compression, gas modulus K_g is calculated by using the ratio of specific heats of gas (γ) and ambient hydrostatic pressure (P_0) (Eq. 7):

$$K_g = \gamma P_0 \qquad (7)$$

Finally, gas content (n_g) (gas volume/sediment volume) is calculated, where gas content is determined as a fraction of total sediment volume (Eq. 8):

$$n_g = n'_g n \qquad (8)$$

4.2.3 Acoustic impedance inversion

Acoustic impedance inversion produces an impedance model of the subsurface, which can be used to remotely predict physical properties of sediments, including seismic velocity, porosity, density and mean grain-size (Wagner et al., 2012; Gloaguen et al., 2014; Götz et al., 2014; Vardy, 2015). By combining seismic velocity derived from acoustic impedance inversion with rock physics models, it is possible to estimate *in situ* gas saturation from seismic reflection data (Lu and McMechan, 2002; Bellefleur et al., 2012; Riedel and Shankar, 2012). Here, we use the genetic algorithm of Vardy (2015) to perform the acoustic impedance inversion of the seismic reflection data acquired in Ardmucknish Bay.

4.2.3.1 Genetic algorithms

Genetic algorithms are mathematical search algorithms, mimicking the mechanics of natural selection (Goldberg, 1989). Starting with a randomly initiated population (in our case, of impedance models), genetic algorithms use three main operators, including selection, cross-over and mutation, to generate the best synthetic model, i.e., impedance model in this study (Goldberg, 1989; Stoffa and Sen, 1991; Sen and Stoffa, 1992, 1996).

In the first generation, for each impedance model, seismic reflectivity series are produced, and convolved with the source wavelet to generate a synthetic seismic trace (based on convolutional theory, where the seismic response is the convolution of Earth reflectivity with the source wavelet, see Yilmaz (1987)) (Fig. 4.3). Following the generation of synthetic traces, residuals are calculated, i.e., difference between the field and synthetic seismic reflection data trace amplitudes (Eq. 9) (Vardy, 2015):

$$E(m) = \sum_{j=1}^{J} \left| S_{field}^{j} - S_{synth}^{j} \right| \qquad (9)$$

where $E(m)$ is the residual for model m, S_{field} and S_{synth} are the field and synthetic trace seismic amplitudes, and J is the number of time samples on each trace (Fig. 4.3).

To assess the likelihood of a particular model being propagated forward from the current generation to the next generation, a posteriori probability density function (PPD) can be calculated for each model (Eq. 10) (Sen and Stoffa, 1996; Vardy, 2015):

$$L(m) = \frac{\sum_{n=1}^{N} E(n)}{E(m)} \qquad (10)$$

where *L(m)* is the likelihood of a model *m*, *E(m)* is the residual for model *m* and *N* is the number of models in the current generation.

To populate the subsequent generation (selection operator), we use a Stochastic Remainder sampling technique, where models having a likelihood PPD better than the average PPD of the current generation are propagated forward into the next generation (Sivaraj and Ravichandran, 2011; Vardy, 2015) (Fig. 4.3). The remaining models in the new generation are subsequently populated by a random selection of models from the previous generation. This can include models having a higher PPD than the average PPD, and also those with a lower PPD than the average PPD. This ensures we maintain a well distributed parameter space (Fig. 4.3).

In the next generation, values between two impedance models are exchanged depending upon cross-over probability, and mutated into a randomly generated value depending on the mutation probability. Therefore new impedance models are generated that preserve a significant proportion of the features of the previous generation of models, but have also evolved to develop new features, not present in the original models. Similarly to the previous generation, synthetic traces are produced for each impedance models, and residuals are calculated. The likelihood PPD of each impedance model is calculated and suitable impedance models are carried into the next generation. This process continues until the number of generation reaches the maximum generation (Fig. 4.3). It is important to clarify that the term “generation” used in this chapter is a specific term for genetic algorithms, corresponding to the term “iteration” during standard inversion.

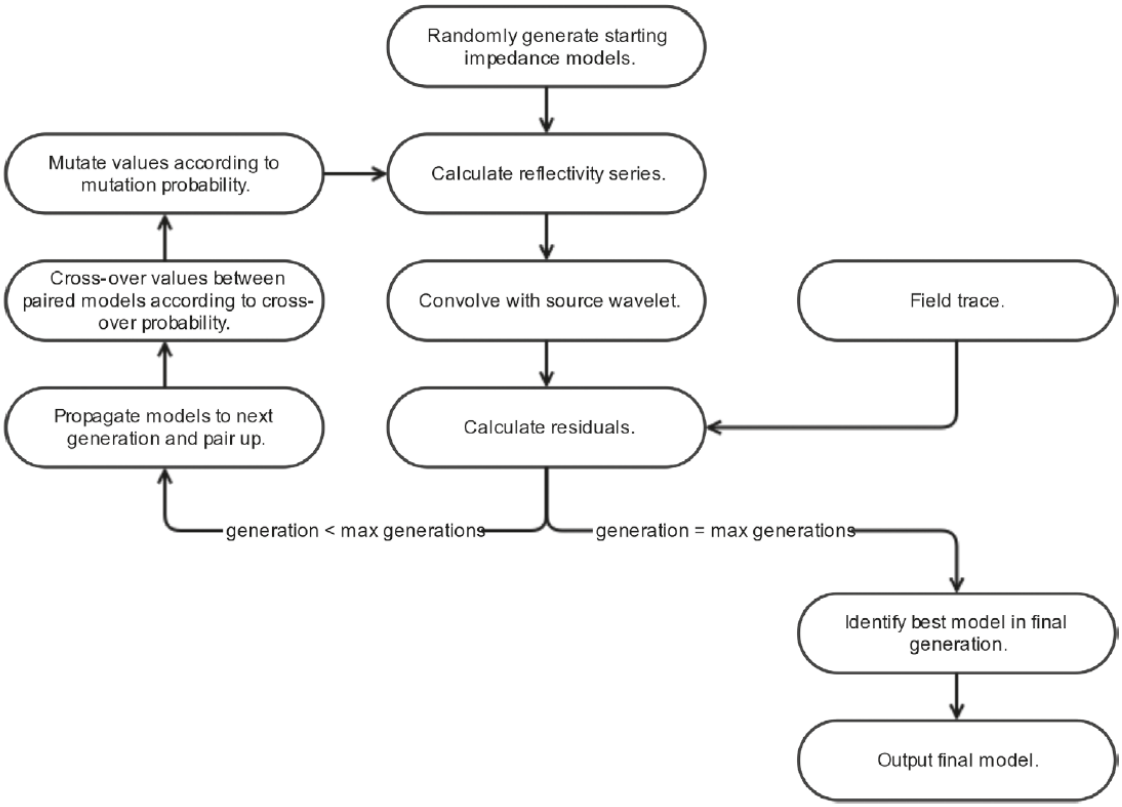

Figure 4.3 *Flow chart illustrating the process of a genetic algorithm used in acoustic impedance inversion (Vardy, 2015). Randomly populated acoustic impedance models are subject to selection, cross-over and mutation operators. Once the maximum generation is reached, the best synthetic model is output as the final impedance model.*

To select the value of input parameters for our genetic algorithm, i.e., the maximum number of generations, number of models in each generation, cross-over and mutation probabilities, first we inverted a pre-release seismic reflection trace (boomer) coincident with the Core 6 location (Fig. 4.4a and 4.4b). MSCL velocity and density data were used to calculate the acoustic impedance variation along Core 6 (Fig. 4.2). A set of values were tested for each of the above input parameters, based on the published literature (Vardy, 2015), and those providing the smallest residual between synthetic and real (pre-release boomer) seismic traces are determined to be the optimum input parameters for acoustic impedance inversion (Fig. 4.5). The maximum number of generation is selected as 500, as beyond 500 generations, there is no significant change in the residuals (Fig. 4.5a-c). Having 900 models per generation is associated with c. 4% residual error. Although 1100 models per generation have slightly smaller residual error, c. 3.5%, it is associated with increased computational cost, i.e., inversion time

being around two days. Therefore, the number of models in each generation is selected as 900 (Fig. 4.5a). Cross-over probability of 0.6, and mutation probability of 0.2 give the optimum results (Fig. 4.5b and 4.5c). These values are subsequently used during acoustic impedance inversion of the syn- and post-release seismic reflection datasets.

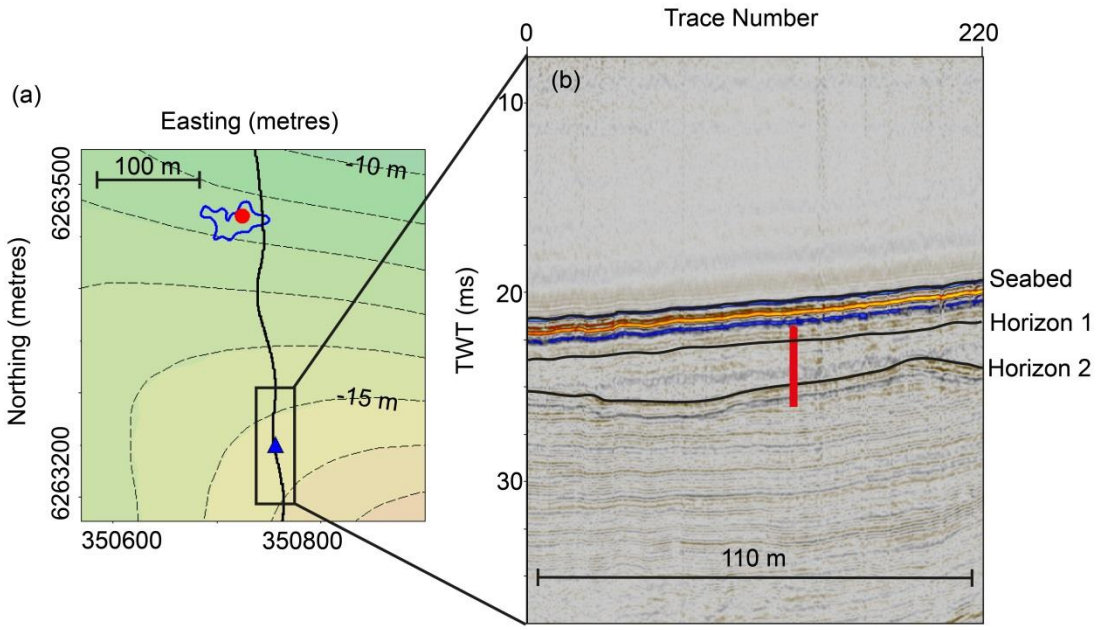

Figure 4.4 *Location of Core 6 and a pre-release boomer seismic reflection profile acquired in Ardmucknish Bay.* ***(a)*** *Core 6 (blue triangle) location with respect to the injection site. The diffuser is indicated by the red dot. The blue polygon corresponds to the combined chimney area, where syn-release chimneys were mapped on seismic reflection data (Cevatoglu et al., 2015). The black line is the pre-release boomer track line.* ***(b)*** *Location of Core 6 with respect to the pre-release boomer seismic reflection data. See also Chapter 2, Fig. 2.3 for the location of Core 6.*

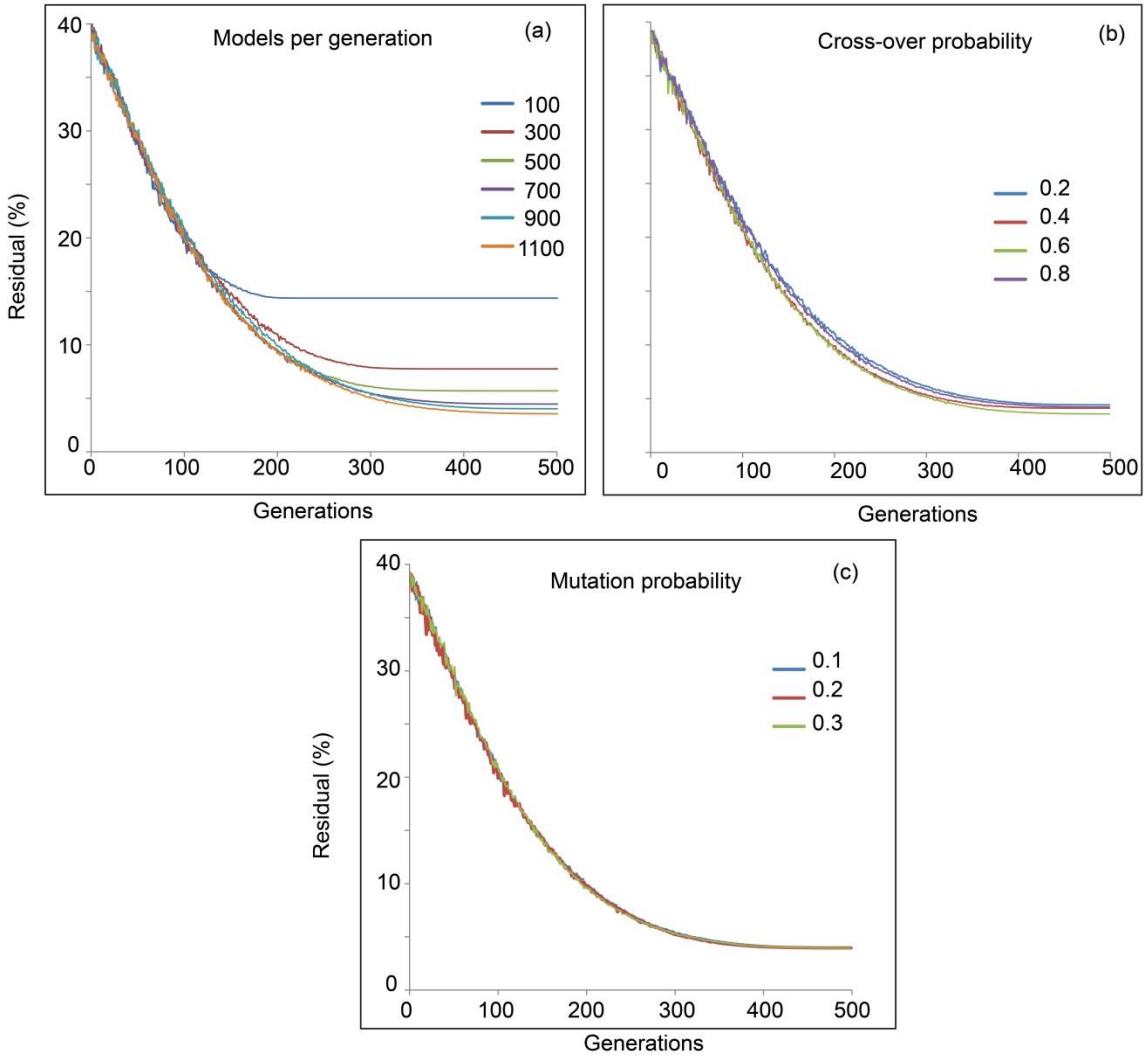

Figure 4.5 *Evolution of residuals for varying values of input parameters during acoustic impedance inversion of a pre-release boomer trace.* ***(a)*** *Test for number of models per generation.* ***(b)*** *Test for cross-over probability.* ***(c)*** *Test for mutation probability. Optimum parameters are chosen as: 500 generations, 900 models per generation, cross-over probability of 0.6, and mutation probability of 0.2.*

4.2.3.2 Seismic reflection data processing flow

As stated by Vardy (2015), convolutional seismic theory requires: (1) no diffracted energy; (2) no internal multiples; and (3) the seismic wavelet to be stationary (no wavefield spreading or attenuation). To ensure these requirements, we performed the following processing flows for Chirp and boomer seismic reflection data:

- Chirp data

- Vibroseis correlation (correlation with the source sweep, 1.5-13.0 kHz) (Quinn et al., 1998),
- Stolt F-K migration, time migration to correct for dipping geometry, compensating for diffraction energy using RMS velocities varying between 1500-1600 m/s,
- True Amplitude Recovery, to compensate for spherical divergence,
- *Q* compensation, to correct for attenuation. *Q* values calculated in Chapter 2 are used for this correction.

- Boomer data

- Ormsby band-pass filtering, to remove energy outside the source bandwidth,
- Predictive deconvolution, to reduce low energy reverberation,
- Stolt F-K migration, time migration to correct for dipping geometry, compensating for diffraction energy using RMS velocities varying between 1500-1600 m/s,
- True Amplitude Recovery, to compensate for spherical divergence,
- *Q* compensation, to correct for attenuation. *Q* values calculated in Chapter 2 are used for this correction.

In addition to these steps above, impedance inversion was limited to above the seabed multiple, for both Chirp and boomer seismic reflection datasets, to fulfil requirement 2. Finally, to compare synthetic and real seismic traces, both are normalized against the seabed trace amplitude of the pre-release boomer data, at Core 6 location.

4.2.3.3 Consolidation correction

As a result of using a convolutional approach, the wavelengths of the impedance model are constrained by the bandwidth of the seismic wavelet (1.5-13.0 kHz for Chirp and 0.5-4.0 kHz for boomer). Therefore, acoustic impedance inversion does not include the long-wavelength trend caused by sediment compaction, i.e., the long-wavelength consolidation trend. Thus, the long-wavelength consolidation trend should be added to

the short-wavelength relative impedance sections to get the final absolute impedance sections (Wagner et al., 2006; Bui et al., 2011; Wagner et al., 2012).

For the consolidation correction to be applied above and along Horizon 2, we used the consolidation trend derived from the impedance profile of Core 6 (Fig. 4.6a). However, as Core 6 penetration is limited (Fig. 4.4b), this core could not provide consolidation information for glacio-marine sediments located below Horizon 2. To constrain an average consolidation trend for glacio-marine sediments beneath Horizon 2, acoustic impedance profiles were compiled from the published literature (Table 4.2; Fig. 4.6a). An average consolidation trend for glacio-marine sediments can be derived from the variations in impedance profiles on Fig. 4.6a. It is noteworthy that, acoustic impedance data of Lake Windermere glacio-lacustrine sediments are also used in this study, as the consolidation trend of these glacio-lacustrine sediments is similar to those of glacio-marine sediments, improving our interpretation (Fig. 4.6a). From Fig. 4.6b, acoustic impedance increase above and along Horizon 2, due to consolidation, is c. 20 m/s g/cm^3 per metre; whereas an increase of c. 40 m/s g/cm^3 per metre is found along the impedance profiles of regional glacio-marine and glacio-lacustrine sediments. After inversion, these consolidation corrections are applied to relative acoustic impedance sections to get the final absolute impedance sections.

Sediment type	Location	Age	Water depth (m)	Core length (m)
Glacio-marine[a]	***Svalbard***, Van Keulenfjorden fjord	3 Ka BP	82	5.4
Glacio-marine[b]	***Norway***, Lofoten Islands continental slope	18 Ka BP	1178	16
Glacio-marine[c]	***Scotland***, Loch Linnhe	pre-Holocene	94	9
Glacio-lacustrine[d]	***England***, Lake Windermere	pre-Holocene	27	8

[a] Kempf et al. (2013)

[b] Baeten et al. (2014)

[c] John Howe, pers. comm.

[d] Miller (2014)

Table 4.2 *Key properties of sediments used in this study to derive a consolidation trend for glacio-marine sediments located beneath Horizon 2.*

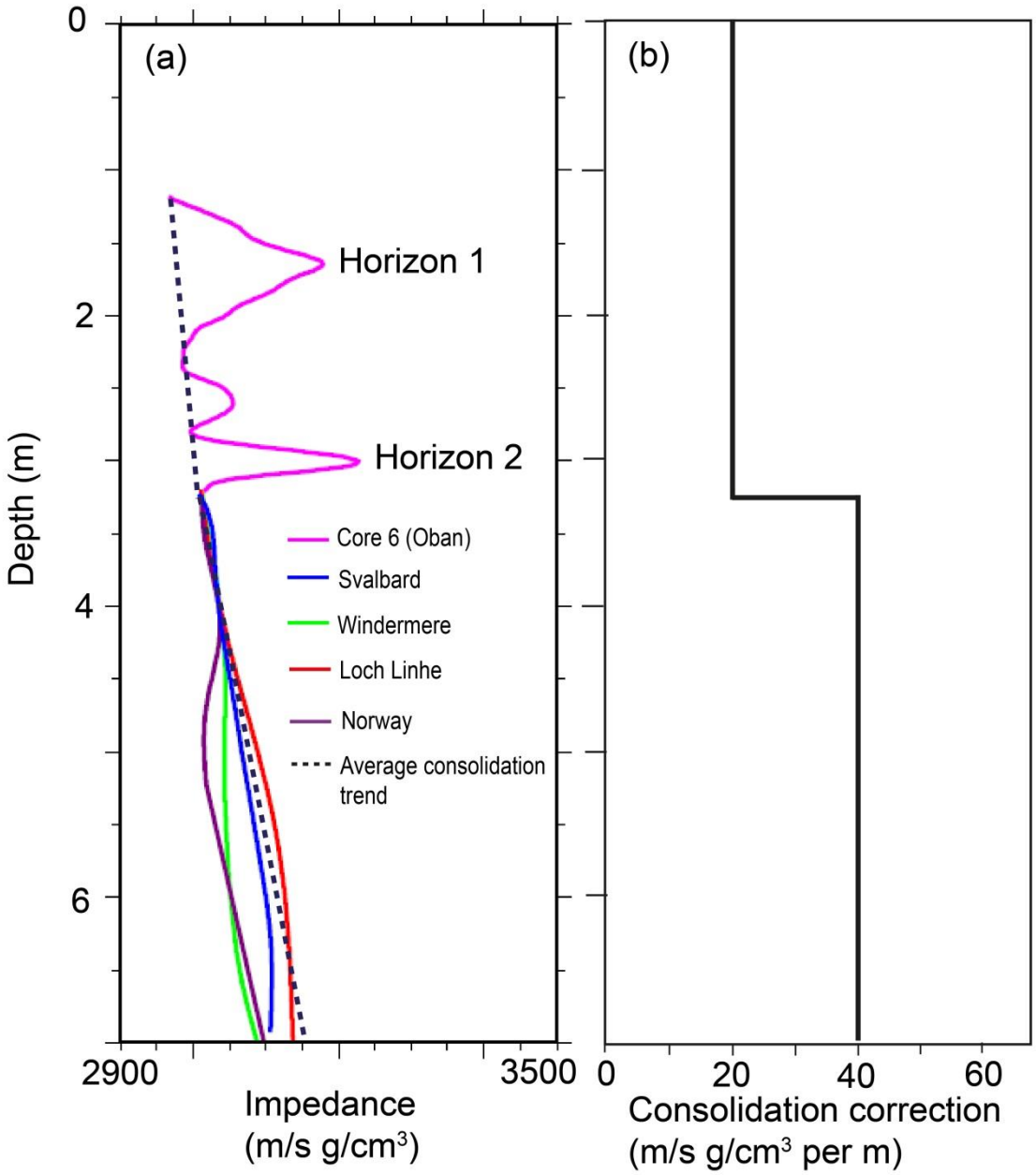

Figure 4.6 *Generation of consolidation correction for Ardmucknish Bay sediments.* ***(a)*** *Acoustic impedance data from Core 6 and regional glacio-marine and glacio-lacustrine sediments.* ***(b)*** *Consolidation correction.*

4.3 Results

4.3.1 Thickness analysis above Horizon 2 and seismic P-wave velocity variations

The isopach map generated from the pre-release seismic reflection (Chirp) data indicates a gentle thickening of the seabed-Horizon 2 interval eastwards, with thickness varying between 3.5-6.0 ms (2.8-4.8 m depth, assuming V_{p1}=1575 m/s), within the combined chimney area (Fig. 4.7a). Day 0 and Day 1 isopach maps are quite similar to the Day minus 2 isopach map, except of small thickness changes around the diffuser (Fig. 4.7b and 4.7c). At Day 2, the thickness of the seabed-Horizon 2 interval is larger in the vicinity of the injection site, notably to the SE, compared to the pre-release isopach map, with the maximum thickness being 5.75 ms (Fig. 4.7d). The isopach map from Day 12 shows a significant increase of thickness in the vicinity of the diffuser, compared to the pre-release isopach map, pronounced notably immediately to the NE and SE of the injection site (Fig. 4.7e). At Day 13, a general increase of thickness is observed, located mainly to the W of the combined chimney area, as well as around the diffuser (Fig. 4.7f). Day 34 and Days 706-707 isopach maps are mostly similar to that of the pre-release data, with the exception of small thickness changes observed around the diffuser (Fig. 4.7g and 4.7h).

Temporal thickness changes of the seabed-Horizon 2 interval between syn/post-release and pre-release seismic reflection surveys are illustrated on Fig. 4.8. At Day 0 and Day 1, the maximum change in thickness is up to c. 0.25 ms and 0.5 ms, respectively (Fig. 4.8a and 4.8b). At Day 2, the largest thickness change is between c. 0.5-0.75 ms, in the vicinity of the diffuser (Fig. 4.8c). At Day 12, the thickness variation is significantly pronounced, with the maximum thickness change being c. 1.25 ms to the NE of the diffuser (Fig. 4.8d). At Day 13, the largest thickness change is observed around the diffuser, between c. 0.5-0.75 ms (Fig. 4.8e). Day 34 and Days 706-707 have relatively smaller thickness change, up to of c. 0.25 ms, observed around the diffuser (Fig. 4.8f and 4.8g). Note that these thickness variations are only valid if the anomaly area is well sampled both on pre-release and syn/post-release. For instance, thickness anomalies at the edges of the combined chimney area are probably artefacts due to lack of consistent sampling (Fig. 4.8).

Thickness of the seabed-Horizon 2 interval on pre-, syn- and post-release seismic reflection data (Fig. 4.7) are used to calculate syn- and post-release P-wave velocities above Horizon 2, within the combined chimney area (using Eq.1, V_{p1}=1575 m/s, see Section 4.2.1) (Fig. 4.9). On Fig. 4.9, we are only showing seismic velocity anomalies. From Day 0 to Day 2, the seismic velocity above Horizon 2 is smaller compared to its pre-release value (V_{p2}=1400-1574 m/s between Day 0 to Day 2 compared to V_{p1}=1575 m/s at Day minus 2) (Fig. 4.9a-c). Further, the spatial extent of the area with reduced seismic velocity is larger on Day 2 compared to previous days (Fig. 4.9a-c). The largest velocity reduction during the overall seismic survey is observed at Day 12, where V_{p2} decreases to c. 1200-1300 m/s around the injection site (Fig. 4.9d). On Day 13, the minimum seismic velocity around the diffuser is between 1400-1500 m/s (Fig. 4.9e). On the same day, to the W of the combined chimney area, a seismic velocity anomaly (V_{p2}=1200-1300 m/s) is also observed. However, this area is not well sampled, thus the seismic velocity anomaly is interpreted here as an artefact (Fig. 4.9e). On Day 34, the seismic velocity is between 1500-1574 m/s around the diffuser (Fig. 4.9f). The velocity anomaly on Days 706-707, immediately to the NE of the diffuser, is likely to be an artefact due to lack of frequent sampling (Fig. 4.9g).

To better illustrate the temporal seismic P-wave velocity changes above Horizon 2, the largest velocity anomalies, as well as the mean velocity, are calculated for a circular area of 10 m diameter, around the diffuser (Table 4.3). Pre-release average seismic velocity is also given for comparison. From Day 0 to Day 12, there is a gradual decrease in seismic velocity above Horizon 2, with the largest velocity reduction being down to V_{p2}=1246 m/s at Day 12, during the overall seismic surveys (Table 4.3). Between Days 13-34, the mean and minimum seismic velocities show a gradual increase within the circular area around the diffuser (Table 4.3). At Days 706-707, the minimum and mean seismic velocities show a slight decrease compared to Day minus 2. However, as stated above, these variations are most likely artefacts, due to lack of frequent sampling. The velocity changes above Horizon 2 will be discussed in discussion.

In the next section, we will use these seismic velocities to calculate gas content above Horizon 2 within the combined chimney area.

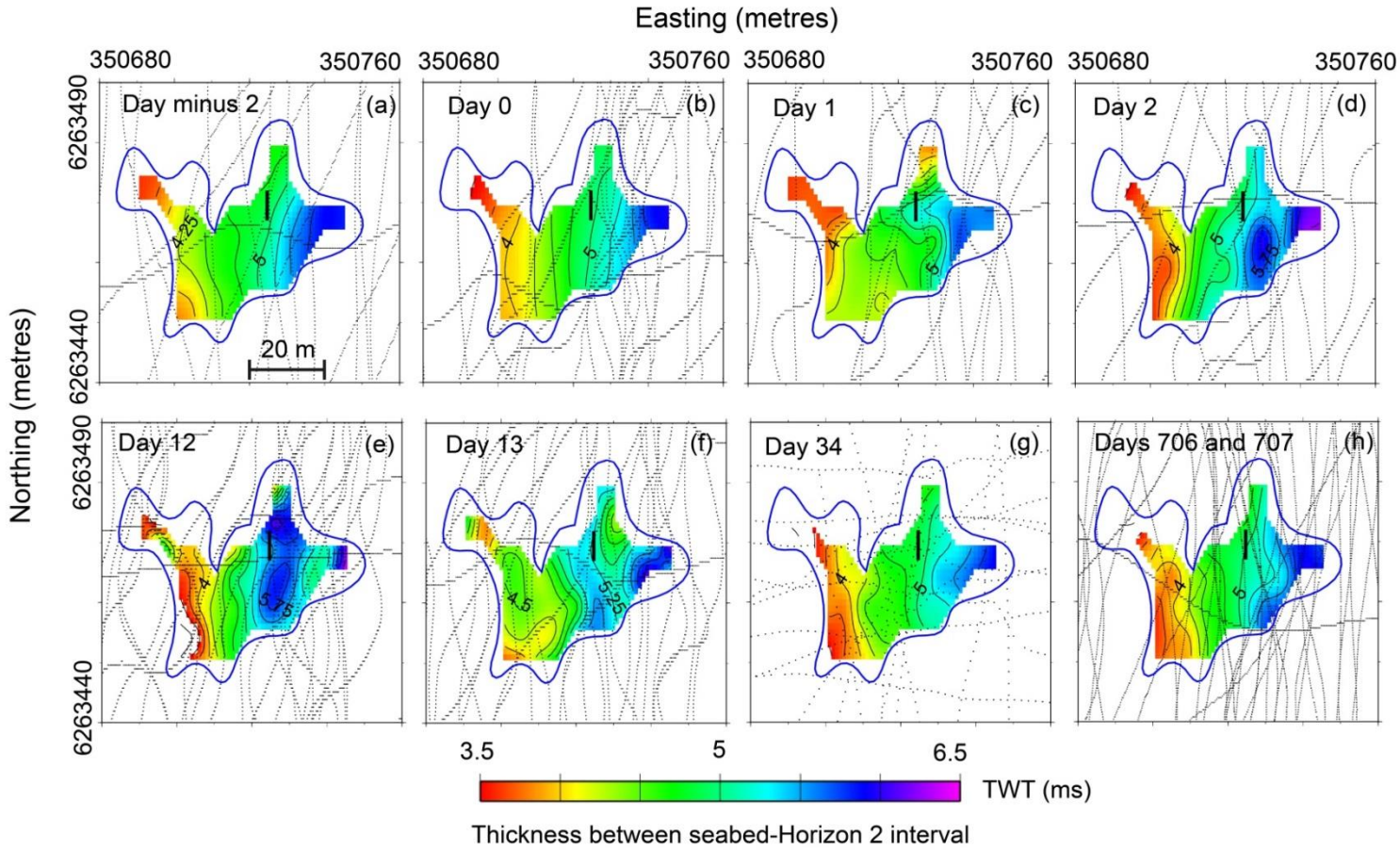

Figure 4.7 *Isopach maps of the seabed-Horizon 2 interval from seismic reflection data acquired in Ardmucknish Bay.* ***(a)*** *Day minus 2.* ***(b)*** *Day 0.* ***(c)*** *Day 1.* ***(d)*** *Day 2.* ***(e)*** *Day 12.* ***(f)*** *Day 13.* ***(g)*** *Day 34.* ***(h)*** *Days 706-707. The diffuser is indicated by the black line and the blue polygon corresponds to the combined chimney area. Seismic lines are given by black dotted lines. Thickness contours are every 0.25 ms.*

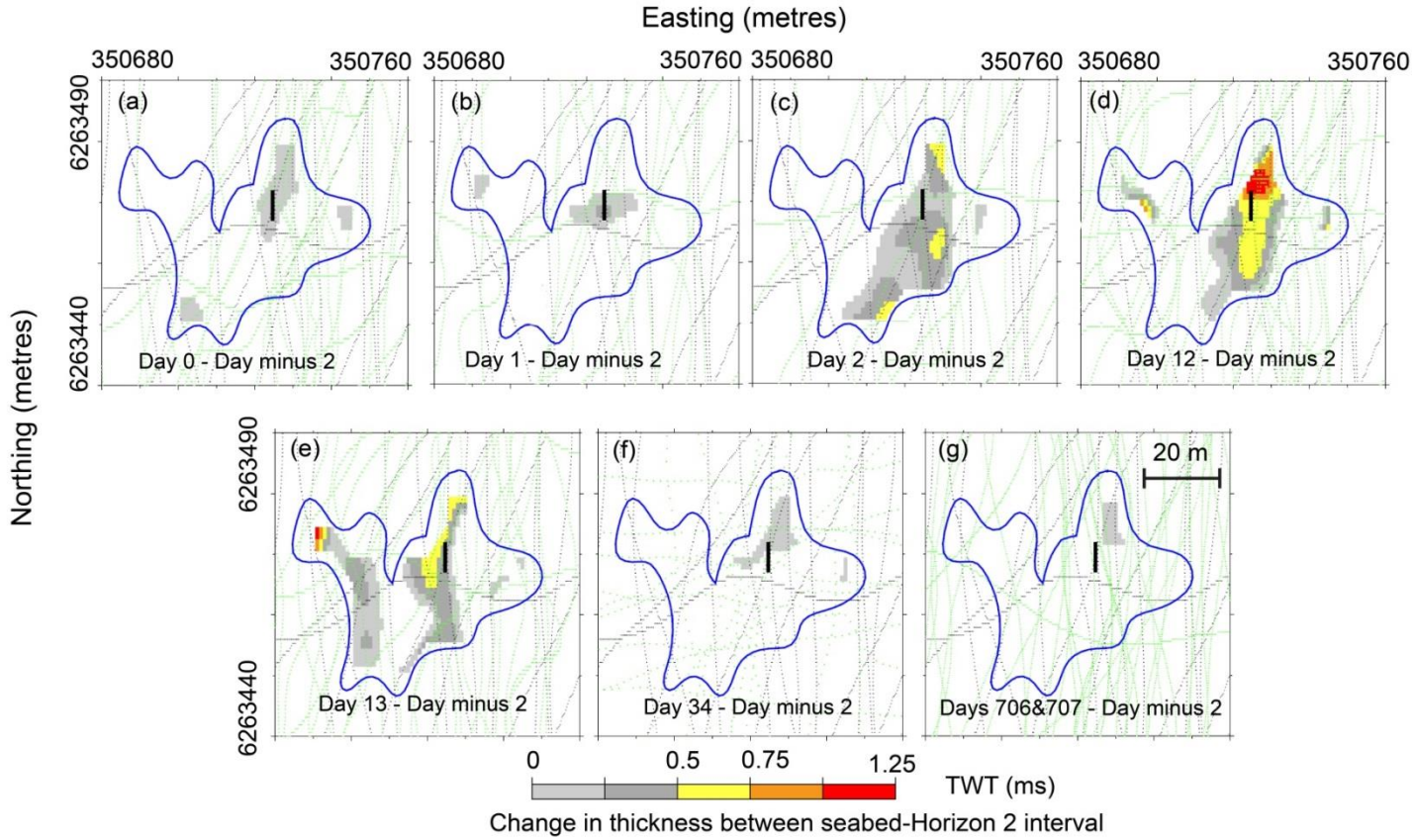

Figure 4.8 *Change in thickness of seabed-Horizon 2 interval between syn-/post-release and Day minus 2 seismic reflection data.* ***(a)*** *Between Day 0 and Day minus 2.* ***(b)*** *Between Day 1 and Day minus 2.* ***(c)*** *Between Day 2 and Day minus 2.* ***(d)*** *Between Day 12 and Day minus 2.* ***(e)*** *Between Day 13 and Day minus 2.* ***(f)*** *Between Day 34 and Day minus 2.* ***(g)*** *Between Days 706-707 and Day minus 2. The diffuser is indicated by the black line and the blue polygon corresponds to the combined chimney area. Black dotted lines indicate pre-release seismic reflection survey lines, and green dotted lines are the syn- and post-release seismic lines.*

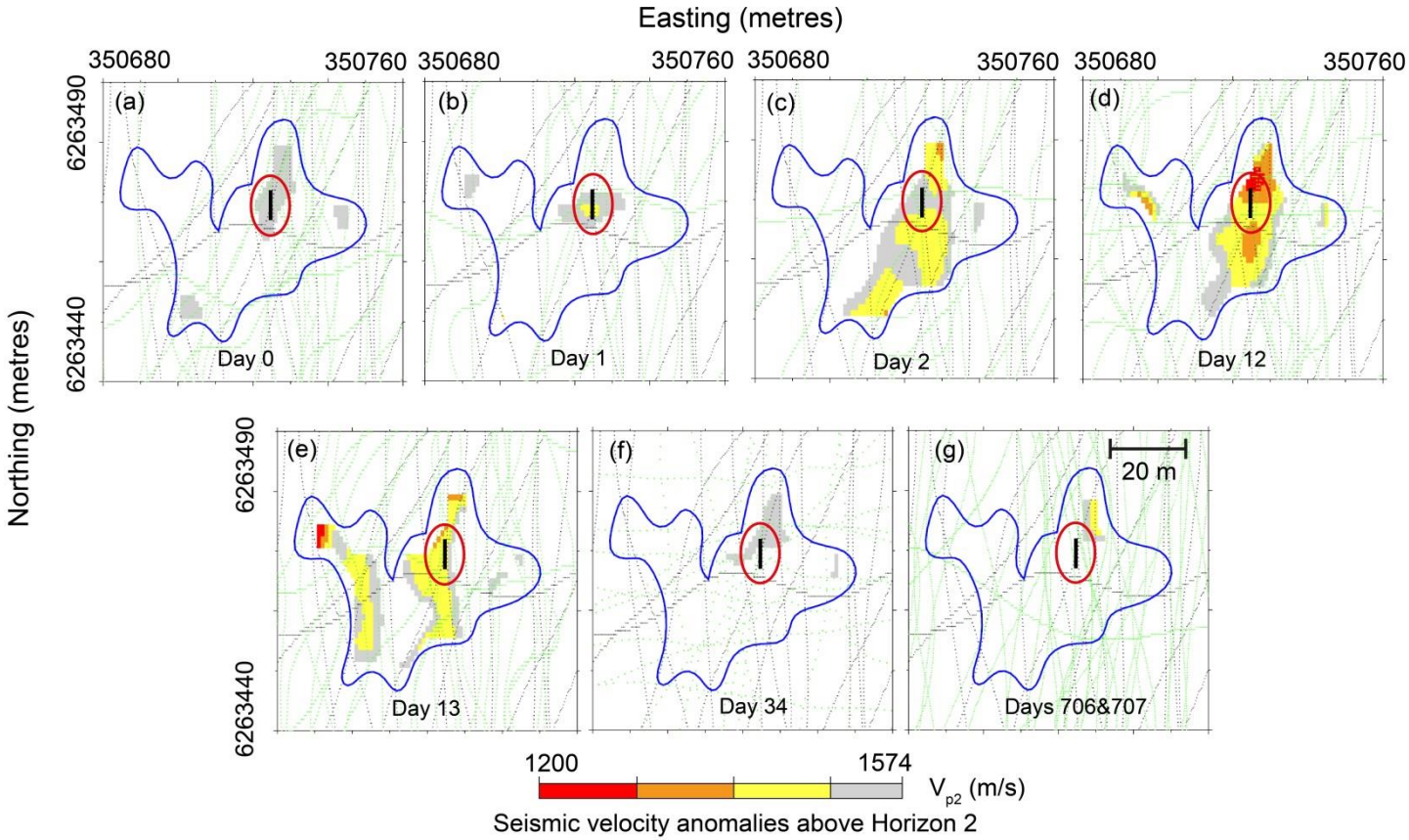

Figure 4.9 *Seismic P-wave velocity above Horizon 2 calculated for syn- and post-release seismic reflection surveys.* ***(a)*** *Day 0.* ***(b)*** *Day 1.* ***(c)*** *Day 2.* ***(d)*** *Day 12.* ***(e)*** *Day 13.* ***(f)*** *Day 34.* ***(g)*** *Days 706-707. The diffuser is indicated by the black line. Black dotted lines indicate pre-release seismic reflection survey lines, and green dotted lines are the syn-/post-release seismic lines. Red circle of 10 m diameter is the area for which mean and minimum seismic velocities are calculated (Table 4.3).*

Days	Minimum seismic velocity (m/s)	Mean seismic velocity (m/s)
Day minus 2	1575	1575
Day 0	1507	1560
Day 1	1483	1558
Day 2	1457	1502
Day 12	1246	1380
Day 13	1389	1504
Day 34	1536	1575
Days 706-707	1515	1530

Table 4.3 *Mean and minimum seismic P-wave velocities above Horizon 2 on pre-, syn- and post-release seismic reflection datasets. The largest velocity drop occurs at Day 12, with V_{p2}=1246 m/s above Horizon 2 within a circular area of 10 m diameter.*

4.3.2 CO_2 quantification above Horizon 2

The Anderson and Hampton compressible fluid model (Anderson and Hampton, 1980b) was used to determine the CO_2 content above Horizon 2 for the syn-release surveys. Gas quantification was completed for a circular area of 10 m diameter around the diffuser (illustrated on Fig. 4.9), as well as for the combined chimney area. For CO_2 estimates within the circular area, we use the value of the minimum seismic velocities calculated for each day (Table 4.3). For CO_2 estimates within the combined chimney area, we use seismic velocities mapped on Fig. 4.9a-f. The CO_2 content for Days 706-707 is not calculated, as seismic velocity anomalies for these days are thought to be artefacts (Fig. 4.9g), which is supported by seismic attenuation and reflection coefficient analysis indicating lack of CO_2 above Horizon 2 on these days (see Chapter 3).

The Anderson and Hampton compressible fluid model requires several key parameters including: the mineral bulk modulus K_m; frame bulk modulus K_f; water bulk modulus K_w; gas bulk modulus K_g; sediment shear modulus G; sediment fractional porosity n; sediment bulk density p_s, and the ratio of specific heats γ. Most of these parameters are taken from Anderson and Hampton (1980b) and Mavko et al. (2009), reporting results from laboratory experiments for different sediment types (Table 4.4). Grain-size analysis on Core 6 showed that sediments above Horizon 1 are coarse sandy sediments, whereas mostly fine sands are found between Horizon 1-Horizon 2 interval (Fig. 4.2). To constrain a range of CO_2 content above Horizon 2, we performed our

calculations considering (1) only coarse sand and, (2) only fine sand above Horizon 2 (Table 4.4). This allows us to constrain the upper limit (using coarse sand), as well as the lower limit (using fine sand) of CO_2 content above Horizon 2 from Day 0 to Day 34.

Sediment type: Coarse sand	Values
K_m, mineral bulk modulus	37 GPa[a]
K_f, frame bulk modulus	1.9 GPa[b]
K_w, water bulk modulus	2.3 GPa[b]
P_0, ambient hydrostatic pressure	299 KPa
γ, ratio of specific heats	1.293[a]
n, fractional porosity	0.35[b]
ρ_s, sediment bulk density	2150 kg/m^3 [b]
G, shear modulus	0.23 GPa[b]
Sediment type: Fine sand	**Values**
K_m, mineral bulk modulus	37 GPa[a]
K_f, frame bulk modulus	0.7 GPa[b]
K_w, water bulk modulus	2.3 GPa[b]
P_0, ambient hydrostatic pressure	299 KPa
γ, ratio of specific heats	1.293[a]
n, fractional porosity	0.45[b]
ρ_s, sediment bulk density	1960 kg/m^3 [b]
G, shear modulus	0.45 GPa[b]

[a]Mavko et al. (2009)
[b]Anderson and Hampton (1980b)

Table 4.4 *Values of parameters used in Anderson Hampton compressible fluid model to calculate CO_2 content above Horizon 2. Ambient hydrostatic pressure is the sum of atmospheric pressure, 12 m water column pressure and 4 m overburden pressure.*

CO_2 content estimates above Horizon 2 (n_g, gas volume/total sediment volume, see Section 4.2.2), within the circular area, are given in Table 4.5. Considering only coarse sandy sediments above Horizon 2, CO_2 content varies between 0.005-0.025% on the syn-release data, with the maximum CO_2 content observed at Day 12 (Table 4.5). Considering only fine sandy sediments above Horizon 2, CO_2 content varies between

0.003-0.015% on the syn-release data, with the maximum CO_2 content observed at Day 12 (Table 4.5). These CO_2 content values are the upper and lower limits of the true gas content above Horizon 2, as the grain size of sediments above Horizon 2 varies from coarse sands to fine sands.

Days	Coarse sand	Fine sand
	CO_2 content (%)	CO_2 content (%)
Day 0	0.006	0.003
Day 1	0.007	0.004
Day 2	0.008	0.005
Day 12	0.025	0.015
Day 13	0.011	0.007
Day 34	0.005	0.003

Table 4.5 *Variation of CO_2 content above Horizon 2 within a circular area around the diffuser. Seismic velocities used in the CO_2 content estimates are those from Table 4.3 (minimum seismic velocities).*

The CO_2 content within the combined chimney area above Horizon 2 is mapped for syn-release surveys (Fig. 4.10). The CO_2 content is calculated assuming only coarse sand above Horizon 2, thus Fig. 4.10 illustrates the upper limit of CO_2 saturation above Horizon 2. The largest CO_2 content is observed in a concentrated area at Day 12, with gas saturation being c. 0.025% of the total sediment volume, immediately to the NE of the diffuser (Fig. 4.10d). This largest CO_2 content corresponds to the area where seismic velocity of V_{p2}=1246 m/s was mapped on Day 12, within the circular area (Fig. 4.10d; Table 4.3).

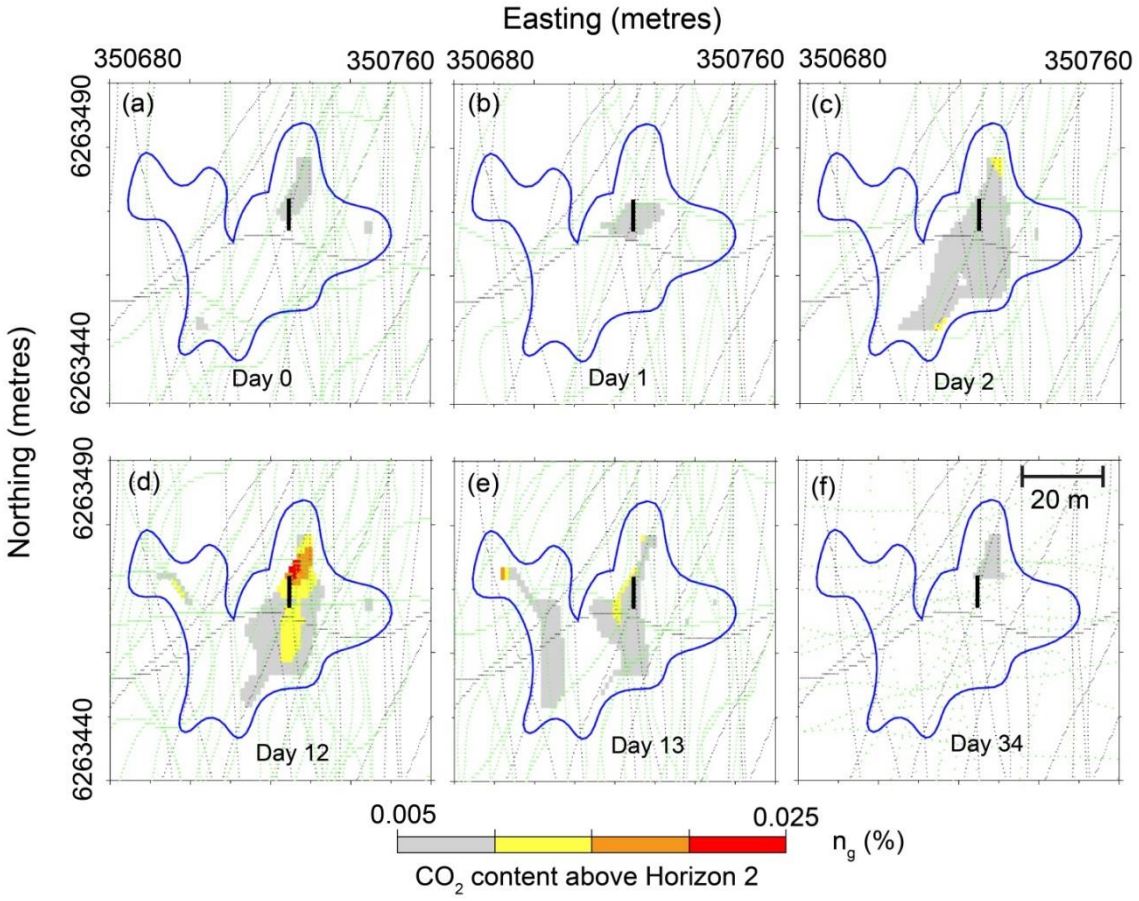

Figure 4.10 *CO_2 content above Horizon 2 within the combined chimney area. The diffuser is indicated by the black line and the blue polygon corresponds to the combined chimney area. Black dotted lines indicate pre-release seismic reflection survey lines, and green dotted lines are the seismic lines of the day, for which, CO_2 content is calculated.*

The CO_2 gas content maps presented on Fig. 4.10 are used to calculate the CO_2 volume (V_{gas}) *in situ* above Horizon 2, within the combined chimney area (Fig. 4.11) (Eq. 11):

$$V_{gas} = xyz\, n_g \qquad (11)$$

where V_{gas} is the CO_2 volume *in situ* for each grid cell, x is the width of the cell, y is the length of the cell, z is the depth value at each cell (using thickness values of seabed-Horizon 2 interval from Fig. 4.7), and n_g is the CO_2 content (gas volume/sediment volume, see Eq. 8).

Fig. 4.11 illustrates V_{gas} for the syn-release datasets at each grid cell (in dm^3, $1dm^3=10^{-3}$ m^3). On Days 0 and 1, V_{gas} is between 0.1-0.3 dm^3 above Horizon 2 (Fig. 4.11a and 4.11b). At Day 2, the largest CO_2 volume is found around the diffuser, c. 0.3-0.6 dm^3 of CO_2 (Fig. 4.11c). The maximum CO_2 volume throughout the release period is observed at Day 12 around the diffuser, c. 0.9-1.2 dm^3 of CO_2 (Fig. 4.11d). The concentrated area with the largest V_{gas} at Day 12 (Fig. 4.11d) correlates with the area where the largest seismic velocity anomaly was mapped at Day 12 (V_{p2}=1246 m/s) (Fig. 4.9d). From Day 13 onwards, CO_2 volume above Horizon 2 shows a decrease compared to Day 12 (Fig. 4.11e and 4.11f).

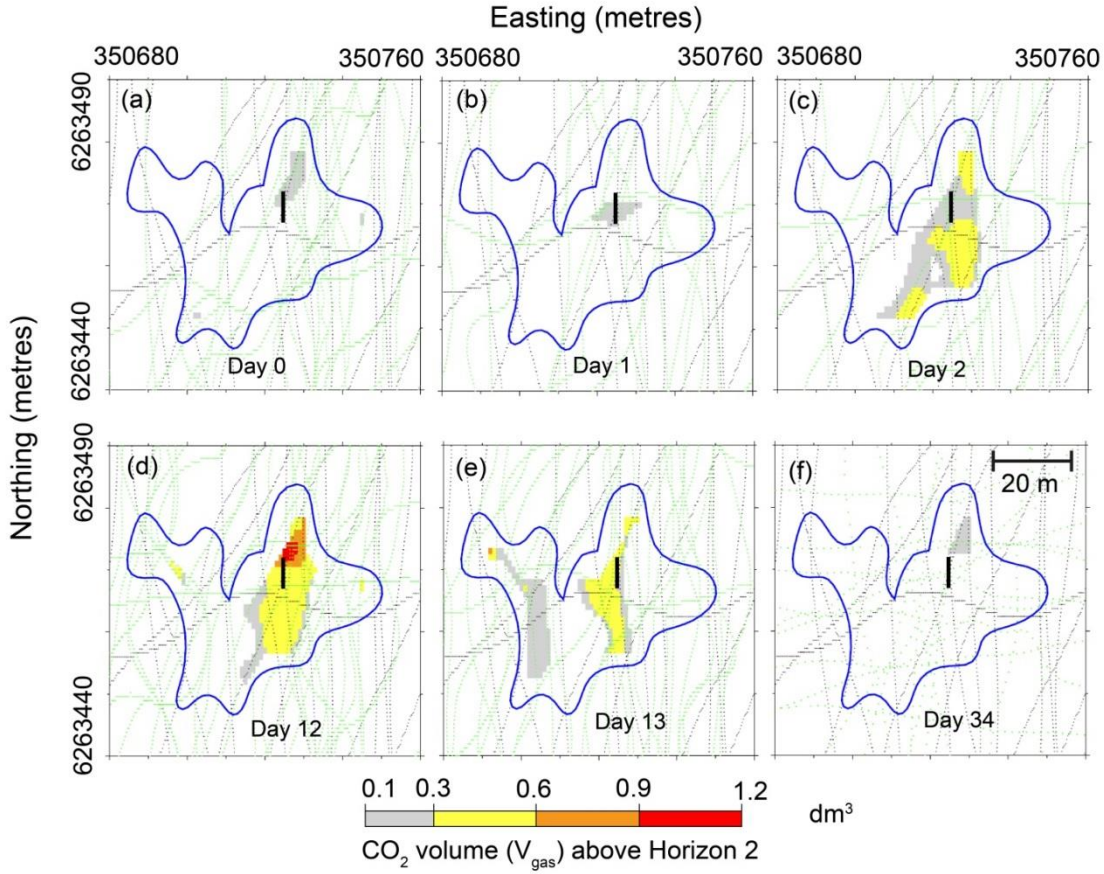

Figure 4.11 *CO_2 volume (V_{gas}) above Horizon 2 within the combined chimney area.* ***(a)*** *Day 0.* ***(b)*** *Day 1.* ***(c)*** *Day 2.* ***(d)*** *Day 12.* ***(e)*** *Day 13.* ***(f)*** *Day 34. The diffuser is indicated by the black line and the blue polygon corresponds to the combined chimney area. Black dotted lines indicate pre-release seismic reflection survey lines, and green dotted lines are the seismic lines of the day, for which, V_{gas} is calculated.*

The total CO_2 volume within the combined chimney area, above Horizon 2, is calculated by summing CO_2 volume at each grid cell (Fig. 4.11), and this is summarised in Table 4.6.

Days	V_{gas} (dm^3)
Day 0	8.5
Day 1	9
Day 2	91
Day 12	110
Day 13	71
Day 34	5

Table 4.6 *Total CO_2 volume within the combined chimney area above Horizon 2. The largest CO_2 volume is found at Day 12, c. 110 dm^3 CO_2 above Horizon 2, assuming only coarse sand above Horizon 2.*

It should be noted that CO_2 is subject to compression under ambient pressure. Therefore, the combined gas law (Bettelheim et al., 2015) is used to correct for compression, i.e., calculating total CO_2 volume at standard temperature and pressure (STP) conditions (Eq. 12):

$$\frac{P_s V_s}{T_s} = \frac{P_1 V_{gas}}{T_1} \qquad (12)$$

where P_s and T_s are the standard temperature and pressure (0°C and 1 Bar), P_1 and T_1 are the pressure and temperature conditions at the area where CO_2 volume is estimated (Eq. 11; Table 4.6) (P_1=2.96 atm considering atmospheric, hydrostatic (12 m water column) and lithostatic pressure (4 m sediment depth); T_1=11 °C (taken from Maeda et al. (2015), considering same temperature at the seabed and at 4 m sediment depth), V_{gas} is the total CO_2 volume above Horizon 2 calculated in this study (Eq. 11; Table 4.6), and V_s is the volume of CO_2 at standard temperature and pressure conditions. V_s values calculated for each survey day are summarized on Table 4.7 and plotted together with the cumulative injected CO_2 during the QICS experiment (Fig. 4.12).

Days	V_{gas} at STP (dm^3)
Day 0	25
Day 1	26
Day 2	264
Day 12	320
Day 13	205
Day 34	15

Table 4.7 *Total CO_2 volume within the combined chimney area above Horizon 2, corrected for compression. The largest CO_2 volume is found at Day 12, c. 320 dm^3 CO_2 above Horizon 2, assuming only coarse sand above Horizon 2.*

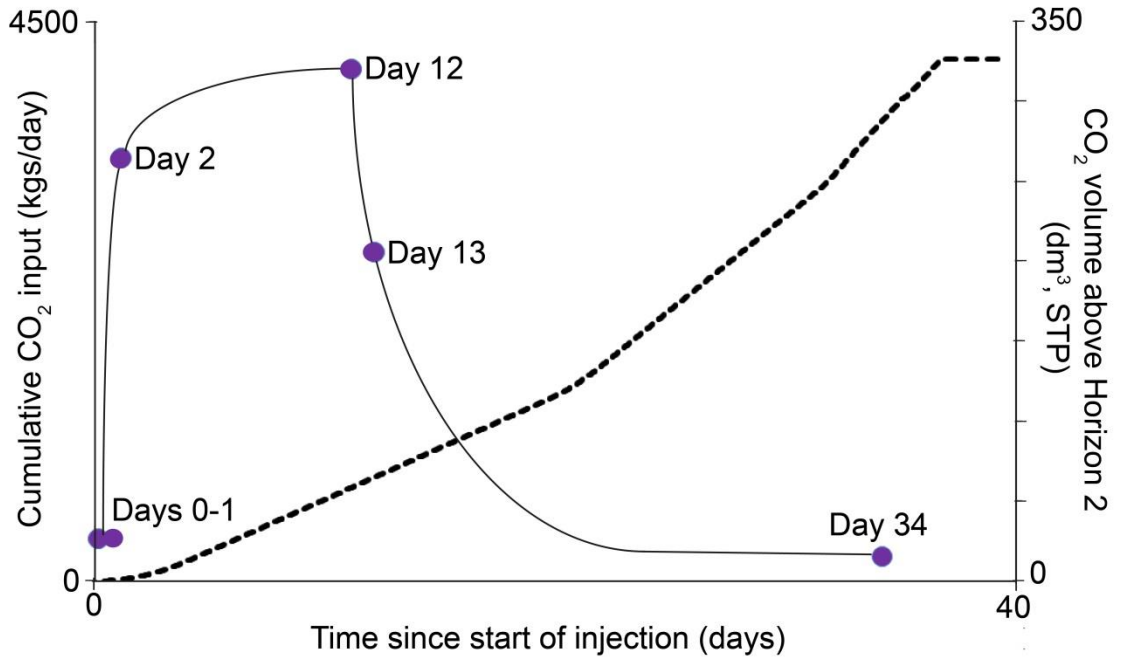

Figure 4.12 *Variation in CO_2 volume above Horizon 2 during injection. CO_2 volume corrected for compression is plotted together with the cumulative CO_2 input in Ardmucknish Bay. From Day 0 to Day 12, CO_2 volume increases up to 320 dm^3 above Horizon 2. From Day 13 onwards, the volume of gas above Horizon 2 decreases.*

These results will be discussed in discussion. In the next section (Section 4.3.3), we present our results from the acoustic impedance inversion of the seismic reflection data acquired pre- and syn-release, to assess impedance variation along Horizon 2 during the QICS experiment.

4.3.3 Acoustic impedance inversion

By using the methodology described in Section 4.2.3, we performed the acoustic impedance inversion of a pre-release seismic reflection (boomer) profile, as well as a syn-release seismic reflection (Chirp) profile (acquired at Day 12). Figure 4.13 illustrates the evolution of an acoustic impedance inversion for one Chirp trace (location indicated on Fig. 4.14e), up to 300 generations (i=2 to i=300). In the first generations, the inversion algorithm generates random impedance models (Fig. 4.13). These models evolve towards a final impedance model of the subsurface which has smaller residuals between the synthetic and real seismic trace amplitudes, with increasing number of generations (Fig. 4.13). At i=300 generations, there is an overall good agreement between reflection amplitudes and reflector polarity between synthetic and real seismic traces, although some discrepancies are observed, especially for Horizon 1 trace amplitudes. The residual error after 300 generations is c. 8% between the real and synthetic seismic traces (Fig. 4.13). Further, at i=300 generations, the impedance model of the subsurface clearly demonstrates an abrupt decrease in acoustic impedance at Horizon 2, from c. 4000 m/s g/cm^3 immediately above Horizon 2 to c. 1000 m/s g/cm^3 at Horizon 2 (Fig. 4.13).

Figure 4.14 illustrates results from the acoustic impedance inversion of whole seismic profiles from the pre-release boomer and syn-release Chirp seismic reflection datasets. The inversion was run for 250 seismic traces for boomer and 350 seismic traces for Chirp data (see Section 4.2.3.1 for inversion parameters). The main results from Fig. 4.14 are:

- For both pre- and syn-release seismic reflection datasets, there is a good agreement between synthetic and real seismic sections, including seismic reflectors amplitude, polarity and geometry (Fig. 4.14a-b and 4.14d-e). The mean residual error between real and synthetic seismic traces is 11% for Chirp, and 7% for boomer data.
- The absolute acoustic impedance section of the syn-release seismic reflection data (Day 12) clearly demonstrates the decrease in acoustic impedance along Horizon 2, compared to the impedance section of pre-release seismic reflection data (Fig. 4.14c and 4.14f). The value of the acoustic impedance at Horizon 2, just above the seismic chimney, decreases to c. 1000-2000 m/s g/cm^3 at Day 12,

compared to its pre-release value of c. 2000-6000 m/s g/cm^3 (Fig. 4.14c and 4.14f).

It is noteworthy that the inverted pre- and syn-release seismic reflection datasets are laterally separated by c. 25 m (Fig. 4.14), emphasizing that when comparing acoustic impedance values on these two datasets, spatial variation of acoustic impedance should also be considered (Fig. 4.14c and 4.14f).

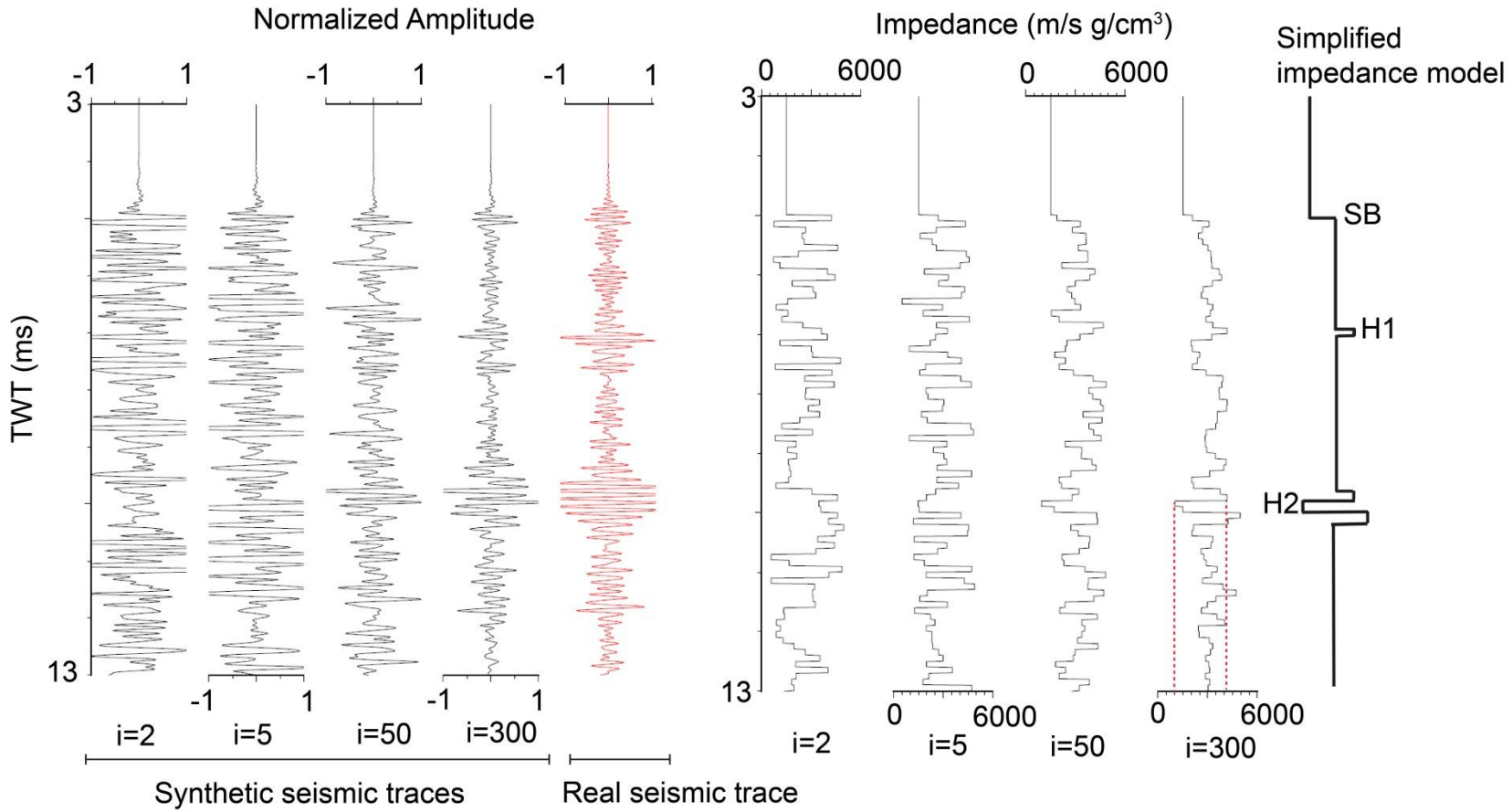

Figure 4.13 *Evolution of acoustic impedance inversion of a single seismic (Chirp) reflection trace acquired at Day 12. At i=300 generations, the acoustic impedance of Horizon 2 decreases from 4000 m/s g/cm^3 to c. 1000 m/s g/cm^3(red dotted lines). A simplified impedance model is also produced (SB, H1 and H2 corresponds to the seabed, Horizon 1 and Horizon 2 stratigraphic boundaries, respectively). Acoustic impedance values below Horizon 2 are questionable, due to lack of reflector continuity within the seismic chimney.*

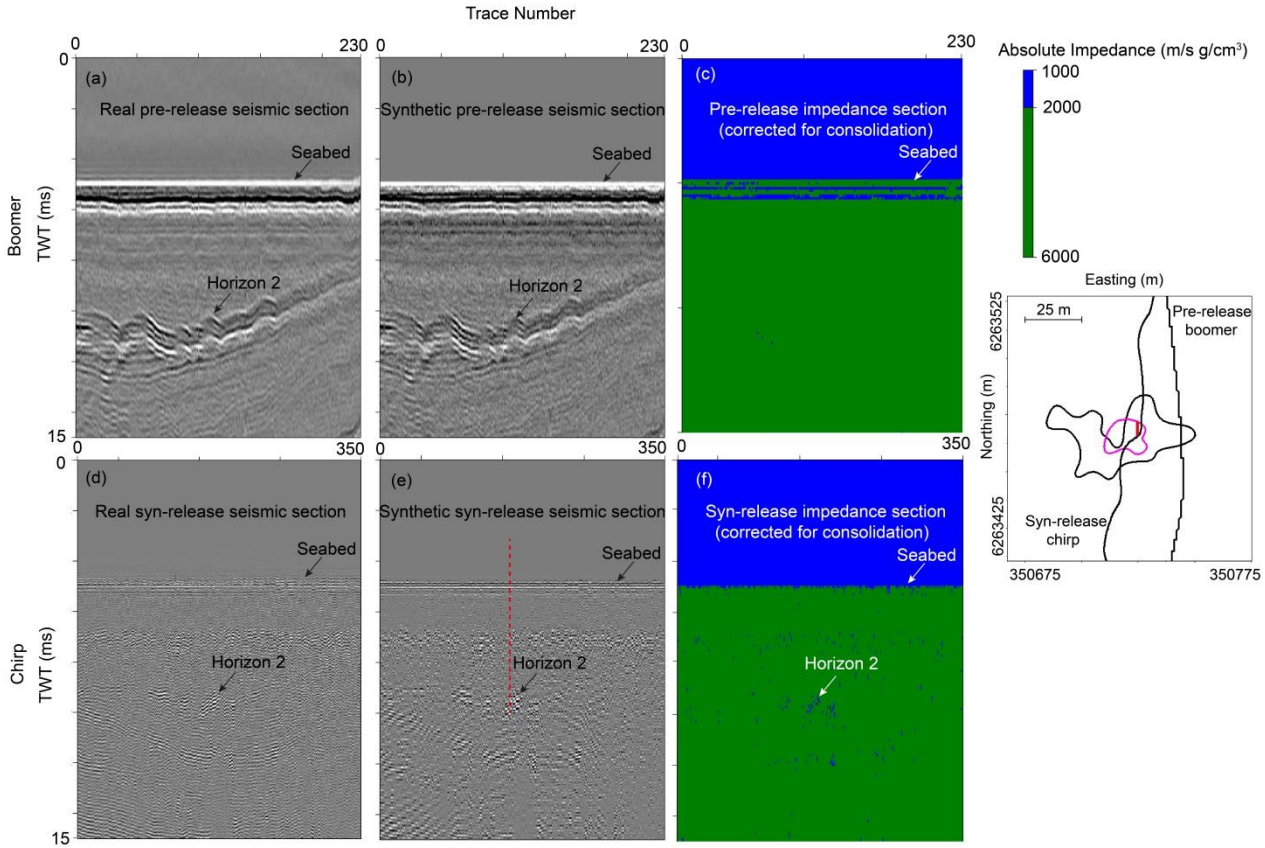

Figure 4.14 *Acoustic impedance inversion of the pre-release boomer and syn-release Chirp seismic reflection datasets.* ***(a)*** *Real pre-release seismic section.* ***(b)*** *Synthetic pre-release seismic section.* ***(c)*** *Absolute impedance section of the pre-release seismic reflection data.* ***(d)*** *Real syn-release seismic section.* ***(e)*** *Synthetic syn-release seismic section.* ***(f)*** *Absolute impedance section of the syn-release seismic reflection data. Inset shows the location of pre-release and syn-release seismic reflection profiles, as well as the diffuser (red line) and the spatial extent of seismic chimneys. Location of the single Chirp trace inverted on Fig. 4.13 is indicated by dashed red line on (**e**).*

4.4 Discussion

4.4.1 Discussion of results

4.4.1.1 Isopach maps, P-wave velocity and CO_2 volume *in situ* above Horizon 2

The apparent increase in thickness of the seabed-Horizon 2 interval, between Day minus 2 and Day 13 (Figs. 4.7b-f and 4.8a-e) is probably caused by CO_2 fluxing above Horizon 2, during the QICS experiment. This observation is consistent with previous findings, as large seabed reflection coefficients and increased seismic attenuation were calculated within the combined chimney area up to Day 13, indicating the presence of CO_2 above Horizon 2 on these days (see Chapter 2, Figs. 2.10 and 2.13). Although the cumulative CO_2 input is larger at Day 34 (Fig. 4.12), it has been previously shown that free gas was leaking at the seabed at this time (15% of the injected CO_2, Blackford et al. (2014)), hence limiting CO_2 accumulation above Horizon 2 within the overburden (Figs. 4.7g and 4.8f). Analysis of seabed and Horizon 2 reflection coefficients, as well as seismic attenuation from post-release seismic reflection data, indicated that the gaseous CO_2 was largely trapped immediately beneath Horizon 2 on Days 706-707 (see Chapter 3). Thickness analysis of the post-release seismic reflection data also supports these findings, as no significant thickness anomalies were detected for the seabed-Horizon 2 interval at these days (Figs. 4.7h and 4.8g).

Seismic P-wave velocity anomalies mapped within the combined chimney area (Fig. 4.9), as well as within a circular area around the diffuser (Table 4.3) clearly demonstrate the impact of CO_2 injection on sediment acoustic properties, during the QICS experiment, where gaseous CO_2 has lowered the seismic velocity above Horizon 2. It is interesting to note that seismic velocities are spatially variable for any given day (Fig. 4.9). For instance, at Day 12, the lowest seismic velocity occurs immediately to the NE of the diffuser, in a concentrated area, (V_{p2}=1246 m/s), whereas relatively larger seismic velocities are observed in a larger area (Fig. 4.9d). This possibly suggests that the CO_2 fluxing is not spatially uniform above Horizon 2, as otherwise we should have detected the same P-wave velocity anomaly within the combined chimney area, in every sample location, between a given day and Day minus 2.

Using seismic P-wave velocities, combined with the Anderson and Hampton compressible fluid model, we calculated CO_2 content and CO_2 volume *in situ* above Horizon 2, from Day 0 to Day 34 (Figs. 4.10-4.12; Tables 4.5-4.7). The increase in CO_2 volume *in situ* above Horizon 2, up to Day 12, is consistent with increasing cumulative CO_2 input within the overburden in Ardmucknish Bay, and suggests a relatively small CO_2 leakage at the seabed at this time (Fig. 4.15). The cumulative CO_2 input at Day 13 is larger compared to previous days, yet the amount of CO_2 above Horizon 2 decreases (Fig. 4.15). This decrease possibly suggests an increased seabed leakage at Day 13, compared to previous days (Fig. 4.15). As the CO_2 volume *in situ* above Horizon 2 is even smaller at Day 34, in contrast to increasing cumulative CO_2 input at this time, this can be interpreted as a further increase in CO_2 leakage rate at Day 34, compared to previous days (Fig. 4.15). Bergès et al. (2015) quantified the CO_2 leakage rate at the seabed at Day 34 by passive hydroacoustics methods, c. 20 kgs/day (Fig. 4.15). Following the cessation of injection at Day 37, the CO_2 leakage at the seabed decreases, and is suggested to reach zero at some time between Day 37 and Day 706, as no CO_2 leakage were detected within the water column from post-release seismic reflection data (see Chapter 3). Fig. 4.15 summarizes the suggested relationship between the CO_2 volume *in situ* above Horizon 2, CO_2 leakage rate at the seabed, as well as the cumulative CO_2 input in Ardmuknish Bay.

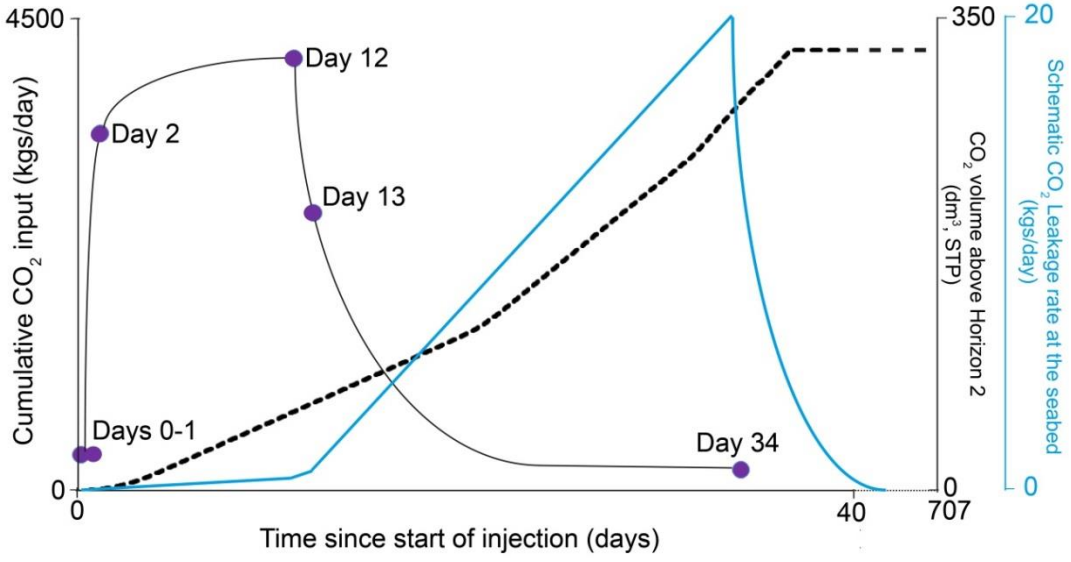

Figure 4.15 *The relationship between the CO_2 volume in situ above Horizon 2, seabed leakage and cumulative CO_2 input. The graph showing seabed leakage should be interpreted as a cartoon.*

4.4.1.2 Acoustic impedance inversion

We showed that the acoustic impedance along Horizon 2, just above seismic chimneys, decreased to c. 1000-2000 m/s g/cm^3 at Day 12, compared to its pre-release value of c. 4000 m/s g/cm^3 (Figs. 4.13 and 4.14). This is most likely caused by the injected CO_2 accumulating immediately below Horizon 2, and reducing the seismic P-wave velocity and sediment density, thus lowering acoustic impedance (Figs. 4.13 and 4.14). The results from acoustic impedance inversion are in agreement with previous observations, where Horizon 2 reflection coefficients were also shown to dramatically decrease on the syn-release seismic reflection datasets from 0.04 to -0.12 (see Chapter 2, Fig. 2.9 and Table 2.4).

In future work, the changes in acoustic impedance will be related to *in situ* CO_2 volume, immediately beneath Horizon 2. There exists several empirical relationships, which allow the calculation of the seismic P-wave velocity from acoustic impedance (Shumway, 1960; Hamilton, 1972; Bachman, 1985; Hamilton, 1987; Richardson and Briggs, 1993). However, these relationships will not correctly estimate seismic velocity from acoustic impedance for Ardmucknish Bay sediments, as they are developed for gas-free sediments. Therefore, there is a need for laboratory experiments to better constrain an empirical relationship between acoustic impedance and seismic velocity for the Ardmucknish Bay unconsolidated gassy sediments. This seismic velocity can then be used to calculate CO_2 content/volume immediately beneath Horizon 2, using an appropriate rock physics model.

4.4.2 Source of errors in gas quantification

Thickness variations of the seabed-Horizon 2 interval are used to calculate seismic P-wave velocities, *in situ* CO_2 content /volume estimates (Figs. 4.9-4.12; Tables 4.3-4.7). It is noteworthy that errors in thickness analysis will affect seismic velocity estimates above Horizon 2, which in turn will have a major impact on CO_2 content/volume calculations. For a picking error of 10 samples, both for the seabed and Horizon 2, on seismic reflection (Chirp) data (sampling rate=0.02 ms, corresponding to 0.2 ms picking error), seismic P-wave velocities decrease by c. 100 m/s within the circular area, compared to the estimates presented in Section 4.3.1 (Table 4.8). It is clear that for a smaller seismic velocity, the gas content and volume estimates will be

higher, compared to the values presented in Section 4.3.2, i.e., as of more than double of the current estimates (Table 4.8). These calculations show that the Anderson and Hampton compressible fluid model is very sensitive to the value of seismic velocity (Eq. 2), and possible errors in seismic velocity estimates, due to errors in thickness analysis, will result in underestimating *in situ* gas content/volume above Horizon 2. Further, it is interesting to note that, even if the CO_2 volume estimates are recalculated, taking into account errors in thickness analysis, these new volume estimates represent a very minor fraction of the total injected volume in Ardmucknish Bay, possibly implying that most of the gas was trapped below Horizon 2, or dissolved, during the QICS experiment.

Days	Minimum velocity (actual)	Minimum velocity (error of 0.2 ms)	V_{gas} at STP (best estimates)	V_{gas} at STP (error of 0.2 ms)
Day 0	1507 m/s	1387 m/s	25 dm^3	72.5 dm^3
Day 1	1483 m/s	1369 m/s	26 dm^3	75 dm^3
Day 2	1457 m/s	1353 m/s	264 dm^3	590 dm^3
Day 12	1246 m/s	1156 m/s	320 dm^3	765 dm^3
Day 13	1389 m/s	1283 m/s	205 dm^3	476 dm^3

Table 4.8 *Effect of thickness estimate errors on seismic velocity and CO_2 volume. For an error of 10 samples in picking, V_{gas} estimates significantly increase above Horizon 2.*

Another potential source of error is the choice of rock physics model. The Anderson and Hampton compressible fluid model (Anderson and Hampton, 1980a, b) uses Gassmann fluid substitution equations (Gassmann, 1951) to calculate the composite bulk modulus of gassy sediments (Eqs. 4-6). Gassmann fluid substitution equations are based on several assumptions, including: (1) the porous material is isotropic and homogenous; (2) the pore space is well connected and in pressure equilibrium; (3) the medium is a closed system; and (4) there is no chemical interaction between the fluids and the rock frame (Gassmann, 1951). Many authors have discussed the strength and limitations of Gassmann's equations, emphasizing that these equations might have inherent errors, as several key assumptions are violated in case of natural geological systems, notably isotropy and well connected porosity assumptions (Mavko and Mukerji, 1995; Berryman, 1999; Wang, 2001; Smith et al., 2003; Han and Batzle, 2004; Adam et al., 2006). Further, Gassmann's equations are suggested to work best for

low frequencies (< 100 Hz), where seismic waves induced pore pressure is equilibrated throughout the pore space (Mavko and Mukerji, 1995; Adam et al., 2006). Some authors suggest that towards ultrasonic frequencies (c. 10^6 Hz), Gassmann's equations might not predict seismic velocities as accurately as predictions performed for much lower frequencies, c. 100 Hz (Mavko and Jizba, 1991; Adam et al., 2006). However, for seismic frequencies between 1-10 kHz, i.e., the bandwidth appropriate for Chirp and boomer data, experimental results show good correlation between measured seismic velocities and those calculated using Gassmann's equations for saturated sediments (Murphy, 1984; Cadoret et al., 1995).

Bubbles in sediments are capable of vibratory motion, with the highest resonance occurring at bubble resonance frequency. Previous work has shown that below the resonance frequency, the medium behaves as a single phase, compressible material, thus is associated with lower seismic velocities; whereas, above the bubble resonance frequency, the medium behaves as a biphasic material, producing seismic velocities similar to those of gas-free sediments (Anderson and Hampton, 1980b; Leighton, 1994; Fu et al., 1996; Wilkens and Richardson, 1998; Gardner, 2000; Leighton, 2007b). Thus, above bubble resonance frequency, the acoustic response of sediments is controlled by *in situ* fluid saturation, as well as bubble dynamics (Leighton, 1994). Best et al. (2004) modelled the acoustic response of Dibden Bay gas-bearing sediments, using the Anderson and Hampton geoacoustics model, where they observed a dramatic increase in seismic P-wave velocity, for insonifying frequencies near the bubble resonance frequency. In addition, they obtained seismic velocities similar to those of gas-free sediments, for insonifying frequencies above the bubble resonance frequency (Best et al., 2004). These observations indicate that, in the case of bubble resonance, we might have underestimated the seismic velocity decrease above Horizon 2, thus resulting in an underestimate of the *in situ* gas content/volume. The Anderson and Hampton geoacoustics model (Anderson and Hampton, 1980b) is applicable for marine sediments containing Type III bubbles, where bubble size is larger than the sediment pore space (Anderson et al., 1998a). Bubble resonance frequency for sediments in Ardmucknish Bay can be calculated by using the Minaert formula (Minnaert, 1933) (Eq. 13):

$$f_0 = \frac{1}{2\pi a}\sqrt{\frac{3\gamma P_0}{\rho_s}} \qquad (13)$$

where f_0 is the bubble resonance frequency (Hz), a is the bubble radius (m), γ is the ratio of specific heats for the gas, P_0 is the ambient pressure (Pa), and ρ_s is the sediment bulk density (kg/m^3).

If we assume only coarse sand (grain size between 0.5-1 mm) above Horizon 2, as well as bubble size double the mean grain size (Type III bubbles), the bubble resonance frequency at 4 m depth below the seafloor (at Horizon 2) is between 4-8 kHz using Eq. 13. Similarly, considering only fine sandy sediments above Horizon 2 (grain size between 125-250 μm), as well as bubble size double the mean grain size (Type III bubbles), we obtain bubble resonance frequency between 15-34 kHz at 4 m below the seabed. These calculations indicate that we possibly underestimated the upper limit of CO_2 content/volume above Horizon 2 due to bubble resonance within our seismic frequency range (1.5-13.0 kHz for Chirp; 0.5-4.0 kHz for boomer) (Fig. 4.12; Tables 4.5-4.7). However, for a sediment column made of fine sand above Horizon 2, our seismic frequency range (both Chirp and boomer) is below the bubble resonance frequency, thus the lower limit of CO_2 content/volume estimates above Horizon 2 remain correct (Table 4.5).

The Anderson and Hampton compressible fluid model assumes homogenous fluid saturation within the pore space, where gas saturation is the same at the pore scale at any location in the sediment (Anderson and Hampton, 1980a, b). However, several authors also investigated patchy gas saturation in marine sediments, where patches of gas are surrounded by dry or partially saturated regions (White, 1975; Dutta and Seriff, 1979; Murphy, 1984; Mavko and Mukerji, 1998; Toms-Stewart et al., 2009). Compared to uniform saturation, patchy saturation is associated with larger gas saturation estimates (Tinivella and Carcione, 2001; Qian et al., 2014; Tóth et al., 2014b). Therefore, by assuming uniform saturation, we underestimate the *in situ* CO_2 content/volume above Horizon 2 (Fig. 4.12; Tables 4.5-4.7). It is also important to note that the accuracy of the input parameters is crucial in determining reliable gas saturation with the Anderson and Hampton geoacoustics model. In this chapter, the values of these parameters are taken from experimental results (Table 4.4). However, our *in situ* CO_2

quantification estimates can be significantly improved by verifying the accuracy of these parameters, i.e., completing laboratory based measurements on the Ardmucknish Bay sediments.

Finally, the Anderson and Hampton compressible fluid model is not the only rock physics model to calculate *in situ* gas volume from seismic reflection data (see Introduction). In future, other rock physics models can be used to calculate the CO_2 volume above and below Horizon 2, and these results can be subsequently compared to gas content estimates completed with the Anderson and Hampton compressible fluid model. Further, quantification of dissolved gas within the overburden from geochemical data will certainly allow the investigation of the accuracy of gaseous CO_2 volume estimates from this work.

4.5 Conclusion

Free gas within sediment pore space changes the acoustic properties of sediments, and these changes can be used together with rock physics models to estimate *in situ* gas saturation. Here we showed that the controlled CO_2 injection in Ardmucknish Bay lowered the seismic P-wave velocity above Horizon 2 (maximum reduction observed at Day 12, of c. 330 m/s) (Table 4.3), and reduced the acoustic impedance along Horizon 2 (of c. 3000 m/s g/cm^3 at Day 12) (Figs. 4.13 and 4.14). Using the Anderson and Hampton compressible fluid model, we calculated the *in situ* CO_2 content/volume above Horizon 2, where gas volume systematically increased from Day 0 Day 12 above Horizon 2, c. up to 320 dm^3 of CO_2, with increasing cumulative CO_2 injected, and gradually decreased from Day 13 onwards, possibly due to increased leakage at the seabed into the overlying water column, compared to previous days (Fig. 4.15).

Source of errors in gas quantification estimates are discussed. Any errors in thickness analysis are shown to affect seismic P-wave velocity calculations, thus resulting in an underestimate of the *in situ* CO_2 content/volume above Horizon 2, within the combined chimney area (Table 4.8). However, even taking into account errors in thickness analysis, the recalculated CO_2 volume estimates correspond to a very minor fraction of the total injected volume, possibly implying that the majority of gas was trapped below Horizon 2, or dissolved. Further, due to bubble resonance above Horizon

2, the upper limit of CO_2 content is likely underestimated, whereas the lower limit remains correct, for our seismic frequency range (Table 4.5). Additionally, we might have inherent errors due to simplifying assumptions in the Anderson and Hampton compressible fluid model.

In future work, acoustic impedance inversion will be performed for seismic reflection data acquired up to Days 706-707, to better constrain the temporal variation of acoustic impedance along Horizon 2 syn-release and post-release. With laboratory measurements, we can produce an empirical relationship to relate acoustic impedance to seismic velocity for the Ardmucknish Bay unconsolidated sediments. Seismic velocities can then be used to calculate the *in situ* CO_2 content immediately beneath Horizon 2, using various rock physics models. Further, the accuracy of the gas saturation estimates above Horizon 2 can be investigated by using mass-balance calculations, if the amount of dissolved CO_2 is known from geochemical data. Finally, acquisition of 3D seismic reflection data can greatly enhance our gas quantification estimates in Ardmucknish Bay, allowing a significant improvement in spatial and temporal resolution.

Chapter 5

Near-surface fluid flow activity in the vicinity of Sleipner Carbon Capture and Storage site in the Central North Sea

Abstract

As part of the ECO_2 project, the James Cook cruise 077 (*JC077*) surveyed the Central North Sea in September 2012 to investigate the near-surface fluid flow activity in the vicinity of the Sleipner Carbon Capture and Storage (CCS) site, with particular attention to the Hugin Fracture, located at 25 km N of the carbon dioxide (CO_2) injection site.

A multidisciplinary dataset was acquired using various instruments and sensors mounted on Autosub 6000, including side-scan sonar, 2D high-resolution seismic reflection profiler, Eh, pH and pCO_2 sensors and a colour camera, as well as seabed video surveying with HYBIS, vibrocoring, CTD water sampling, and shipboard multibeam bathymetry surveying. Contrary to the observations from the CO_2 Plume Area, South of the Plume Area and Middle Area, a range of physical, geochemical and visual observations reveal active fluid flow at the Hugin Fracture Area, mainly located in the vicinity of the Hugin Fracture, and at the abandoned 16/4 well site. The shallow overburden around the Sleipner CCS site is shown to act as a preferential fluid migration pathway, both for biogenic and thermogenic fluids, suggesting a hydraulic connection to the underlying sediments at different depths. The nucleation and growth of the Hugin Fracture is proposed to be controlled by tectonic and non-tectonic processes, including the transtensional stress regime and the differential compaction above a buried tunnel valley system. The findings from this study call into question the general shallow seal integrity above the Utsira Formation, and emphasize the crucial importance of near-surface site surveying around ongoing and planned CCS sites.

5.1 Introduction

The Sleipner CCS is the longest operated offshore carbon sequestration project in Europe, where anthropogenic CO_2 has been injected into the Utsira Sand saline aquifer since 1996. Previous research conducted within the ECO_2 project, led by GEOMAR and University of Bergen, discovered evidence of active fluid flow in the vicinity of Sleipner CCS site in the Central North Sea. Seismic chimneys and bright spots within the overburden were detected on 3D seismic reflection data by GEOMAR, in the Southern Viking Graben (Karstens and Berndt, 2015). A 3 km long seabed fracture (named the Hugin Fracture), located 25 km N of the Sleipner CCS site, was discovered by the University of Bergen in 2011, with the aid of a synthetic aperture sonar (HISAS) mounted on an autonomous underwater vehicle (AUV Hugin), deployed from *R/V G.O Sars* (Landschulze and Pedersen, 2013a; Landschulze and Pedersen, 2013b; Pedersen et al., 2013; Landschulze et al., 2014a; Landschulze et al., 2014b). This newly discovered fracture was found to be associated with significant fluid flow activity from the analysis of geophysical and geochemical data, as well as seabed photography (Landschulze and Pedersen, 2013a; Landschulze and Pedersen, 2013b; Pedersen et al., 2013; Landschulze et al., 2014a; Landschulze et al., 2014b). The pore water isotopic composition of the rising fluids mainly indicates a biogenic origin; however, small admixtures of thermogenic gas has also been detected, interpreted as fluid leakage from deeper gas reservoirs at the Hugin Fracture (Haeckel et al., 2013).

These findings determined the research objectives of the *JC077* cruise, where the near-surface fluid flow activity in the vicinity of Sleipner CCS site was investigated between 2^{nd}-28^{th} of September 2012, on board *R/V James Cook* (Fig. 5.1). During the *JC077* cruise, led by National Oceanography Centre Southampton (NOCS), four survey areas were thoroughly investigated as part of the ECO_2 project, including the Hugin Fracture Area, Middle Area, CO_2 Plume Area and South of the Plume Area (Fig. 5.1). A multidisciplinary approach was undertaken, using various geophysical instruments, geochemical and optical sensors mounted on Autosub 6000 (an autonomous underwater vehicle developed by NOCS), as well as seabed video photography with HyBIS (a remotely operated vehicle developed by NOCS), vibrocoring, CTD water sampling, and shipboard multibeam bathymetry surveys. This chapter provides an overview of the Sleipner CCS operations and a summary of the fluid flow activity within the

overburden above the Utsira Sand, followed by a description of data acquisition during the *JC077* cruise, data processing, main results, discussion and conclusions.

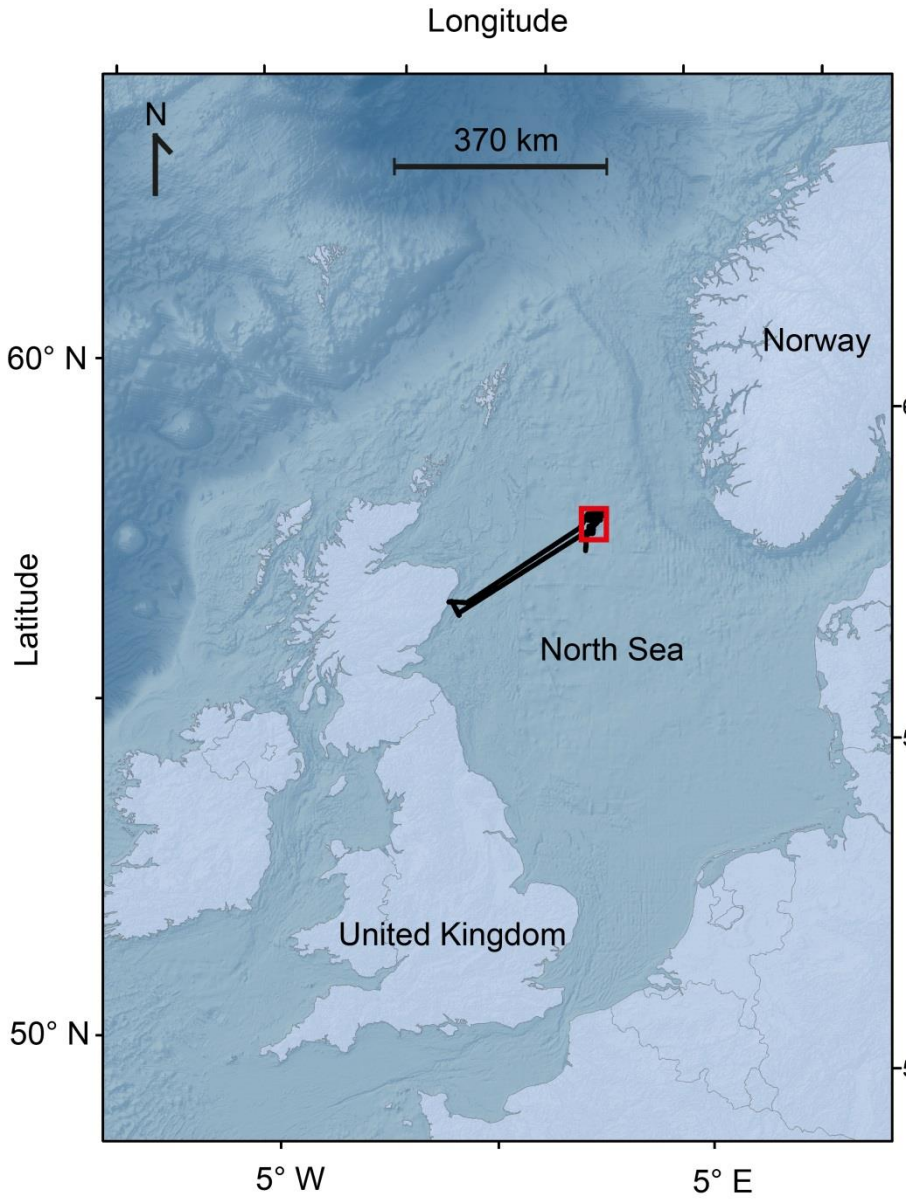

Figure 5.1 *Map of the JC077 cruise track lines. The JC077 cruise took place in the Central North Sea between 2nd-28th of September 2012, on board R/V James Cook. The red rectangle corresponds to the overall spatial extent of the areas surveyed during the JC077 cruise, including the Hugin Fracture Area, Middle Area, CO_2 Plume Area, and South of the Plume Area. Please see Figs. 5.9 and 5.10 for enlarged views of the surveyed areas within the red rectangle. Track lines are indicated as solid black lines.*

5.2 Overview of Sleipner Carbon Capture and Storage

The world's first industrial-scale offshore carbon sequestration project, Sleipner CCS, operated by Statoil and its partners, involves the injection of CO_2 at around 800-1000 m depth, into the Utsira Sand, a regional saline aquifer located in the Norwegian part of the North Sea (Fig. 5.2). CO_2 which is separated from the natural gas produced at the Sleipner West Field (Norwegian block 15/9), has been reinjected at the Sleipner East Field since 1996, at a rate of 1Mt/year, with more than 14 Mt of CO_2 injected up to March 2015 (Baklid et al., 1996; Cavanagh and Haszeldine, 2014) (Fig. 5.2). The injection is scheduled to continue until 2020.

The Sleipner West Field is the second largest gas field in the North Sea (Korbøl and Kaddour, 1995). The CO_2 content varies between 4-9.5%. In order to meet the Troll Gas Sales Agreement, this high CO_2 content needs to be reduced to 2.5% or less (Holloway, 2005). For that reason, the natural gas, produced via 18 production wells drilled from a wellhead platform (Sleipner B), is transferred to a process and treatment platform (Sleipner T), where the gas is first separated to condensate and water (Fig. 5.2). The excess CO_2 is then removed by amine absorption processes from the condensate. After the regeneration process separating the amine from CO_2, CO_2 is then transported to Sleipner East Platform A, and is injected underground into the Utsira Sandstone Reservoir (Fig. 5.2). As emitting the captured CO_2 in Sleipner T platform directly into the atmosphere would result in an increase of 3% of the total Norwegian emissions, as well as imposing taxes on Statoil introduced by Norwegian authorities (Kongsjorden et al., 1998), various alternatives were investigated, including usage of CO_2 in enhanced oil recovery, injection into the Sleipner East Gas Reservoir, as well as CO_2 storage within the Utsira Formation. The latter was Statoil's ultimate decision, leading to the first initiative in offshore geological carbon sequestration.

The CO_2 injection in Sleipner occurs by means of a single deviated well, sub-horizontal at the injection point, at 1012 m below the seabed (Fig. 5.2). This configuration is crucial to avoid contamination from the injected CO_2 (Gluyas and Mathias, 2013). Before injection, CO_2 is compressed to its dense supercritical state, allowing it to occupy less volume in the storage reservoir. At the top and the bottom of the Utsira Sand, the temperature varies between 29 °C and 36 °C, resulting in the injected CO_2 remaining in its supercritical phase (Chadwick et al., 2004a). At this

supercritical stage, the relatively high density difference between the formation fluids and the CO_2 leads to strong buoyancy forces, resulting in the upward migration of CO_2 within the overburden.

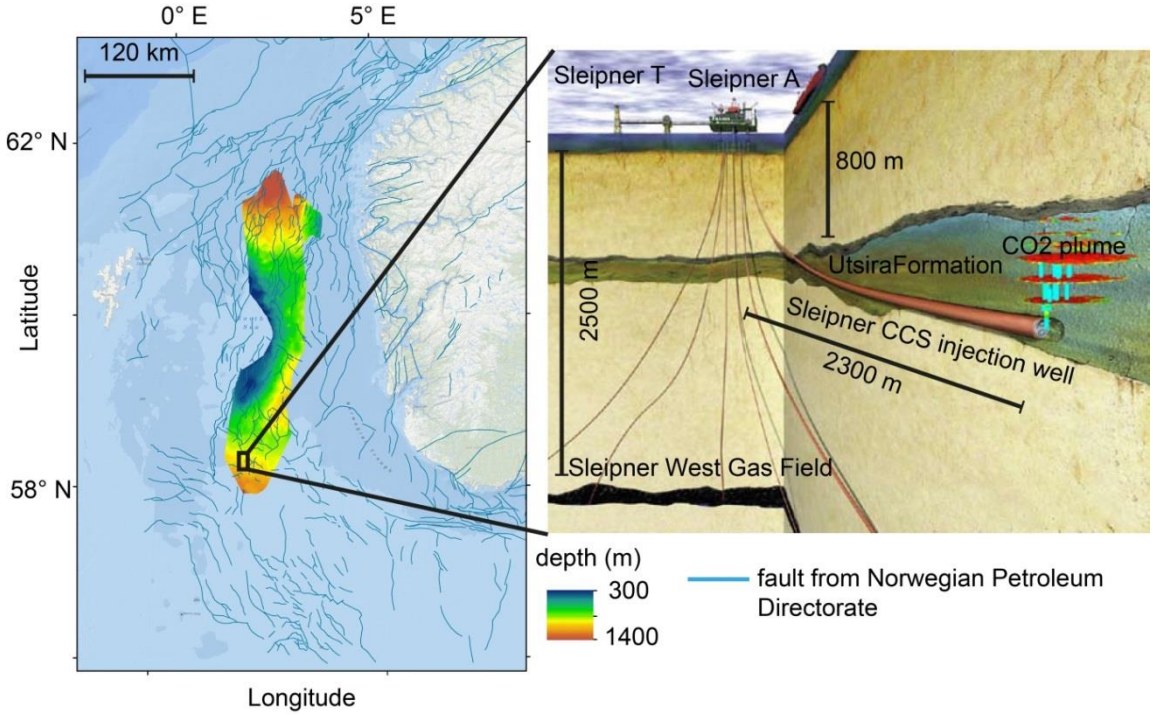

Figure 5.2 *Distribution of the Utsira Sand in the North Sea and block diagram summarizing geological carbon sequestration in Sleipner (modified from Statoil). Fault positions from Norwegian Petroleum Directorate are superimposed on the location map. The sub-seafloor depth of the Utsira Sand (colour scale) varies between 300-1400 m. CO_2 is injected via a 2300 m long deviated well into the Utsira saline aquifer at 1012 m depth.*

5.2.1 The Utsira Sand Storage Reservoir, its caprock and the underlying units

The Utsira Sand is located along the Viking Graben in the Norwegian sector of the North Sea (Fig. 5.3). The Viking Graben is a major tectonic structure resulting from the extensional tectonism dominating from Permian and throughout Mesozoic era (Gregersen et al., 1997). After the cessation of the rifting in the Early Cretaceous, the North Sea Basin experienced thermal subsidence, which was followed by the deposition of mainly mud-dominated, thick, Cenozoic post-rift sediments of the Shetland, Rogaland, Hordaland and Nordland lithostratigraphic groups (Isaksen and Tonstad,

1989; Glennie, 1990; Jackson and Stoddart, 2005). Over the same period, the Scandinavian and British land masses have undergone up to six phases of relative uplift from Paleocene to Miocene, resulting in onlap sequences identified in the seismic reflection data (Galloway et al., 1993; Head et al., 2004) (Fig. 5.4). Successive Pleistocene glaciations affected the North Sea, leading to episodic erosion and infill of the basin, with typical glaciomorphological observations including subglacial tunnel valleys and ploughmarks (Sejrup et al., 2000; Lonergan et al., 2006; Graham et al., 2011; Dowdeswell and Ottesen, 2013).

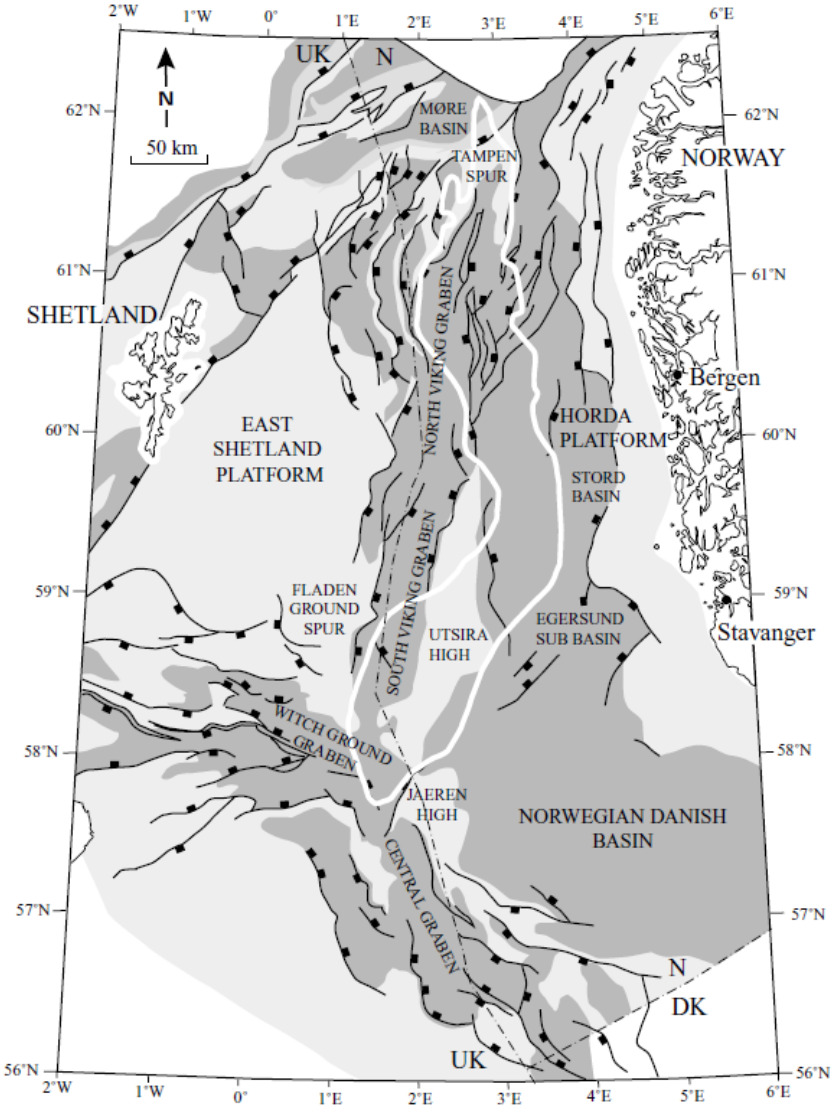

Figure 5.3 *The major geological domains in the Norwegian North Sea (Gregersen and Johannessen, 2001). The Utsira Sand (white polygon) lies within the Viking Graben.*

Regional mapping of the Utsira sand reveals that it has an elongated geometry, extending about more than 400 km from N to S, and 50-100 km from W to E (Fig. 5.2). Covering an area of about $2.6x10^4$ km^2, the Utsira Sand is formed by two distinct depositional basins with low-connecting hydraulic contact (Fig. 5.2). In the southern depocentre, the top of the Utsira sand lies between 600-1150 m sub-seafloor, with a maximum thickness of 300 m (Chadwick et al., 2000). Where CO_2 has been injected into the southern depocentre, the Utsira Sand forms a tabular basinally-restricted unit, with the depth beneath the seafloor varying between 800-1100 m, and with thickness of around 250 m (Figs. 5.2 and 5.4). Core data analysis shows that Utsira Sand sediments are mostly uncemented, fine to medium-grained sand, with occasional coarse grained beds (Holloway et al., 2000). The Utsira Sand has a characteristic geophysical well log signature with blocky log pattern, low gamma ray, low sonic velocity and resistivity values (Gregersen and Johannessen, 2007). Within the storage reservoir, several thin shale layers, up to 1-2 m thick, are also identified from wireline log data with high gamma ray values, predicted to provide horizontal permeability barriers for the rising CO_2 (Chadwick et al., 2004b). In addition to thin intra-reservoir shale layers, a 5-6.5 m thick shale unit (Correlatable Mudrock or Shale Drape) is also identified from 3D seismic and wireline log data, separating the main part of the Utsira Sand from the overlying, eastward thickening sand wedge (Zweigel et al., 2000; Chadwick et al., 2004b; Furre and Eiken, 2014) (Fig. 5.4). This thick shale unit has been interpreted to be geologically similar to the main seal, the overlying Nordland shales (Gregersen and Johannessen, 2001; Zweigel et al., 2004).

The top of the Utsira Sand is relatively smooth, dipping to the S, with localized domes and valleys (Fig. 5.4). In contrast to its top, the base of the Utsira Sand is more complex, characterized by numerous mound diapirs, typically 1-2 km in diameter and around 100 m high, resulting from sediment injection and/or mobilization within the underlying Hordaland shales (Chadwick et al., 2008) (Fig. 5.4). The presence of these mud diapirs at the base of Utsira Sand is interpreted to cause local depressions within the reservoir, which are proposed to possibly act as traps or channels for the injected CO_2 (Arts et al., 2000; Holloway et al., 2000). No faults have been reported from within the Utsira Sand, except for a few polygonal reverse faults penetrating the very lowermost part of reservoir, initiating from the Hordaland shales beneath (Zweigel et al., 2004).

Porosity estimates from the Utsira Sand vary between 27% to 31%, and locally up to 42%, consistent with the regional porosity estimates from well logs, ranging from 35% to 40% (Torp and Gale, 2004). In addition to its high porosity, Utsira Sand has high permeability, i.e., 1-3 Darcy, resulting overall in high CO_2 storage capacity, in the order of 0.3 Gt, considering only structural trapping at the top of the reservoir (Chadwick et al., 2008). This estimate is relatively small, compared to other studies where the storage capacity is predicted to range between 20-60 Gt (Lindeberg et al., 2009). The large range in the storage capacity estimates is due to the different limiting factors considered, including pressure build-up within the reservoir and CO_2 leakage within the overburden (Andersen et al., 2014). The total pore volume of the Utsira Sand is estimated to be around 6 x 10^{11} m^3, illustrating the large storage capacity of the saline aquifer (Verdon et al., 2013).

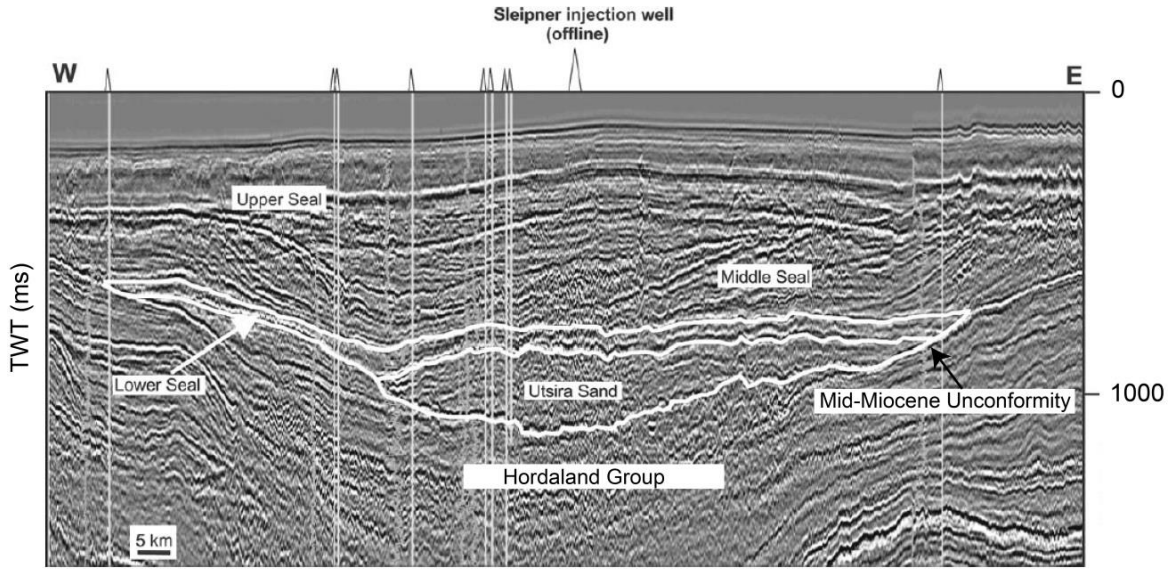

Figure 5.4 *Seismic reflection data illustrating Utsira Sand, its caprock and the underlying units in the Sleipner area. The 250 m thick Utsira Sand Formation is overlained by Quaternary glacio-marine sediments (Upper Seal) and Nordland Shales of Pliocene age (Middle and Lower Seal) (modified after Chadwick et al. (2004b)).*

The late Oligocene shales of the Hordaland group form the underlying unit of the Utsira Formation (Figs. 5.4 and 5.5). The Hordaland Unit is mainly characterized by polygonal faulting, sand injection, and sediment mobilization (Løseth et al., 2009). The top of the Hordaland Group is interpreted as a regional unconformity, known as the Mid-Miocene unconformity (Jordt et al., 1995) (Fig. 5.4). The overlying Nordland

Group includes the Utsira Sand at its lower part, which is a thick sandy unit of Late Miocene-Early Pliocene age, pinching out to the E and W (Deegan and Scull, 1977; Isaksen and Tonstad, 1989; Gregersen et al., 1997) (Fig. 5.4). The Utsira Sand sediments are interpreted to be basinal lowstand marine deposits, sandwiched between prograding highstand units (Chadwick et al., 2000).

The caprock sequence of the Utsira Sand is divided into three main units, with the lower two corresponding to Nordland shales of Pliocene age, and the overlying Quaternary glacio-marine clays and glacial tills (Chadwick et al., 2004a) (Figs. 5.4 and 5.5). The Lower Seal, formerly known as a shale drape (Holloway et al., 2000), consists of 50-100 m thick shales, extending 50 km W and 40 km E, and beyond the predicted migration distance of the injected CO_2 (Zweigel et al., 2000). The Lower Seal is interpreted to be the most efficient sealing unit for the Utsira Sand, due to its high shale proportion, c. 80% of the total volume (Gregersen and Johannessen, 2001). The Lower Seal is overlapped by westwards prograding clinoforms, up to 500 m thick. This Middle Seal is mainly composed of fine-grained sediments around the Sleipner area, with coarser sandy facies occurring locally towards the extremities and upwards. The major factors controlling sediment input and progradation during the Mid-Late Pliocene are suggested to result from the uplift of Scandinavia and glacio-eustasic process (Gregersen et al., 1997; Gregersen and Johannessen, 2007). The overlying Pleistocene to Holocone unit, the Upper Seal, truncates the underlying Pliocene shales, forming a basal unconformity.

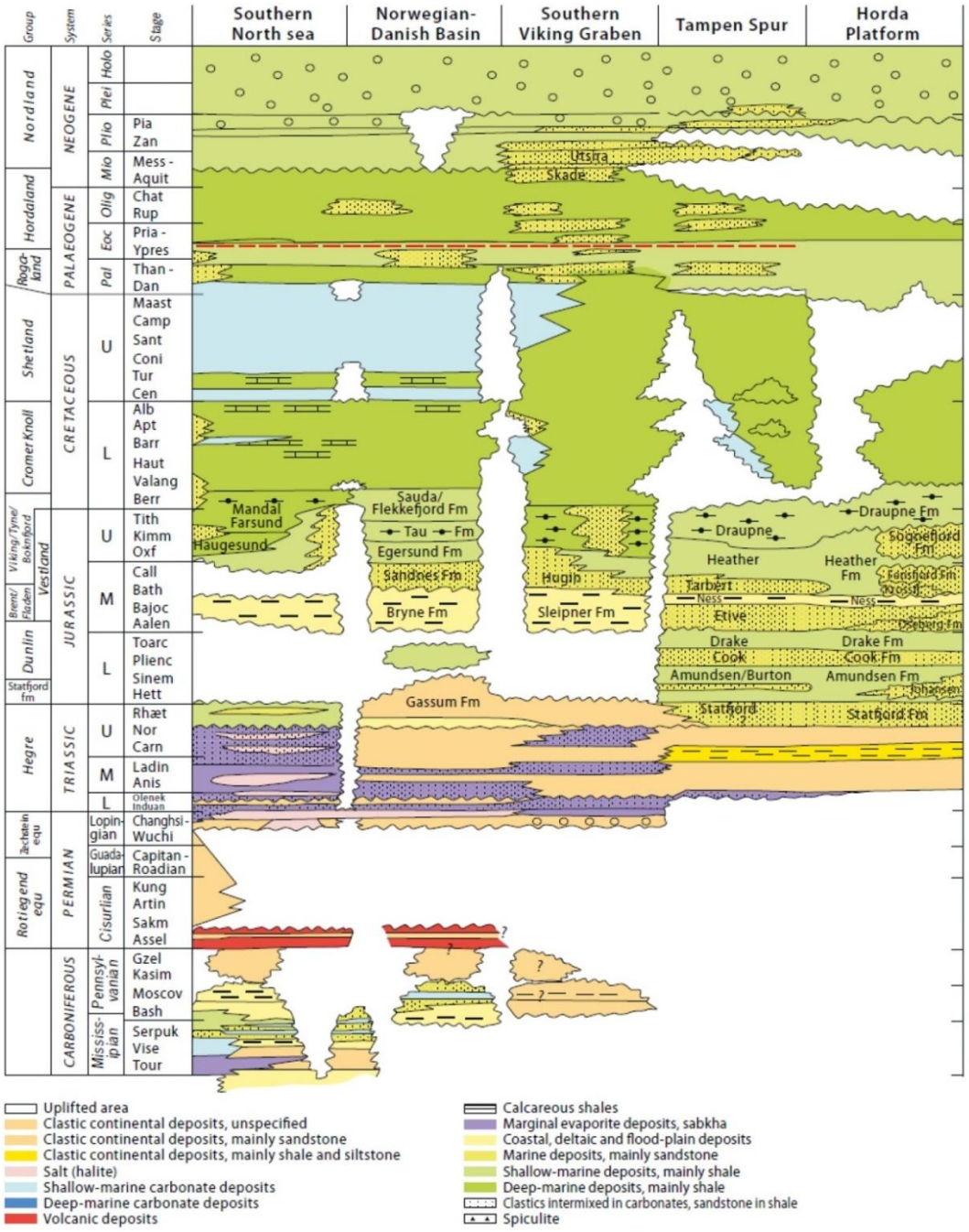

Figure 5.5 *The lithostratigraphic chart of the North Sea (courtesy of Norwegian Petroleum Directorate). CO_2 is injected into the Utsira Sand in the Southern Viking Graben Area. Nordland shales form the caprock of the Utsira Sand, while Hordaland shales are the closest underlying unit.*

5.2.2 The current state of the injected CO_2

The Sleipner CCS site has been accompanied by several research projects, during which a combination of technologies has been used to monitor the behaviour of

the injected CO_2. To date, seven time-lapse 3D seismic reflection surveys (1999, 2001, 2002, 2004, 2006, 2008, 2010) and a single 2D high-resolution survey (2006) have been acquired over the storage area, confirming that the injected CO_2 is, to date, securely trapped below the top of the Utsira Formation, with no evidence of leakage into the overburden (Chadwick et al., 2006; Arts et al., 2008; Chadwick et al., 2009; Eiken et al., 2011; Boait et al., 2012; Furre and Eiken, 2014) (Fig. 5.6a). The latest seismic reflection data acquired in 2010 supports the results from 1999, confirming that the injected CO_2 has given rise to nine high reflectivity sub-horizontal stratigraphic layers within the reservoir, ranging from layer 1 (c. 50 m above the injection point) to layer 9 (the top of the Utsira Sand), interpreted as the result of the strong acoustic impedance contrast between the CO_2-saturated sandy layers and the overlying sediments (Arts et al., 2004a; Furre and Eiken, 2014) (Fig. 5.6a). Among many attempts to quantify the thickness of the topmost layer (Williams and Chadwick, 2012; White et al., 2013), the latest seismic data reveal that the maximum thickness of layer 9 is around 11 m (Furre and Eiken, 2014).

Most of the CO_2 (more than 2/3 of the total injected volume) is found to be partially trapped below the thin intra-reservoir shale layers and Correlatable Mudrock before reaching the top of the Utsira Formation (Eiken et al., 2000; Bickle et al., 2007; Hermanrud et al., 2009) (Fig. 5.6a). 3D seismic reflection data indicate that CO_2 rose to Layer 9 in less than three years, up to 200 m above the injection point, through a vertical structure, interpreted as a seismic chimney, being the main conduit for the vertical CO_2 migration and the main feeder of the laterally expanding thin layers (Arts et al., 2004a; Chadwick et al., 2005; Arts et al., 2008) (Fig. 5.6a). The presence of this chimney suggests that the lateral continuity of the intra-reservoir shale layers has been broken in some places, resulting in the upward migration of the injected CO_2 to the top of the reservoir (Hermanrud et al., 2009). The largest velocity push-down on seismic data has been observed from 1994 to 1999 below the chimney, in the order of 30 ms, confirming the presence of a highly saturated CO_2 column above the injection point (Arts et al., 2004a; Arts et al., 2004b; Arts et al., 2008).

From 2001 seismic reflection data onwards, it has been shown that the injected CO_2 has been extending laterally in all directions, with the maximum growth being to the N, up-dip, following the overlying topography (Fig. 5.6b). The growth of the CO_2 plume is complex, with an increase in the brightness and extent of the topmost and

middle layers, and a more steady-state (or even shrinking and dimming) amplitude and size changes for the deeper levels (Chadwick et al., 2009; Boait et al., 2012). The map view of the CO_2 plume shows that it has an elliptical shape oriented NNE-SSW, with higher reflection amplitudes on its centre, covering an area of 3.1 km^2 in 2008 (Eiken et al., 2011).

Although significant uncertainties remain in the quantitative analysis of CO_2, including physical properties of CO_2-saturated rock, fine-scale distribution of dispersed CO_2, and precise geometry of the intra-reservoir shale layers, recent studies estimate the CO_2 saturation to be up to 20% of the available pore space in case of uniform distribution, and up to 80% of the total pore space in case of patchy saturation (Chadwick and Noy, 2010; Ghosh et al., 2015). These results are in agreement with other studies, suggesting more than 30% of CO_2 within the pore space (Chadwick et al., 2005; Boait et al., 2012; Queißer and Singh, 2013).

In addition to structural/stratigraphic traps discussed above, which are the predominant trapping mechanism in the early stages of geologic sequestration (IPCC, 2005), residual trapping, dissolution, and mineral trapping have also been proposed to enhance the storage security in Sleipner. During CO_2 migration, some of the CO_2 is left behind and becomes disconnected from the rest of the plume, or, residually trapped within the pore space by capillary forces. It has been shown that residual CO_2 saturation can reach up to 25% for many typical storage reservoirs (Zhang et al., 2009). In the case of Utsira Formation, the solubility trapping is estimated to become the dominating mechanism from 300 to 5000 years after the injection period (Chadwick et al., 2008). The maximum amount of dissolved CO_2 has been simulated, showing that up to 25% of the total volume injected will be dissolved between 300-20000 years, strongly depending on the permeability (Ennis-King and Paterson, 2007). Using typical values for storage sites, the maximum amount of dissolved CO_2 within the formation water is calculated to be around 3% of the total gas injected during the injection period, emphasizing that solubility trapping is a long process, being less efficient in the early stages of geologic sequestration (Thibeau and Mucha, 2011). While 3D time-lapse seismic data has been considered as the key tool to monitor the injected CO_2 in Sleipner, time-lapse gravity measurements acquired in 2002, 2005 and 2009 led to better constraints on the CO_2 plume density within the reservoir, i.e., 720 (+/-80) kg/m^3, which in turn refine the dissolution rate calculations (Alnes et al., 2011). Geochemical

reaction of the dissolved CO_2 with some minerals can lead to solid carbonate precipitate, known as mineral trapping, considered to be the most permanent type of CO_2 storage (Gunter et al., 1993).

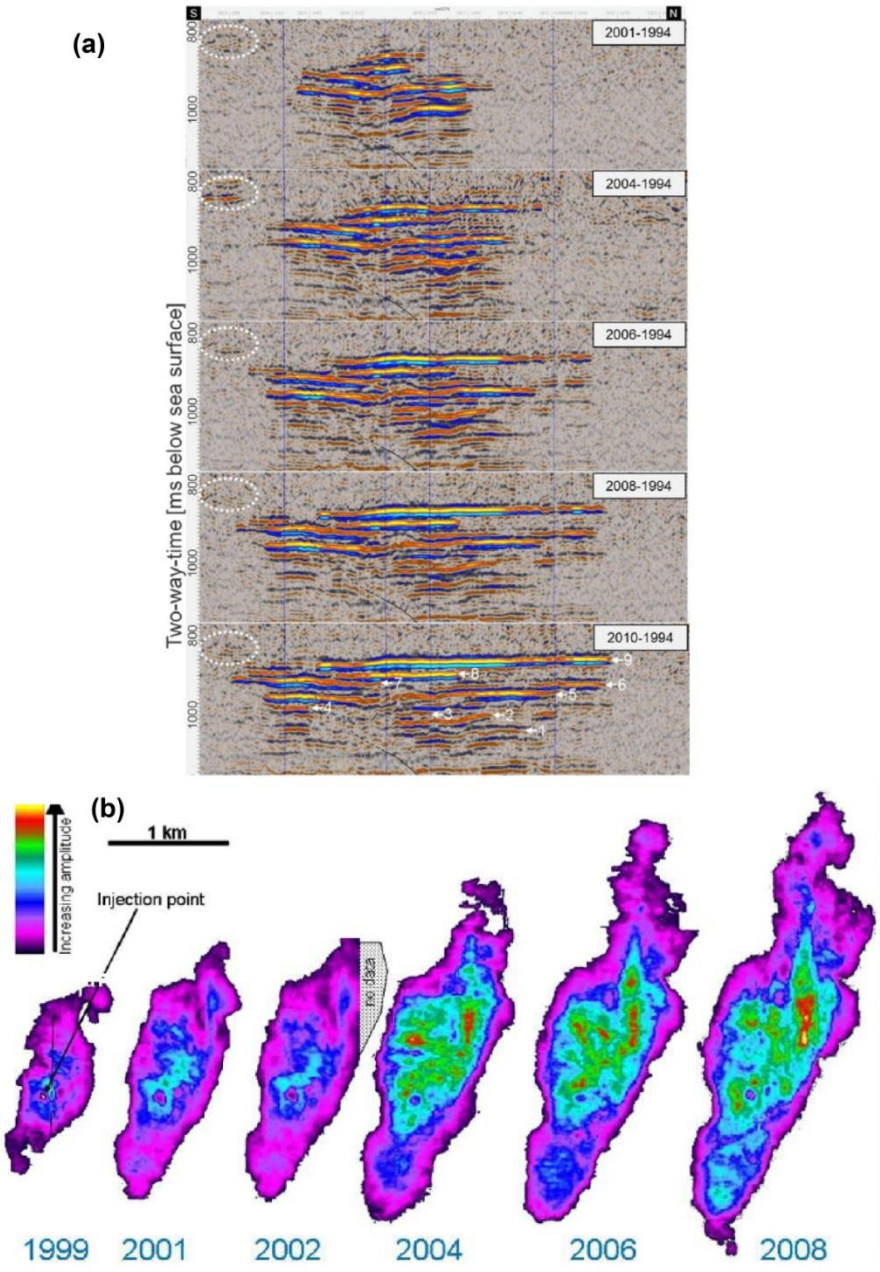

Figure 5.6 *3D time-lapse seismic imaging of the Sleipner CO_2 plume.* ***(a)*** *3D Time-lapse seismic reflection data acquired between 1994-2010, illustrating the migration of CO_2 within the storage reservoir (Furre and Eiken, 2014). The white dashed ellipses indicate the area used as a reference for the time-lapse repeatability.* ***(b)*** *The growth of the CO_2 plume between 1999-2008 (Eiken et al., 2011).*

5.2.3 Fluid flow activity within the overburden above the Utsira Sand Reservoir

Natural shallow gas accumulations and gas chimneys have been widely observed on the seismic reflection data over the Sleipner storage complex. Prior to CO_2 injection, Heggland (1997) reported the presence of high seismic amplitude anomalies within the overlying Pliocene sequence, seismic chimneys reaching the seabed, as well as buried pockmarks close to seabed, possibly indicating sustained gas seepage from deeper gas reservoirs. The significant fluid flow activity within Hordaland shales, including sediment mobilization, mud diapirism and vertical fluid migration via polygonal faults have been well-documented (Cartwright, 1994; Hurst et al., 2003; Løseth et al., 2003; Løseth et al., 2009). Most of the seismic chimneys and bright spots identified by Heggland (1997) within the overburden of the Utsira Sand have been found to be localized above mud volcanoes and fractures, emphasizing the strong spatial correlation between various fluid flow structures in the vicinity of Sleipner, possibly indicating a significant hydraulic connectivity between deeper and shallower stratigraphic units in this area.

The analysis of a merged 3D seismic dataset (ST98M3 and ST9407 surveys), acquired prior to CO_2 injection in Southern Viking Graben, clearly reveals the widespread occurrence of bright spots mainly located at Top Utsira, sand wedge and Upper Pliocene stratigraphic horizons, whereas vertical seismic anomalies are found to be mostly confined within the Pliocene sequence (Karstens and Berndt, 2015) (Fig. 5.7). Seismic wavelets from the Top of Utsira have been found to show polarity reversals, interpreted as the acoustic evidence of gas accumulations (Karstens and Berndt, 2015). In the same study, bright spots occurring at Upper Pliocene have been correlated with narrow pipe-like features beneath, suggesting a possible hydraulic connectivity with deeper sequences (Karstens and Berndt, 2015). Based on their acoustic character, three different types of large-scale vertical chimneys, reaching the seabed and/or terminating close to the seabed, have also been identified by Karstens and Berndt (2015), with the width of the chimneys ranging between 100-1000 m (Fig. 5.7). These chimneys have been found to originate deep in the overburden, i.e. 500-800 m depth, cross-cutting Nordland shales, interpreted as the seismic evidence of fluid migration in the Sleipner area, before CO_2 injection (Karstens and Berndt, 2015). The

observed fluid flow activity within the overburden in Sleipner is proposed to originate as a result of the gas migration from deeper hydrocarbon reservoirs into the Utsira Sand via mud diapirs at its base. Seal-breaching of the overlying Nordland shales is likely to arise from the combination of continuous gas supply from deep reservoirs, loading of the Fennoscandian ice sheet, and weakening of the seal due to deformation by mud mobilization and fault activity.

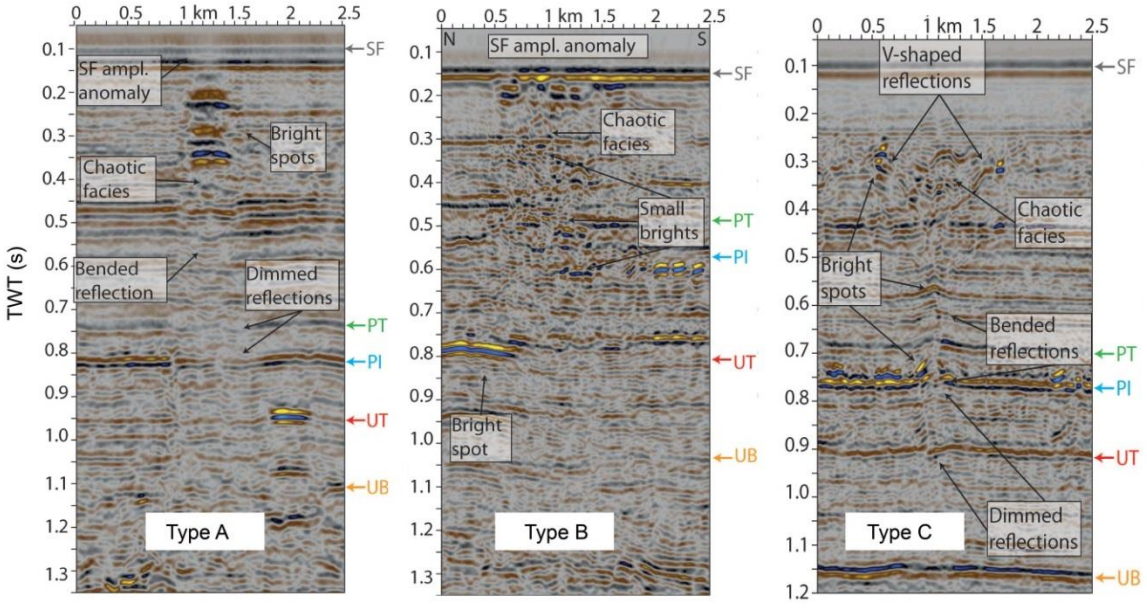

Figure 5.7 *Bright spots and three different types of seismic chimneys identified on the 3D seismic reflection data in Sleipner, acquired prior to CO_2 injection (modified after Karstens and Berndt (2015)). Type A chimneys are characterized by more than two bright spots at their top with polarity reversal. Most of the type A chimneys terminate close to the seabed, or even reach the seabed. Type B chimneys have more chaotic seismic signature than Type A chimneys. They are formed by smaller patchy bright spots and disturbed seismic reflectors. Type C chimneys are more meandering compared to Type A and B chimneys. They locate below buried tunnel valleys, characterized by V-shape reflections. All these three type of chimneys can be traced down to the Top of Pliocene or Top of Utsira. SF, PT, PI, UT, UB correspond to seafloor, Top-Pliocene, Intra-Pliocene, Utsira Top and Utsira Base, respectively.*

The paleo-fluid migration pathways within the overburden in the Sleipner area have also been reported by Nicoll (2012) from the analysis of a 3D seismic reflection dataset (ST9407 survey) acquired before CO_2 injection. Bright spots detected within the overburden at 300-700 m depth have been found to preferentially align in SW-NE

direction, suggesting structural/stratigraphic control on the spatial location of these anomalies. This same observation has also been noted in previous studies, where the upward migration of fluids is likely to be constrained by faults and lineaments within the Sleipner overburden (Borgos et al., 2002). Similarly to bright spots, seismic chimneys detected on this 3D seismic dataset (Nicoll, 2012) mostly locate above Hordaland unit mud diapirs, indicating a possible hydraulic connection between different stratigraphic layers, confirming observations by Heggland (1997).

From post-injection 3D seismic studies of the Sleipner site, in addition to the acoustic changes detected within the Utsira Sand due to CO_2 injection, various high amplitude seismic anomalies have been detected at different levels within the overburden, including both Quaternary and Pliocene, as well as Top Utsira, interpreted as being possible natural gas accumulations in the Sleipner area (Zweigel, 2000; Borgos et al., 2002). Some of these anomalies are suggested to be linked to the mud volcanoes at the base of the reservoir, confirming observations from pre-injection studies (Zweigel, 2000; Carlsen et al., 2001; Borgos et al., 2002). Bright spots mapped within the Middle Seal have been found to occur at topographic highs, indicating the structural control on the spatial location of seismic amplitude anomalies, whereas bright spots within the Lower Seal are spatially more dispersed (Chadwick et al., 2008).

Another interesting observation regarding the fluid flow activity in the North Sea is the possible link between buried tunnel valleys and fluid leakage. As stated above, the Early Quaternary geology of the North Sea was dominated by Pleistocene glaciations, where at least three transgression periods are recognised in the last 0.5 Ma years, leading to glaciomorphological structures including ploughmarks and tunnel valleys. The origin of tunnel valleys is mainly attributed to meltwater flow and erosion during ice retreat, incising the underlying sediments (Cameron et al., 1987; Huuse and Lykke-Andersen, 2000; Praeg, 2003). The depth and width of North Sea tunnel valleys vary, ranging typically between 100-500 m and 0.5-6 km respectively, as well as their extension (Huuse and Lykke-Andersen, 2000; Praeg, 2003; Kristensen et al., 2007). Although tunnel valleys might occur in isolation, most have been reported to form an interconnected network of elongate depressions, in an anastomosing pattern (Lonergan et al., 2006). Based on their seismic character and borehole data, tunnel valley sediment infill is reported to be very complex, composed mainly of an acoustically chaotic unit at the base with glacio-fluvial sandy-silty sediments with local gravel, overlain by

horizontally well-laminated glacio-marine, glacio-lacustrine and interglacial silt and clays (Praeg, 2003; Lonergan et al., 2006; Kristensen and Huuse, 2012). Several seismic velocity anomalies including push-up and pull-down effects have been observed beneath the tunnel valleys from the seismic reflection data (Kristensen and Huuse, 2012) (Fig. 5.8). Apart from seismic velocity effects imaged beneath tunnel valleys, correlating with variations in sediment infill, dimming of seismic amplitudes in the underlying reflectors and low seismic velocities within the tunnel valleys have been interpreted as evidence of shallow gas inside the valley (Kristensen and Huuse, 2012) (Fig. 5.8).

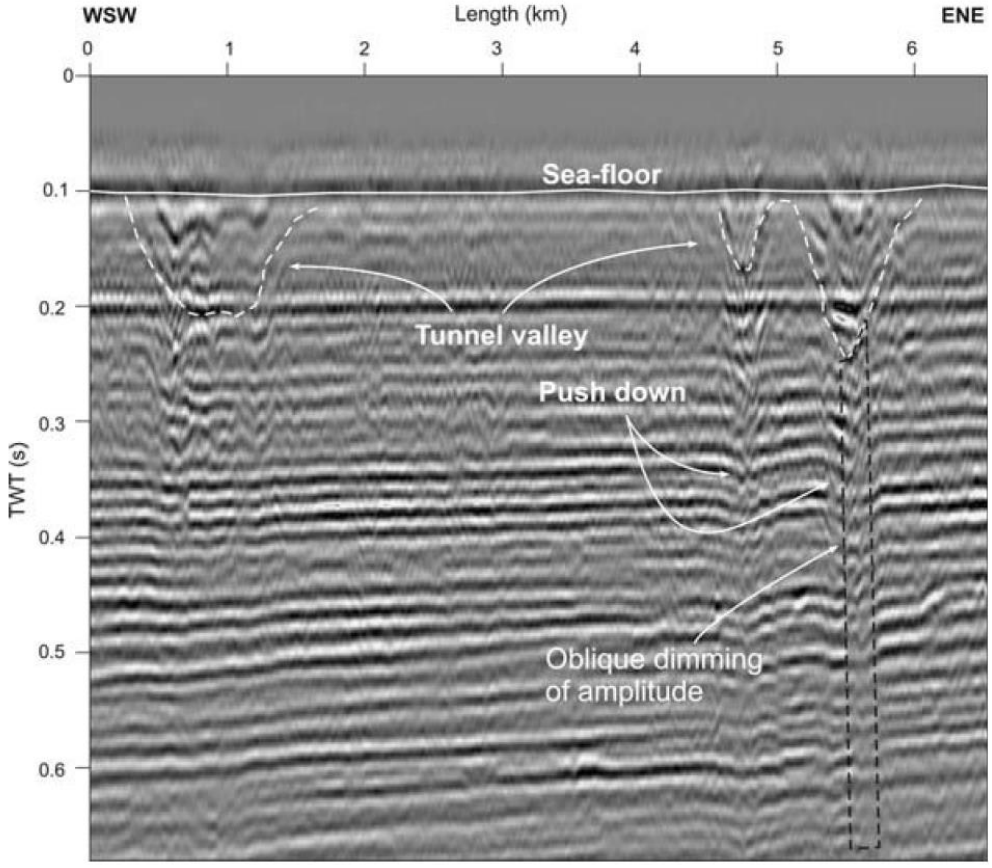

Figure 5.8 *An example of a seismic section from North Sea, illustrating buried tunnel valleys (Kristensen and Huuse, 2012). Velocity anomalies are found beneath the tunnel valleys. On the E-NE part of the seismic profile, high amplitude seismic anomalies are detected within the tunnel valley, as well as dimming of seismic reflections below, interpreted as shallow gas.*

In previous studies, it was noted that bright spots were widely observed in the vicinity of these buried tunnel valleys, suggesting a close connection between glacial

features and fluid flow (Fichler et al., 2005). Pleistocene tunnel valleys imaged within the overburden in the North Sea are suggested to possibly act as preferential pathways during upward fluid migration, weakening seal integrity in the vicinity of Sleipner CCS site (Karstens and Berndt, 2015). Glacial, cross-cutting channels with permeable sandy sediment infill have also been reported by Nicoll (2012) in the Pleistocene succession of the North Sea, with the shallowest valleys identified at 150 m below seabed. These glacial channels are proposed to form an interconnected network of preferential gas migration pathways within the overburden, in the case of CO_2 leakage from the Utsira Sand (Nicoll, 2012). In summary, the considerable size, high porosity and the interconnected pattern of the tunnel valleys have been proposed to allow and enhance the upward fluid migration in the North Sea within the overburden.

5.3 Data acquisition and processing

During the *JC077* cruise, a multidisciplinary approach was taken to investigate the near surface fluid flow activity in the vicinity of Sleipner CCS site on board *R/V James Cook*. Four areas of interest were selected, including the Hugin Fracture Area, Middle Area (the area between Hugin Fracture and Sleipner CCS site), CO_2 Plume Area and South of the Plume Area (Figs. 5.9 and 5.10).

Ten AUV geophysical surveys (M59-M68) with 708 km of track lines, corresponding to 141 hours of survey, were successfully completed in these areas, using seismic reflection (Chirp) and side-scan sonar mounted on Autosub 6000 (Figs. 5.9 and 5.10, see also Appendix B), allowing continuous imaging of the seabed and shallow subsurface (Table 5.1). In addition to geophysical data, a combination of various chemical sensors mounted on Autosub 6000, including pH, Eh, and pCO_2 sensors, as well as video photography, were simultaneously used to detect possible leakage (formation fluids, natural gas and CO_2) from the seabed to the overlying water column in the Central North Sea. In addition to Autosub 6000, a robotic underwater vehicle, HyBIS, completed 11 dives in the selected areas, allowing seabed video surveying and acquisition of grab samples. The shipboard multibeam system (EM710) was regularly used during the cruise, providing bathymetry and backscatter data. In conjunction with these, sediment vibrocores and water samples (CTD) were also collected to enhance detection of the biogeochemical and physical changes related to fluid flow activity.

Dive	Area	Day	Altitude	Line Spacing
M59	South of the Plume	05/09/2012	12 m	150 m
M60	Middle Area	07/09/2012	12 m	100 m
M61	Hugin Fracture	08/09/2012	12 m	150 m
M62	Hugin Fracture	09/09/2012	3 m	150 m
M63	Middle Area	10/09/2012	3 m	50 m
M64	Hugin Fracture	15/09/2012	12 m	150 m
M65	CO_2 Plume	17/09/2012	12 m	150 m
M66	CO_2 Plume	20/09/2012	3 m	150 m
M67	Middle Area	21/09/2012	4 m	50 m
M68	Regional	22/09/2012	12 m	1000 m

Table 5.1 *Summary of Autosub 6000 missions. Ten dives were completed during the JC077 cruise in the Central North Sea.*

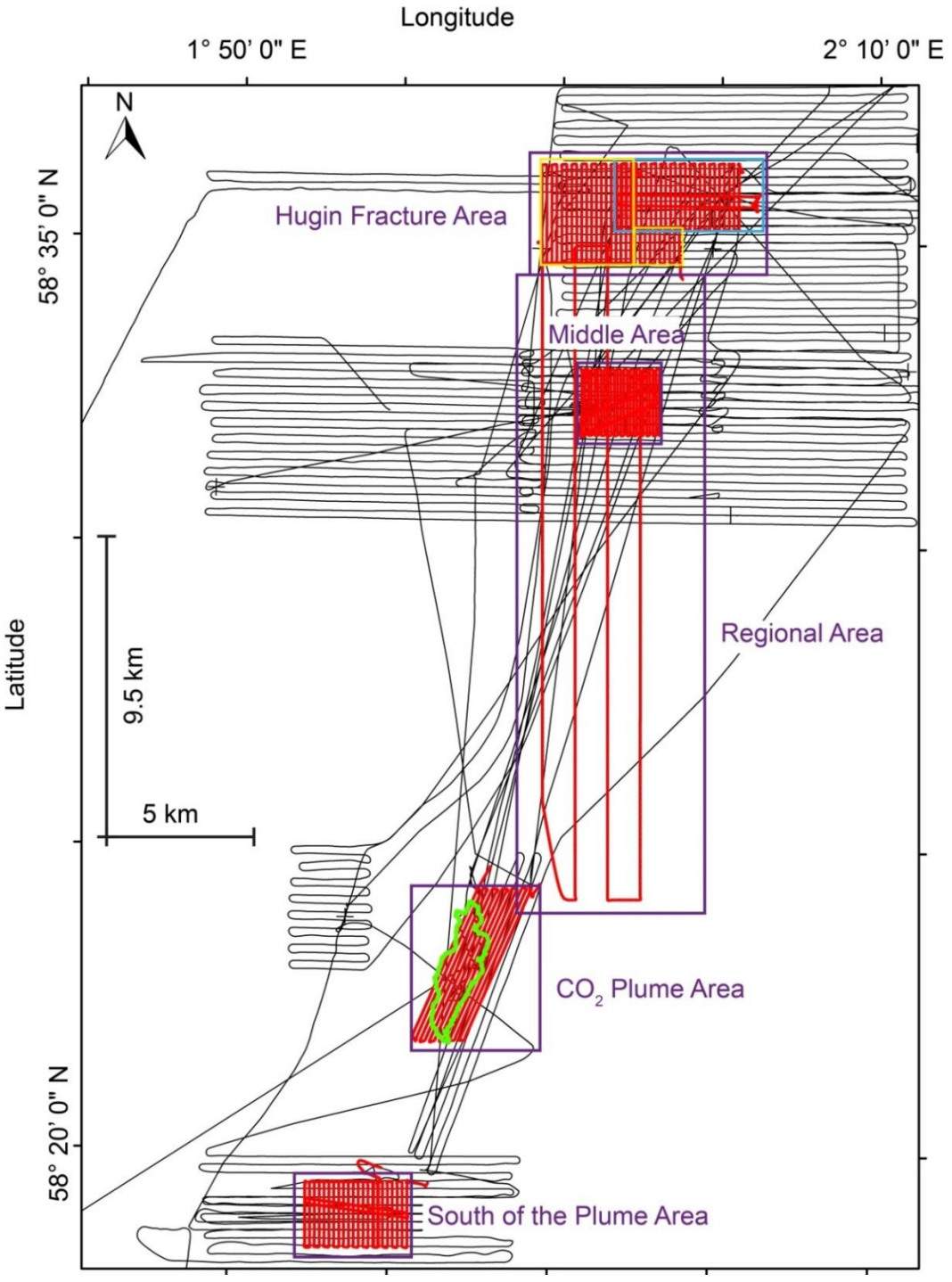

Figure 5.9 *Multibeam, Chirp and side-scan sonar track lines (with Autosub 6000 flying altitude at 12 m). Four areas were surveyed (purple rectangles), with Hugin Fracture Area (M61 (blue rectangle) and M64 (yellow rectangle)), Middle Area (M60), CO_2 Plume Area (M65) and South of the Plume Area (M59) shown. Regional lines were also acquired during M68 survey. The extent of the CO_2 plume in 2010 (provided by Statoil) is indicated by the green polygon. Black solid lines are multibeam track lines, and red solid lines are Autosub 6000 track lines.*

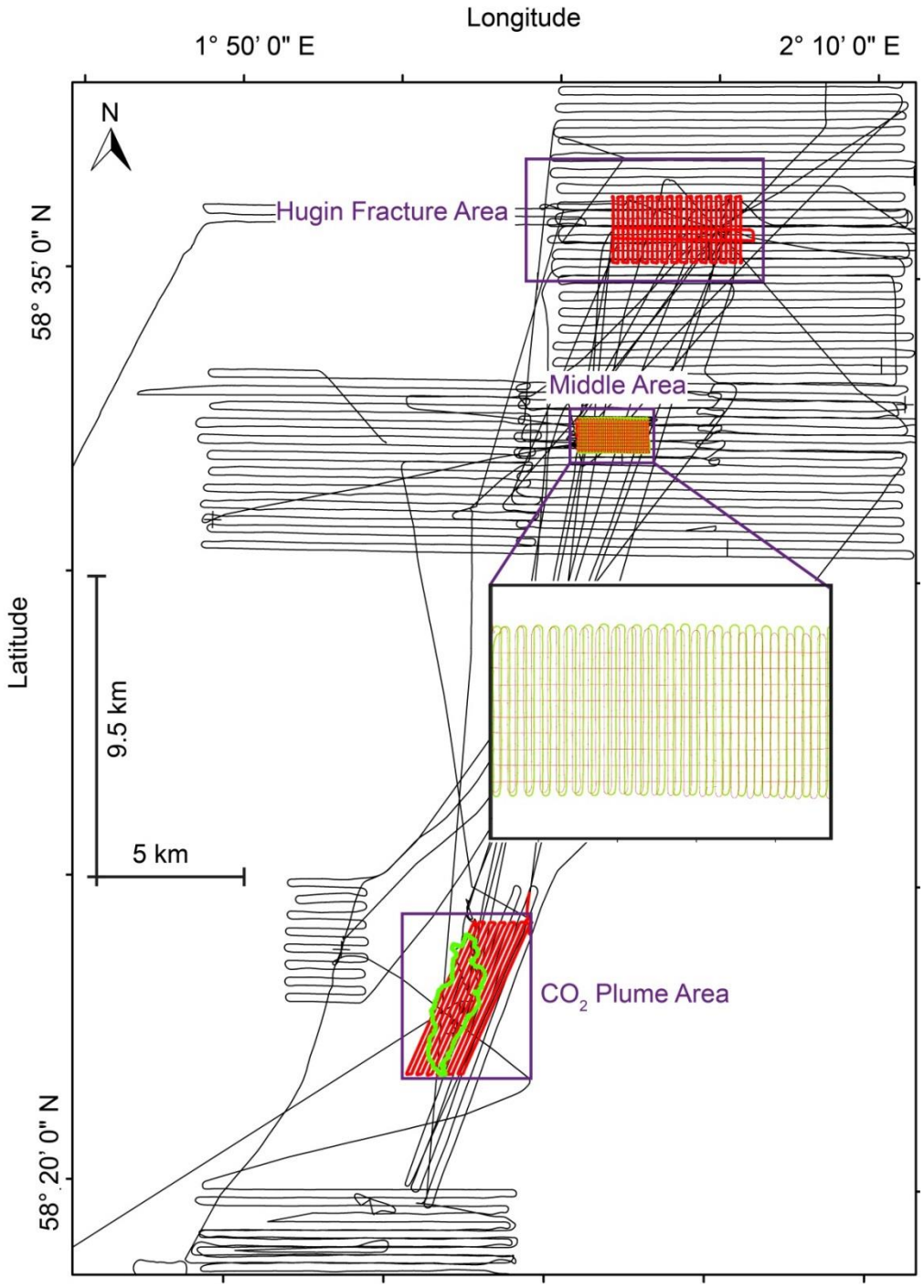

Figure 5.10 *Multibeam, Chirp and side-scan sonar track lines (with Autosub 6000 flying altitude at 3 m). Three areas were surveyed (purple rectangles), with Hugin Fracture Area (M62), Middle Area (M63 (green lines) and M67 (red lines)) and CO_2 Plume Area (M66) shown. The extent of the CO_2 plume in 2010 (provided by Statoil) is indicated by the green polygon. A zoom of the Middle Area surveys is also given in inset box. Black solid lines are multibeam track lines, and red solid lines are Autosub 6000 track lines.*

5.3.1 High-resolution 2D seismic reflection data acquisition and processing

Chirp sub-bottom profilers are high frequency, normal incidence marine systems using frequency modulated and amplitude and phase compensated sweeps, with a large bandwidth ranging generally between 1-24 kHz, and a highly repeatable source signature (Schock et al., 1989; Panda et al., 1994; Gutowski et al., 2002). The wide bandwidth allows vertical resolution on the order of decimetre scale for the top c. 30 m of sediments (Bull et al., 1998; Quinn et al., 1998). The horizontal resolution of Chirp data, varying mainly from 1 to 2 m, depends on different parameters such as beam angle and dominant frequency of the source, as well as compressional sediment wave velocity, towfish altitude and pulse rate of the system (Quinn et al., 1998). As a result of the match filtering processes, which is the autocorrelation of the source sweep or Klauder wavelet, Chirp data represents an improved signal to noise ratio compared to seismic images acquired with short-pulse, single-frequency profilers (Schock and LeBlanc, 1990). As mentioned by LeBlanc et al. (1992), to have the same performance with the Chirp sonar, conventional sonars should generate a pulse with a peak power 100 times larger. Chirp sub-bottom profilers have been widely used in geophysical, geotechnical and archaeological studies (Quinn et al., 1997a, b; Bull et al., 1998; Quinn et al., 1998; Kim et al., 1999; Pinson et al., 2008).

During the *JC077* cruise, high-resolution 2D seismic reflection (Chirp) data were acquired using an Edgetech 2200-M Modular Sonar System, mounted on Autosub 6000. The source sweep used during seismic data acquisition was a high frequency Chirp sweep, developed by Gutowski et al. (2002), that oscillated between 2-13 kHz for 32 ms, with sine squared 8^{th} envelope (Fig. 5.11). The Chirp data were sampled at 43.4 kHz. The maximum penetration was around c. 5 metres (for V_p=1500 m/s) throughout the surveys (Figs. 5.9 and 5.10).

The Edgetech 2200-M Modular Sonar System records the seismic reflection data in two formats: uncorrelated (raw) data and correlated data (autocorrelation of the Chirp sweep within the system). Here, we are interested in the raw seismic data, as it allows us to fully control the data quality. All seismic data were recorded in Edgetech's original jsf format. During seismic data acquisition, several parameters including navigation, altitude, depth, pitch, roll, and heading were not merged simultaneously

within the seismic headers. Therefore, before signal processing, the first step was to import these parameters into seismic data headers, which were recorded separately by Autosub 6000. A script was written and run on MATLAB (see Appendix C), to merge the missing parameters with the seismic data, using a common time base.

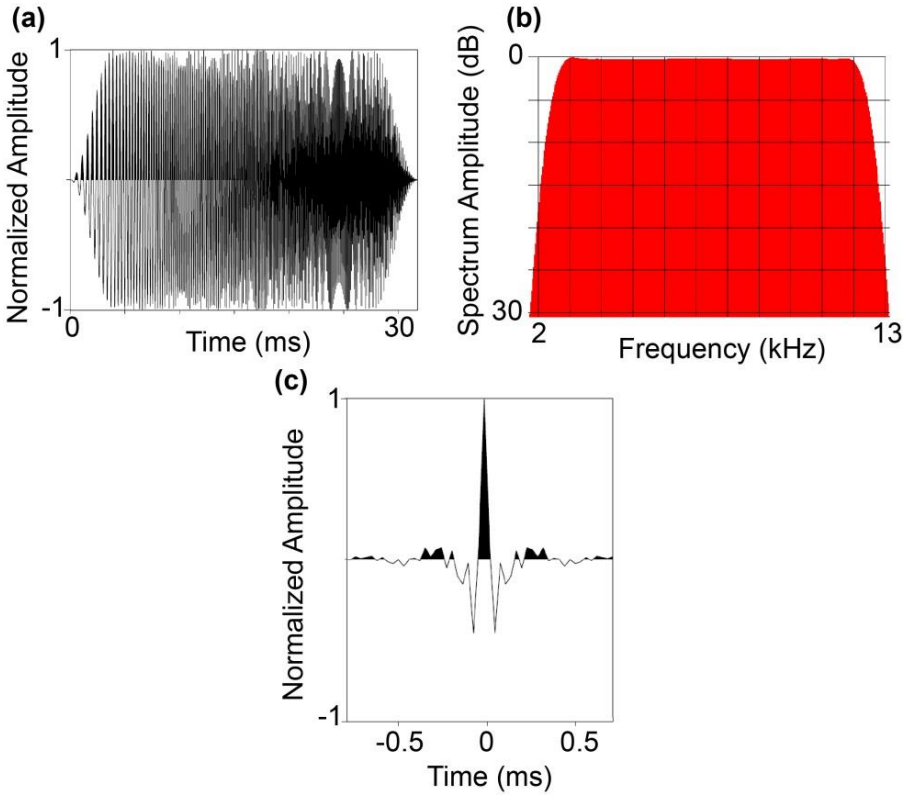

Figure 5.11 *The seismic source used during Autosub 6000 seismic reflection data acquisition in the Central North Sea.* ***(a)*** *Time domain representation of the Chirp sweep used in this study.* ***(b)*** *Power spectrum of the Chirp sweep given in (a).* ***(c)*** *Autocorrelation of the Chirp sweep given in (a).*

In order to convert the jsf data into segy, we modified the existing code "jsf2segy", which was originally written by Tom O'Brien in 2004 (USGS, Woods Hole Coastal and Marine Science Centre). This revised code let us to convert uncorrelated jsf data to uncorrelated segy data. Thus, the seismic data in this new format (segy) can be easily imported into any seismic processing software for further analysis. A manual for the jsf2segy code was also written (see Appendix D). The seismic Chirp data were processed using ProMax. Due to high data quality, seismic reflection data processing consisted of simple steps (Fig. 5.12): Correlation of the raw data with the source sweep, Ormsby band-pass filtering (1000-2000-10000-12000 Hz), minimum phase predictive deconvolution, trace mixing (3 traces), true amplitude recovery, trace muting,

and instantaneous amplitude correction. The processed Chirp data were then imported into the seismic interpretation software Petrel v. 2013, where depth correction was applied using the onboard multibeam bathymetry data.

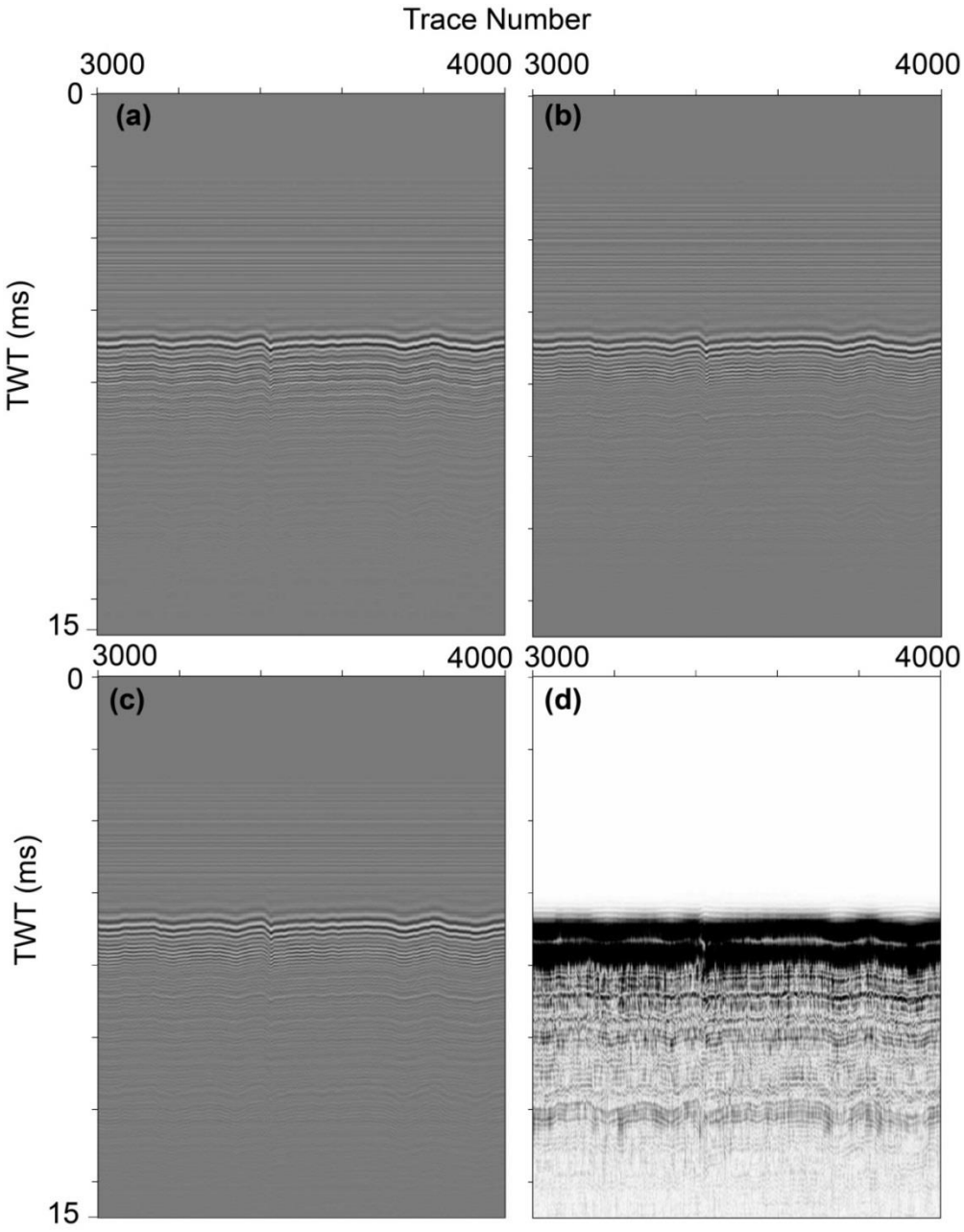

Figure 5.12 *Seismic reflection (Chirp) data processing steps for a random seismic line (M62) acquired during the JC077 cruise with Edgetech 2200-M Modular Sonar System mounted on Autosub 6000.* ***(a)*** *Correlation and band-pass filtering applied.* ***(b)*** *Deconvolution applied.* ***(c)*** *Three trace mixing and true amplitude recovery applied.* ***(d)*** *Final seismic section with top mute and instantaneous amplitude correction applied.*

In addition to the seismic Chirp dataset acquired during the *JC077* cruise, 24 TOPAS sub-bottom 2D seismic profiles acquired within the Hugin Fracture Area (courtesy of the University of Bergen), in June 2012 during *CGB/G.O Sars* cruise, have been used in this study (Fig. 5.13). TOPAS data acquisition used a Chirp sweep oscillating between 2-6 kHz, a ping interval of 400-1000 ms and a trace length of 150-400 ms. TOPAS seismic reflection data were already processed, and are used in this thesis to supplement Autosub 6000 Chirp data, allowing an integrated interpretation.

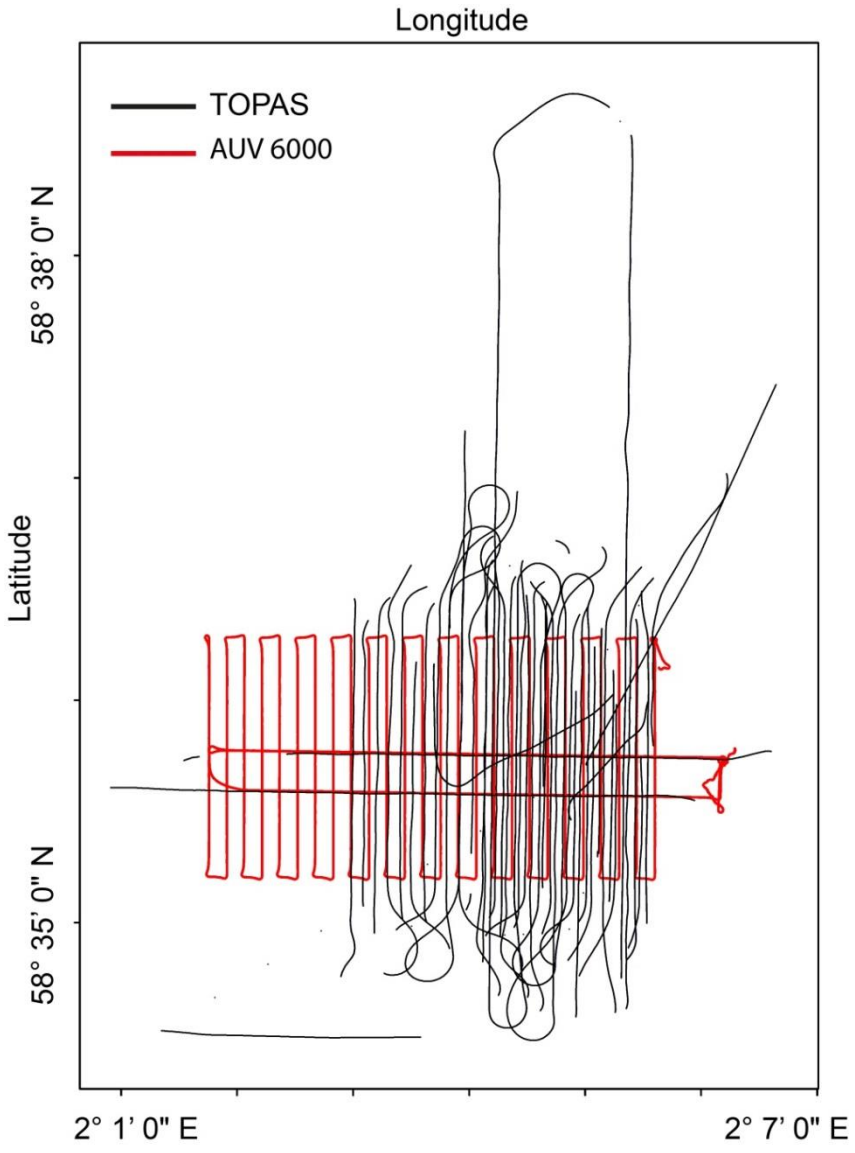

Figure 5.13 *Track lines of the TOPAS sub-bottom seismic reflection profiles. These 24 seismic profiles were acquired in the Hugin Fracture Area (courtesy of the University of Bergen). Autosub 6000 Mission 61 survey lines are also indicated on the figure by solid red lines. Solid black lines are TOPAS track lines.*

Root Mean Square (RMS) seismic amplitudes (A_{RMS}) were calculated for Chirp and TOPAS seismic reflection data. For a selected time window, RMS seismic amplitudes were calculated on Petrel using the following Eq. 1:

$$A_{RMS} = \sqrt{\frac{A_1^2 + A_2^2 + \cdots + A_m^2}{m}} \quad (1)$$

where *m* is the total number of samples within the selected time window. After the extraction of RMS seismic amplitudes along trace, these values were gridded and RMS seismic amplitudes maps produced. These maps were used to better constrain the change in seismic amplitudes due to near-surface fluid flow within the overburden in the Central North Sea.

5.3.2 Side-scan sonar and multibeam bathymetry data acquisition and processing

In addition to Chirp data acquisition, side-scan data were acquired with Edgetech 2200-M Modular Sonar mounted on Autosub 6000. This side-scan sonar was operated at 410 kHz, with one-way beam being 0.3°, and 200 m swath. Survey speed was about 2.8 knots and the ping rate was c. 0.3 m. Following each Autosub 6000 deployment (Figs. 5.9 and 5.10), the side-scan data in jsf format were first converted to xtf format with the DISCOVER 4200 MP software and amplitude corrections were then applied (29 dB for Gain and 18 dB for TVG over 100 m at 12 m altitude, and 25 dB for Gain and 20 dB for TVG over 100 m at 3 m altitude). After being merged with the navigation, the side-scan data were mosaicked with PRISM software. The side-scan mosaics were generally processed at 0.5 m (pixel size), though some smaller specific areas were processed at 0.1 m to have a better resolution.

Multibeam bathymetry data were acquired by shipboard multibeam shallow water system EM710 (Figs. 5.9 and 5.10). Bathymetry data were processed with CARIS HIPS software. The data were corrected against sound velocity provided by CTD profiling. A calibration survey has been also conducted offshore for the transducer orientation. Line spacing was 250 m, and the resolution is c. 5 m. Survey speed was

around 6 knots and ping rate was c. 1.5 m. Bathymetry data were found to have significant noise, thus outliers were removed by manual editing. Side-scan sonar and multibeam bathymetry data were both processed by Dr. Tim Le Bas from NOCS.

The navigation performance was evaluated during the cruise for different flying altitudes of Autosub 6000. By comparing the location of known seabed pipeline and cable infrastructure on multibeam and side-scan sonar data, it was determined that the accuracy of the navigation data acquired at 12 m altitude is significantly better (less than 2 m positioning error) compared to the data acquired at 3 m altitude (several metres). Although the larger navigation errors at 3 m flying altitude were minimized during data processing, it should be noted that the navigation performance at 12 m altitude is more reliable.

5.3.3 Autosub 6000 images and HyBIS video surveying

A 5 M-pixel digital downward looking colour camera was mounted on Autosub 6000 during the *JC077* cruise, providing high-quality images of the seabed. After each mission, a file including the time at which the frame was taken, the altitude of Autosub 6000 at this time, water depth, and the navigation data was provided by Autosub 6000 engineers. The number of images taken per mission is significant with c. 60000-70000 frames/mission (Figs. 5.9 and 5.10). In this thesis, we are only showing image data from Autosub 6000 3 m altitude missions, as the image resolution is significantly higher compared to other Autosub 6000 missions.

HyBIS is a multi-purpose survey and sampling robotic underwater vehicle (ROV) developed in 2008, with depth capability of 6000 m, and was used during the *JC077* cruise to undertake targeted investigations (Fig. 5.14). The sampling module used during the video surveys comprised a 0.5 m^3 clam-shell grab with a payload capacity of 750 kg and closure force of 4 tonnes. Unlike conventional ROVs, HyBIS is suspended by a cable directly from the ship. The navigation of HyBIS was successfully provided using the vessel's Sonardyne USBL tracking system with a mini-transponder beacon on the HyBIS vehicle. A total of 11 dives in selected areas (Fig. 5.14), with almost 13 hours of video surveying, as well as collection of 5 grab samples, were completed during the *JC077* cruise (Table 5.2).

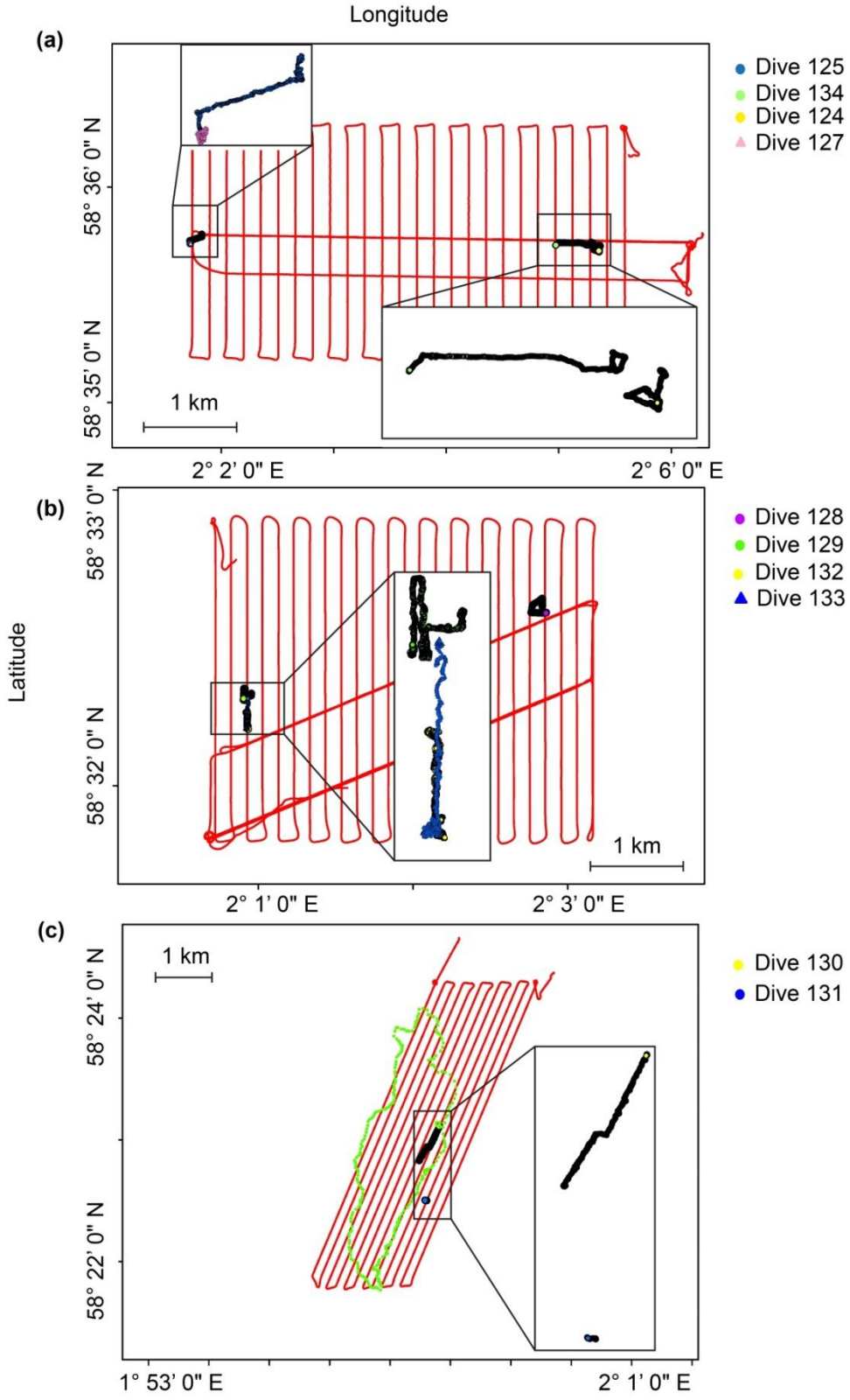

Figure 5.14 *Maps showing the survey track lines for HyBIS dives.* ***(a)*** *HyBIS dives in the Hugin Fracture Area.* ***(b)*** *HyBIS dives in the Middle Area.* ***(c)*** *HyBIS dives in the CO_2 Plume Area. The spatial extent of CO_2 plume in 2010 is also given in (c) (green polygon).*

	Date	Area	Grab Sample
124	15/09/2012	Hugin Fracture	Yes
125	16/09/2012	Hugin Fracture	Yes
126	16/09/2012	failed	No
127	16/09/2012	Hugin Fracture	Yes
128	17/09/2012	Middle Area	No
129	17/09/2012	Middle Area	No
130	18/09/2012	CO_2 Plume	No
131	18/09/2012	CO_2 Plume	Yes
132	19/09/2012	Middle Area	No
133	19/09/2012	Middle Area	No
134	21/09/2012	Hugin Fracture	Yes

Table 5.2 *List of HyBIS dives and summary data. 11 dives were successfully completed (except Dive 126) in the Central North Sea at different areas.*

5.3.4 Sediment vibrocore operations

Twenty-seven sediment vibrocores were successfully recovered with the BGS vibrocorer within different areas of survey in the Central North Sea (Fig. 5.15; Table 5.3). For every target location, 2 or 3 vibrocores were recovered to be analysed separately both for chemical and physical changes within the subsurface, as well as some archive cores (Table 5.3). Once the vibrocorer was deployed from *R/V James Cook* and reached the seabed, the motor was switched on, and the progress of penetration into the sediments was monitored and digitally recorded. After reaching the maximum penetration, the retract mechanism returned the core barrel on deck. The core was then removed from within the core barrel for further analysis.

In this work, we used some of the vibrocore geophysical logs to generate synthetic seismograms. Standard Multi Sensor Core Logger (MSCL-S) measurements were carried in British Ocean Sediment Core Facility (BOSCORF) in Southampton, providing physical information along the cores, including density, seismic P-wave velocity and magnetic susceptibility. Following these measurements, acoustic impedance (*AI*) profiles and reflection coefficient (*RC*) values were produced using these following equations (Eqs. 2 and 3):

$$AI = \rho_s V_p \qquad (2)$$

$$RC = \frac{\rho_{s2} V_{p2} - \rho_{s1} V_{p1}}{\rho_{s2} V_{p2} + \rho_{s1} V_{p1}} \qquad (3)$$

where ρ_{s1} and ρ_{s2} are sediment density, and V_{p1} and V_{p2} are seismic velocities.

By convolving the reflection coefficient values with the source sweep (Fig. 5.11a), synthetic seismograms were generated. Identical seismic processing steps were applied to the synthetic seismograms and real seismic reflection data to optimise the comparison. Where data gaps occur, reflection coefficient profiles were interpolated before convolution with the source sweep. Real seismic traces were chosen to intersect the core location where possible.

In addition to synthetic seismograms, some results from geochemical pore water analysis of the split core sections, completed by Dr. Anna Lichtschlag at NOCS (Table 5.3), have been provided to this study, to improve our geophysical interpretations. The pore water analysis of these vibrocores allows the detection of possible tracers of fluid leakage within the sediments, as well as characterizing the near surface sediment geochemistry in the vicinity of Sleipner CCS site.

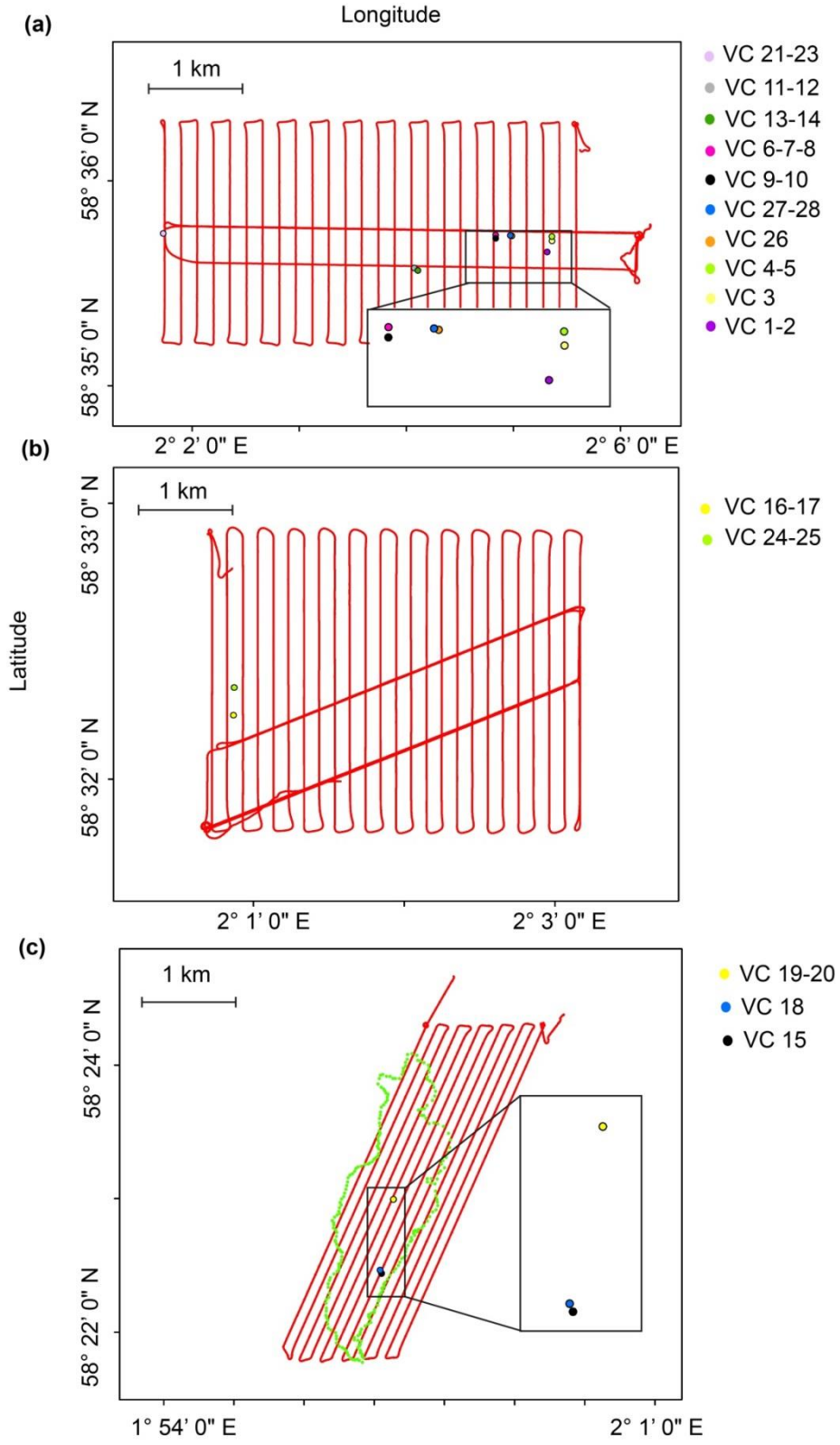

Figure 5.15 *Maps showing the vibrocore locations.* ***(a)*** *Vibrocores collected in the Hugin Fracture Area.* ***(b)*** *Vibrocores collected in the Middle Area.* ***(c)*** *Vibrocores collected in the CO_2 Plume Area. The spatial extent of CO_2 plume in 2010 (green polygon) is also given in (c).*

Vibrocore	Latitude	Longitude	Area	Length of core (m)	Analysis
VC01	58.59472	2.088233	Hugin Fracture	2.92	geochemistry
VC02	58.59472	2.088233	Hugin Fracture	2.88	archive
VC03	58.59562	2.088983	Hugin Fracture	2.95	geochemistry
VC04	58.59598	2.08895	Hugin Fracture	3.3	geochemistry
VC05	58.59598	2.08895	Hugin Fracture	2.81	archive
VC06	58.59603	2.080217	Hugin Fracture	3.49	geophysics
VC07	58.59603	2.080217	Hugin Fracture	3.37	archive
VC08	58.59603	2.080217	Hugin Fracture	3.5	geochemistry
VC09	58.59577	2.080217	Hugin Fracture	3.35	archive
VC10	58.59577	2.080217	Hugin Fracture	3.79	geochemistry
VC11	58.59325	2.0676	Hugin Fracture	3.15	archive
VC12	58.59325	2.0676	Hugin Fracture	2.6	geochemistry
VC13	58.59305	2.068167	Hugin Fracture	2.38	archive
VC14	58.59305	2.068167	Hugin Fracture	2.46	geochemistry
VC15	58.37452	1.951283	CO_2 Plume	2.35	geochemistry
VC16	58.5373	2.014183	Middle Area	2.82	geochemistry
VC17	58.5373	2.014183	Middle Area	1.92	archive
VC18	58.37492	1.95095	CO_2 Plume	2.7	archive
VC19	58.38378	1.95385	CO_2 Plume	1.6	archive
VC20	58.38378	1.95385	CO_2 Plume	3.2	geochemistry
VC21	58.59578	2.028433	Hugin Fracture	1.86	archive
VC22	58.59558	2.028433	Hugin Fracture	failed	archive
VC23	58.59578	2.028433	Hugin Fracture	1.94	geochemistry
VC24	58.53897	2.014217	Middle Area	2.98	geochemistry
VC25	58.53897	2.014217	Middle Area	1.54	archive
VC26	58.59598	2.082717	Hugin Fracture	3.1	geophysics
VC27	58.59602	2.082483	Hugin Fracture	1.63	archive
VC28	58.59602	2.082483	Hugin Fracture	3	geochemistry

Table 5.3 *Vibrocores recovered during the JC077 cruise and related informations. Vibrocores were recovered in different areas of interest. Archive cores were both studied for geochemistry or geophysics analysis when necessary.*

5.3.5 Water column geochemistry

An Eh water column redox potential sensor mounted on Autosub 6000 and a CTD rosette were both used during the *JC077* cruise, to detect possible leakage of fluids in the Central North Sea. The CTD rosette consists of Niskin sampling bottles closed at predefined depths, allowing the retrieval of water samples for different depths. The water column sampling strategy during the *JC077* cruise comprised 4 bottom water samples at 2 m intervals from the seabed and 1 surface water at 5 m depth. A total of 63 CTD measurements within different areas were completed. Once the CTD rosette was on deck, water samples were collected from the Niskin bottles for further analysis. Gas concentrations of these water samples were determined by gas chromatography using a headspace equilibration method with a reported accuracy and precision of <1%. In this thesis, we are only using the results on methane (CH_4) data from CTD measurements, which were provided by Dr. Doug Connelly from NOCS.

An Eh redox potential sensor is an electrochemical device comparing the voltage difference between the seawater against a silver–silver (Ag-AgCl) chloride reference electrode in a potassium chloride (KCl) solution. The Eh sensor developed by Ko-ichi Nakamura (National Institute of Advanced Industrial Science and Technology, Tsukuba, Japan) (Henry et al., 2002; Baker et al., 2005), was used during Autosub 6000 dives (Figs. 5.9 and 5.10) to detect changes in the sea water geochemistry in terms of reduction potential. The Eh values presented in this thesis are in volts recorded by Seabird CTD on the Autosub 6000, which correspond to converted values of raw electrode output by the Eh transformer.

5.4 Results

5.4.1 Greater Sleipner Area

Fig. 5.16 illustrates the multibeam bathymetry data acquired in the Central North Sea during the *JC077* cruise. The depth values gently vary between 80-111 m throughout the survey area, deepening northwards.

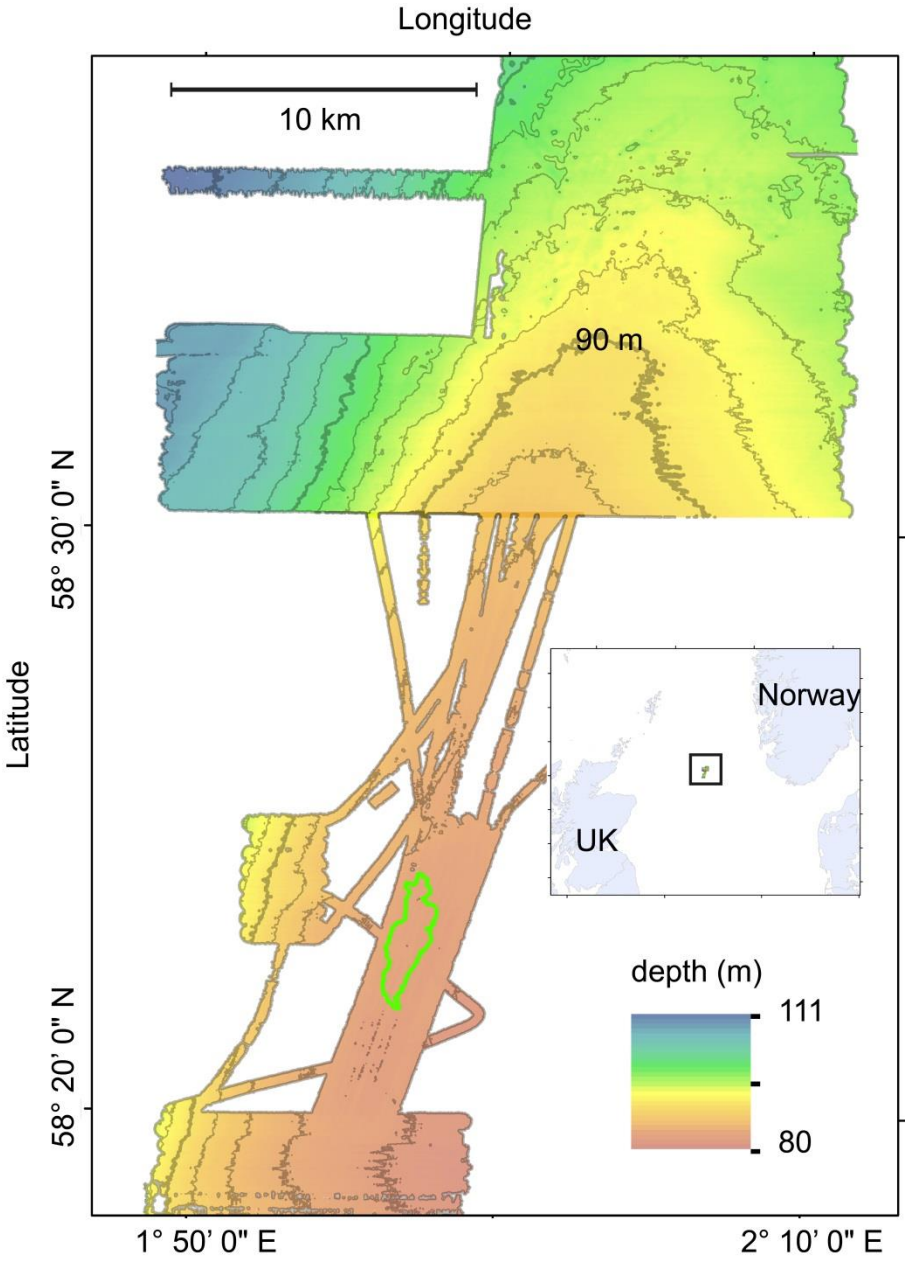

Figure 5.16 *Multibeam bathymetry data acquired during the JC077 cruise in the Central North Sea. See inset for the survey location. The spatial extent of the 2010 Sleipner CO_2 plume is superimposed on the bathymetry data (green polygon).*

Dissolved CH_4 concentrations from the CTD water column samples are illustrated in Fig. 5.17. CH_4 levels within the CO_2 Plume Area and Middle Area are within the range of 0-30 ppm. Hugin Fracture Area shows increased dissolved CH_4 concentrations compared to background levels, c. between 30-77.2 ppm.

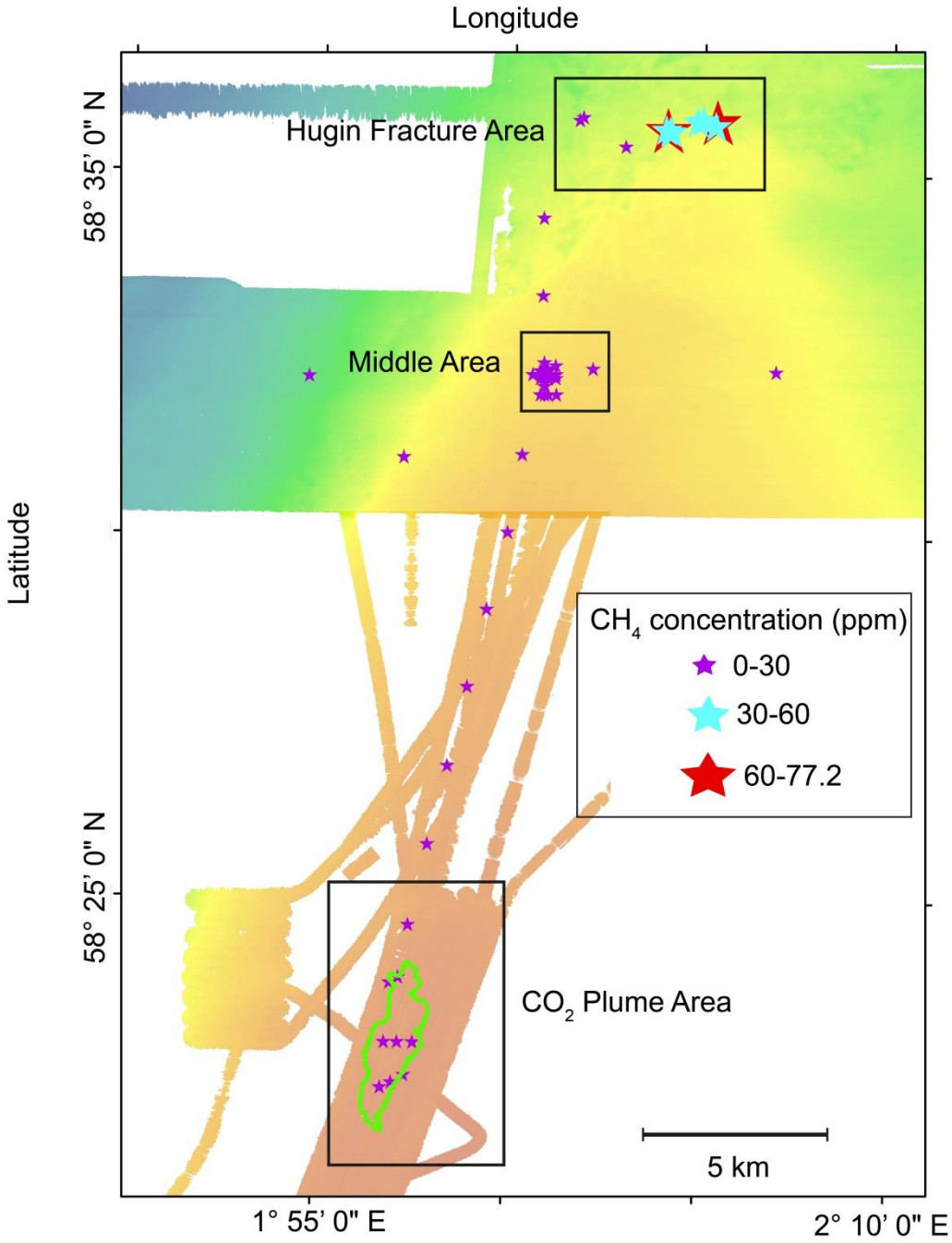

Figure 5.17 *Dissolved CH_4 concentrations from CTD samples in the Central North Sea. Hugin Fracture Area has increased CH_4 levels, c. between 30-77.2 ppm.*

5.4.2 CO_2 Plume Area and South of the Plume Area

The side-scan mosaics from the southern part of the total area investigated during the *JC077* cruise, including the CO_2 Plume Area (M65) and the South of the Plume Area (M59), are shown in Fig. 5.18.

Within the CO_2 Plume Area, two distinct backscatter patterns are clearly imaged on the side-scan data: low backscatter regions represented by shades of grey, and localized, high backscatter areas represented by white (Fig. 5.18a). In contrast, the South of the Plume Area is mainly dominated by low backscatter returns (Fig. 5.18b). In addition, some linear features oriented NE-SW are observed on the side-scan image within the CO_2 Plume Area (Fig. 5.18a).

Analysis of video photography, as well as observations during HyBIS Dives 130 and 131 across the CO_2 Plume Area (Table 5.2), indicate that low backscatter areas correspond to sandy seabed while high backscatter returns represent shell hashes of varying size deposited on the seafloor (Fig. 5.18a). Dark grey areas indicate dredge tracks and the NE-SW oriented linear features are seabed pipelines (Fig. 5.18a). There is no clear evidence of seabed fluid flow throughout these two areas, with the absence of bacterial mats, pockmarks, and bubbles (Fig. 5.18).

5.4.3 Middle Area

The side-scan mosaic of the Middle Area (M60) is given in Fig. 5.19. The seabed is mainly characterized by low backscatter returns, except a few areas with high backscatter responses (Fig. 5.19). Observations from four HyBIS dives (Table 5.2), as well as seabed photography within the Middle Area, indicate that low backscatter areas on the side-scan mosaic correspond to a sandy seabed, whereas high backscatter areas represent shell hashes on the seafloor (Fig. 5.19). Similar to the observations from the CO_2 Plume Area and South of the Plume Area, there is no evidence of seabed fluid flow activity at this site.

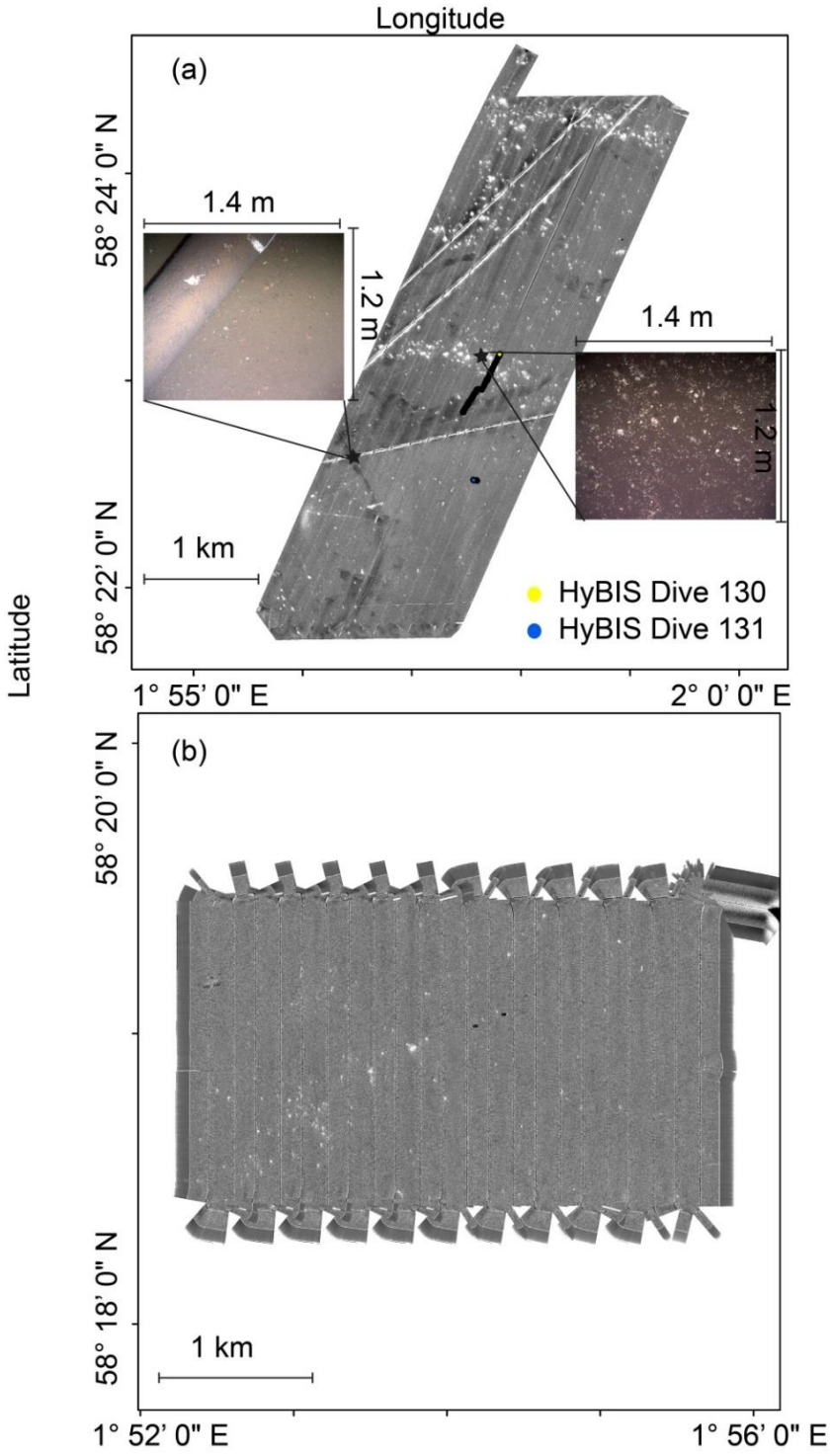

Figure 5.18 *Side-scan mosaics from the CO_2 Plume Area (Autosub 6000 Dive M65; flying altitude 12 m), and South of the Plume Area (Autosub 6000 Dive M59; flying altitude 12 m).* ***(a)*** *Two HyBIS dives are completed in the CO_2 Plume Area (Dives 130 and 131), as well as seabed photography (Autosub 6000 Dive M66; flying altitude 3 m)* ***(b)*** *Side-scan mosaic from the South of the Plume Area, showing a featureless seabed. There is no evidence of seabed fluid flow activity at both of these sites.*

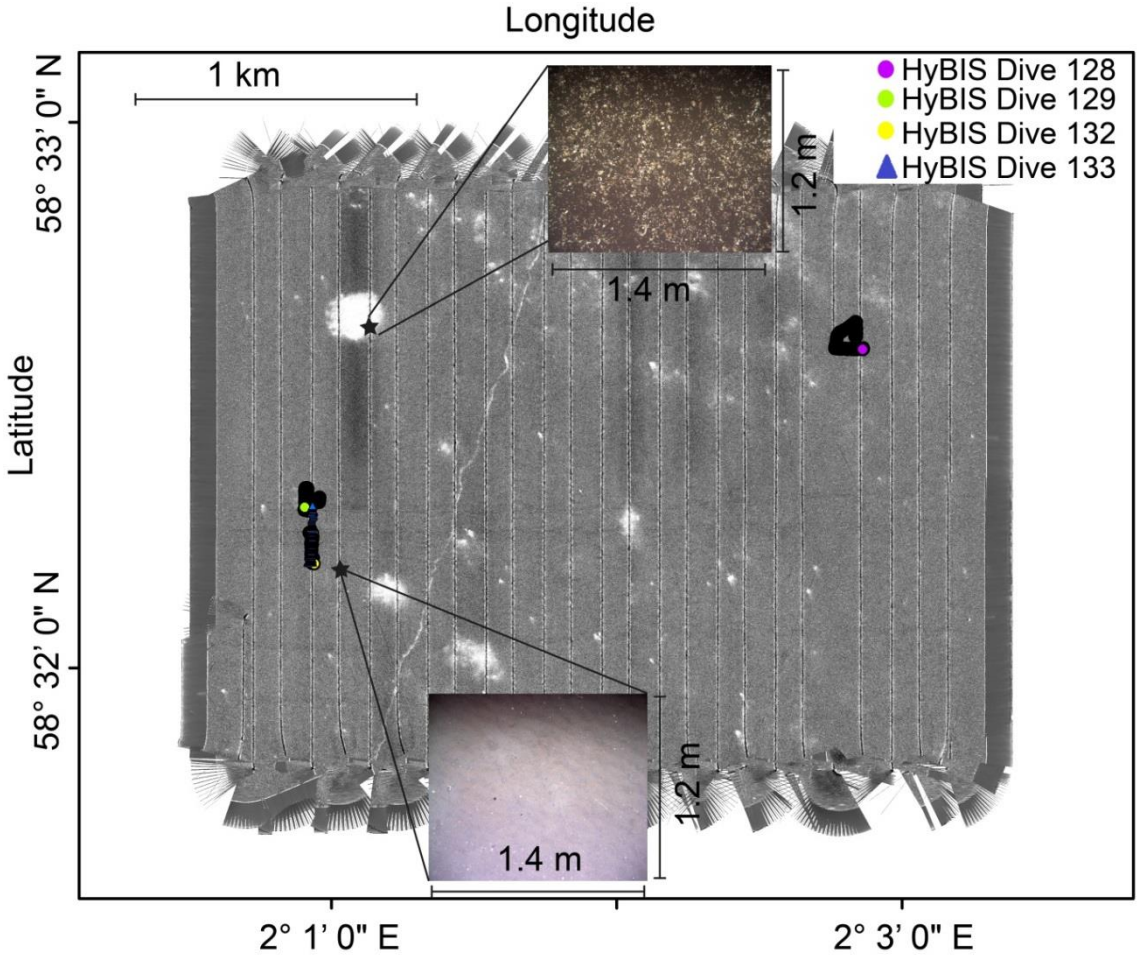

Figure 5.19 *Side-scan mosaic of the Middle Area (Autosub 6000 Dive M60; flying altitude 12 m). Four HyBIS dives are completed in this area (Dives 128, 129, 132, 133), as well as seabed photography (Autosub 6000 Dive M63; flying altitude 3 m). There is no evidence of seabed fluid flow activity at this site.*

5.4.4 Hugin Fracture Area

5.4.4.1 Surface

Side-scan mosaic of the Hugin Fracture Area, located at around 25 km N of the Sleipner CCS site, is shown on Figs. 5.20-5.22. The Hugin Fracture is located on the E of the side-scan mosaic, and appears as a sharp discontinuity on the seabed (Fig. 5.20). The fracture imaged on this side-scan data is around 1.6 km long, up to c. 5 m wide, and has a very complex surface geometry (Figs. 5.21 and 5.22). Eastwards, the Hugin Fracture is composed of two zig-zagging, small fault segments, oriented NE-SW, and imaged over c. 260 m (Segment A) (Figs. 5.21 and 5.22). These two faults segments are connected to each other via small fault bends in NW-SE direction (Figs. 5.21 and 5.22).

Apart from zig-zagging segments, ring structures are also present within the Segment A (Figs. 5.21 and 5.22). At the end of the Segment A, a more significant fault bend (the main fault bend) with NW-SE orientation, located 260-420 m from the E, connects the Segment A to the adjacent Segment B (Figs. 5.21 and 5.22). The Segment B is around 1.2 km long, has mainly a linear geometry oriented NE-SW; however small faults bends and step overs oriented NW-SE are also found along strike, resulting in eight zig-zagging fault segments (Figs. 5.21 and 5.22). Contrary to Segment A, Segment B is more discontinuous towards its end, thus a possible surficial fault trace is indicated on Fig. 5.21. The multiple segments observed along the Hugin Fracture, linked with fault bends and step overs, indicate en echelon fault geometry on the surface (Figs. 5.21 and 5.22). Local branching fault segments are also observed throughout the Hugin Fracture (Figs. 5.21 and 5.22). A horizontal westward displacement of c. 15 m along the main fault bend is detected from the side-scan mosaic (Figs. 5.21 and 5.22).

Multibeam bathymetry data superimposed on the side-scan mosaic of the Hugin Fracture Area is illustrated in Fig. 5.23. The depth values along the Hugin Fracture vary between 93-94 m (Fig. 5.23). The Segment B has a shallower bathymetry compared to the Segment A (Fig. 5.23). Along the main fault bend a small depression zone is observed to the N (Fig. 5.23).

Analysis of Autosub 6000 pictures, as well as observations from HyBIS dives (Table 5.2), show that the seabed within the Hugin Fracture Area is mainly composed of sandy sediments (low backscatter regions) with some localized zones of shell hashes (high backscatter areas) (Fig. 5.24a and 5.24b). In addition, evidence of fluid flow were identified along the Hugin Fracture, and in the vicinity of the well 16/4-2 (Fig. 5.24c-j). At the well 16/4-2 site, video photography revealed clear evidence of active fluid flow, including bacterial mats, reduced dark sediment patches and water column bubbles (Fig. 5.24c; HyBIS Dives 125 and 127). Regarding the Hugin Fracture, seabed fluid flow evidence were identified throughout this seabed discontinuity, including bacterial mats and reduced dark sediment patches, whereas no bubbles were imaged within the water column above the fracture (Fig 5.24d-j; HyBIS Dives 124 and 134). In addition, the seabed fluid flow activity was found to be continuous throughout the fracture, along the Segments A and B, as well as the main fault bend (Fig 5.24d-j; HyBIS Dives 124 and 134). Apart from along the Hugin Fracture and the well 16/4-2, there is no visual evidence of fluid flow activity elsewhere in this area.

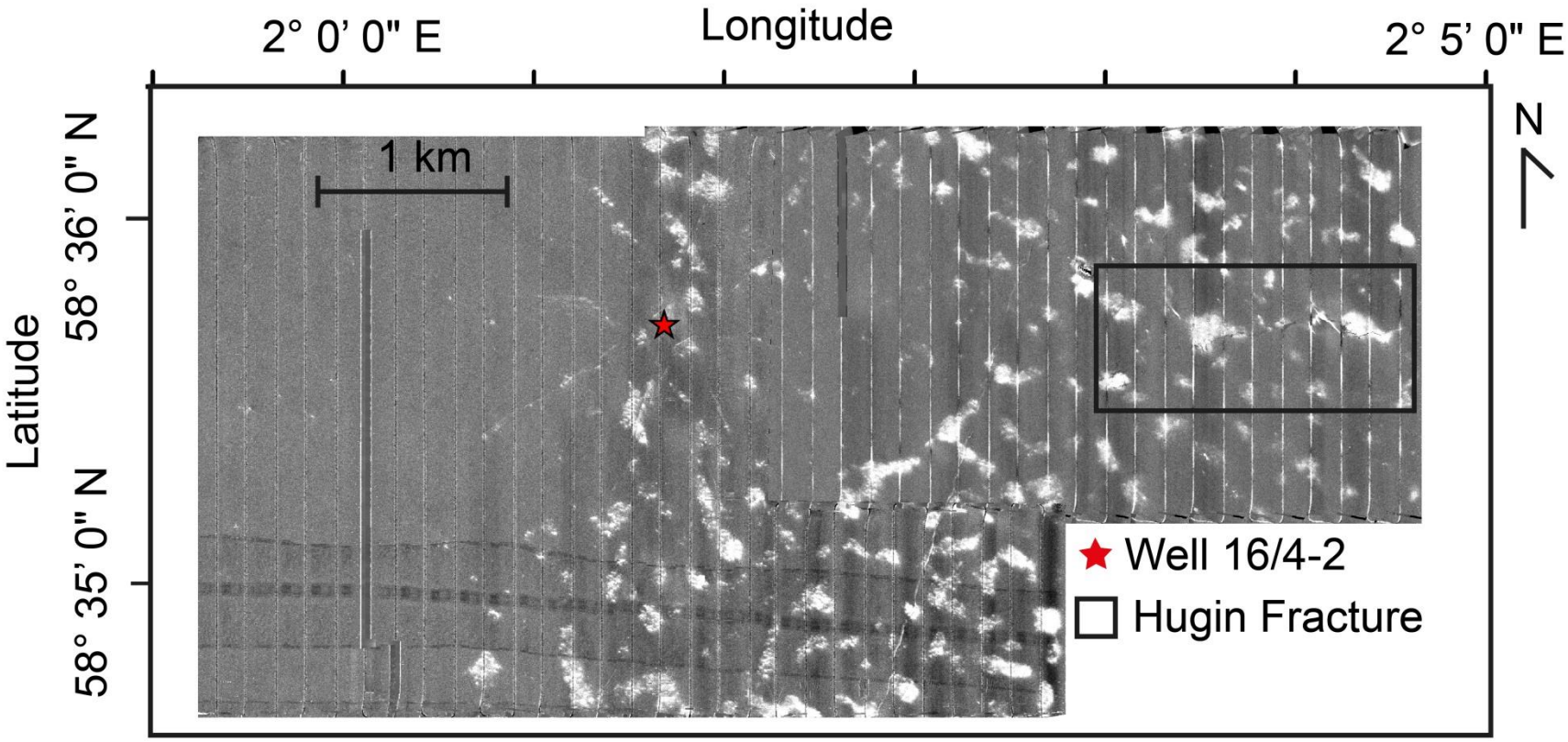

Figure 5.20 *Side-scan mosaic of the overall Hugin Fracture Area (Autosub 6000 Dives M61 and M64; flying altitude 12 m). The Hugin Fracture is imaged as a sharp discontinuity on the seabed within the black rectangle area. The abandoned well 16/4-2 site is also indicated by red star.*

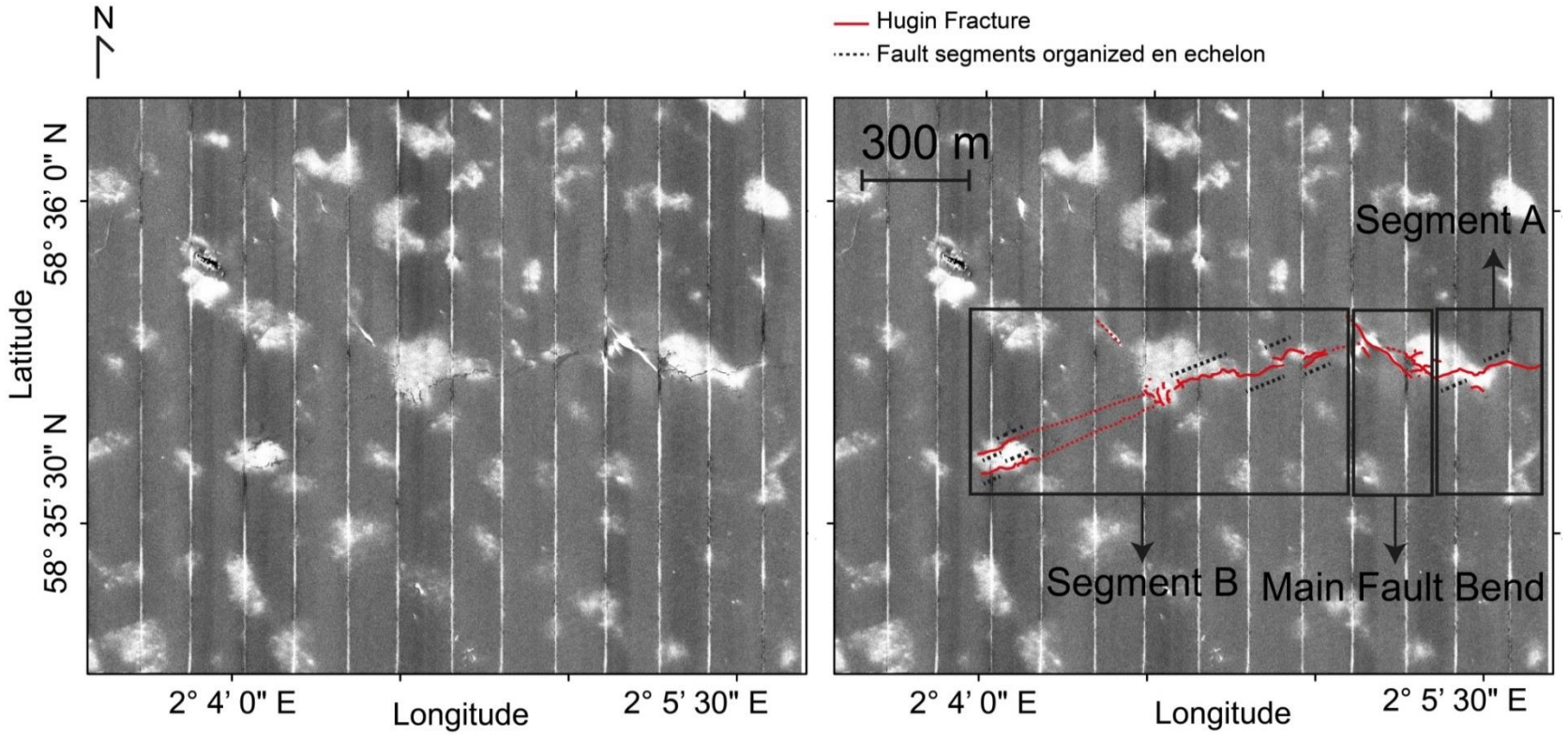

Figure 5.21 *Hugin Fracture surface fault geometry (Autosub 6000 Dive M61; flying altitude 12 m). The fracture is c. 1.6 km long, up to 5 m wide, and is formed by two main segments. The Segment A is composed of two small segments oriented NE-SW. The Segment B includes eight small fault segments oriented NE-SW. The Segment B is connected to the Segment A by a main fault bend. The fault trace which can be directly traced on the seabed is indicated by solid red line. A possible fault extent along the Segment B is indicated by dotted red lines. The dashed black lines represent the orientation of the small fault segments within the main Segments A and B.*

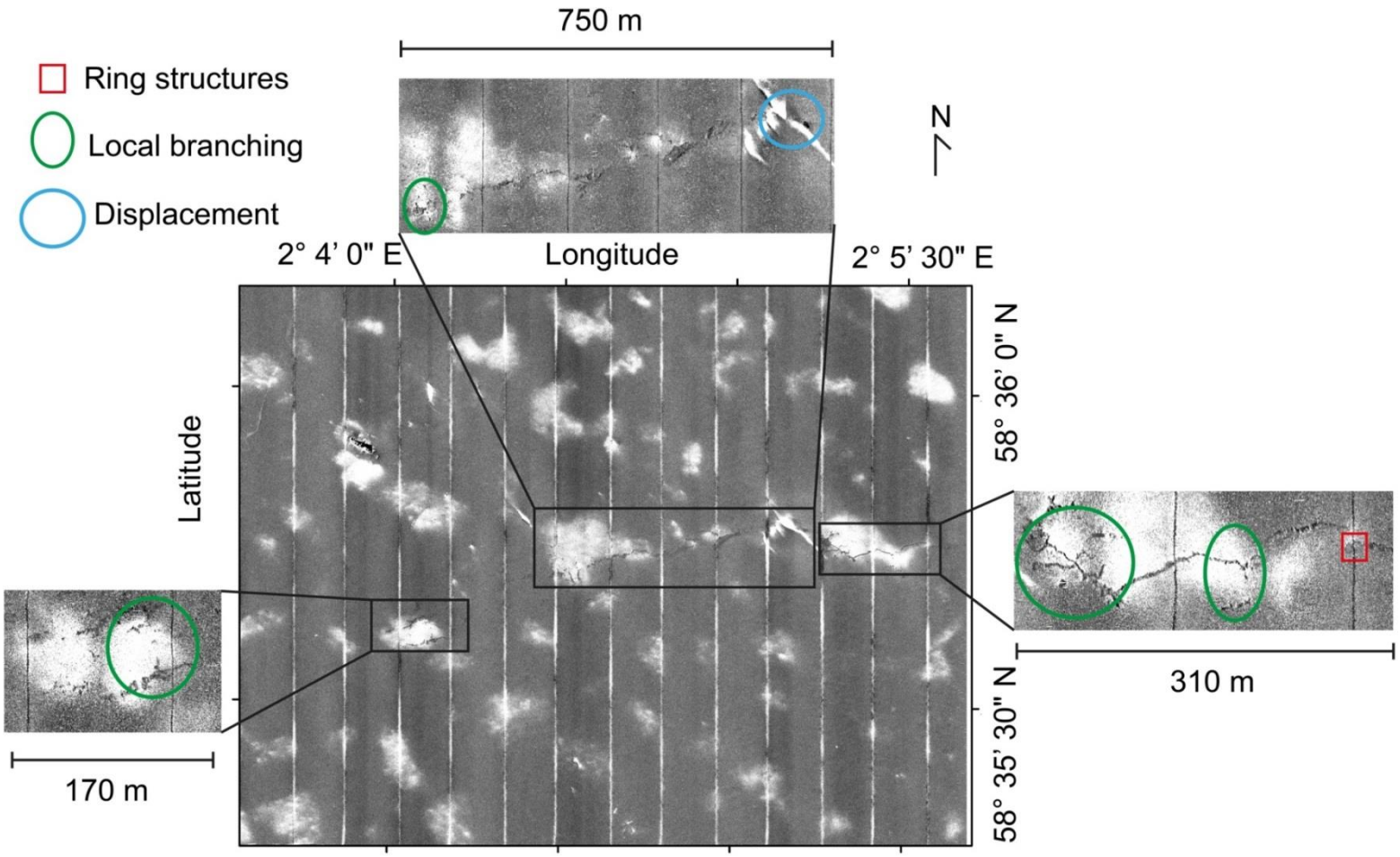

Figure 5.22 *Enlarged side-scan sonar images of the Hugin Fracture (Autosub 6000 Dive M62; flying altitude 3m). Zig-zagging fault segments, local fault branches (green circle), ring structures (red rectangle), and horizontal displacement along the main fault bend (blue circle) are identified.*

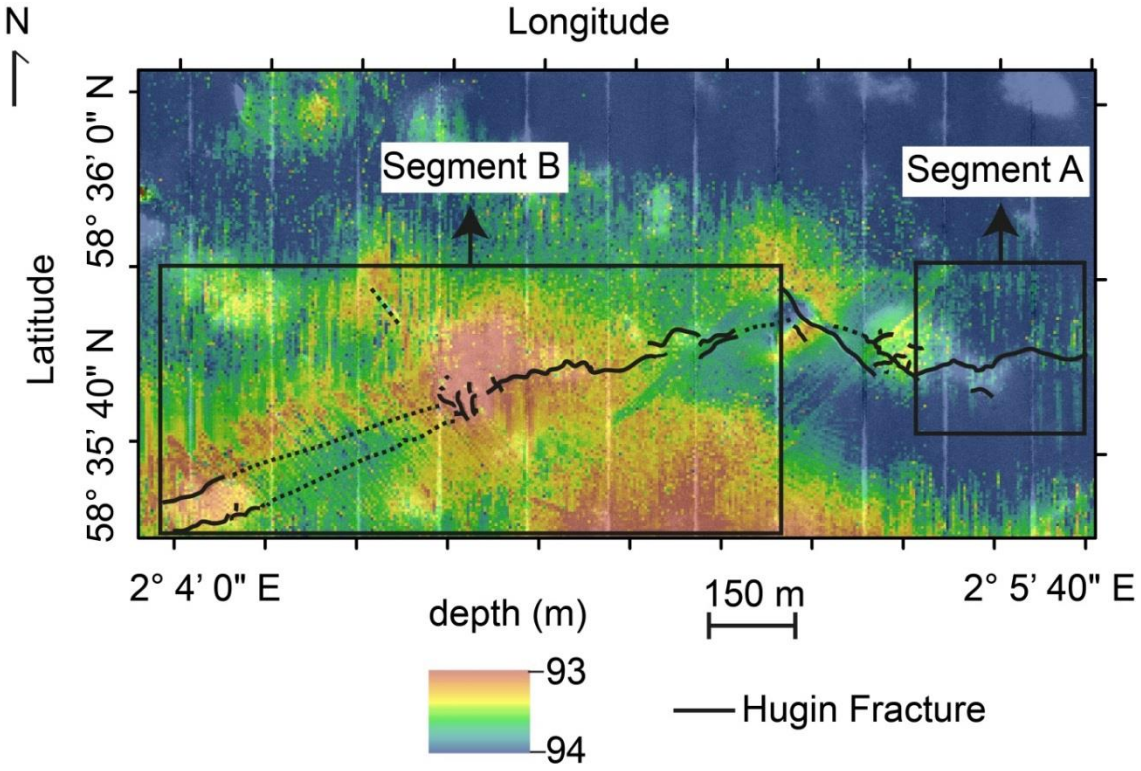

Figure 5.23 *Multibeam bathymetry data superimposed on the side-scan mosaic of the Hugin Fracture Area (Autosub 6000 Dive M61; flying altitude 12 m). The depth values along the Hugin Fracture range between 93 m and 94 m. The outline of the fracture is given with solid black lines. Possible fault extent on the seabed along the Segment B is indicated by black dotted lines.*

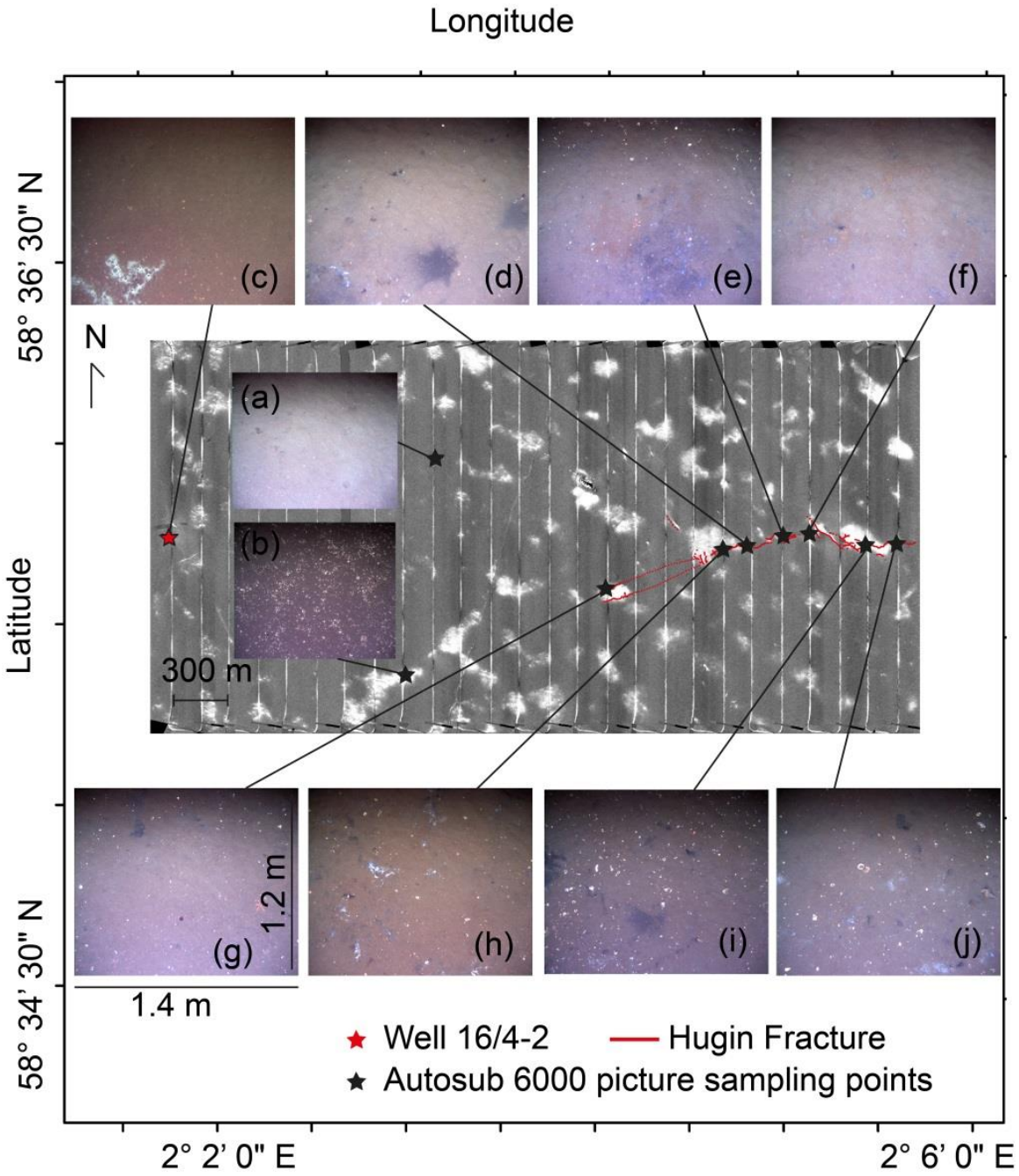

Figure 5.24 *Autosub 600 pictures acquired within the Hugin Fracture Area (Autosub 6000 Dive M62; flying altitude 3 m). The seabed is mainly composed of* ***(a)*** *sandy sediments, and* ***(b)*** *local shell hashes.* ***(c-j)*** *There is an increased fluid flow activity along the Hugin Fracture and the well 16/4-2, illustrated by bacterial mats and reduced dark sediments on the seabed, as well as water column bubbles.*

An Eh sensor mounted on Autosub 6000 during M61 detected changes in seawater geochemistry within the Hugin Fracture Area (Koichi Nakamura, pers. comm.) (Fig. 5.25). A rapid drop of Eh values occurred when the electrodes encountered reduced fluids rising from the seabed, followed by a longer logarithmic

recovery (Fig. 5.25b). The spatial extent of the areas where Eh reductions are identified is given in Fig. 5.25c. These Eh anomalies are found to be along, and in the vicinity of the Hugin Fracture, whereas Eh values remained relatively constant within the rest of the investigated areas (Fig. 5.25).

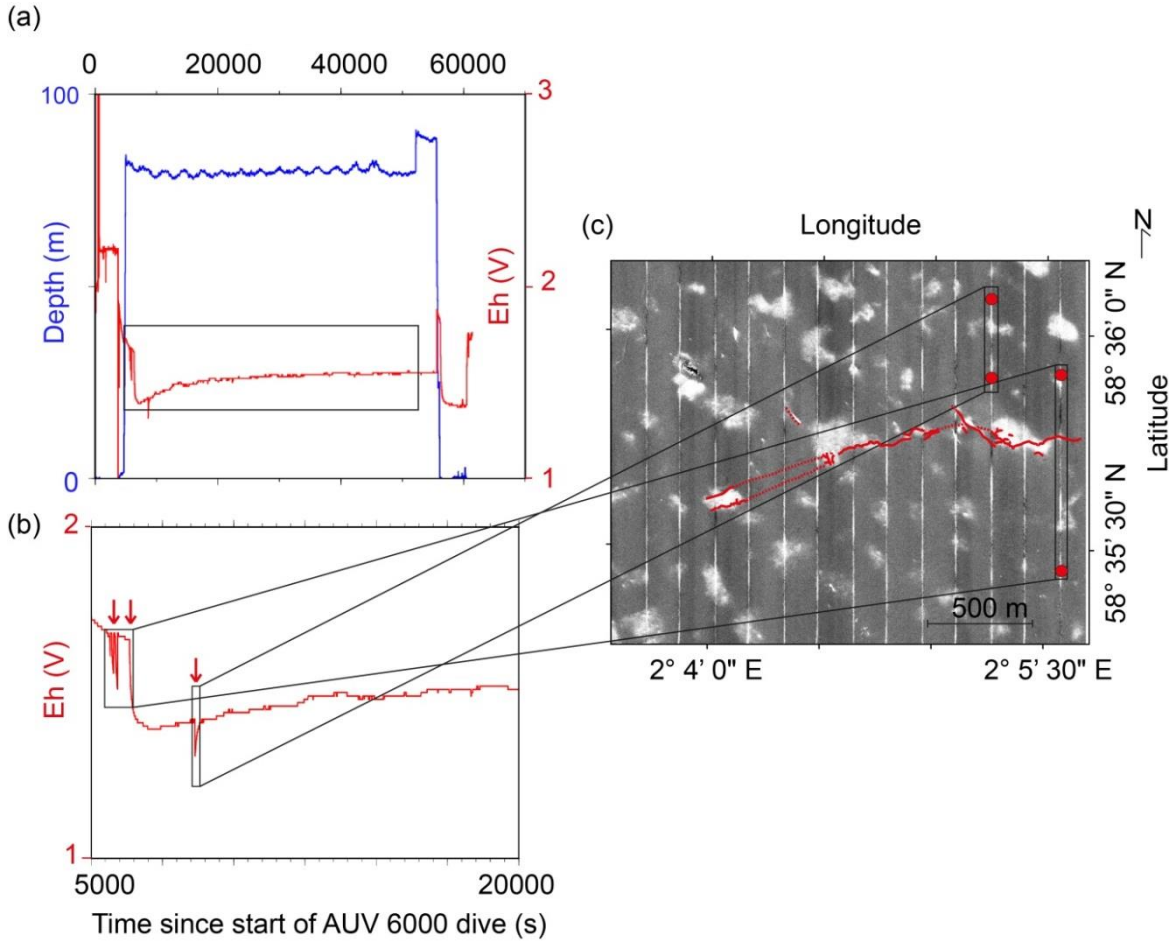

Figure 5.25 *Results from Eh sensor mounted on Autosub 6000 during the JC077 cruise.* ***(a)*** *The variation in Eh (in V, red line) and depth of Autosub (blue line) during the M61 Dive. The black rectangle indicates the Eh values of interest following the stabilization of depth.* ***(b)*** *Eh sudden drops (red arrows) recorded during M61 Dive. Note the steep drop of the Eh values when electrodes encountered reduced fluids.* ***(c)*** *The spatial location of the areas corresponding to Eh anomalies.*

5.4.4.2 Subsurface

2D seismic reflection data were analysed to better characterize the Hugin Fracture, including, fault geometry, displacement, spatial extent, and associated fluid flow activity, as well as the surrounding geology. The subsurface is imaged down to 6 ms (c. 5 m assuming V_p= 1500 m/s) on seismic reflection (Chirp) data, and to 80 ms (c. 60 m assuming V_p= 1500 m/s) on TOPAS seismic reflection data (Figs. 5.26 and 5.27).

Within the seismic reflection data, several stratigraphic units can be identified (Figs. 5.26 and 5.27; Table 5.4). The first reflector imaged is the seabed, being a continuous reflector separating the water column above, from the sediment package beneath (Figs. 5.26 and 5.27; Table 5.4). The sediment package just beneath the seabed, referred to as Unit A, represents internally continuous, sub-parallel reflectors (Figs. 5.26 and 5.27; Table 5.4). The stratigraphic unit below Unit A, referred to as Unit B, is located c. 1-1.5 ms below the seabed, and has sub-parallel reflectors with high amplitude seismic reflectivity (Figs. 5.26 and 5.27; Table 5.4). The seismic horizon separating Unit A from Unit B is referred to as R1 (Figs. 5.26 and 5.27; Table 5.4). The Unit B is imaged down to c. 2-3 ms below the seabed (Figs. 5.26 and 5.27; Table 5.4). Below the Unit B, a sediment package with internally continuous, sub-parallel reflectors is detected (Figs. 5.26 and 5.27; Table 5.4). This unit, referred to as Unit C, represents folding between 6-8 ms below the seabed (Figs. 5.26 and 5.27; Table 5.4). The seismic boundary between the Unit B and Unit C is referred as R2 (Figs. 5.26 and 5.27; Table 5.4). The seismic imaging is limited to within the topmost part of Unit C on Chirp dataset (Fig. 5.27). On TOPAS seismic reflection dataset, the Unit C is imaged down to 80 ms below the seabed (Fig. 5.26; Table 5.4).

On Chirp and TOPAS seismic reflection data, the Hugin Fracture appears as a sharp, sub-vertical discontinuity, offsetting the near-surface sediments. Analysis of TOPAS seismic reflection data suggest that the fracture can be traced down to c. 80 ms (60 m assuming V_p=1500 m/s) below the seabed (Fig. 5.26). The maximum displacement along the fracture was found to be quite small, on the order of 30 cm (Figs. 5.26 and 5.27). Following the identification of the Hugin Fracture from seismic reflection data, the spatial extent of the fracture is mapped (Fig. 5.28). Although being very similar to the fault trace determined from side-scan mosaics (Figs. 5.20-5.22), fault detection over some areas is significantly improved after fault analysis on seismic

reflection data, particularly along Segment B (Fig. 5.28). Apart from the segments and fault bends detected on the side-scan data (Figs. 5.20-5.22), an area composed of small fault segments has also been identified to the NW of the Hugin Fracture (Fig. 5.28). Hence, these fault segments will be referred to as individual faults (Fig. 5.28). The direction of fault throw is indicated on Fig. 5.28, where the downthrow side along the segment A is mainly to the S and the downthrow side along the segment B is predominantly to the N (Fig. 5.28).

Seismic stratigraphic boundaries	Depth (TWT)	Description
Seabed	0 ms	A seismic reflector separating the water column from the Unit A. The Unit A is composed of sub-parallel seismic reflectors.
R1	1-1.5 ms	A seismic reflector separating the Unit A from the Unit B. The Unit B has internally sub-parallel reflectors and high amplitude reflectivity. Unit B is imaged down to c. 2-3 ms below the seabed.
R2	6 ms	A seismic reflector separating Units B and C. Unit C is composed of sub-parallel reflectors. Reflector folding is observed between 6-8 ms below the seabed within the Unit C. Seismic imaging is limited to the topmost part of Unit C on Chirp data, while the same unit is imaged down to c. 80 ms below the seabed on TOPAS seismic reflection data.

Table 5.4 *Summary of seismic reflectors and sediment packages imaged on the seismic reflection data. The seismic imaging is limited to c. 6 ms below the seabed on Chirp data, and down to 80 ms below the seabed on TOPAS seismic reflection data.*

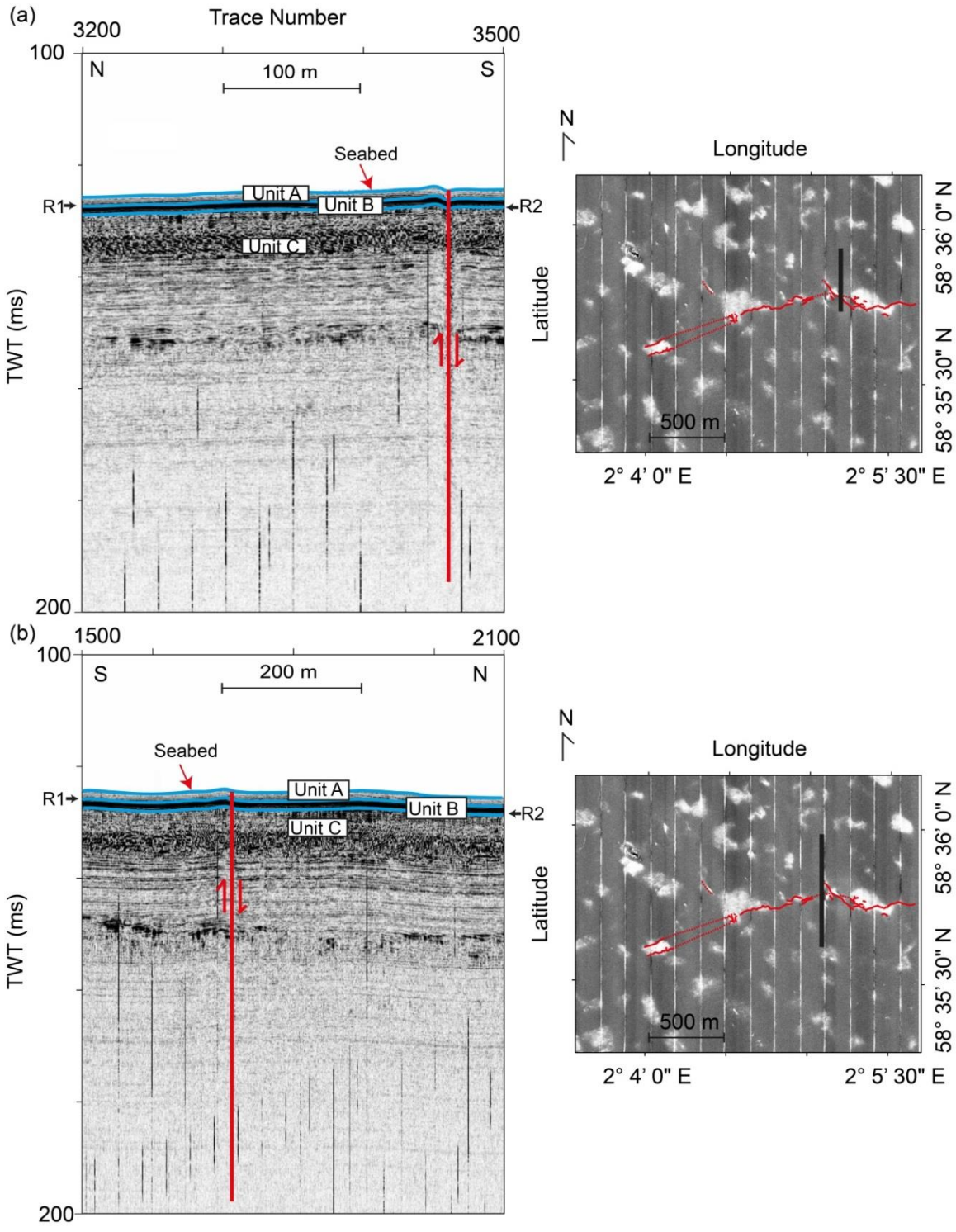

Figure 5.26 *TOPAS seismic reflection data analysis.* ***(a)*** *and* ***(b)*** *Examples from TOPAS 2D seismic reflection dataset. The Hugin Fracture (red line) can be traced down to 80 ms below the seabed. The location of the seismic data (solid black line), and the surficial fault trace (solid red line) detected on the side-scan data are given. Displacement along the fault, as well as geological units imaged are also indicated.*

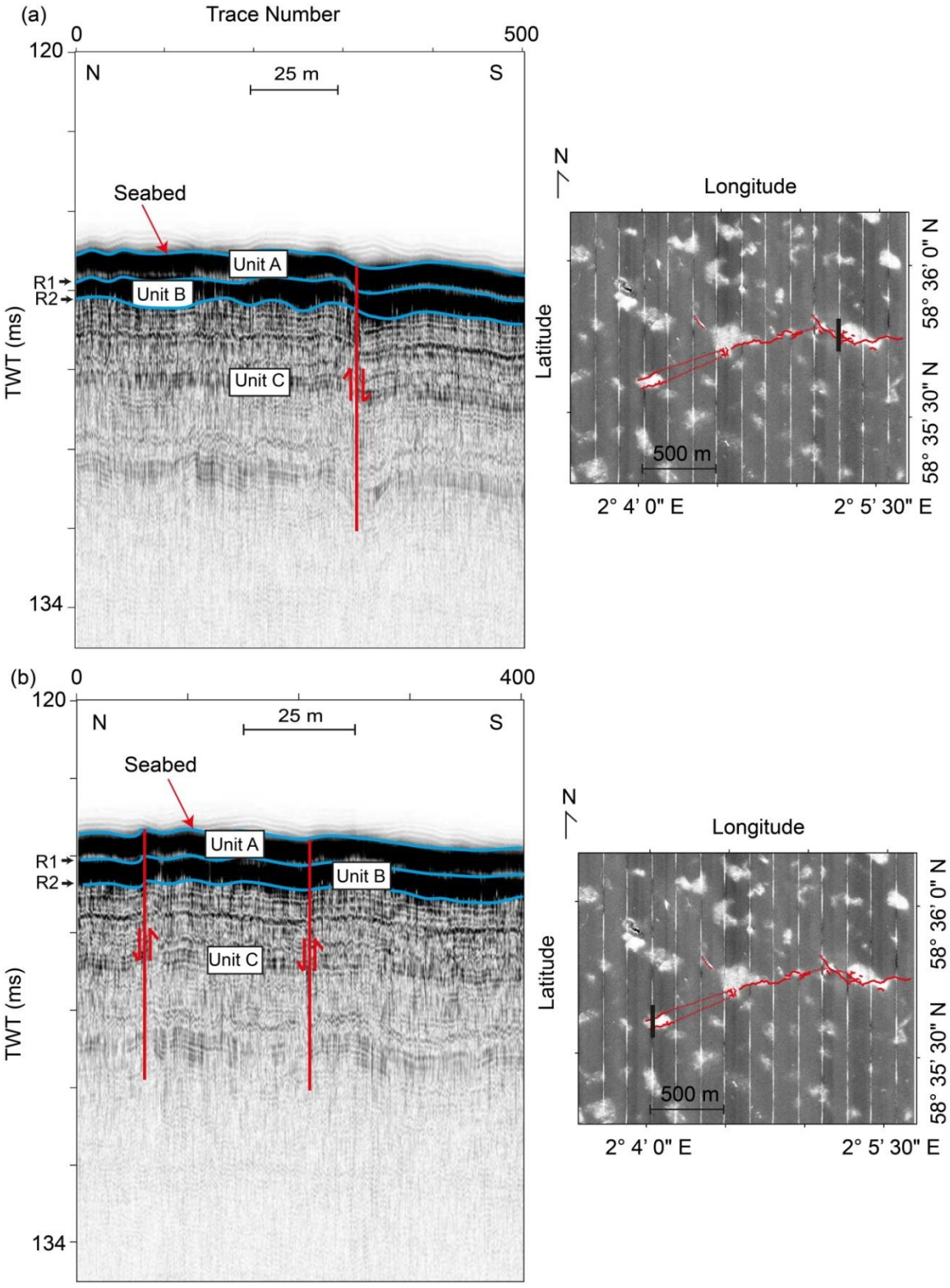

Figure 5.27 *Seismic reflection (Chirp) data analysis.* ***(a)*** *and* ***(b)*** *Examples from 2D Chirp dataset. The Hugin Fracture can be traced down to 6 ms below the seabed. The location of the seismic data (solid black line), and the surficial fault trace (solid red line) detected on the side-scan data are given. The displacement along the fault, as well as the geological units imaged are also indicated.*

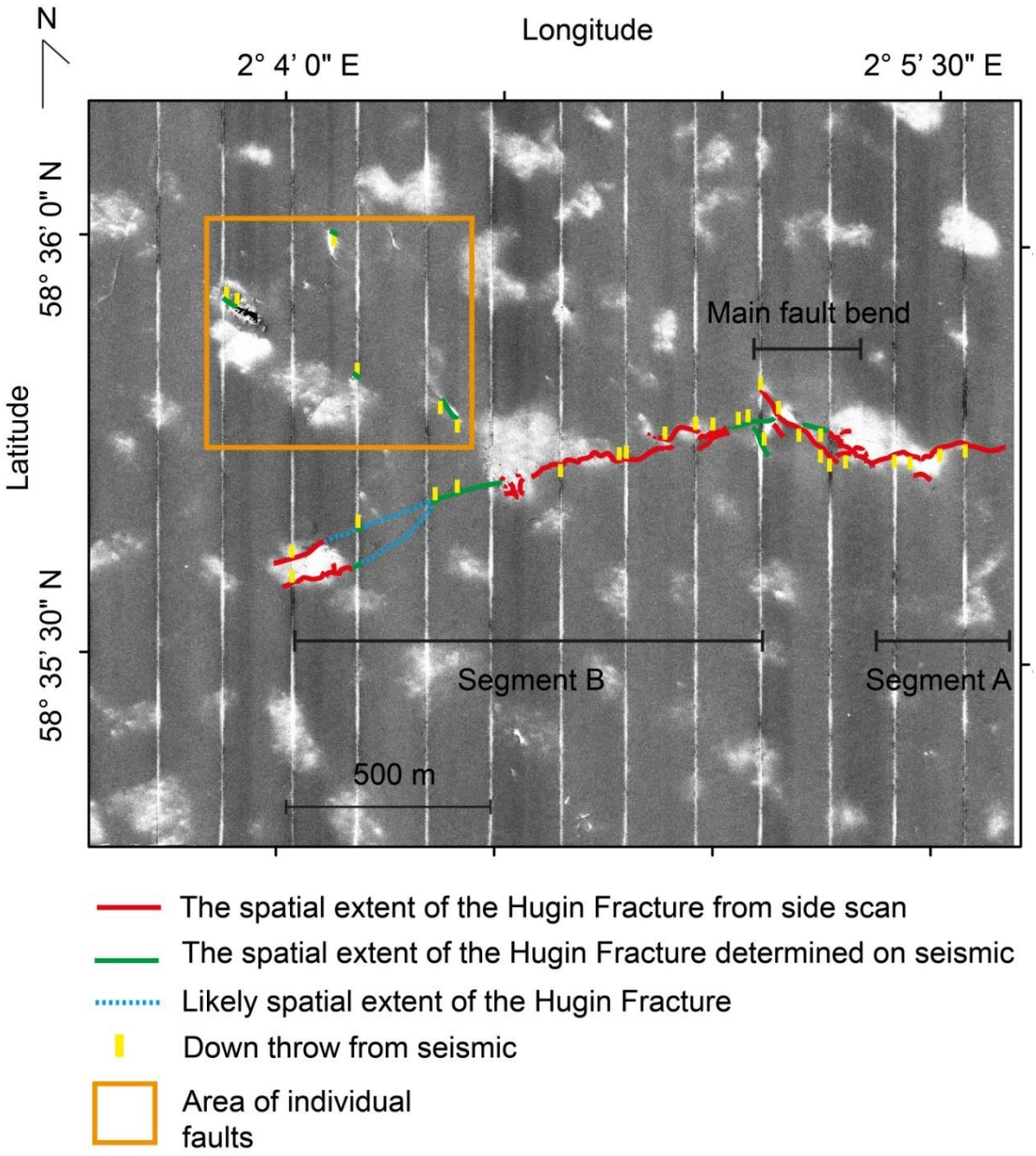

Figure 5.28 *The spatial extent of the Hugin Fracture improved after seismic data analysis. Solid red line indicates the spatial extent of the Hugin Fracture from the analysis of side-scan data. Solid green lines represent the spatial extent of the Hugin Fracture determined after seismic reflection data analysis. Dotted blue lines indicate the likely spatial extent of the fracture along Segment B. Note that to the NW of the Hugin Fracture, an area of individual faults has been detected on seismic data (orange rectangle). The fault throw direction is indicated by solid yellow lines.*

Analysis of TOPAS and Chirp seismic reflection data reveals high amplitude seismic anomalies within the overburden, as well as acoustic anomalies within the water column in the Hugin Fracture Area (Figs. 5.29-5.31). On TOPAS seismic reflection data, the enhanced reflectivity within the overburden occurs down to 10 ms (c. 7.5 m assuming V_p=1500 m/s) below the seabed, located to the NW and S of the Hugin Fracture (Fig. 5.29). On Chirp seismic reflection data, seismic amplitude anomalies are within 1-1.5 ms (c. 1 m assuming V_p=1500 m/s) below the seabed, located along the Hugin Fracture, as well as at the abandoned well site 16/4-2 (Figs. 5.30 and 5.31). Water column anomalies on TOPAS seismic reflection data occur to the NW of the Hugin Fracture, where individual faults have been previously mapped (Fig. 5.29a). Seabed fluid leakage was also detected during the *JC077* survey, where rising fluids at the well site 16/4-2 caused Autosub 6000 to take avoidance, with an increase of its altitude, shown by the apparent abrupt deepening of the seabed on the seismic reflection profile (Fig. 5.31).

Root Mean Square (RMS) seismic amplitude maps, superimposed on the side-scan data, illustrate seismic amplitudes down to 3 ms below the seabed on the Chirp seismic reflection data, and down to 15 ms on TOPAS seismic reflection data (Fig 5.32). The eastern part of the Hugin Fracture Area, including the Hugin Fracture, has been found to have slightly larger amplitudes compared to the western side of the survey area from the Chirp seismic reflection dataset (Fig. 5.32a). The largest seismic amplitude anomalies are found along the Hugin Fracture, as well as at the abandoned well site from Chirp data (Fig. 5.32a). The RMS seismic amplitude map from TOPAS seismic reflection data indicates that acoustic anomalies are located to the S and W of the Hugin Fracture, while remaining parts have similar RMS seismic amplitudes (Fig. 5.32b).

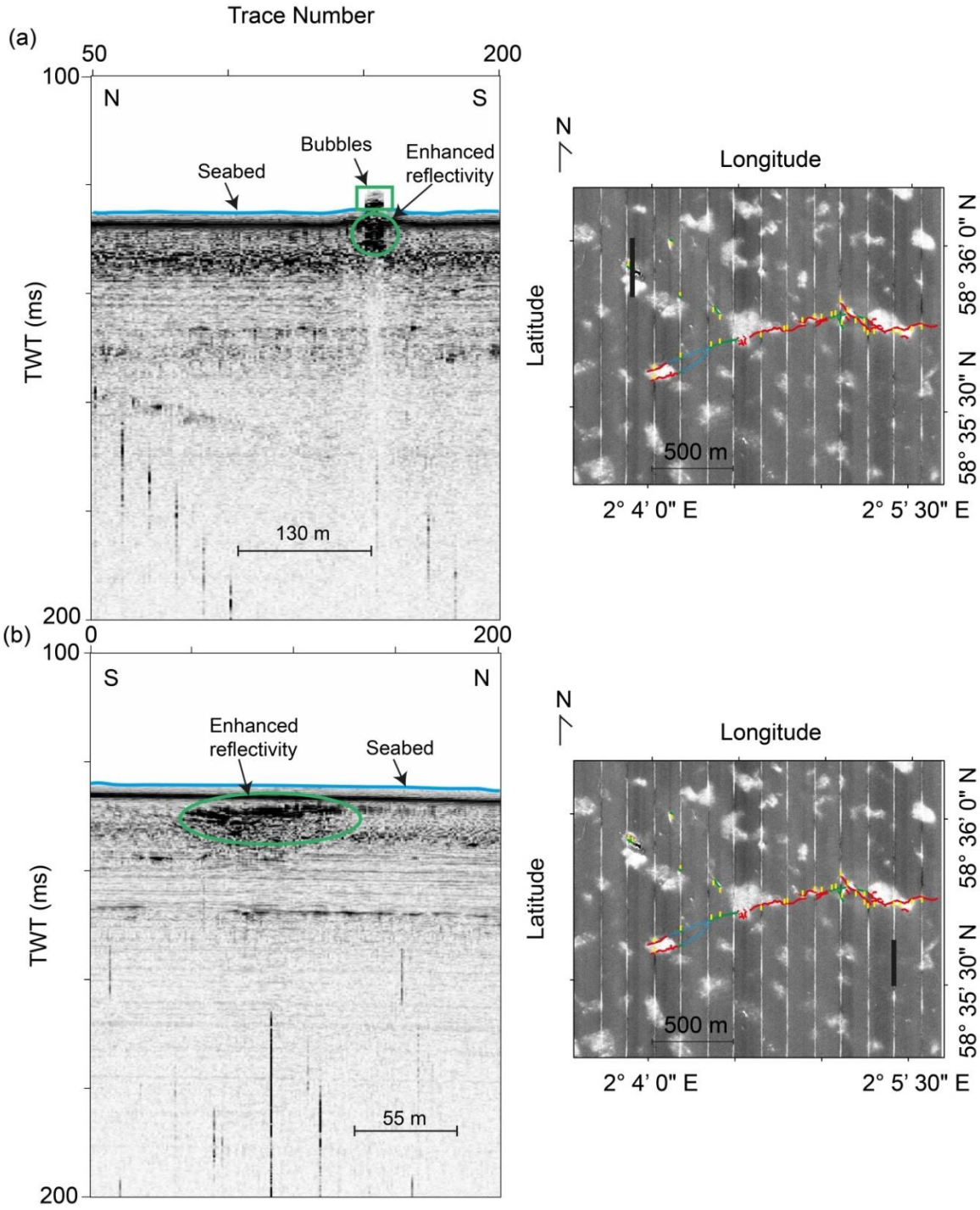

Figure 5.29 *Acoustic amplitude anomalies from TOPAS seismic reflection data.* ***(a)*** *A TOPAS seismic reflection profile, illustrating enhanced reflectivity within the overburden, as well as water column anomalies.* ***(b)*** *A TOPAS seismic reflection profile represents high amplitude seismic anomalies. Acoustic anomalies are indicated by green ellipses. The location of seismic profiles (solid black line), and the fault trace determined after seismic reflection data analysis are given, superimposed on side-scan mosaic of the Hugin Fracture Area.*

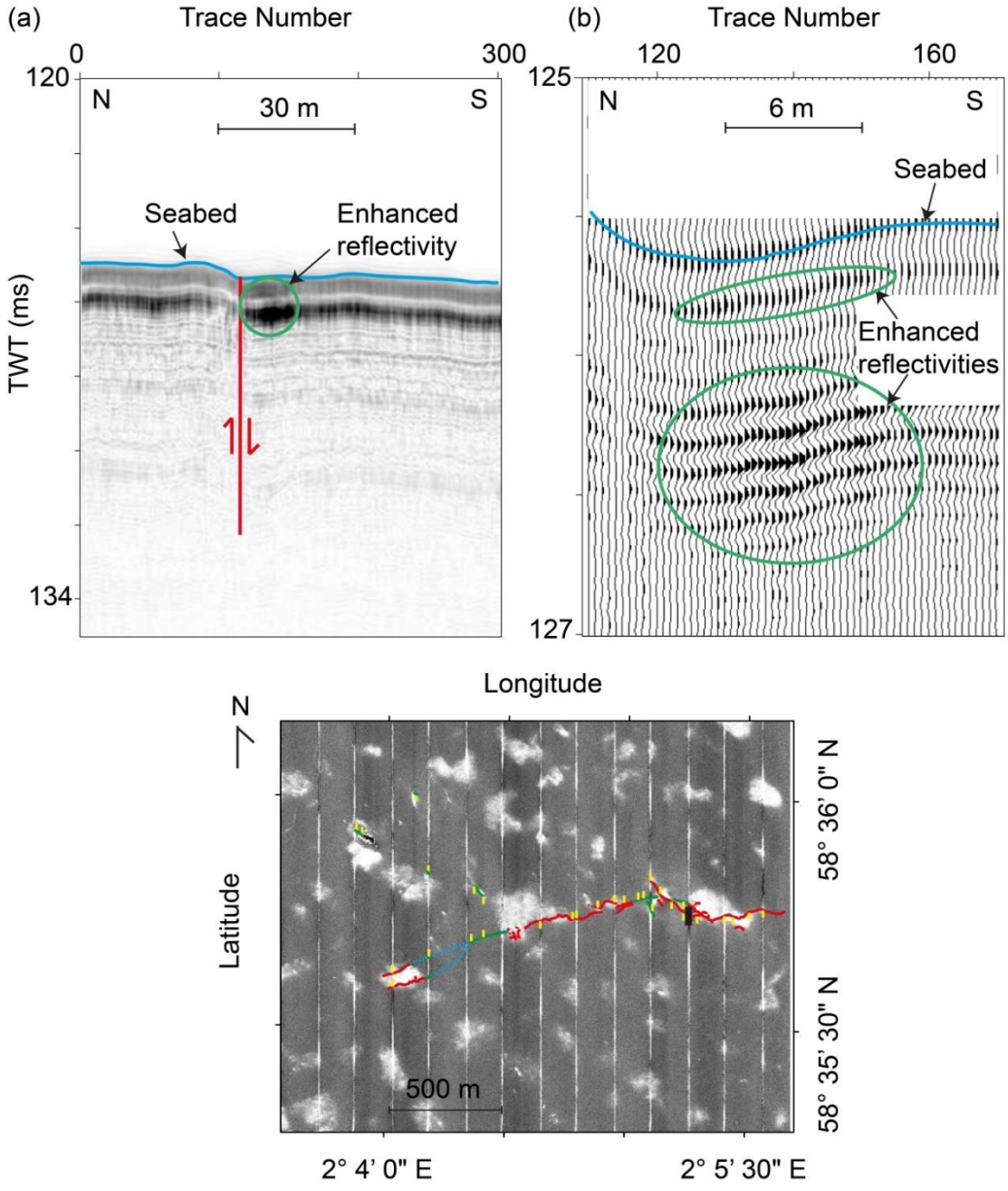

Figure 5.30 *Acoustic amplitude anomalies from seismic reflection (Chirp) data within the overburden.* ***(a)*** *A Chirp seismic reflection profile, located along the Hugin Fracture, illustrating enhanced reflectivity within the overburden.* ***(b)*** *Wiggle trace representation of the same seismic reflection profile. Acoustic anomalies are indicated by green ellipses. The location of the seismic reflection profile (solid black line), and the fault trace determined after seismic reflection data analysis are given, superimposed on side-scan mosaic of the Hugin Fracture Area.*

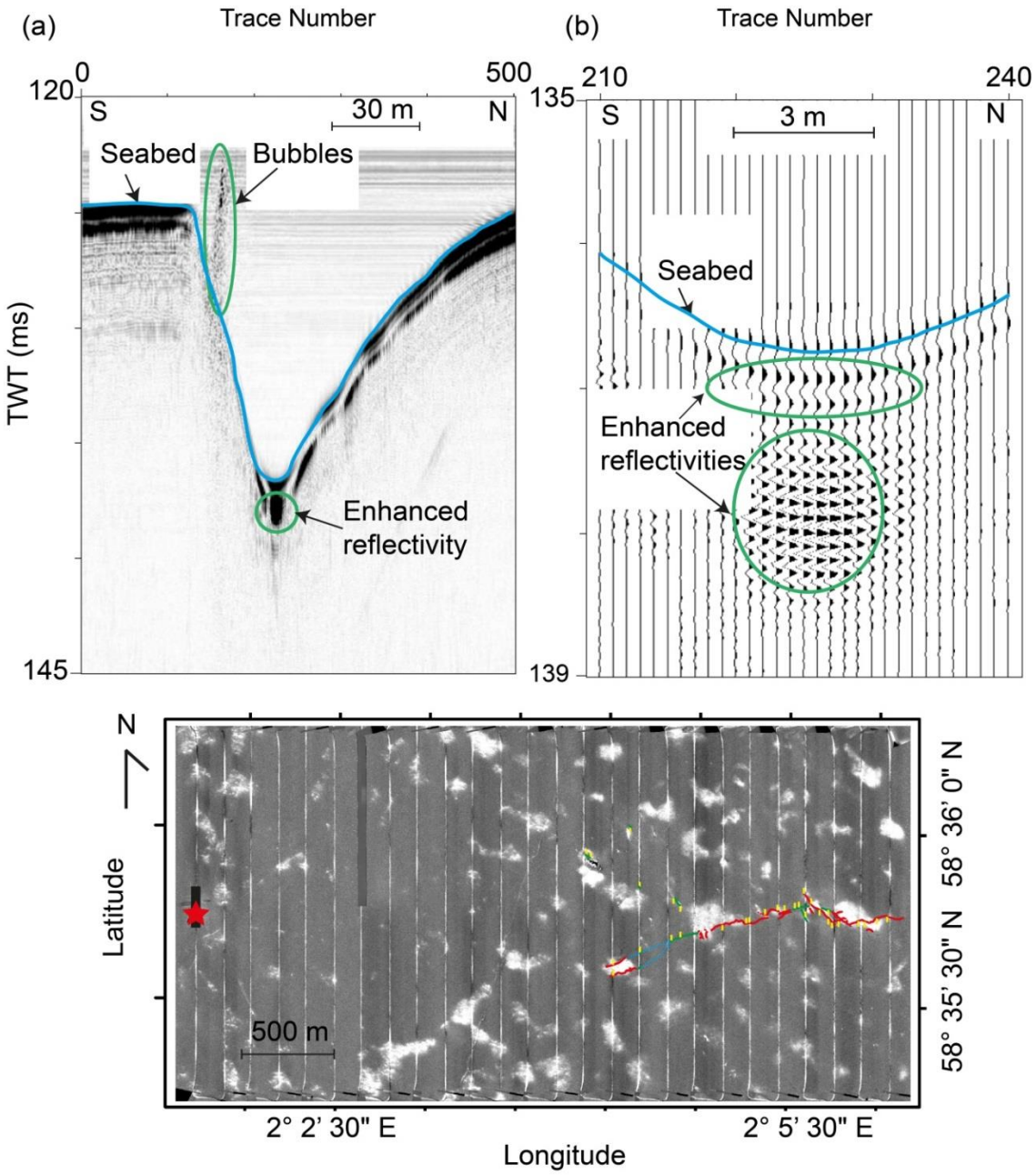

Figure 5.31 *Acoustic amplitude anomalies from seismic reflection (Chirp) data within the overburden and water column.* ***(a)*** *A Chirp seismic reflection profile, located at the abandoned well site 16/4-2 (red star), illustrating enhanced reflectivity within the overburden, as well as bubbles in the water column.* ***(b)*** *Wiggle trace representation of the same seismic reflection profile showing the enhanced reflectivity within the overburden. Acoustic anomalies are indicated by green ellipses. The location of the seismic profile (solid black line), and the fault trace determined after seismic reflection data analysis are given, superimposed on side-scan mosaic of the Hugin Fracture Area.*

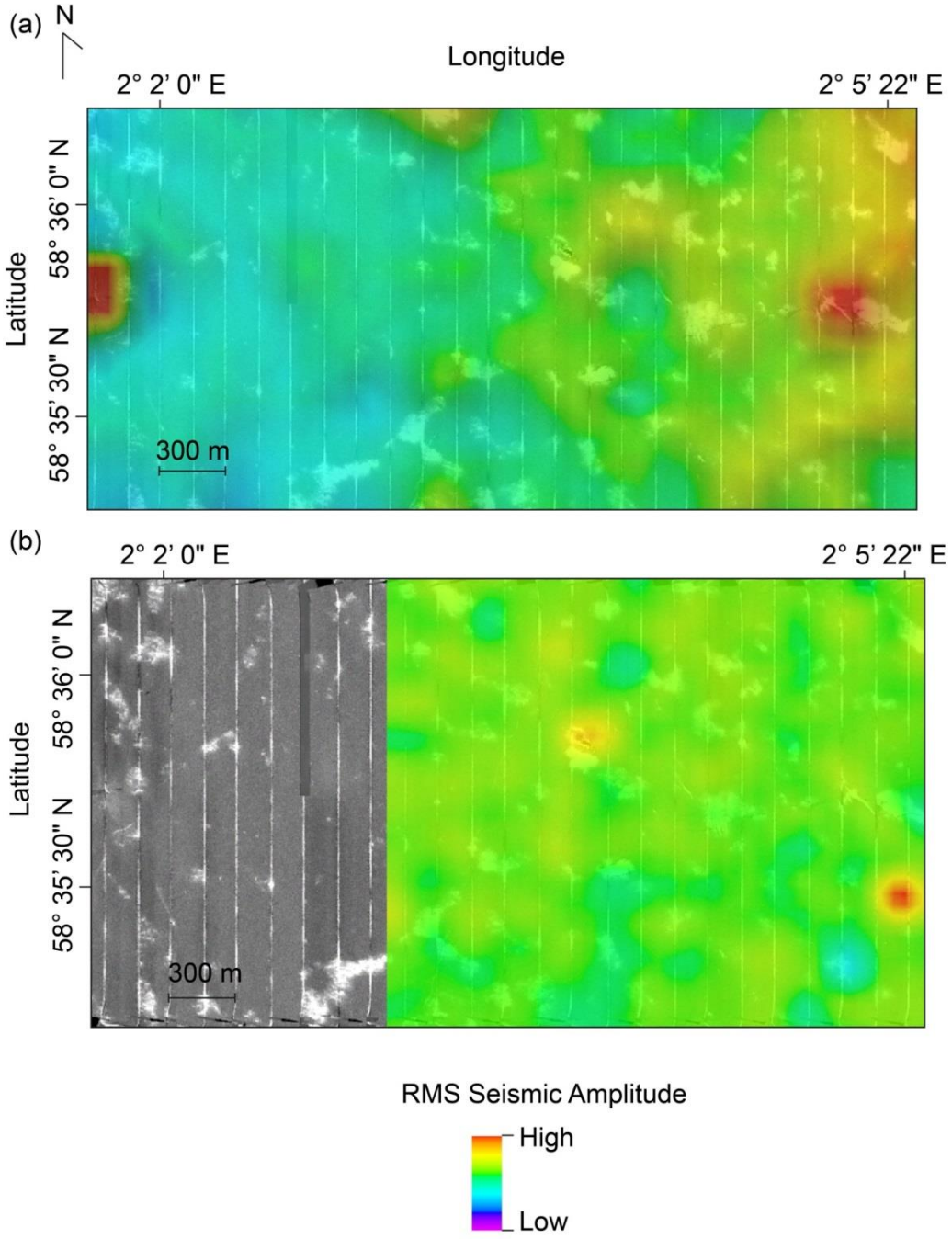

Figure 5.32 *RMS seismic amplitude anomalies from Chirp and TOPAS seismic reflection data within the Hugin Fracture Area.* ***(a)*** *RMS seismic amplitude map from Chirp seismic reflection data, from the seabed down to 3 ms beneath. Seismic amplitude anomalies are detected along the Hugin Fracture and at the abandoned well site.* ***(b)*** *RMS seismic amplitude map from TOPAS seismic reflection data, from the seabed down to 15 ms beneath. Enhanced reflectivity is to the S and W of the Hugin Fracture.*

5.4.4.3 Vibrocore data analysis

To better characterize the geochemical composition of fluids seeping from the Hugin Fracture, geochemical analyses of pore fluids were undertaken from vibrocores (Anna Lichtschlag, pers. comm) (Figs. 5.33 and 5.34; Table 4.3). In this thesis, only the results from VC 08 are presented, together with the reference core measurements (VC 01), as they were found to show the most interesting geochemical anomalies (Fig. 5.34).

Signs of low sulphate and high sulphide pore waters (Fig. 5.34a), were found in sediments sampled 25 m N of the Hugin Fracture (VC 08), compared to a reference core recovered 150 m S of the fracture (VC 01) (Fig. 5.34b). Contrary to the absence of sulphide along VC 01, geochemical sampling indicated a high variability in sulphide concentration overall the VC 08 (Fig. 5.34). The maximum sulphide concentration is found to be c. 6 mmol/l at c.1 m depth (Fig. 5.34a). Between c. 1-2 m, a gradual decrease in sulphide concentration, from 6 mmol/l to 1.2 mmol/l, is observed (Fig. 5.34a). From c. 2 m depth to the end of the VC 08, little variations in sulphide concentration are measured, with concentrations ranging between c. 1-4 mmol/l (Fig. 5.34a). The sulphate concentration along the reference core VC 01 is found to be constant, c. 28 mmol/l, whereas, sulphate concentration is significantly lower along VC 08, with the maximum concentration being 15 mmol/l (Fig. 5.34). The chloride (Cl) concentration is reduced by nearly 50% within sediments in the vicinity of the Hugin Fracture, compared to the reference site, from c. 500 mmol/l on VC 01 to c. 300 mmol/l on VC 08, indicating meltwater input (Fig. 5.34). Further, increased levels of CH_4, c. up to 800 mmol/l, were also measured on the top 50 cm of sediments along VC 08 (Fig. 5.34a), while no CH_4 was detected at the reference site (Fig. 5.34b).

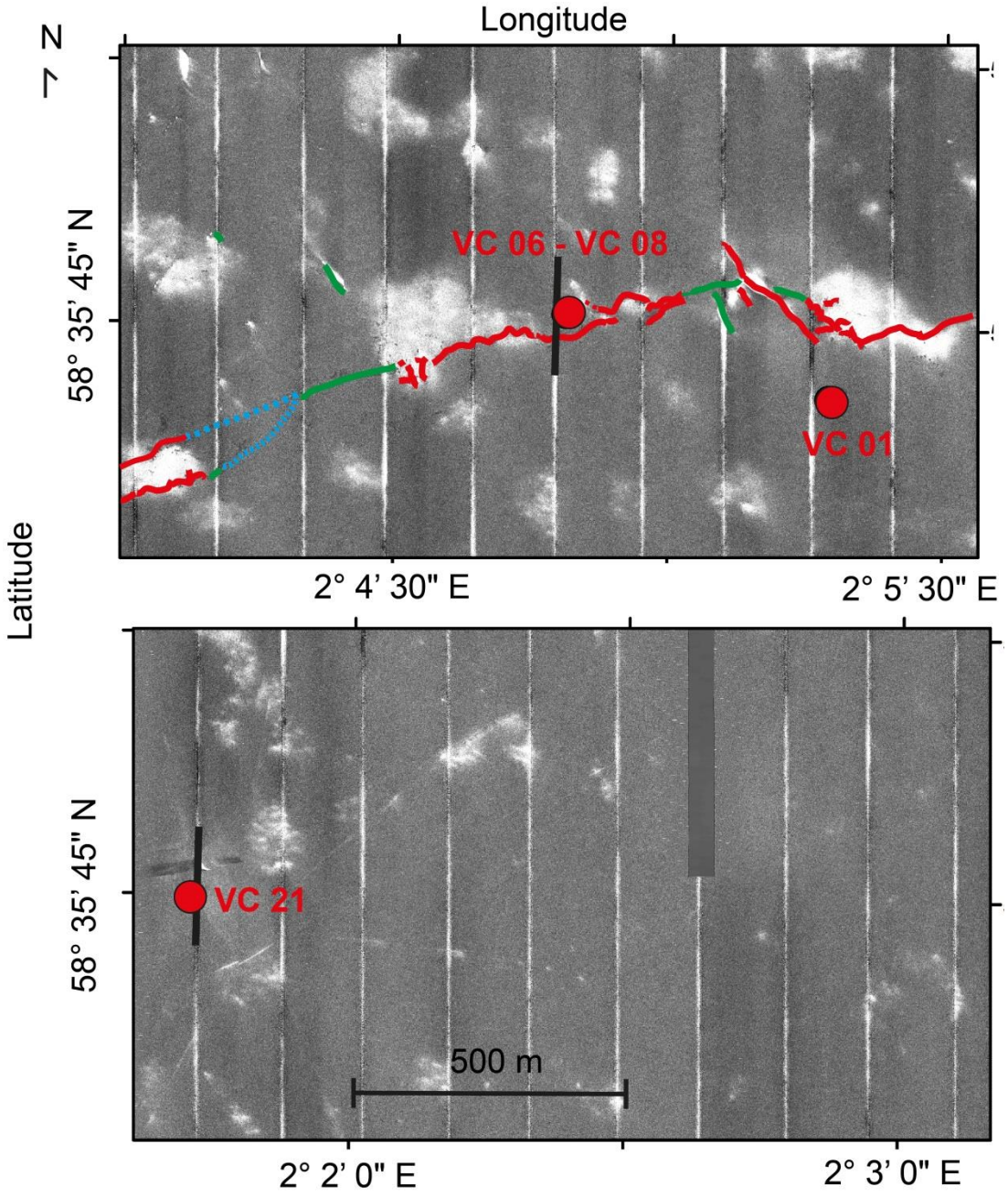

Figure 5.33 *Location of the vibrocores recovered during the JC077 cruise in the Hugin Fracture Area. Vibrocore locations are indicated by red dots. Synthetic seismograms were generated for VC 06 and VC 21. Synthetic seismograms are compared to real seismic reflection data (black lines). The spatial extent of the Hugin Fracture is also indicated.*

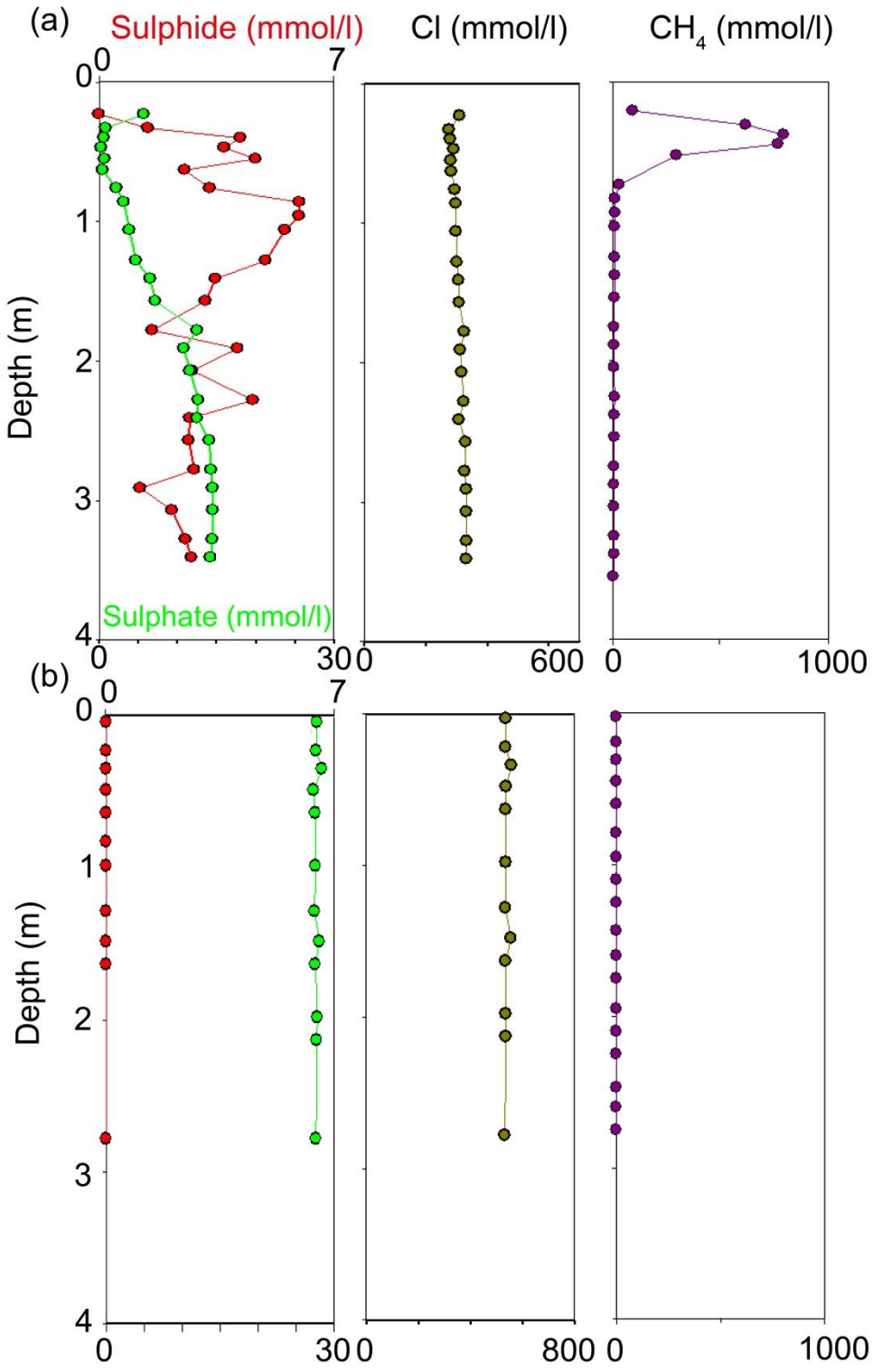

Figure 5.34 *Pore water analysis for VC 01 and VC 08.* ***(a)*** *Dissolved sulphate, sulphide, chloride and methane concentration measured from VC 08, recovered in the vicinity of the Hugin Fracture.* ***(b)*** *Concentration of the same elements at the reference site (VC 01), located 150 m S of the Hugin Fracture. Vibrocore locations are indicated on Fig. 5.33.*

Synthetic seismograms have been produced for VC 06 and VC 21, using the MSCL data, and are presented together with real seismic reflection traces intersecting the core location, or acquired close to the relevant core (Figs. 5.35 and 5.36). MSCL data along VC 06 indicates density and seismic velocity changes at the topmost c. 50 cm of the core, with acoustic impedance values varying between 3580-4010 m/s g/cm^3 (Fig. 5.35). From 50 cm depth beneath, no significant anomalies were measured along VC 06, with acoustic impedance values being constant, c. between 3900-4000 m/s g/cm^3 (Fig. 5.35). It is interesting to note that the depth interval at which physical anomalies were measured along VC 06 (the topmost c. 50 cm of the core) coincides with the depth range where increased methane concentrations were measured on geochemical profiles along VC 08 (Fig. 5.34). There is a good agreement between the real and synthetic data for VC 06 (Fig. 5.35). The MSCL measurements along VC 21, the closest core to the abandoned well 16/4-2, indicates an almost gradual increase in the acoustic impedance values down to 1 m depth, from 3900 m/s g/cm^3 at the seabed to 4030 m/s g/cm^3 at 1 m depth. From 1 m depth beneath, a gradual decrease in the acoustic impedance values is observed, from 4030 m/s g/cm^3 at 1 m depth to 3800 m/s g/cm^3 at 1.75 m depth (Fig. 5.36). Synthetic and real data show a good agreement for VC 21, while small changes are likely due to changes in location (Fig. 5.36).

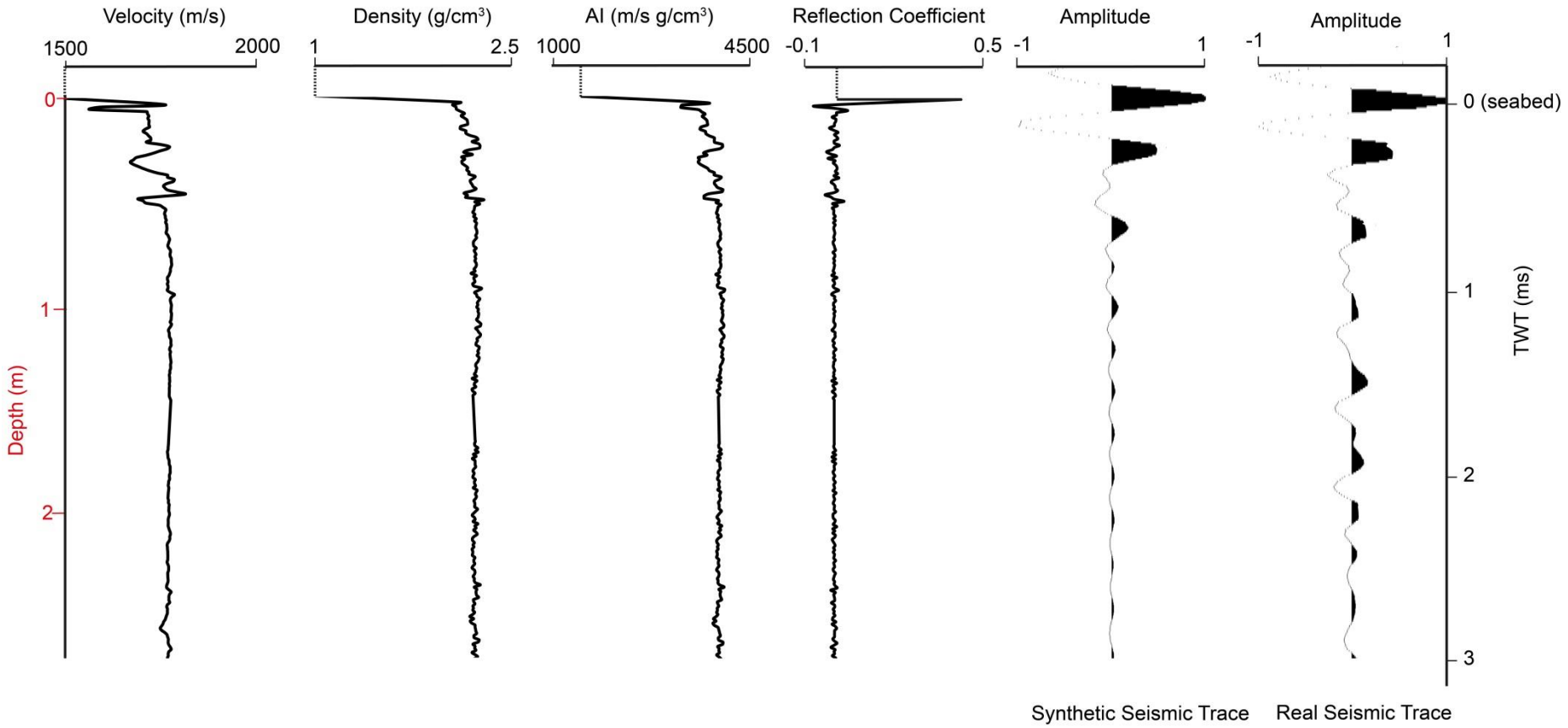

Figure 5.35 *MSCL measurements down VC 06. Acoustic impedance (AI) and reflection coefficient profiles are calculated, followed by the generation of a synthetic seismogram. The location of VC 06 and the real seismic profile are given on Fig. 5.33. Changes in seismic amplitudes between the real and synthetic data are possibly due to the difference in location.*

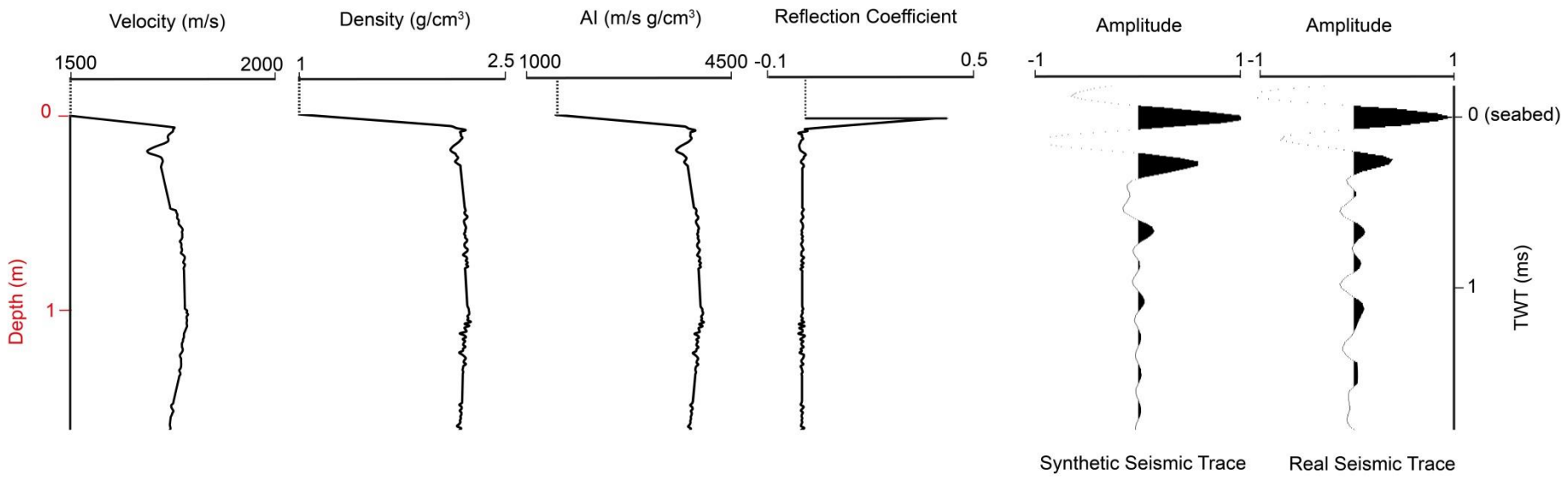

Figure 5.36 *MSCL measurements down VC 21. Acoustic impedance (AI) and reflection coefficient profiles are calculated, followed by the generation of a synthetic seismogram. The location of VC 21 and the real seismic profile are given on Fig. 5.33. There is a good agreement between real and synthetic seismic trace. Changes in seismic amplitudes between the real and synthetic data are due to the small changes in location.*

5.5 Discussion

Side-scan sonar and multibeam bathymetry data acquired over the CO_2 Plume Area, South of the Plume Area and Middle Area show no geomorphological evidence of seabed fluid flow, for example pockmarks and mud volcanoes (Figs. 5.16, 5.18-5.19), which are primarily attributed to active seabed fluid venting due to excess pore pressure within the overburden (Berndt, 2005; Plaza-Faverola et al., 2012). There is no visual evidence of seabed fluid flow including bubbles in the water column, methane-derived authigenic carbonates, bacterial mats and dark sediment patches on the seabed, from HyBIS video surveying and Autosub 6000 near bottom photography over these areas (Figs. 5.18 and 5.19; Tables 5.1 and 5.2), which are frequently observed at submarine cold seeps worldwide (Dupré et al., 2007; Foucher et al., 2010; Greinert et al., 2010). In addition, CTD water column sampling over these areas reveals CH_4 levels consistent with background concentrations in the North Sea, c. 0-30 ppm, confirming a lack of seabed fluid venting (Fig. 5.17).

In comparison, the Hugin Fracture Area (Figs. 5.9 and 5.10) has a complex geology and fluid flow activity. Side-scan and 2D high-resolution seismic reflection (Chirp) data collected during the *JC077* cruise confirms the presence of the Hugin Fracture, imaged on the seabed and within the overburden (Figs. 5.20-5.22, 5.27-5.28). The complex pattern of segmentation observed in map view along the Hugin Fracture is typical of strike-slip faulting, where adjacent segments step aside and form an echelon type fault geometry, interacting with each other (Sylvester, 1988; Aydin and Schultz, 1990; Peacock, 1991; Zachariasen and Sieh, 1995) (Figs. 5.21-5.22, 5.28). The fault bends imaged on the side-scan data, either single bends at individual fault terminations within the main Segments A and B, or the double bend imaged between the main segments A and B, link adjacent fault segments, probably resulting in a through-going strike-slip fault zone in the Hugin Fracture Area (Cunningham and Mann, 2007; Aydin and Berryman, 2010) (Figs. 5.21-5.22, 5.28). Previous studies noted that the frequency of fault bends per kilometre tends to decrease with increasing fault slip for strike-slip faults (Otsuki and Dilov, 2005; De Joussineau et al., 2007). It was also demonstrated that large fault steps accommodate larger magnitude fault slips (De Joussineau et al., 2007; Shaw and Dieterich, 2007). The frequency of fault steps within the segments A and B may suggest similar slip rates along these two segments (Figs. 5.21-5.22, 5.28).

In addition, as the fault step linking the Segments A and B is significantly larger compared to the other bends along strike, the fault offset can be consequently greater (Figs. 5.21-5.22, 5.28). Although the direction of the horizontal displacement in map view is not easily determined, especially along the main Segments A and B, westward movement along the fault bend separating these two segments suggests a left lateral (sinistral) strike-slip displacement along the Hugin Fracture with the maximum displacement being 15 m (Figs. 5.21-5.22, 5.28). Local fault branches imaged on the side-scan data (Figs. 5.20-5.22) are interpreted as secondary cracking and splaying within the area, commonly found associated with strike-slip faulting (Zachariasen and Sieh, 1995; Belardinelli et al., 2000) (Figs. 5.21-5.22, 5.28). The generation of these secondary fractures have been shown to facilitate the linkage between an echelon array of discontinuities leading to fault nucleation and development (Brogi, 2011).

Strike-slip fault systems have also been shown to correspond to sub-vertical or nearly vertical discontinuities on seismic reflection profiles (Appelgate et al., 1992; Bartolome et al., 2012). The submeter scale vertical displacement imaged on seismic reflection data suggests a synchronous dip slip component along the Hugin Fracture, in addition to horizontal slip, suggesting an overall oblique slip faulting, or transtensional stress regime, dominating throughout the Hugin Fracture (Figs. 5.26 and 5.27). The area of individual faults detected to the NW of the Hugin Fracture from seismic reflection data suggest a growing active fault network within the area (Fig. 5.28). The current maximum horizontal stress in the North Sea is reported to be oriented E-W, which clearly explains the orientation of different fault segments as well as fault bends in the Hugin Fracture Area (Brudy and Kjørholt, 2001; Grollimund et al., 2001; Hillis and Nelson, 2005).

Seismic attribute analysis (similarity) of 3D seismic reflection data reveals the presence of buried glacio-fluvial channels and tunnel valleys, widespread in the Hugin Fracture Area (Landschulze and Pedersen, 2013b; Pedersen et al., 2013; Landschulze et al., 2014a). These glacio-morphological features have different extent and orientations, and form an interconnected network of elongate depressions, in an anastomosing pattern (Landschulze and Pedersen, 2013b). Time slices from the Quaternary sediment package down to 276 ms (c. 210 m assuming V_p=1500 m/s) indicate that the Hugin Fracture is located above the edge of a buried glacio-fluvial channel/tunnel valley (Landschulze and Pedersen, 2013a; Landschulze et al., 2014a) (Fig. 5.37). This crucial

observation led to the hypothesis that Hugin Fracture might have formed due to the brittle failure of shallow, clay-rich sediments caused by the differential compaction above the edge of the underlying tunnel valley system (Landschulze and Pedersen, 2013a; Landschulze and Pedersen, 2013b; Pedersen et al., 2013; Landschulze et al., 2014a; Landschulze et al., 2014b). The buried tunnel valley/paleo-channel system below the Hugin Fracture is shown to be mainly sand-filled, thus permeable, and is partially gas-charged (Furre et al., 2014), which is in agreement with previous studies where gas-related bright spots have been commonly observed within the buried tunnel valleys (Fichler et al., 2005; Huuse et al., 2012; Kristensen and Huuse, 2012). A possible pressure increase within this 1-4 km wide, 50-150 m deep glacial system might have caused the upward migration of biogenic CH_4 (Fig. 5.34), and its subsequent leakage over the Hugin Fracture (Furre et al., 2014). In addition, 3D seismic reflection data revealed a gas-rich horizon of Pliocene Age within the Hugin Fracture Area, which might also be the source of biogenic methane leaking at the Hugin Fracture (Haeckel et al., 2013) (Fig. 5.34). Meltwater seepage at the Hugin Fracture, shown by the decrease in chloride concentration from vibrocores (Fig. 5.34) and push cores (Haeckel et al., 2013; Pedersen et al., 2013), supports the hypothesis of a structural and hydraulic connection between the fracture and at least the underlying permeable channel/ tunnel valley system. In addition, isotopic composition of pore water in core samples collected at the Hugin Fracture revealed small amounts of thermogenic methane suggesting a connection to deeper gas reservoirs, e.g., the underlying Sleipner fields (Haeckel et al., 2013). Faulting within the overburden has been commonly observed in buried tunnel valley settings, however, to date, there is no evidence of surface-breaking faults reported (Lykke-Andersen et al., 1993; Huuse and Lykke-Andersen, 2000; Al Hseinat and Hübscher, 2014).

Apart from the hypothesis of tectonic faulting resulting from the E-W transtensional stress regime dominating in the Central North Sea, and faulting due to the differential compaction above a buried tunnel valley system, another interpretation of the origin of the Hugin Fracture might be polygonal faulting. Polygonal faulting has been widely observed on the seismic reflection data from the Central North Sea, where extensional faults have been mainly suggested to form as a result of volumetric compaction within fine-grained sediments and fluid expulsion (Cartwright and Lonergan, 1996). The close link between these non-tectonic fault systems and fluid

flow has been reported in several studies (Cartwright, 1994; Berndt et al., 2003; Gay et al., 2006; Hustoft et al., 2007), where acoustic indicators of fluids (seismic pipes, bright spots, velocity-push down) were detected at different stratigraphic layers above the polygonal faults, suggesting an episodic fluid expulsion from the underlying polygonal fault system. On the other hand, polygonal faults have been shown to form clear polygonal network patterns in plan view (Lonergan et al., 1998; Lonergan et al., 2006), which is not observed for the Hugin Fracture (Figs. 5.20-5.22, 5.28). In addition, to date, polygonal faults have been only imaged within the overburden, e.g., no propagation to the seabed is observed (Cartwright et al., 2003; Das, 2006; Chen et al., 2011; Cartwright, 2014) (Figs. 5.26 and 5.27). A lack of preferential strike orientation, fault throw and dip range between 10-100 m, and 30°-70°, respectively (Stuevold et al., 2003; Goulty, 2008; Cartwright, 2011), are the key observations for polygonal fault systems worldwide, which are inconsistent with the findings for the Hugin Fracture (Figs. 5.20-5.22, 5.26-5.28). Based on the observations from the Hugin Fracture, the nucleation and growth of the Hugin Fracture is proposed to be controlled by both tectonic and non-tectonic processes, including the E-W transtensional stress regime and differential compaction above a buried tunnel valley system. An origin related to polygonal faulting is likely to be excluded; as major findings from the Hugin Fracture are significantly different than those reported from polygonal fault systems.

Apart from the discovery of a fracture imaged both on the seabed and within the overburden, the analysis of the multidisciplinary dataset acquired over the Hugin Fracture Area reveals the presence of: bacterial mats, reduced dark sediment patches and bubbles detected by seabed video photography (Fig. 5.24); Eh anomalies within the water column (Fig. 5.25), seismic amplitude anomalies on Chirp and TOPAS data (Figs. 5.29-5.32); geochemical anomalies along the vibrocores (Fig. 5.34); and decrease in the acoustic impedance profiles along the vibrocores from the MSCL data analysis (Figs. 5.35 and 5.36). All these biological, geochemical and physical observations have been previously attributed to fluid flow activity worldwide (Eichhubl et al., 2000; Dupré et al., 2007; Arts et al., 2008; Petersen et al., 2010; Sarkar et al., 2012; Blackford et al., 2014; Karaca et al., 2014; Muñoz et al., 2014), and support the presence of an active fluid flow in the Hugin Fracture Area, located mainly along and in the vicinity of the Hugin Fracture, as well as at the abandoned well site 16/4-2. In detail, seabed CH_4 leakage has been demonstrated to be associated with intensive microbial process of

anaerobic methane oxidation coupled to sulphate reduction, leading to detection of bacterial mats, dark sediment patches and seepage of reduced fluids (Thiel et al., 2001; Henry et al., 2002) (Figs. 5.24-5.25, 5.34). Enhanced seismic reflectivity within the overburden, as well as acoustic anomalies within the water column, have been shown to be caused by an increase in the acoustic impedance contrast, being the typical response of sediments containing shallow fluids, or seabed fluid seepage, respectively (Zhang et al., 2012; Blackford et al., 2014) (Figs. 5.29-5.32, 5.35-5.36).

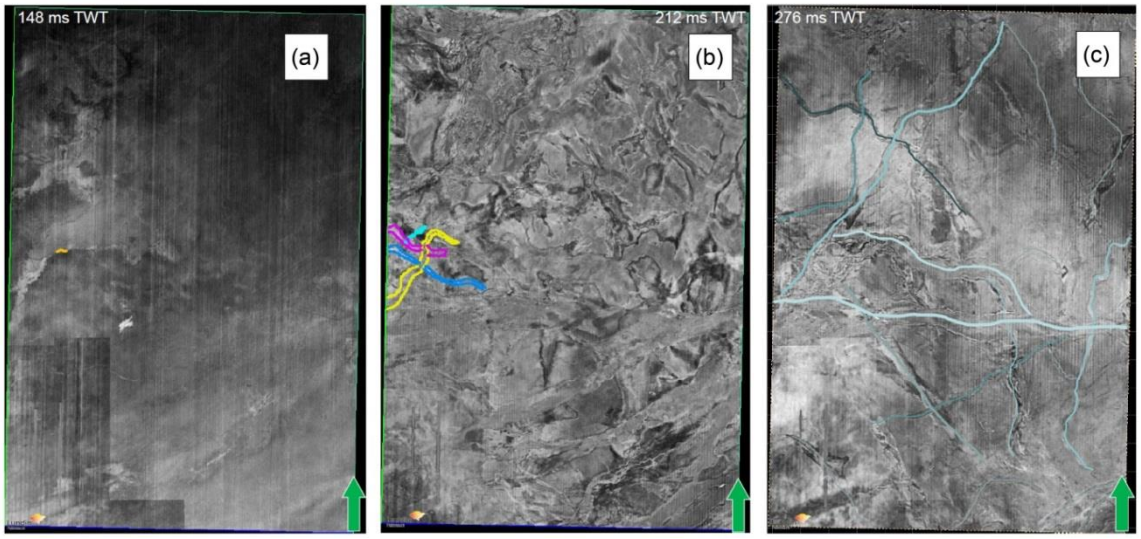

Figure 5.37 *Time slices from the 3D seismic reflection data over the Quaternary sediment package in the Central North Sea (Landschulze et al., 2014a).* ***(a)*** *The time slice at 148 ms TWT (c. 50 m below the seafloor) indicates that the Hugin Fracture (solid orange line) is located above the edge of an alluvial fan.* ***(b)*** *The time slice at 212 ms (c. 120 m below the seafloor) and* ***(c)*** *276 ms (c. 180 m below the seafloor) TWT show buried tunnel valleys/ glacio-fluvial channels widespread in the area. The solid lines in various colours indicate the possible glacio-morphological features identified on the time slices.*

5.6 Conclusion

This chapter reports the results from a multidisciplinary dataset acquired during the *JC077* cruise in the Central North Sea, in September 2012, together with some TOPAS seismic reflection dataset acquired in the Hugin Fracture Area, as part of the ECO_2 project. Following the discovery of the Hugin Fracture in 2011 (Pedersen et al., 2013), various research techniques have been used during the *JC077* cruise, confirming the presence and extent of the Hugin Fracture on the surface and within the subsurface,

as well as the increased fluid flow activity within the Hugin Fracture Area. No evidence of fluid flow activity was detected at the other areas surveyed during the *JC077* cruise in the Central North Sea, including the Middle Area, CO_2 Plume Area and the South of the Plume Area.

The possible origin of the Hugin Fracture, including a tectonic control and non-tectonic processes has been discussed. Based on geological observations, the Hugin Fracture is interpreted to have formed from the interaction of tectonic and non-tectonic processes, including an E-W transtensional stress regime leading to oblique slip faulting with a dominant strike-slip component, and differential compaction above a buried tunnel valley system. An origin related to polygonal faulting is thought to be highly unlikely, as various key observations reported from polygonal fault systems worldwide do not coincide with the observations from the Hugin Fracture.

The possibility of a structural and hydraulic connection between the Hugin Fracture and the interconnected tunnel valley/paleochannel system, as well as deeper gas reservoirs beneath the Utsira Formation, calls for reevaluation of the efficiency of the caprock seal integrity above the Utsira Formation in the Central North Sea. Although various studies indicate that the injected CO_2 at Sleipner is securely confined within the overburden, will never reach the Hugin Fracture Area, and the fracture was present before the start of CO_2 injection in Sleipner (Furre et al., 2014), this study clearly demonstrates that at least the shallow overburden around the CO_2 injection site is prone to act as a preferential fluid migration pathway for biogenic and thermogenic fluids, leading to natural fluid emissions on the seabed. Other undiscovered fractures in the vicinity of the Sleipner CCS site might represent potential leakage pathways for natural and anthropogenic fluids in the long term. Thus, we suggest a more detailed and continuous investigation of the shallow subsurface around the ongoing and planned CCS projects.

Chapter 6

Synthesis and future work

This chapter summarizes the key findings and implications of this thesis, and outlines directions for future work.

6.1 Synthesis and implications

Impacts of free gas on sediment acoustic properties

From the traditional qualitative analysis of high-resolution seismic reflection data acquired syn- and post-release in Ardmucknish Bay (Chapters 2 and 3), as well as in the vicinity of Sleipner CCS site (Chapter 5), several acoustic anomalies were detected, including seismic chimneys, enhanced reflectivity and polarity reversal within the overburden, as well as water column acoustic anomalies, caused by CO_2 fluxing. Time-lapse 2D seismic reflection surveys in Ardmucknish Bay significantly improved our understanding of the type of acoustic anomalies, as well as their temporal and spatial variation, with respect to the quantity of gas injected into the subsurface and/or injection rate. We showed that seismic chimneys were only initially detected below Horizon 2 when the injection rate was 45 kgs/day in Ardmucknish Bay, whereas enhanced reflectivity was imaged even at Day 0 and Day 1, along Horizon 2, when the injection rate was 20 kgs/day. Similarly seismic chimneys were found to reach the seabed when the injection rate was 210 kgs/day, leading to increased CO_2 leakage at the seabed, although they were confined below Horizon 2 for injection rates between 45-85 kgs/day. In addition, the spatial extent of the seismic chimneys largely decreased at Day 34, from 65x40 m to 20x20 m, indicating a more focussed CO_2 flow with increasing injection rate/cumulative amount injected. Following the cessation of the CO_2 injection, there was no evidence of seismic chimneys within the overburden, whereas enhanced reflectivity was imaged along Horizon 2.

A more quantitative approach was used in Chapters 2, 3 and 4, to assess the impact of CO_2 injection on sediment acoustic properties in Ardmucknish Bay (Fig. 6.1). During the syn-release period, the largest acoustic property change was found

associated with Horizon 2 reflection coefficient values, 400% change compared to the pre-release seismic reflectivity (Fig. 6.1). Seismic attenuation above and below Horizon 2, as well as seismic P-wave velocity, were shown to differ from their pre-release values throughout the gas release (Fig. 6.1). The change is less than 25% for Q values from below Horizon 2, as well as seismic P-wave velocity, whereas a c. 45% change was found with Q values above Horizon 2, during syn-release (Fig. 6.1). During the post-release period, Horizon 2 seismic reflectivity was 275% smaller compared to the pre-release seismic reflectivity (Fig. 6.1). In addition, Q above Horizon 2 on the post-release seismic reflection data is similar to the pre-release Q values, suggesting an absence of CO_2 above Horizon 2, after the cessation of injection (Fig. 6.1). No robust values were calculated for the seismic P-wave velocity and Q below Horizon 2 from the post-release seismic reflection data, thus only tentative trends are indicated on Fig. 6.1. It is noteworthy that although Q has been previously shown to be independent of frequency (Pinson et al., 2008), this is valid for gas-free sediments, where intrinsic attenuation can be reliably estimated from seismic reflection data. However, in case of bubbles within the sediment pore space, bubble resonance might have occurred, causing scattering attenuation, and thus making Q estimates presented in this thesis less reliable (Fig. 6.1).

These results have major implications for CCS sites. Firstly, the integration of qualitative and quantitative seismic reflection data analysis significantly improves the detectability of free gas within the subsurface, notably leakage into the overlying layers. To ensure the secure trapping of CO_2 within a storage reservoir, the quantitative methods used in this thesis could be regularly implemented for CCS site studies, which will significantly enhance current interpretations. Further, the cessation of CO_2 injection does not imply that risks of leakage are reduced, as the gaseous CO_2 may still be present within the subsurface, i.e., not completely dissolved. Therefore, after the cessation of CO_2 injection, the injection site should still be regularly monitored.

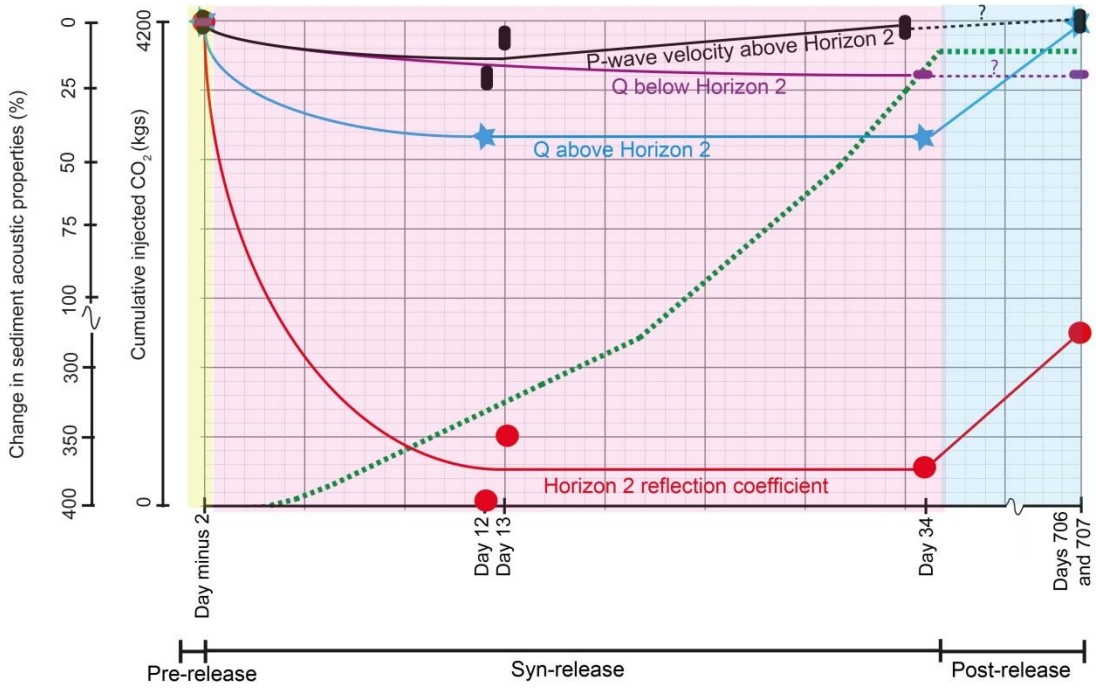

Figure 6.1 *Summary of the change in sediment acoustic properties in Ardmucknish Bay. The cumulative injected CO_2 is indicated by the green dashed line.*

Gas migration mechanisms

In Chapters 2, 3 and 5, we showed that gas migration within the overburden is a very complex process, which is controlled by sediment stratigraphy, stratigraphic geometry, injection rate, cumulative amount of injected gas, and geological discontinuities. Within the scope of the ECO_2 project, most of the acoustic anomalies were imaged along, and in the vicinity of, the Hugin Fracture, where this geological discontinuity acts as a preferential fluid migration pathway for biogenic and thermogenic fluids in the Central North Sea.

In the early stages of the QICS experiment, at Day 0 and Day 1 (with the injection rate being 20 kgs/day), enhanced reflectivity was imaged along Horizon 2 on the seismic reflection data (Fig. 6.2a). Isolated bubble streams were detected within the water column by divers, immediately above the diffuser, indicating that the injected CO_2 leaked into the water column at Day 0 and Day 1, despite the lack of clear acoustic evidence of CO_2 fluxing above Horizon 2 in the seismic reflection data (Fig. 6.2a). At Day 2 (with the injection rate being 45 kgs/day), a few seismic chimneys were imaged below Horizon 2, together with enhanced reflectivity along Horizon 2, more bubbles within the water column, and pockmarks on the seabed, yet no clear acoustic anomalies

were detected above Horizon 2 (Fig. 6.2b). At Day 12 and Day 13, where the injection rate was increased up to 85 kgs/day, seismic chimneys, confined below Horizon 2, were frequently imaged, as well as water column acoustic anomalies above the diffuser (Fig. 6.2c). However, no acoustic anomalies were detected above Horizon 2 at Day 12 and Day 13 with qualitative seismic reflection data analysis (Fig. 6.2c). Quantitative seismic reflection data analysis, including seabed reflection coefficient, seismic attenuation and thickness analysis, supported CO_2 fluxing above Horizon 2 on Day 12 and Day 13 (Fig. 6.2c). Based on the observations between Day 0 and Day 13, we suggest that the sediment stratigraphy was the main mechanism controlling CO_2 migration in the early stages of the QICS experiment, where fracturing occurred within muddy sediments below Horizon 2, and capillary invasion and fluidisation dominated within sandy-silty sediments above Horizon 2. It is important to note that, in contrast to sediment fracturing within muddy sediments, which was clearly imaged on seismic reflection data, capillary invasion and fluidisation were more difficult to resolve, even with high-resolution seismic reflection imaging techniques.

In the later stages of the QICS experiment, at Day 34 (with injection rate being 210 kgs/day), seismic chimneys were no longer confined below Horizon 2, as they were imaged from the diffuser to the seabed (Fig. 6.2d). More bubbles were imaged within the water column, in the vicinity of the diffuser, both by divers and remote monitoring techniques (Fig. 6.2d). These observations led us to conclude that the CO_2 injection rate/cumulative injected volume overrode the stratigraphic control on gas migration on Day 34. Moreover, quantitative analysis of seismic reflection data suggest that the CO_2 fluxing above Horizon 2 was mostly concentrated within the chimney at Day 34 (Fig. 6.2d). Following the cessation of the CO_2, enhanced reflectivity was imaged along Horizon 2, clustering mostly in the NW of the diffuser (Fig. 6.2e). However, no chimneys were detected on the post-release seismic reflection data, after the end of injection (Fig. 6.2e). Quantitative analysis of the seismic reflection data acquired at Days 706 and 707 implies that the gaseous CO_2 was largely trapped beneath Horizon 2, supporting observations from qualitative seismic data analysis (Fig. 6.2e). All these observations led us to conclude that post-release gas migration was controlled by sediment stratigraphic geometry, where a dip of 3.5° along Horizon 2 facilitated gas migration towards shallower depths. Finally, we suggest that if seismic reflection data is

acquired in the distant future in Ardmucknish Bay (for example 100 years), no acoustic anomalies will be detected within the overburden, due to CO_2 dissolution (Fig. 6.2f).

These results have major implications for CCS sites studies. A better understanding of the sediment physical properties is crucial in tracking the injected CO_2 within the overburden. If the injected CO_2 only migrates within the overburden by capillary invasion and fluidisation, small amount of leakage from the storage reservoir to the overlying layers might be difficult to detect, especially if the predictions are only based on lower resolution time-lapse seismic reflection imaging, currently used for CCS site surveys. However, these results are not in disagreement with the potential of 3D time-lapse seismic imaging to detect larger amounts of CO_2 within the storage reservoir, or leakage into the overlying layers. A major observation in this thesis is the disappearance of seismic chimneys, following the cessation of injection. This observation is crucial for subsurface fluid flow investigations, highlighting that the detection of seismic chimneys within the overburden may be indicative of an active fluid flow. For instance, seismic chimneys mapped by Karstens and Berndt (2015) in the North Sea are very likely to indicate active fluid flow in the Southern Viking Graben. On the other hand, multidisciplinary baseline surveys should be completed before any CO_2 injection within the subsurface, preferably ensuring that no geological discontinuities i.e., fracture network, exist in the vicinity of the storage reservoir, which might, in future, channel and facilitate gas leakage into the overlying strata. Similarly, up-dipping stratigraphic geometry might also facilitate gas migration towards shallower depths within the overburden, and possibly leakage to the overlying layers, in case of a caprock failure. Further, the pressure should be regularly monitored during CCS operations, as any pressure build-up caused by CO_2 injection might cause unexpected leakage from the storage reservoir, if this overrides the sealing capacity of the caprock.

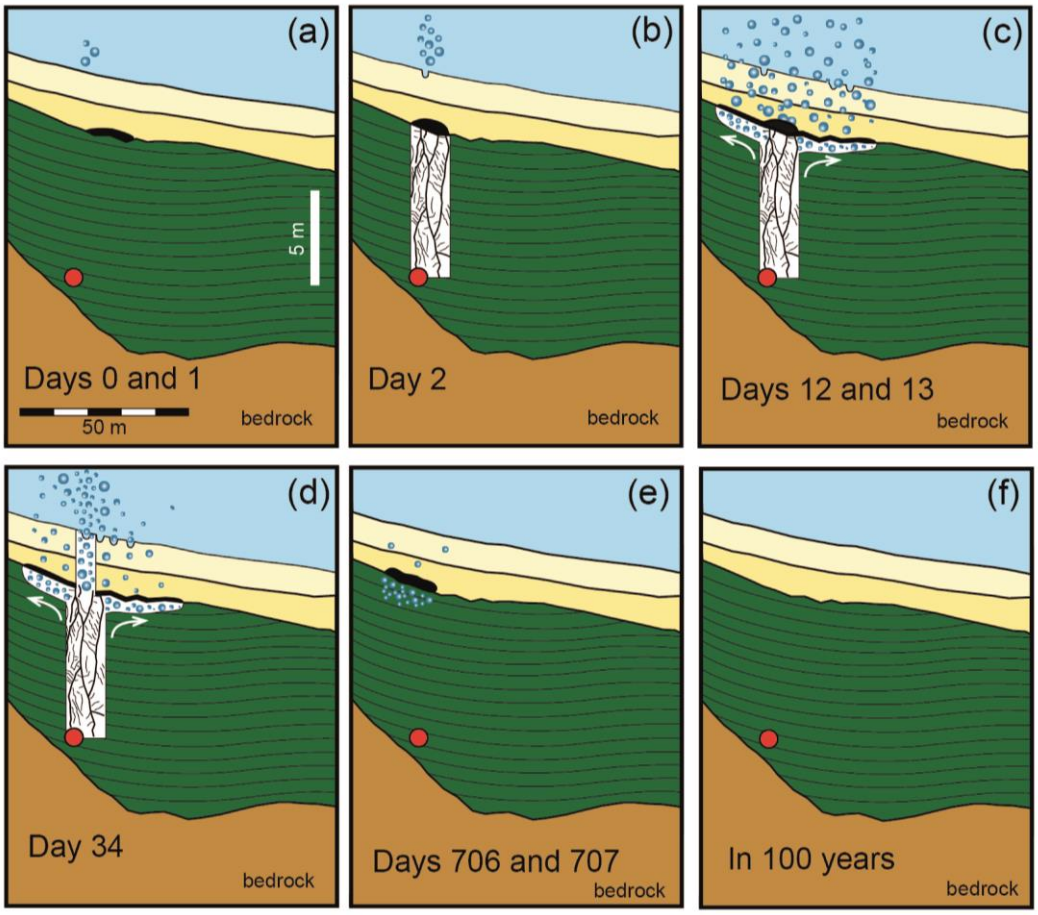

Figure 6.2 *Cartoon illustrating the fate of the injected gaseous CO_2 in Ardmucknish Bay.* ***(a)*** *Days 0 and 1.* ***(b)*** *Day 2.* ***(c)*** *Days 12 and 13.* ***(d)*** *Day 34.* ***(e)*** *Days 706 and 707. No chimneys were detected.* ***(f)*** *In 100 years.*

Best monitoring technologies to detect free gas within the overburden and leakage into the overlying water column

In Chapters 2, 3 and 5, we reported results from the analysis of multidisciplinary datasets acquired as part of the QICS and ECO_2 projects, to remotely and directly investigate fluid flow activity in Ardmucknish Bay, and in the vicinity of Sleipner CCS site. Repeated 2D high-resolution seismic reflection (Chirp and boomer) surveys, acquired in Ardmucknish Bay, as well as high-resolution seismic reflection imaging, using the AUV technology in the Central North Sea, allowed the detection of free gas within the overburden, and leakage into the overlying water column. It is noteworthy that, in the early stages of the QICS experiment, where the amount of gas injected was 20 kgs/day at Day 0 and Day 1, acoustic anomalies were successfully detected on high-

resolution seismic reflection data, outlining the efficiency of high-resolution seismic monitoring in detecting relatively small amount of free gas within the overburden.

Seismic reflection imaging can also give valuable information on geological discontinuities within the overburden, which are, in turn, potential fluid migration pathways within the survey area (Hugin Fracture and associated fluid flow activity in the Central North Sea). Multibeam bathymetry and side scan sonar surveys are complementary to seismic reflection imaging, as they increase the detectability of seabed fluid flow features, gas leakage into the water column, as well as geological discontinuities on the seabed, which largely control the location of seabed seepage (Hugin Fracture, Central North Sea).

Passive hydroacoustics have a significant potential in detecting leakage from the seabed, but most importantly in quantifying seabed gas flux. Using a well-planned hydrophone deployment strategy, even small amounts of leakage can be detected and quantified from hydroacoustics data. The similar gas flux estimates from hydroacoustics data and water column bubble sampling in Ardmucknish Bay, outlines the reliability of gas flux measurements completed with passive hydroacoustics.

Optical and geochemical sensors mounted on Autosub 6000, as well as seabed video surveying completed with HyBIS, provided clear evidence of fluid flow activity in the vicinity of the Hugin Fracture, enhancing and validating observations from seismic reflection and side scan sonar surveys. Similarly, results from various sensors, deployed *in situ* or on board, as well mounted on AUV, confirms CO_2 leakage in Ardmucknish Bay into the water column and atmosphere, supporting observations from seismic reflection and multibeam bathymetry data presented in this thesis (Atamanchuk et al., 2015; Dewar et al., 2015; Maeda et al., 2015; Sellami et al., 2015; Shitashima et al., 2015).

It is clear that, in addition to remote monitoring technologies discussed above, water column sampling and sediment coring are crucial in fluid flow investigations for the marine environment. For instance, increased methane levels were measured at the Hugin Fracture Area from CTD water column sampling, as well as higher CO_2 levels (high pCO_2 and low pH) were found within the water column in the vicinity of the injection site Ardmucknish Bay (Adam et al., 2006; Atamanchuk et al., 2015; Shitashima et al., 2015). Increased levels of dissolved inorganic carbon were measured

in sediment pore waters in the vicinity of the injection site in Ardmucknish Bay (Lichtschlag et al., 2015), while high sulphide and methane levels were measured from vibrocores collected in the Hugin Fracture Area, confirming active fluid flow in the vicinity of Sleipner CCS site.

In summary, for the ongoing and planned CCS projects, the combination of multidisciplinary remote monitoring technologies, either shipboard based measurements or AUV surveys, and water column and sediment sampling, can greatly improve the detection of fluids within the overburden, as well as leakage into the water column and atmosphere. The regular use of AUVs in CCS site surveys could have major advantages. Firstly, if AUVs are used in conjunction with shipboard based measurements, the amount of data acquired within a time period can greatly increase. Further, data acquired with AUVs, e.g., seabed imagery and sediment profiling, have an improved spatial resolution, compared to those acquired on board of a research vessel, due to ability of AUVs to fly at low altitude (few metres above the seabed). Moreover, AUVs are capable of carrying a variety of high sensitivity sensors and instruments, including geophysical, geochemical, optical and oceanographic instruments, which result in the acquisition of multidisciplinary, high quality data over the survey site. Due to the high sensitivity of sensors mounted on AUVs, leakage identification can be greatly improved.

It is clear that remote monitoring techniques allow site surveys to be completed over a much larger area, compared to more localized water column and sediment sampling strategies. Thus, the CO_2 injection area should be monitored on regular intervals with remote techniques. If any fluid leakage is detected on seismic, side scan or multibeam bathymetry surveys, water column and sediment samples can be collected in the vicinity of the suspected leakage area. It is noteworthy that fluid emissions detected with remote monitoring techniques do not necessarily imply CO_2 leakage from the storage reservoir. For instance, only biogenic and a small fraction of thermogenic methane were leaking at the Hugin Fracture, whereas there was no evidence of CO_2 within the shallow overburden (up to 4 m depth below the seafloor) and the overlying water column. Thus, direct sampling techniques are crucial in determining the geochemical composition and origin of leaking fluids in the vicinity of CCS sites.

Quantification of free gas within the overburden

In Chapter 4, we reported results on the quantification of CO_2 content/volume *in situ* above Horizon 2, from the analysis of seismic reflection data, acquired in Ardmucknish Bay. Temporal thickness changes of the seabed-Horizon 2 interval were used to calculate seismic P-wave velocities above Horizon 2. These P-wave velocities were then used together with the Anderson and Hampton compressible fluid model (Anderson and Hampton, 1980b) to quantify gaseous CO_2 above Horizon 2 on the syn-release seismic reflection data. We showed that the amount of CO_2 above Horizon 2 increased up to 320 dm^3 between Day 0 and Day 12, within the combined chimney area, consistent with the increase in injection rate/total injected volume throughout the 12-days of gas release. Between Day 13 and Day 34, the amount of CO_2 above Horizon 2 gradually decreased, in contrast to increasing cumulative CO_2 input within the overburden. These observations led us to conclude that the seabed CO_2 leakage increased at Day 13, compared to previous days, and became even more significant at Day 34.

Fig. 6.3 illustrates the mass flow rate (solid black line) and the hydrophone-determined 24 hours rolling mean seabed leakage (solid blue line) for the period Day 30-Day 36, as well as seabed gas flux determined by diver measurements (black cross) at Day 33. The increase in flow rate at Day 31 from 150 kgs/day to 210 kgs/day coincides with the increase in seabed leakage, up to c. 18 kgs/day (Fig. 6.3). Between Day 32 and Day 34, hydrophone-determined gas leakage is almost constant, in agreement with constant mass flow rate during this period (Fig. 6.3). At Day 33, the seabed gas flux is c. 31.8 kgs/day, measured by divers, corresponding to 15% of the total gas injected at this time (Fig. 6.3). At Day 34, although the mass flow rate is constant, seabed gas flux rapidly increases up to c. 20 kgs/day (Fig. 6.3). Between Day 34 and Day 35, the seabed leakage gradually decreases to c. 15 kgs/day, and then slightly increases up to c. 18 kgs/day at Day 36, mostly consistent with the change in mass flow rate within this time (Fig. 6.3). Results from hydroacoustics data support our hypothesis of increased seabed leakage at Day 34, as the seabed leakage was shown to reach its highest value at Day 34, thus limiting the amount of CO_2 trapped above Horizon 2 at this time (Blackford et al., 2014; Bergès et al., 2015).

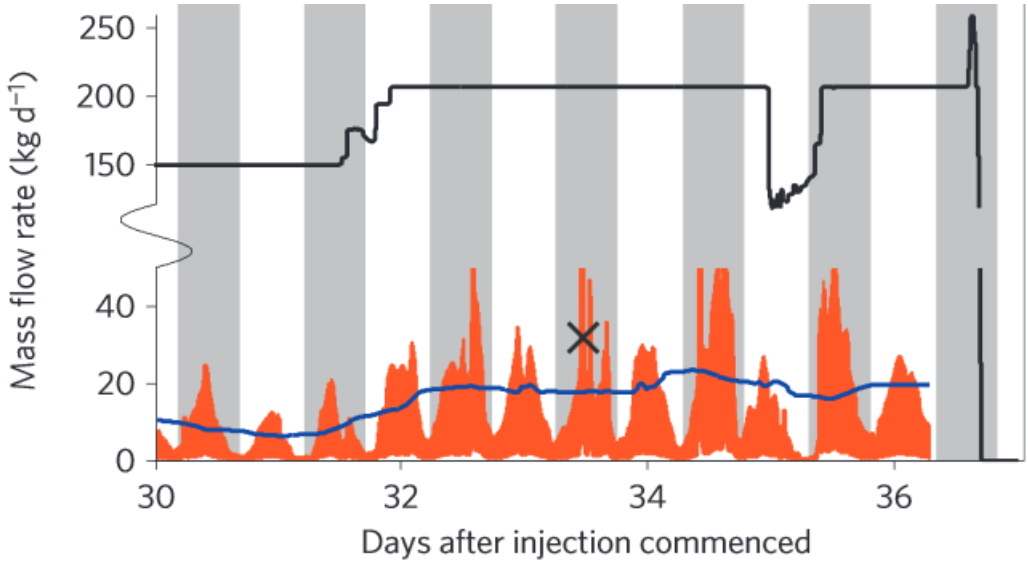

Figure 6.3 *Relationship between the CO_2 injection rate and seabed leakage in Ardmucknish Bay (Blackford et al., 2014). The solid black line correspond to the mass flow rate, orange area represents gas flux estimates from hydroacoustics data inversion, blue line is the 24 hours rolling mean of gas flux estimates from hydrophone data, and black cross is the gas flux measured by divers at Day 33.*

In Chapter 4, we also discussed the reliability of our CO_2 quantification estimates above Horizon 2. We showed that the accuracy of the CO_2 content/volume estimates depends strongly on the accuracy of thickness analysis, as possible errors in thickness analysis lead to underestimate the amount of CO_2 *in situ*. However, although thickness errors are taken into account, the gas volume above Horizon 2 correspond to a very minor fraction of the total injected volume, suggesting that the majority of the gas was either trapped below Horizon 2, or dissolved, during the QICS experiment. Further, due to bubble resonance within our seismic frequency range, we possibly underestimated the upper limit of CO_2 content/volume above Horizon 2, with the Anderson and Hampton compressible fluid model, whereas the lower CO_2 content/volume estimates remain correct. In addition, due to some assumptions in the Anderson and Hampton rock physics model, notably uniform saturation, we might have also underestimated the overall CO_2 content/volume *in situ* above Horizon 2.

The results of this chapter have significant implications for CCS projects. Our analysis revealed that the quantification of gaseous CO_2 within the overburden from seismic reflection data is not a straightforward task to achieve, as various sources of uncertainties remain, notably the selection of the "best" rock physics model which

accurately describes the impact of gaseous CO_2 on sediment acoustic properties, as well as bubble dynamics. Before any CO_2 injection within the subsurface, it is essential to have an improved knowledge of sediment physical properties, as the accuracy of these physical properties largely determines the accuracy of gas saturation estimates. Although repeated 2D seismic reflection data allows the quantification of free gas *in situ*, gas estimates can be significantly improved with 3D time-lapse seismic reflection methods, due to increased resolution, thus leading a better constraint on thickness analysis. Finally, the quantification of dissolved gas within the overburden from geochemical data analysis is crucial in mass balance estimates, which could allow the investigation of the accuracy of free gas estimates from seismic reflection data.

6.2 Future work

In this thesis, we reported results from an experimental CO_2 injection project in Ardmucknish Bay (QICS), and a CCS research project in the Central North Sea (ECO_2). Results from the QICS project improved our understanding on many aspects of fluid flow activity within the subsurface. However, these results might not be directly applicable to ongoing and planned offshore CCS projects, i.e., Sleipner CCS (Norway) or Peterhead CCS (UK) projects, due to differences in geological setting (sediment type, water depths, and injection depths), as well as injection strategy. Therefore, in future, another experimental CCS project might be planned, having a similar geological setting and an injection strategy as those of real CCS projects, where observations from multidisciplinary monitoring technologies can be straightforwardly applied to large-scale carbon sequestration projects. Further, adapting a longer monitoring strategy might allow a better understanding of the impacts of fluid flow activity on the marine environment in the long-term. In addition to the multidisciplinary monitoring techniques used during the QICS experiment, we suggest to use high-resolution 3D time-lapse seismic reflection imaging, which will allow to get a better resolution of the subsurface stratigraphy and gas-related acoustic anomalies, thus significantly improving our understanding of the impacts of free gas on sediment acoustic properties, gas migration within the subsurface, and quantification of gas *in situ*.

Quantification of gas *in situ* within the overburden is a fundamental requirement for CCS operations. In future, we will perform the acoustic impedance inversion of a larger number of seismic reflection profiles, acquired syn- and post-release in

Ardmucknish Bay, to better constrain the impact of CO_2 injection on sediment acoustic properties. Further, we will complete laboratory based measurements to produce an empirical relationship between the acoustic impedance and seismic P-wave velocity for Ardmucknish Bay gassy sediments, allowing the quantification of gas trapped immediately below Horizon 2 on different days.

The disappearance of seismic chimneys on the post-release seismic reflection data is a crucial observation for CCS projects. For future offshore CCS projects, subsurface imaging should be completed with particular attention to seismic chimneys, as they provide information on active fluid flow within the overburden, thus give hints on sediment permeability. If seismic chimneys are imaged within the overburden, notably in the vicinity of the storage reservoir, any CO_2 leakage from the storage site might result in the utilisation of these active chimneys, permitting fluid migration to shallower levels.

Analysis of multidisciplinary dataset acquired in the vicinity of Sleipner CCS site revealed the presence of the Hugin Fracture, located 25 km N of the CO_2 injection site in the Central North Sea. Although there is no evidence of CO_2 leakage at the Hugin Fracture from the current dataset, an increased natural fluid flow activity along the fracture was revealed. Therefore, we suggest to regularly monitor the Hugin Fracture, in addition to existing monitoring studies above the CO_2 Plume Area. Although current studies indicate that the injected CO_2 in Sleipner will never reach the Hugin Fracture (Haszeldine et al., 2014), there may be other fractures in the vicinity of the injection site, which might act as a potential gas migration pathway for the injected CO_2, in case of a caprock failure. This outlines the critical importance of large-scale, multidisciplinary monitoring around CCS sites.

Appendices

Appendix A

The reflection coefficient variations for Horizon 2 and the seabed, calculated over the entire survey area and the 2D Chirp and boomer seismic reflection acquisition geometry

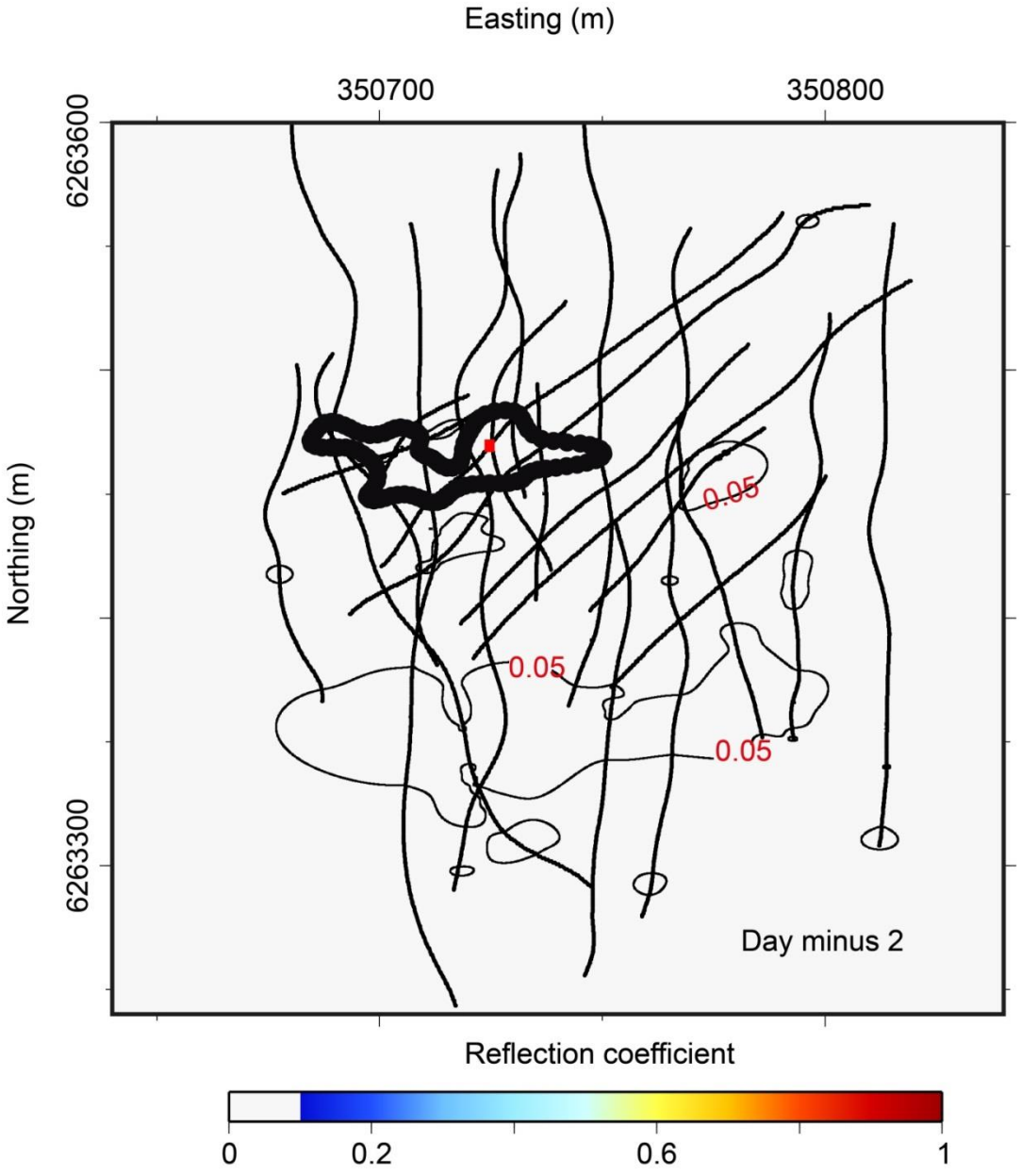

Figure A.1 *Horizon 2 reflectivity changes within the 2D seismic survey area at Day minus 2.*

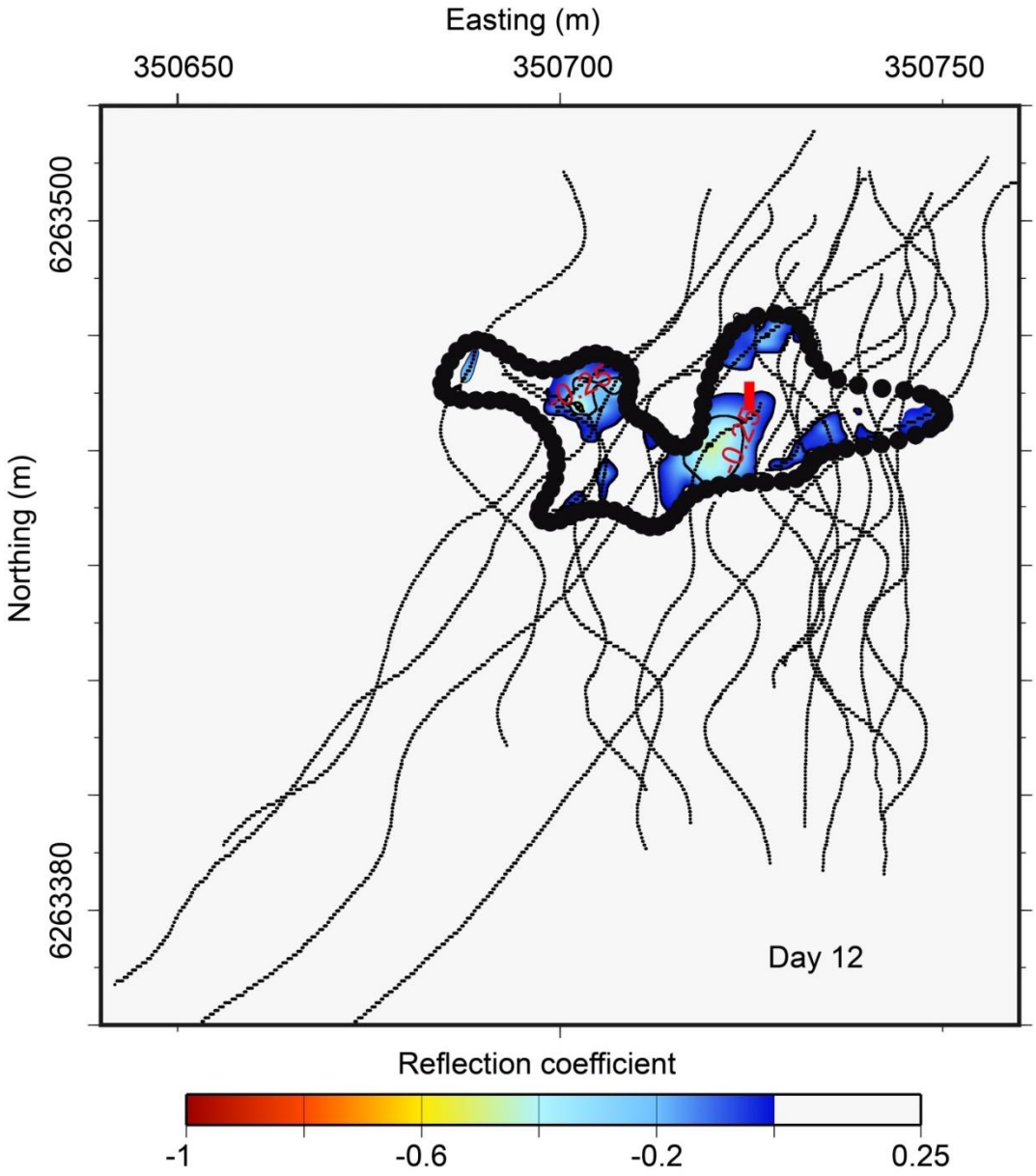

Figure A.2 *Horizon 2 reflectivity changes within the 2D seismic survey area at Day 12.*

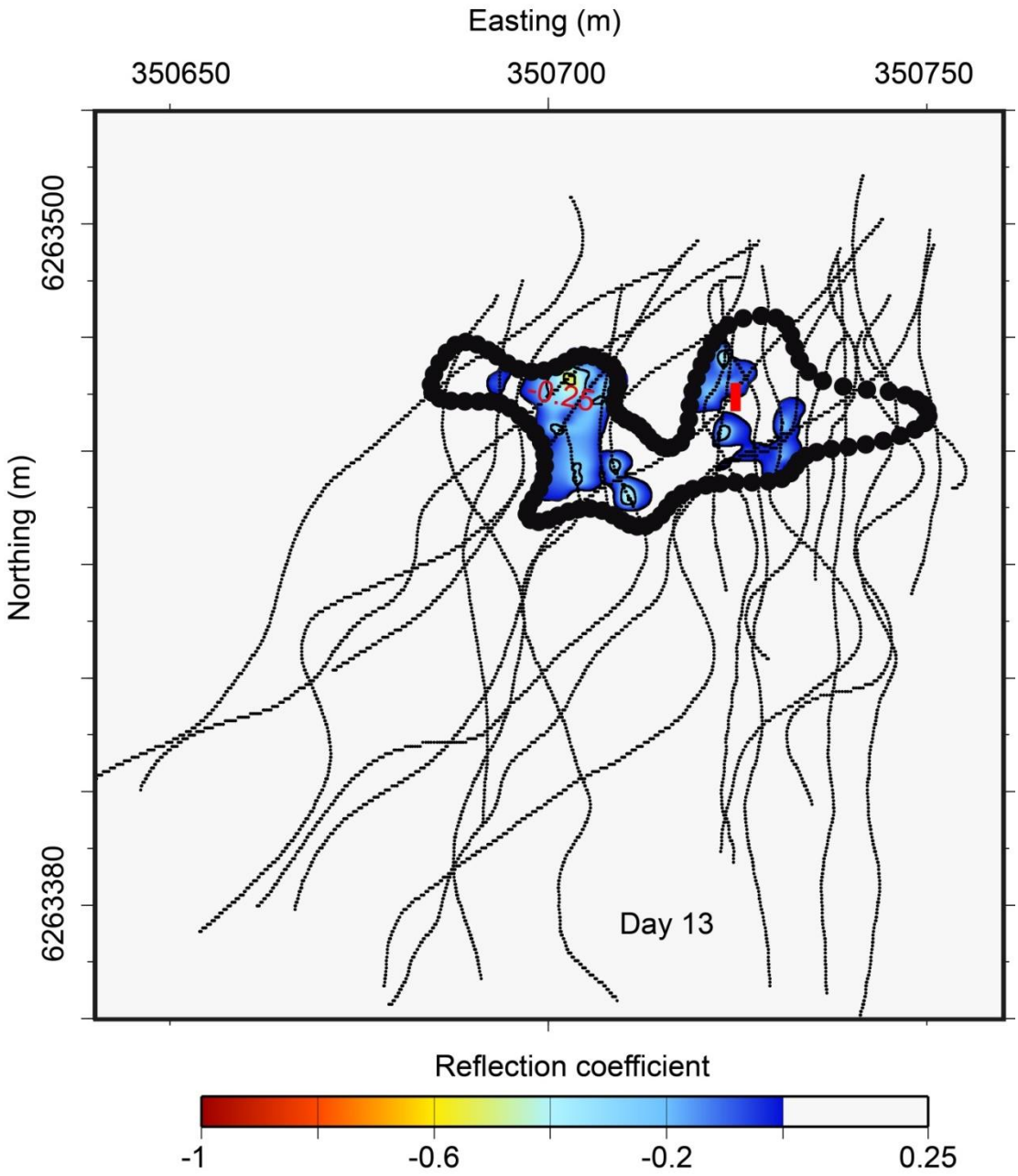

Figure A.3 *Horizon 2 reflectivity changes within the 2D seismic survey area at Day 13.*

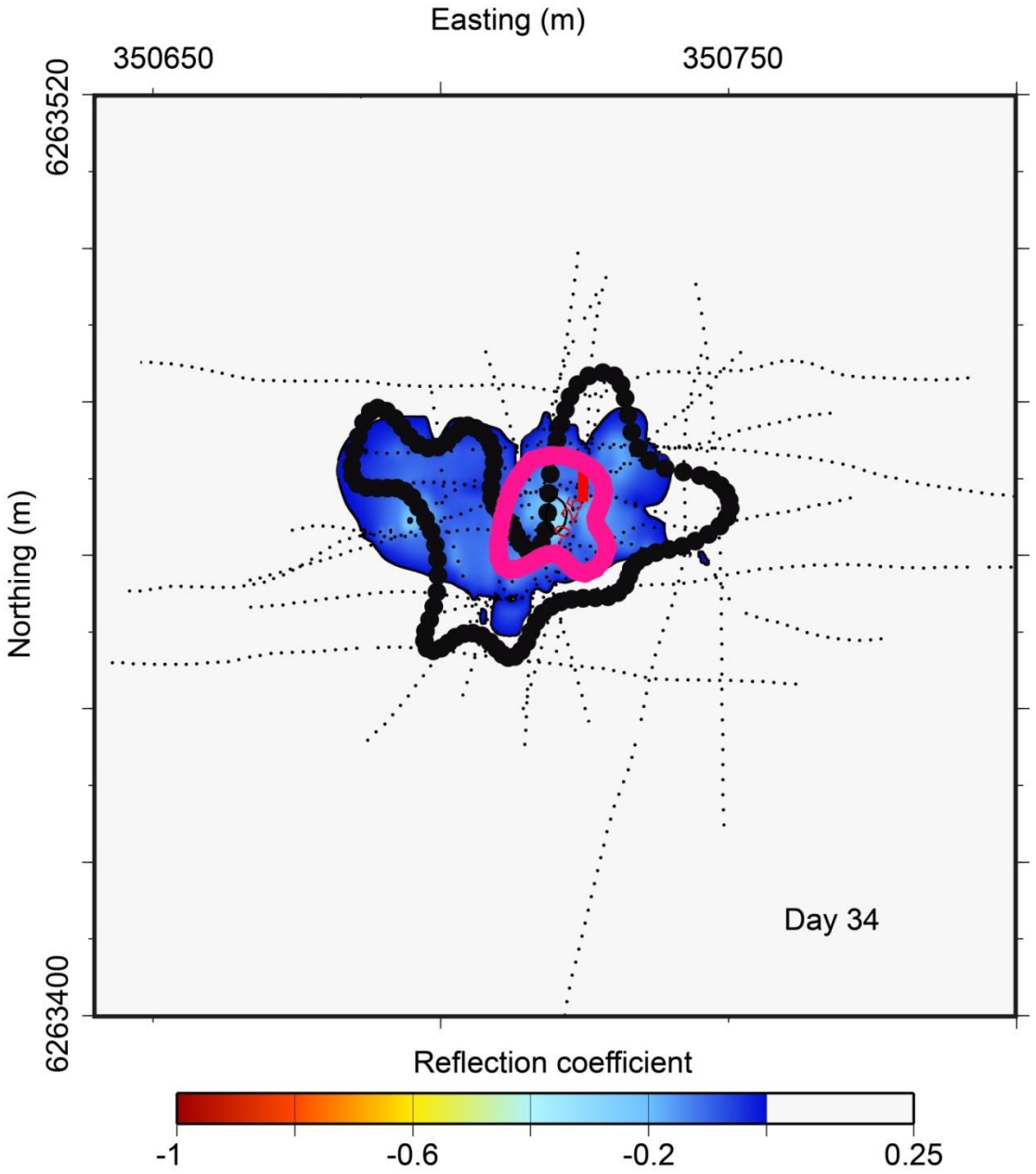

Figure A.4 *Horizon 2 reflectivity changes within the 2D seismic survey area at Day 34.*

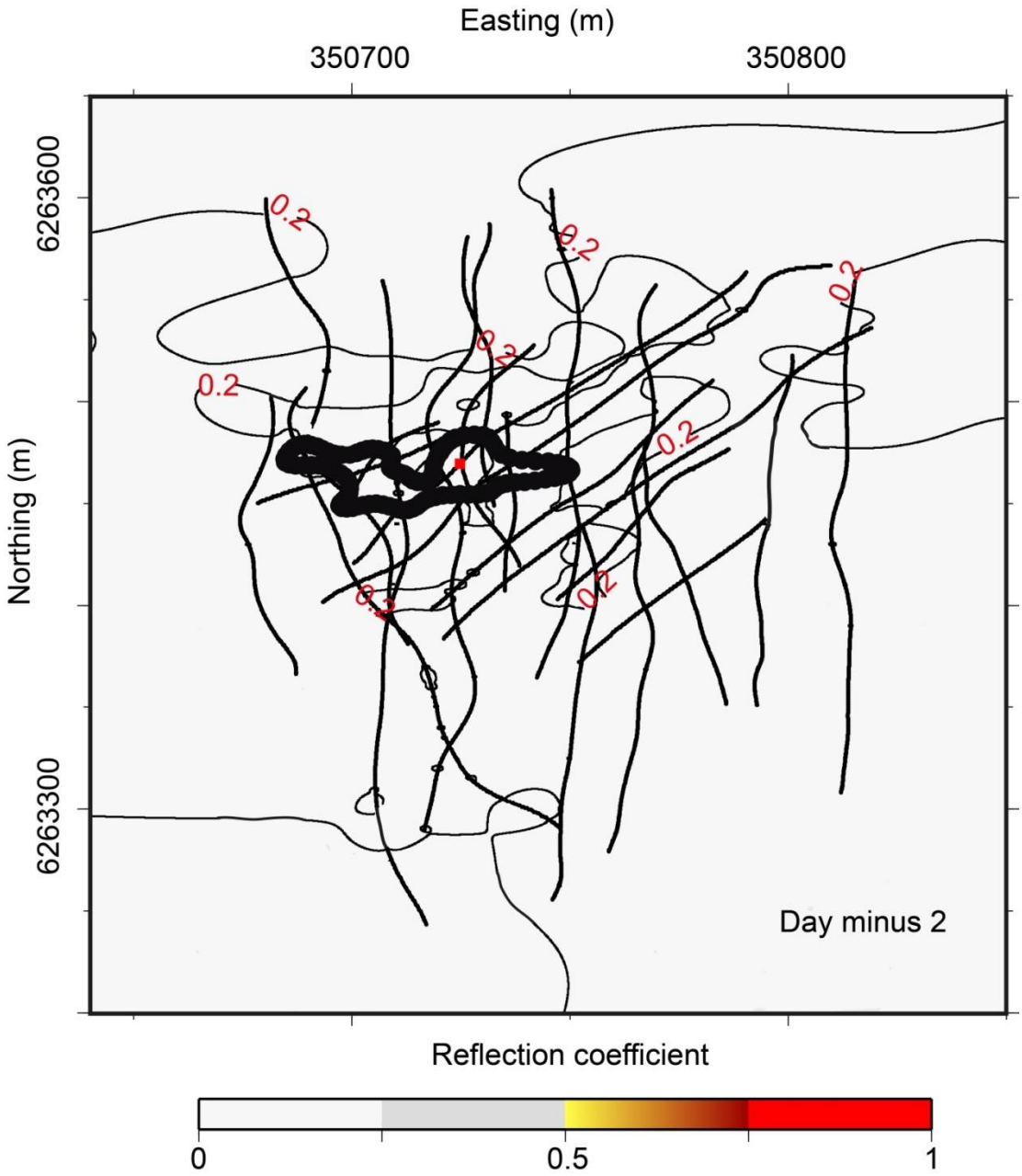

Figure A.5 *The seabed reflectivity changes within the 2D seismic survey area at Day minus 2.*

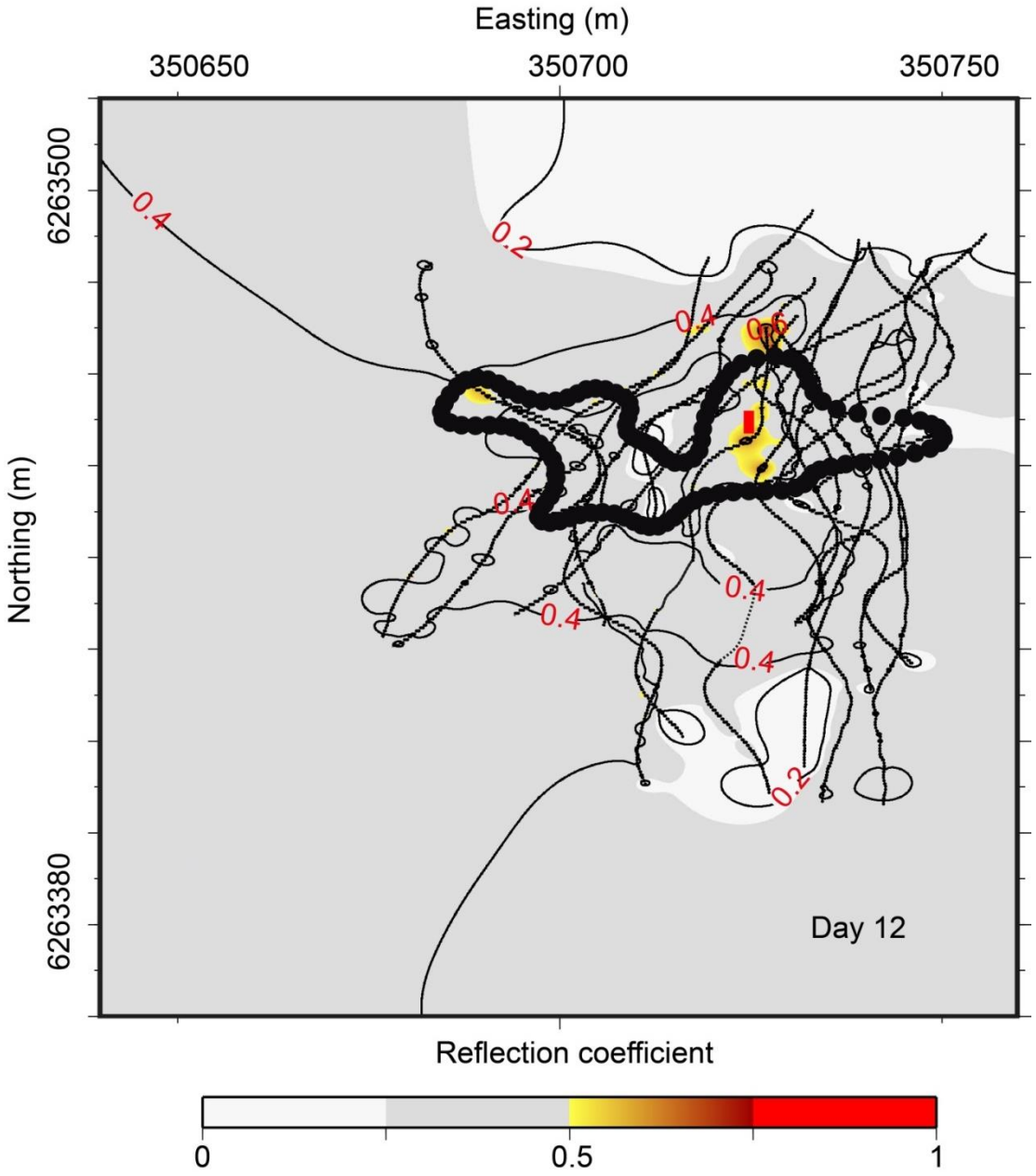

Figure A.6 *The seabed reflectivity changes within the 2D seismic survey area at Day 12.*

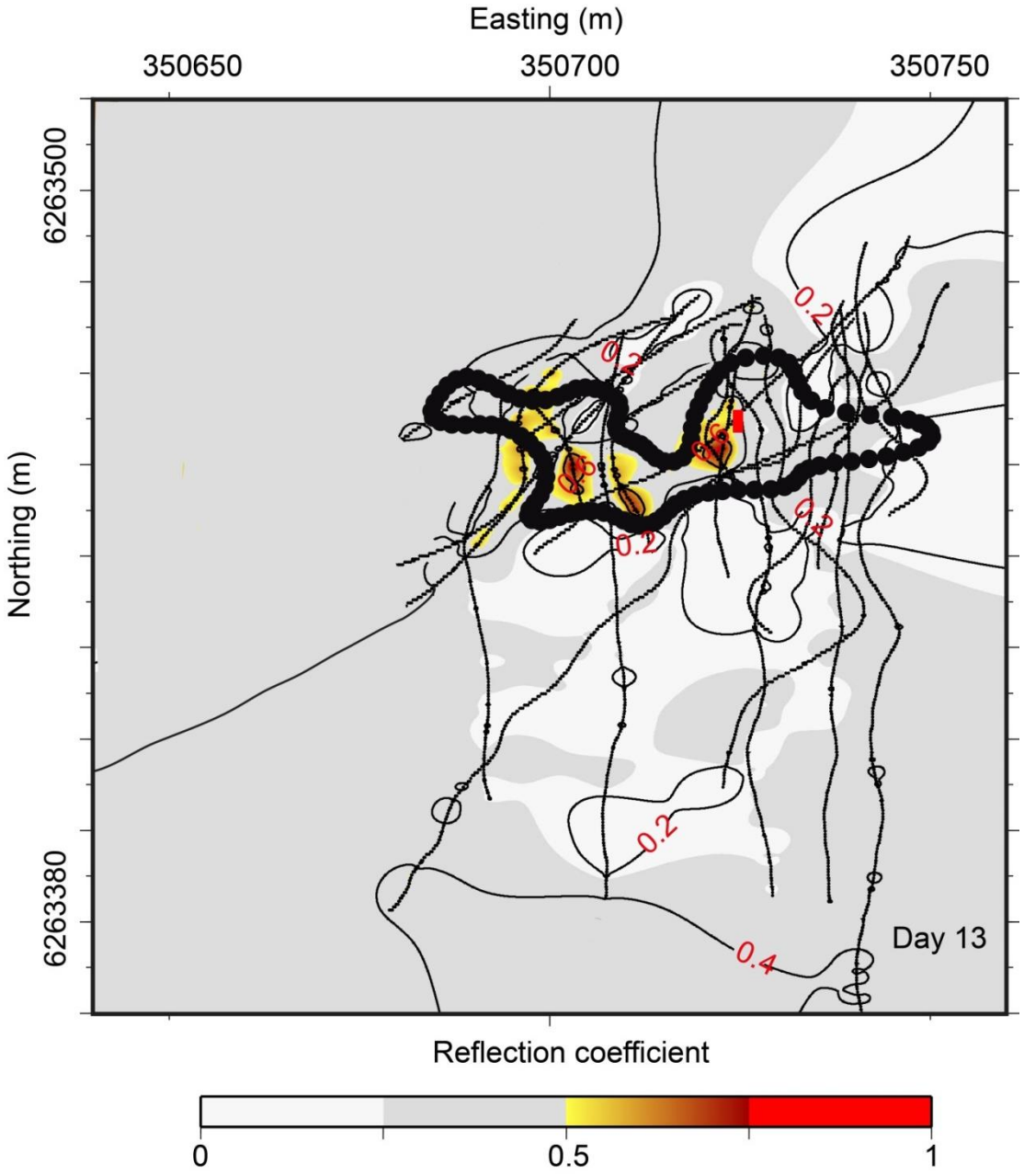

Figure A.7 *The seabed reflectivity changes within the 2D seismic survey area at Day 13.*

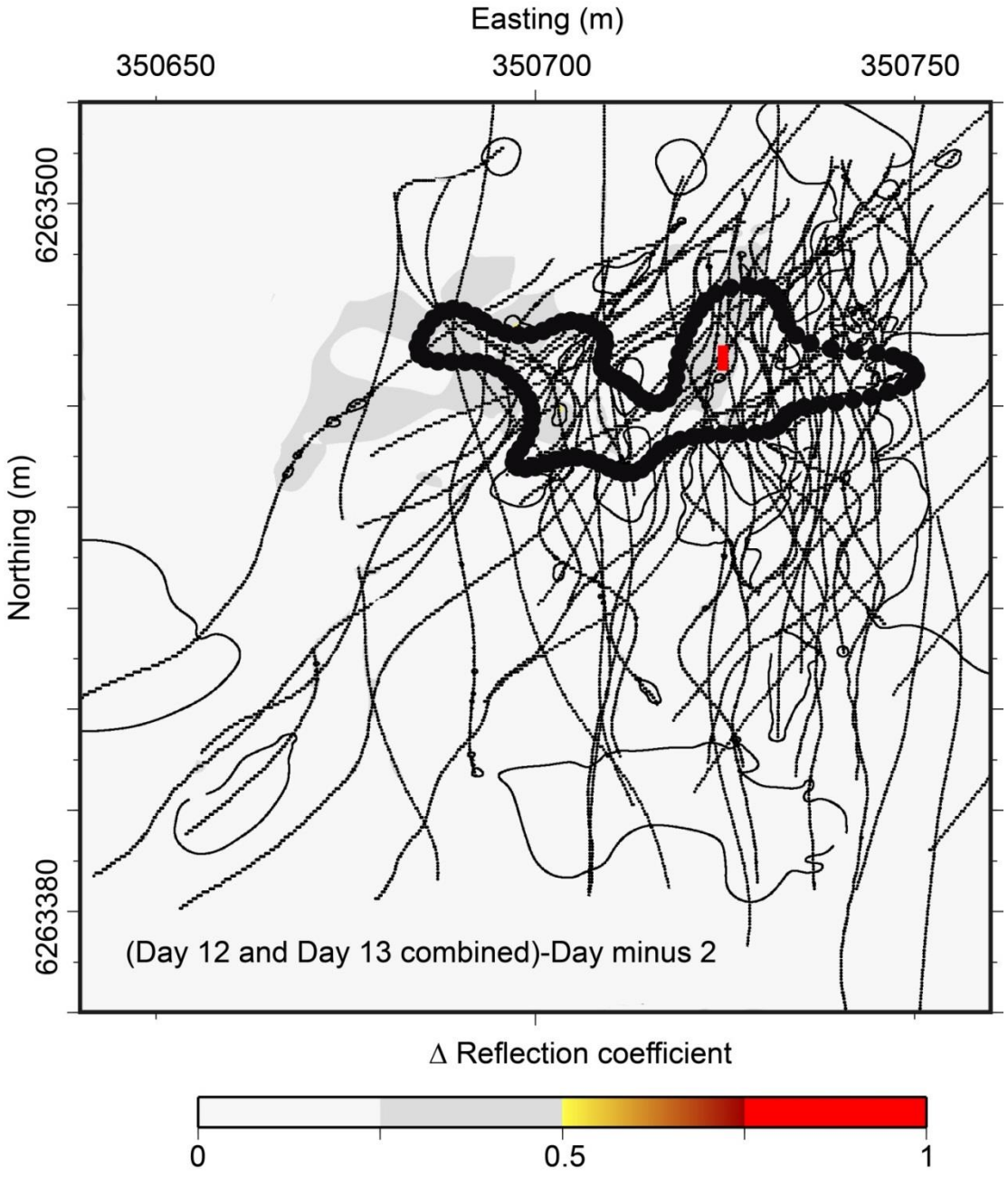

Figure A.8 *The difference in reflectivity changes for the seabed between Day 12-Day 13 and Day minus 2, within the 2D seismic survey area.*

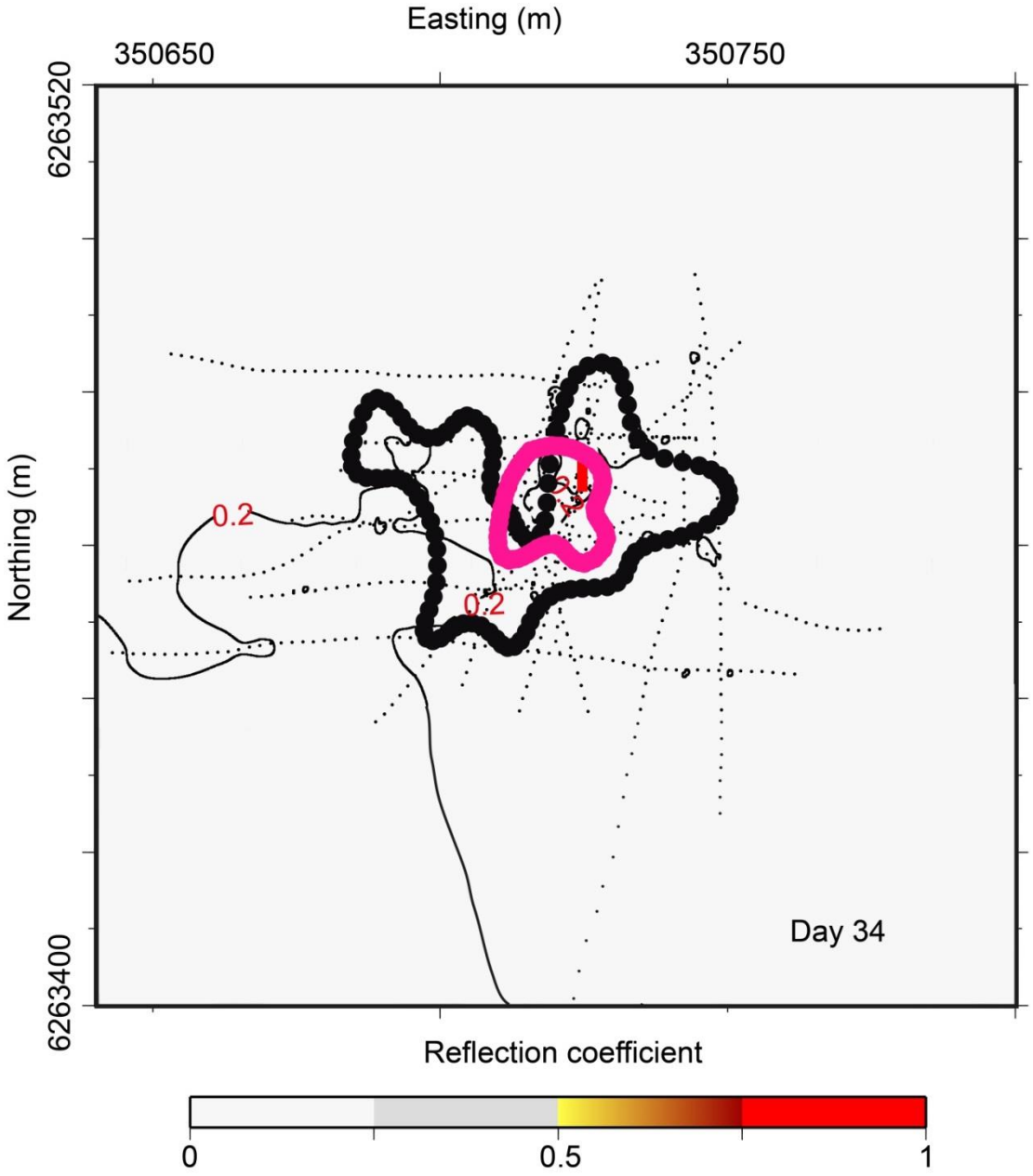

Figure A.9 *The seabed reflectivity changes within the 2D seismic survey area at Day 34.*

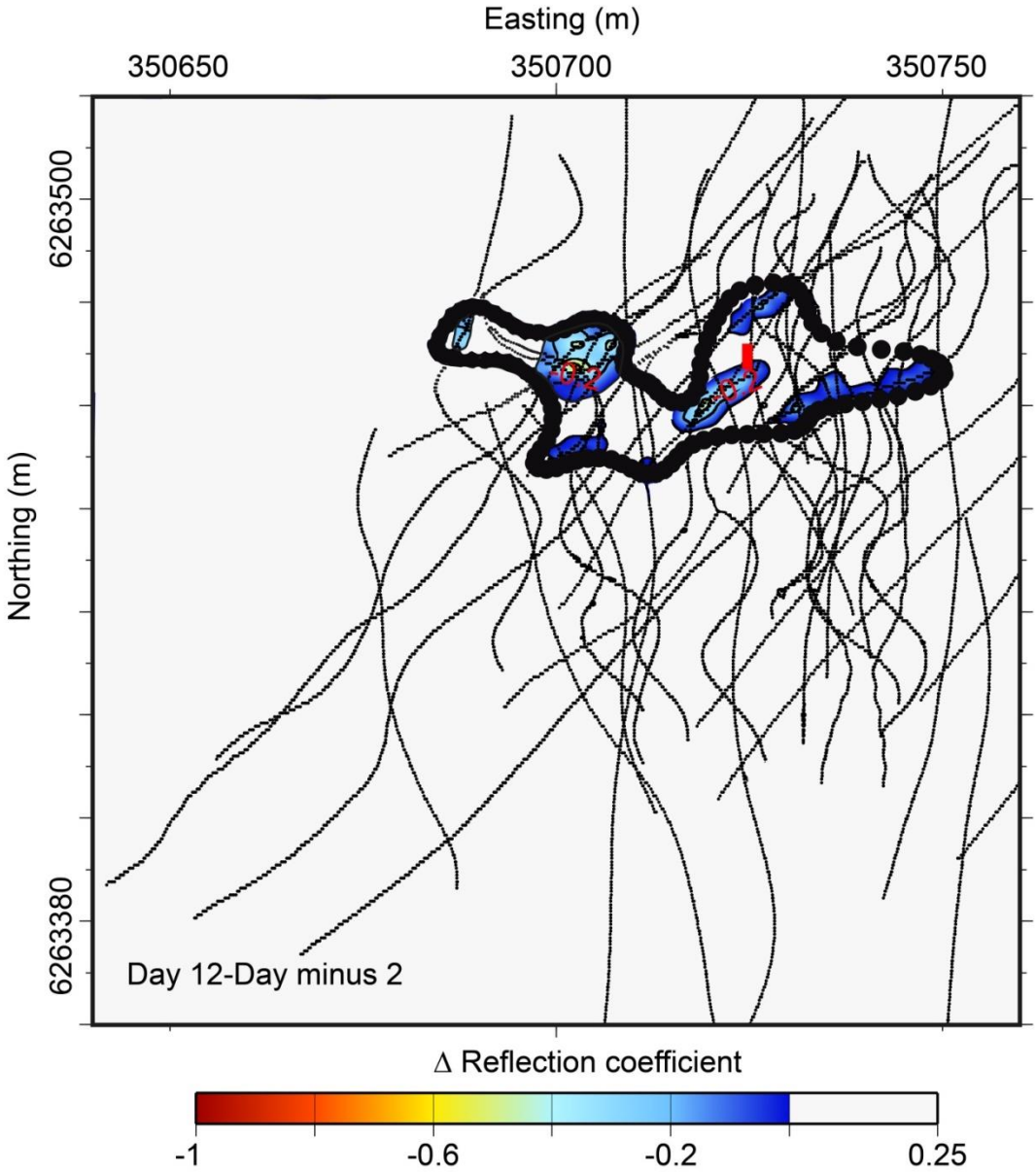

Figure A.10 *Horizon 2 reflectivity changes between Day minus 2 and Day 12, within the 2D seismic survey area.*

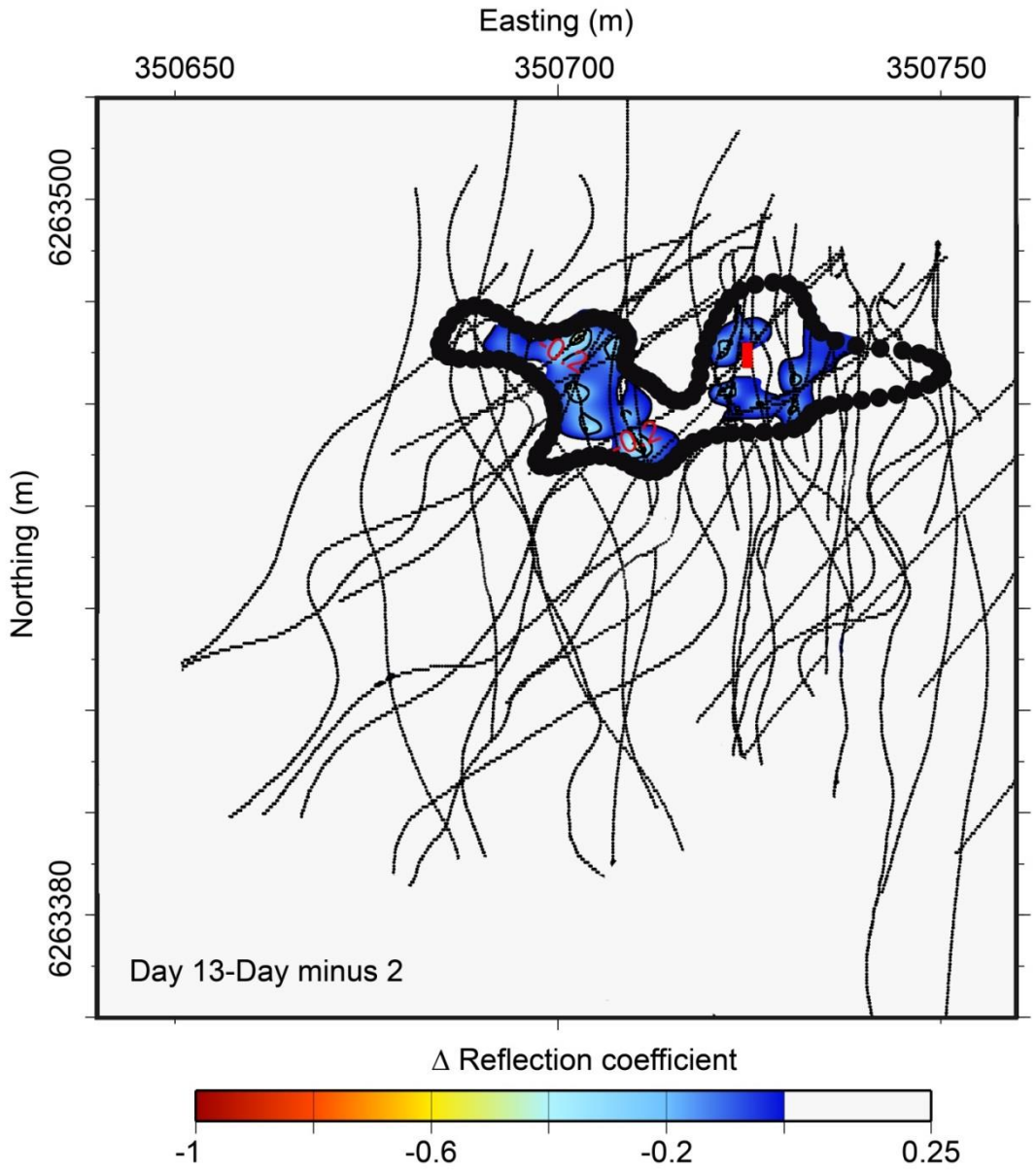

Figure A.11 *Horizon 2 reflectivity changes between Day minus 2 and Day 13, within the 2D seismic survey area.*

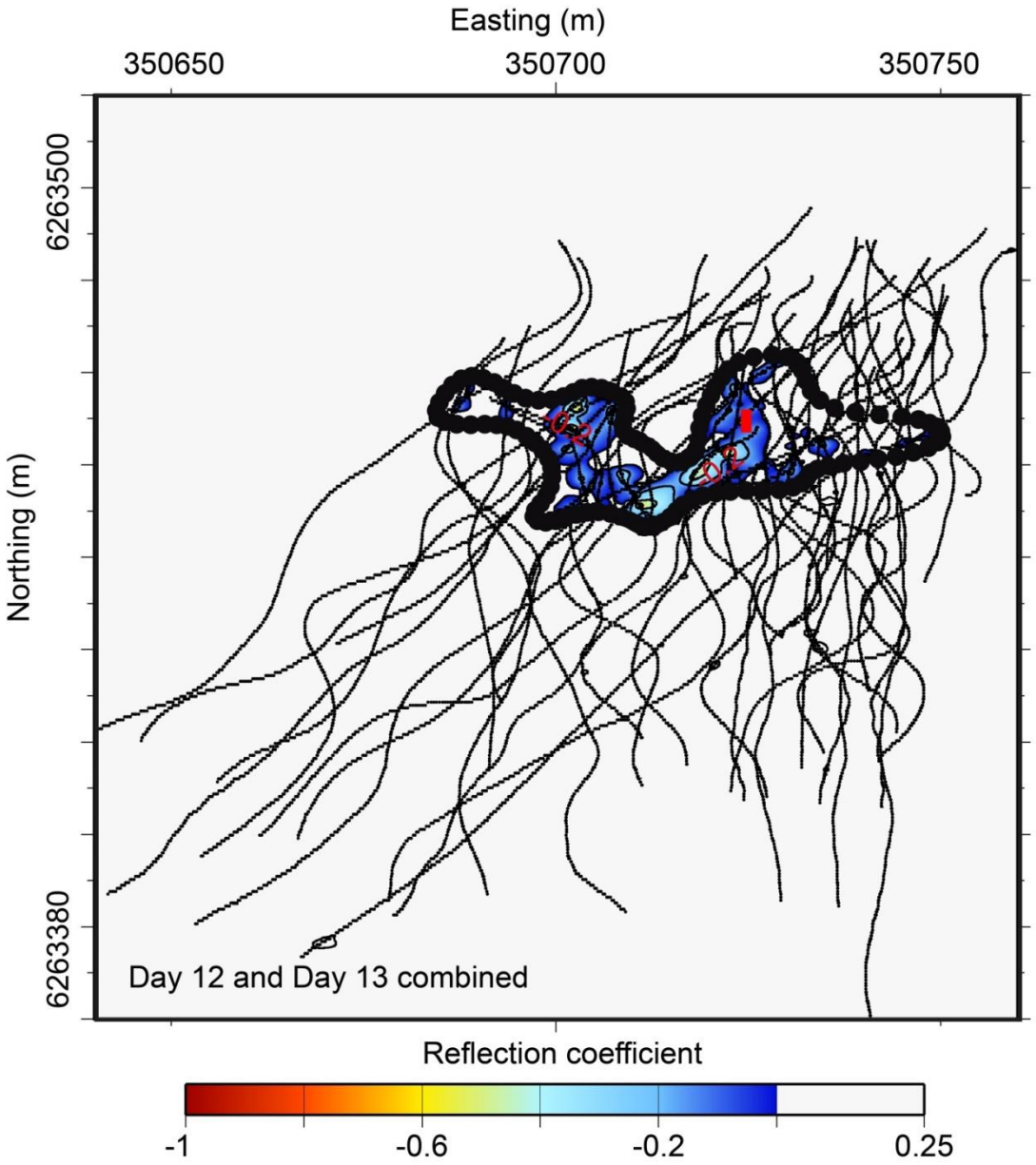

Figure A.12 *The combined reflectivity changes for Horizon 2 from Day 12 and Day 13, within the 2D seismic survey area.*

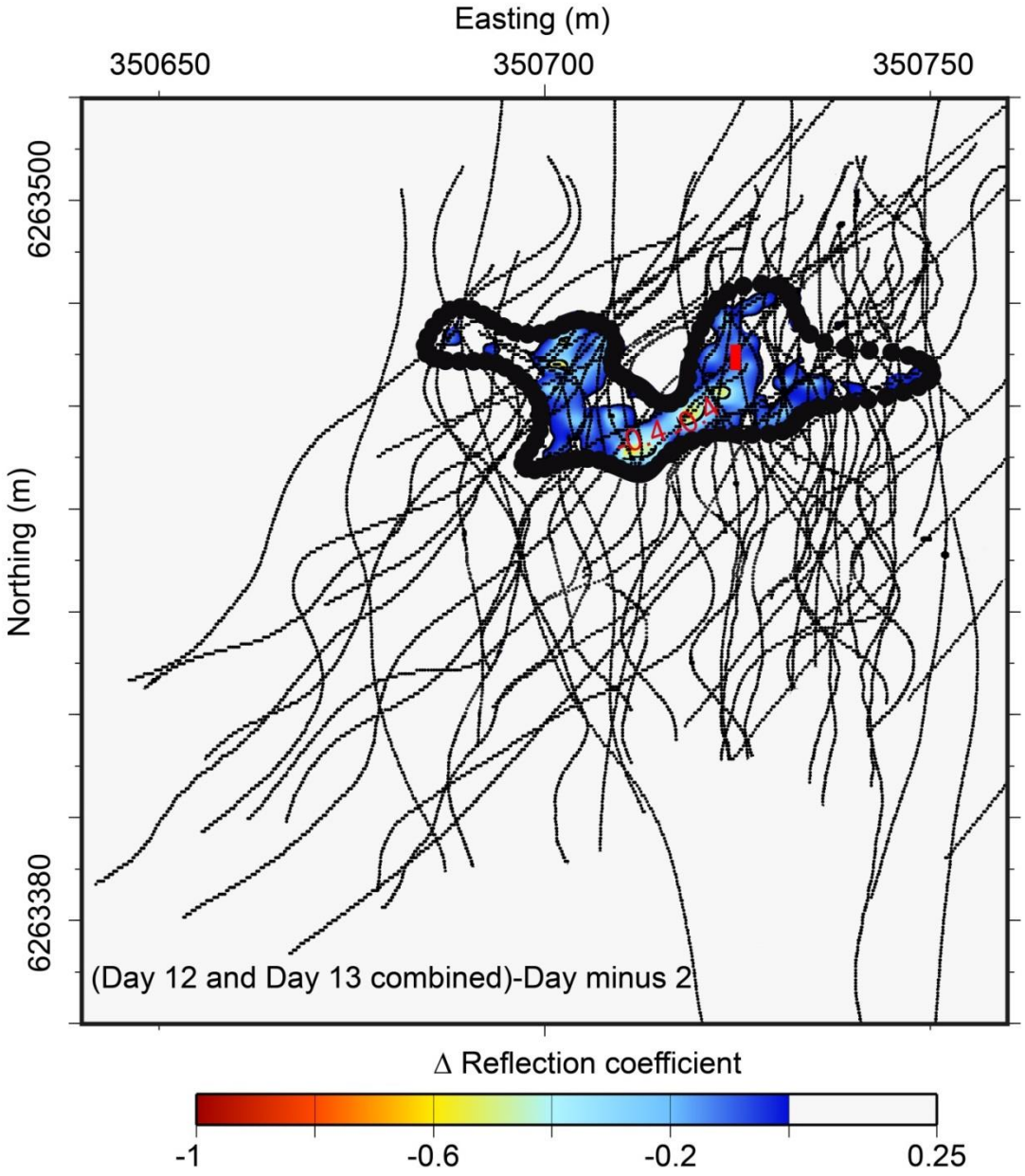

Figure A.13 *The difference in reflectivity changes for Horizon 2 between Day 12-Day 13 and Day minus 2, within the 2D seismic survey area.*

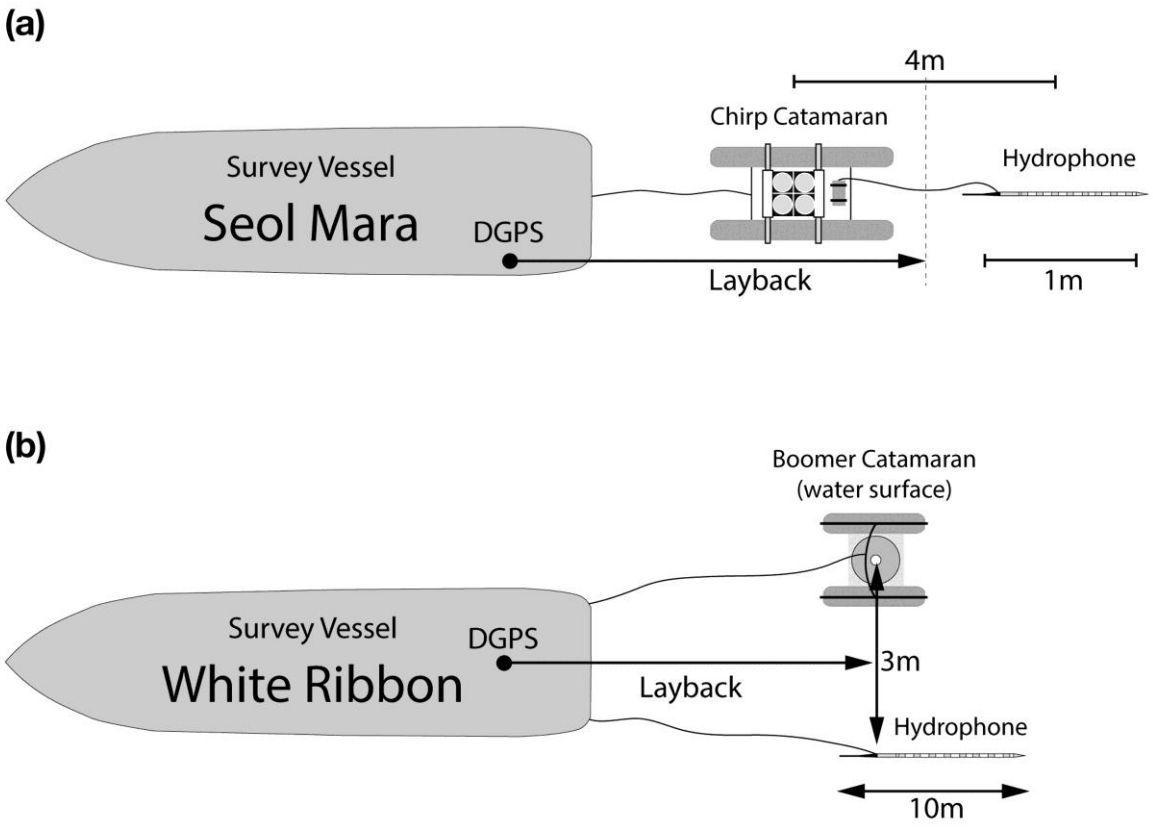

Figure A.14 *Diagrams summarising acquisition geometries for* ***(a)*** *Chirp and* ***(b)*** *Boomer seismic reflection surveying. The data was corrected for layback (the distance between the DGPS position and common mid-point). Both hydrophones were towed within 30 cm of water surface.*

Appendix B

Geophysical instruments mounted on Autosub 6000

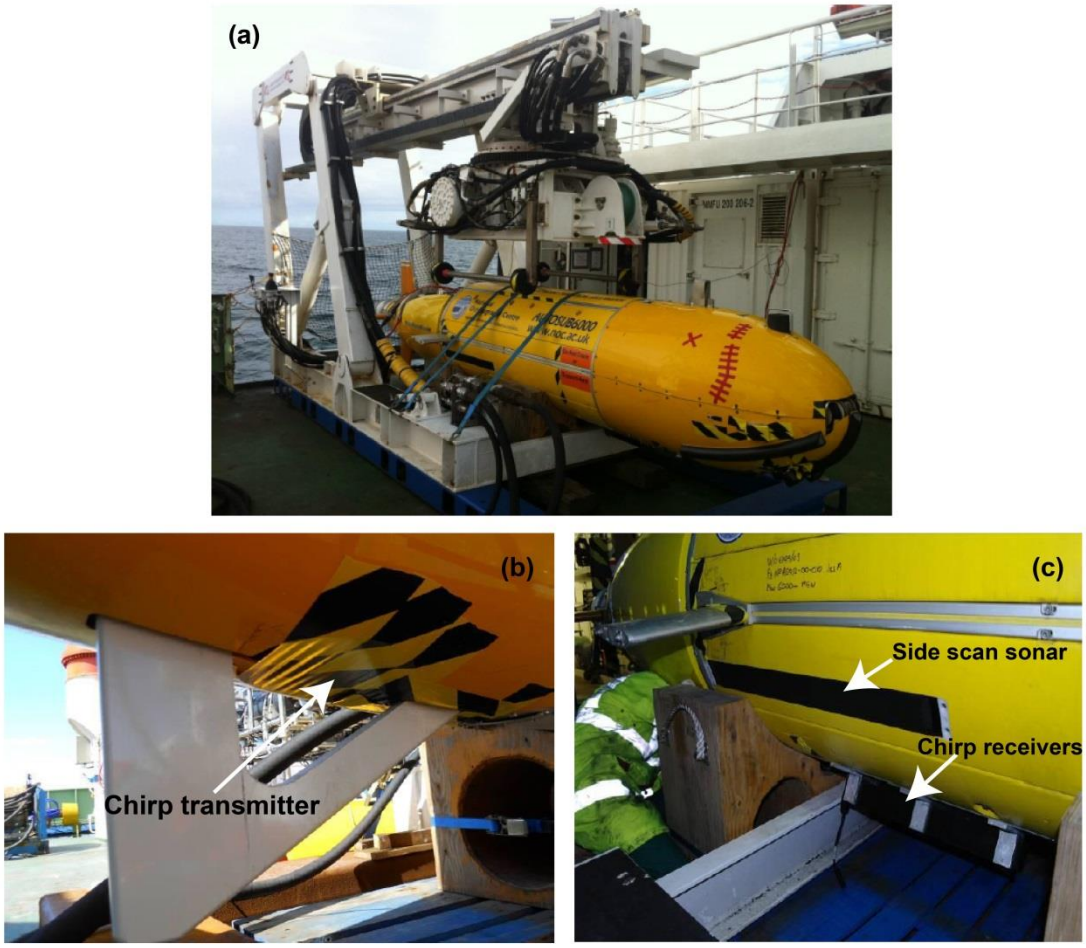

Figure B.1 *Autosub 6000 and geophysical instruments.* ***(a)*** *Autosub 6000 deployment.* ***(b)*** *Chirp transmitter.* ***(c)*** *Side scan sonar and chirp receivers.*

Appendix C

Merging navigation with seismic data headers

```
clear all;
close all;

% Load nav file
[navFileName, navFilePath]=uigetfile('*.mat', 'Select navigation file');
navFile = sprintf('%s%s', navFilePath, navFileName);
navData=load(navFile);

navTime = navData.usTme;
navLat = navData.usNorth;
navLon = navData.usEast;
navDepth = navData.usDepth;
navPitch = navData.usPitch;
navRoll = navData.usRoll;
navHeading = navData.usHeading;
navSpeed = navData.usSpeed;
navAltitude = navData.usAltitude;


% Load jsf file
[jsfFileName,jsfFilePath]=uigetfile('*.jsf', 'Select jsf file'); %open file and assign handle
jsfFile = sprintf('%s%s', jsfFilePath, jsfFileName);
jsfFileID = fopen(jsfFile, 'r');

if -1 == jsfFileID
   display ('cannot open JSF file.');
end

% Open file to write
outputFileID = fopen([jsfFileName(1:end-4), '_output.jsf'], 'w');
if -1 == outputFileID
   display('cannot open output JSF file');
end

messageCount = 0;
copyTime = navTime;
minIndex = 1;
lastPingTime = 0;

disp(sprintf('Begins...\n'));
while (1)
   header = fread(jsfFileID, 8, 'uint16');
   if size(header,2) ~= 1
      break;
   end
```

```
    fwrite(outputFileID, header, 'uint16');

    byteCount = header(7) + header(8) * 256 * 256;
    subNo = floor(header(4) / 256);
    chan = mod(header(5), 256);
    messageType = header(3);
    sonarData = fread(jsfFileID, byteCount, 'uchar');
    if size(sonarData,2) ~= 1
      break;
    end


    if messageType == 80
        messageCount = messageCount+1;
        pingTime = sonarData(1) + ( sonarData(2)+( sonarData(3)+ sonarData(4)*256
)*256 )*256;
        msToday = sonarData(201) + ( sonarData(202) + ( sonarData(203) +
sonarData(204) * 256 ) * 256 ) *256;
        pingTime = pingTime + (msToday/1000 - floor(msToday/1000));

        [minVal, minIndex] = min( abs( pingTime - copyTime ) );

        pingNumber = sonarData(9) + ( sonarData(10) + ( sonarData(11) +
sonarData(12) * 256 ) * 256 ) *256;
%           if pingTime ~= lastPingTime
%              lastPingTime = pingTime;
%              [minVal, minOffset] = min( abs( copyTime - pingTime ) );
%              minIndex = minIndex + minOffset-1;
%              copyTime = copyTime(minOffset:end);
%           end
%
        % check if Nav valid
        if minVal >4 %seconds ???
           disp(sprintf('Nav data invalid, time diff = %d seconds',minVal));
        end

       % timeError(messageCount, :) = [pingNumber, pingTime, navTime( minIndex ),
minIndex, minVal, subNo, chan];

         %          bit 0: lat lon valid
         %          bit 2: speed valid
         %          bit 3: heading valid
         %          bit 5: pitch roll valid
         %          bit 6: altitude valid
         %          bit 9: depth valid
         %
         %          000010 01101101
        validityFlagLowKnown = bin2dec( '01101101' );
        validityFlagHighKnown = bin2dec( '000010' );
        validityFlagLow = sonarData(31);
```

```
        validityFlagHigh = sonarData(32);

        sonarData(31) = bitor( uint8(validityFlagLowKnown) , uint8(validityFlagLow) );
        sonarData(32) = bitor( uint8(validityFlagHighKnown) , uint8(validityFlagHigh)
);

        longi = int32( 10000 * 60 *navLon(minIndex)  );    %  1 degree = 600,000
(miniute of arc * 10^-4)
        sonarData(81:84) = byteSplit32(longi);

        lati = int32( 10000 * 60 * navLat(minIndex) );     % 1 degree = 600,000 (miniute
of arc * 10^-4)
        sonarData(85:88) = byteSplit32(lati);

        coUnits = 2; % Coordinate Units hard coded to 2
        sonarData(89:90) = byteSplit16(coUnits);

        depth = int32 ( 1000 * navDepth(minIndex) ); % depth in millimeters
        sonarData(137:140) = byteSplit32(depth);

        altitude = int32( 1000 * navAltitude(minIndex) ); %altitude in millimeters
        sonarData(145:148) = byteSplit32(altitude);

        heading = uint16( 100 * navHeading(minIndex) ); % Heading (0 to 360) in units
of 1/100 degree
        sonarData(173:174) = byteSplit16(heading);

        pitch = int16( navPitch(minIndex) * 32768 / 180 ); % Scale by 180/32768 to get
degrees
        sonarData(175:176) = byteSplit16(pitch);

        roll = int16( navRoll(minIndex) * 32768 / 180 ); % Scale by 180/32768 to get
degrees
        sonarData(177:178) = byteSplit16(Rollet et al.);

        speed =  int16( 1.9455 * navSpeed(minIndex) * 10 ); %  speed unit: tenths of a
knot
        sonarData(195:196) = byteSplit16(speed);

        % compute time info
        % need function timeConvert() in timeConvert.m file
        [hour, minutes, seconds, days, years] = timeConvert(pingTime);
        sonarData(187:188) = byteSplit16(hour);
        sonarData(189:190) = byteSplit16(minutes);
        sonarData(191:192) = byteSplit16(seconds);
        sonarData(197:198) = byteSplit16(days);
        sonarData(199:200) = byteSplit16(years);

       fwrite(outputFileID, sonarData, 'uint8');
   else
```

```
      fwrite(outputFileID, sonarData, 'uint8');
  end

   if mod(messageCount,100)==0
     disp(sprintf(['message ', num2str(messageCount), '...\n']));
   end

end

disp('Finished...');
fclose(jsfFileID);
fclose(outputFileID);
```

Appendix D

Jsf2Segy Converter Manual

The jsf2segy package is a free software, written by Tom O'Brien (USGS, Woods Hole Coastal and Marine Science Center) in 2004, with last update in 2005. It allows the conversion of Edgetech jsf 512i seismic data format to SEGY Rev_1. This manual describes briefly different folders which come up with this application, summarizes necessary actions that should be taken in order to convert properly jsf format into segy with special emphasis on different steps regarding the compilation of the code.

1) Introduction to different components

Once the package is downloaded from the website (http://sioseis.ucsd.edu/), the user notices that four different folders are present: jsf2segy, lstjsf, msg80, msg82. Each folder has different purposes:

- ⇨ Jsf2segy is the main folder allowing the conversion of jsf format into segy format.
- ⇨ Lstjsf permits to see total numbers of records, lists different data channels (formats) present in a jsf file: envelope, raw (uncorrelated), analytic (correlated) or real for subbotom; port and starboard for sidescan) and provides few parameters of the jsf file header.
- ⇨ Msg80 and Msg82 list some elements of Edgetech message 80/82 jsf files. In other words, they lead to visualize the total number of records on the jsf input file, as well as list Side-Scan Sonar and Subbotom message headers in a more complete way.

2) Deciding what is necessary

If the user has some prior knowledge about the content of the data collected and/or has got JsfFileViewer Application (developed by Edgetech itself) to investigate the input file, the usage of lstjsf, msg80 and msg82 can be skipped. Otherwise, in order to be able to check if the data is converted properly from jsf to segy, the input jsf file should be analysed with using these three tools.

3) Compilation of the code

Although the code is ready, it should be compiled under Unix like environment. To accomplish the compilation, the user needs to have a look to "Makefile", present in each folder: it describes how to compile the related code:

Jsf2segy: gcc jsf2segy.c ascebc.c utils.c –g –m32 –lm –o jsf2segy (compilation of jsf2segy.c creates jsf2segy command)

Lstjsf: gcc lstjsf.c utils.c –g –m32 –lm –o lstjsf (compilation of lstjsf.c creates lstjsf command)

Msg80: gcc msg80.c utils.c –g –m32 –lm –o msg80 (compilation of msg80.c creates msg80 command)

Msg82: gcc msg82.c utils.c –g –m32 –lm –o msg82 (compilation of msg82.c creates msg82 command)

4) Work with the code

Once the code is compiled, it is sufficient to type commands recently created on the terminal. This shows how to use the command and its applications.

jsf2segy

mc4g11@sarge.noc.soton.ac.uk> jsf2segy

jsf2segy ... extracts subbottom data from Edgetech JSF formatted files

Usage: jsf2segy - options first then full path to input file name

Options -e Get Envelope subbottom data

-a Get Analytic (correlated) subbottom data and make Envelope

-r Get Real subbottom data

-u Get Raw (uncorrelated) subbottom data

-o Path and name of output file

Example: jsf2segy –a Data10.jsf –o Data10.sgy ➔ convert analytic (correlated) Data10.jsf to analytic Data10.sgy

jsf2segy –u Data10.jsf –o Data10.sgy ➔ convert raw (uncorrelated) Data10.jsf to raw Data10.sgy

lstjsf

mc4g11@sarge.noc.soton.ac.uk>lstjsf

lstjsf ... Lists Edgetech JSF formatted files

Usage: lstjsf - options full path to input file name

Options -c Get count of Subbottom and Sidescan records

-s List Sidescan Sonar message header

-b List Subbottom message header

Example: lstjsf –c Data10.jsf ➔ Count how many records are in the Data10.jsf file

msg80

mc4g11@sarge.noc.soton.ac.uk>msg80

msg80 ... Lists Edgetech JSF formatted files

Usage: msg80 - options full path to input file name

Options -c Get count of Subbottom and Sidescan records

-s List Sidescan Sonar message header

-b List Subbottom message header

Example: msg80 –s Data10.jsf ➔ List Side-Scan Message Header of the Data10.jsf file

msg82

mc4g11@sarge.noc.soton.ac.uk>msg82

msg82 ... Lists Edgetech JSF formatted files

Usage: msg82 - options full path to input file name

Options -c Get count of Subbottom and Sidescan records

-s List Sidescan Sonar message header

-b List Subbottom message header

Example: msg82 –b Data10.jsf ➔ List Subbotom Message Header of the Data10.jsf file

5) Several notes for the user

In addition to available possibilities of jsf2segy package, the source code can also be improved, depending on the necessities. Therefore, with the aim of extracting the raw data collected by Edgetech 2200-M system, and converting it into segy format, the original code is modified. Thus, the actual code can deal both with uncorrelated (Götz et al.) and correlated (analytic) data formats and the segy data can be easily imported into any seismic processing softwares.

BIBLIOGRAPHY

Adam, L., Batzle, M., Brevik, I., 2006. Gassmann's fluid substitution and shear modulus variability in carbonates at laboratory seismic and ultrasonic frequencies. Geophysics 71, F173-F183.

Al Hseinat, M., Hübscher, C., 2014. Ice-load induced tectonics controlled tunnel valley evolution–instances from the southwestern Baltic Sea. Quaternary Science Reviews 97, 121-135.

Alnes, H., Eiken, O., Nooner, S., Sasagawa, G., Stenvold, T., Zumberge, M., 2011. Results from Sleipner gravity monitoring: Updated density and temperature distribution of the CO_2 plume. Energy Procedia 4, 5504-5511.

Andersen, O., Nilsen, H.M., Lie, K.-A., 2014. Reexamining CO_2 storage capacity and utilization of the Utsira Formation, ECMOR XIV-14th European Conference on the Mathematics of Oil Recovery, Sicily, Italy.

Anderson, A., Abegg, F., Hawkins, J., Duncan, M., Lyons, A., 1998a. Bubble populations and acoustic interaction with the gassy floor of Eckernförde Bay. Continental Shelf Research 18, 1807-1838.

Anderson, A., Abegg, F., Hawkins, J., Duncan, M., Lyons, A.P., 1998b. Bubble populations and acoustic interaction with the gassy floor of Eckernförde Bay. Continental Shelf Research 18, 1807-1838.

Anderson, A.L., Hampton, L.D., 1980a. Acoustics of gas-bearing sediments I. Background. The Journal of the Acoustical Society of America 67, 1865-1889.

Anderson, A.L., Hampton, L.D., 1980b. Acoustics of gas-bearing sediments. II. Measurements and models. The Journal of the Acoustical Society of America 67, 1890-1903.

Andreassen, K., Hart, P.E., MacKay, M., 1997. Amplitude versus offset modeling of the bottom simulating reflection associated with submarine gas hydrates. Marine Geology 137, 25-40.

Annunziatellis, A., Beaubien, S., Bigi, S., Ciotoli, G., Coltella, M., Lombardi, S., 2008. Gas migration along fault systems and through the vadose zone in the Latera caldera (central Italy): implications for CO_2 geological storage. International Journal of Greenhouse Gas Control 2, 353-372.

Anstey, N., 1977. Seismic Interpretation: The Physical Aspects: Being a Record of the Short Course, The New Seismic Interpreter. International Human Resources Development Corporation, Boston,USA.

Appelgate, B., Goldfinger, C., MacKay, M.E., Kulm, L.D., Fox, C.G., Embley, R.W., Meis, P.J., 1992. A left-lateral strike-slip fault seaward of the Oregon Convergent Margin. Tectonics 11, 465-477.

Arts, R., Chadwick, A., Eiken, O., Thibeau, S., Nooner, S., 2008. Ten years' experience of monitoring CO_2 injection in the Utsira Sand at Sleipner, offshore Norway. First Break, Special Topic CO_2 sequestration 26, 65-72.

Arts, R., Eiken, O., Chadwick, A., Zweigel, P., van der Meer, B., Kirby, G., 2004a. Seismic monitoring at the Sleipner underground CO_2 storage site (North Sea). Geological Society, London, Special Publications 233, 181-191.

Arts, R., Eiken, O., Chadwick, A., Zweigel, P., Van der Meer, L., Zinszner, B., 2004b. Monitoring of CO_2 injected at Sleipner using time-lapse seismic data. Energy 29, 1383-1392.

Arts, R.J., Zweigel, P., Lothe, A.E., 2000. Reservoir geology of the Utsira Sand in the Southern Viking Graben area–a site for potential CO_2 storage, 62nd EAGE Conference, Glasgow, Scotland.
Atamanchuk, D., Tengberg, A., Aleynik, D., Fietzek, P., Shitashima, K., Lichtschlag, A., Hall, P.O., Stahl, H., 2015. Detection of CO_2 leakage from a simulated sub-seabed storage site using three different types of pCO_2 sensors. International Journal of Greenhouse Gas Control 38, 121-134.
Aydin, A., Berryman, J.G., 2010. Analysis of the growth of strike-slip faults using effective medium theory. Journal of Structural Geology 32, 1629-1642.
Aydin, A., Schultz, R.A., 1990. Effect of mechanical interaction on the development of strike-slip faults with echelon patterns. Journal of Structural Geology 12, 123-129.
Azdarpour, A., Asadullah, M., Junin, R., Manan, M., Hamidi, H., Daud, A.R.M., 2014. Carbon dioxide mineral carbonation through pH-swing process: a review. Energy Procedia 61, 2783-2786.
Ba, J., Cao, H., Carcione, J.M., Tang, G., Yan, X.-F., Sun, W.-t., Nie, J.-x., 2013. Multiscale rock-physics templates for gas detection in carbonate reservoirs. Journal of Applied Geophysics 93, 77-82.
Bachman, R.T., 1985. Acoustic and physical property relationships in marine sediment. The Journal of the Acoustical Society of America 78, 616-621.
Bachu, S., 2008. CO_2 storage in geological media: Role, means, status and barriers to deployment. Progress in Energy and Combustion Science 34, 254-273.
Bachu, S., Celia, M.A., 2009. Assessing the potential for CO_2 leakage, particularly through wells, from geological storage sites, Carbon Sequestration and Its Role in the Global Carbon Cycle, AGU Geophysical Monograph Series, 203-216.
Baeten, N.J., Laberg, J.S., Vanneste, M., Forsberg, C.F., Kvalstad, T.J., Forwick, M., Vorren, T.O., Haflidason, H., 2014. Origin of shallow submarine mass movements and their glide planes—Sedimentological and geotechnical analyses from the continental slope off northern Norway. Journal of Geophysical Research: Earth Surface 119, 2335-2360.
Baker, E.T., Massoth, G.J., Nakamura, K.i., Embley, R.W., de Ronde, C.E., Arculus, R.J., 2005. Hydrothermal activity on near-arc sections of back-arc ridges: Results from the Mariana Trough and Lau Basin. Geochemistry, Geophysics, Geosystems 6, 1-14.
Baklid, A., Korbøl, R., Owren, G., 1996. Sleipner Vest CO_2 disposal, CO_2 injection into a shallow underground aquifer, SPE Annual Technical Conference. Society of Petroleum Engineers, Denver, Colorado.
Bala, G., 2013. Digesting 400 ppm for global mean CO_2 concentration. Current Science 104.
Bangs, N.L., Hornbach, M.J., Berndt, C., 2011. The mechanics of intermittent methane venting at South Hydrate Ridge inferred from 4D seismic surveying. Earth and Planetary Science Letters 310, 105-112.
Baristeas, N., Anka, Z., Di Primio, R., Rodriguez, J., Marchal, D., Dominguez, F., 2012. Distribution of hydrocarbon leakage indicators in the Malvinas Basin, offshore Argentine continental margin. Marine Geology 332, 56-74.
Barry, J.P., Buck, K.R., Lovera, C.F., Kuhnz, L., Whaling, P.J., Peltzer, E.T., Walz, P., Brewer, P.G., 2004. Effects of direct ocean CO_2 injection on deep-sea meiofauna. Journal of Oceanography 60, 759-766.
Barry, M., Boudreau, B., Johnson, B., Reed, A., 2010. First-order description of the mechanical fracture behavior of fine-grained surficial marine sediments during gas bubble growth. Journal of Geophysical Research: Earth Surface 115, F04029.

Bartolome, R., Gràcia, E., Stich, D., Martínez-Loriente, S., Klaeschen, D., de Lis Mancilla, F., Iacono, C.L., Dañobeitia, J.J., Zitellini, N., 2012. Evidence for active strike-slip faulting along the Eurasia-Africa convergence zone: Implications for seismic hazard in the southwest Iberian margin. Geology 40, 495-498.
Belardinelli, M.E., Bonafede, M., Gudmundsson, A., 2000. Secondary earthquake fractures generated by a strike-slip fault in the South Iceland Seismic Zone. Journal of Geophysical Research: Solid Earth (1978–2012) 105, 13613-13629.
Bellefleur, G., Riedel, M., Huang, J., Saeki, T., Milkereit, B., Ramachandran, K., Brent, T., 2012. Seismic characterization of gas hydrate accumulations in a permafrost environment: lessons learned from Mallik, Northwest Territories, Canada. Geological Survey of Canada Bulletin 601, 1-14.
Benson, S.M., Hepple, R., Apps, J., Tsang, C.-F., Lippmann, M., 2002. Lessons learned from natural and industrial analogues for storage of carbon dioxide in deep geological formations, Lawrence Berkeley National Laboratory, Berkely, USA.
Bergès, B.J., Leighton, T.G., White, P.R., 2015. Passive acoustic quantification of gas fluxes during controlled gas release experiments. International Journal of Greenhouse Gas Control 38, 64-79.
Berndt, C., 2005. Focused fluid flow in passive continental margins. Philosophical Transactions of the Royal Society of London A: Mathematical, Physical and Engineering Sciences 363, 2855-2871.
Berndt, C., Bünz, S., Mienert, J., 2003. Polygonal fault systems on the mid-Norwegian margin: a long-term source for fluid flow. Geological Society, London, Special Publications 216, 283-290.
Berryman, J.G., 1999. Origin of Gassmann's equations. Geophysics 64, 1627-1629.
Best, A., McCann, C., Sothcott, J., 1994. The relationships between the velocities, attenuations and petrophysical properties of reservoir sedimentary rocks. Geophysical Prospecting 42, 151-178.
Best, A.I., Richardson, M.D., Boudreau, B.P., Judd, A.G., Leifer, I., Lyons, A.P., Martens, C.S., Orange, D.L., Wheeler, S.J., 2006. Shallow seabed methane gas could pose coastal hazard. EOS, Transactions American Geophysical Union 87, 213-217.
Best, A.I., Tuffin, M.D., Dix, J.K., Bull, J.M., 2004. Tidal height and frequency dependence of acoustic velocity and attenuation in shallow gassy marine sediments. Journal of Geophysical Research: Solid Earth 109, B08101, 1-17.
Bettelheim, F.A., Brown, W.H., Campbell, M.K., Farrell, S.O., Torres, O.J., 2015. Introduction to general, organic and biogeochemistry. Cengage Learning, Boston, USA.
Bickle, M., Chadwick, A., Huppert, H.E., Hallworth, M., Lyle, S., 2007. Modelling carbon dioxide accumulation at Sleipner: Implications for underground carbon storage. Earth and Planetary Science Letters 255, 164-176.
Bickle, M.J., 2009. Geological carbon storage. Nature Geoscience 2, 815-818.
Blackford, J., Hattam, C., Widdicombe, S., Burnside, N., Naylor, M., Maul, P., Kirk, K., Wright, I., 2013. CO_2 leakage from geological storage facilities: environmental, societal and economic impacts, monitoring and research strategies, in: Gluyas, J., Mathias, S. (Eds.), Geological Storage of Carbon Dioxide (CO_2): Geoscience, Technologies, Environmental Aspects and Legal Frameworks. Woodhead Publishing, Cambridge, UK, 149-178.
Blackford, J., Stahl, H., Bull, J.M., Berges, B.J.P., Cevatoglu, M., Lichtschlag, A., Connelly, D., James, R.H., Kita, J., Long, D., Naylor, M., Shitashima, K., Smith, D., Taylor, P., Wright, I., Akhurst, M., Chen, B., Gernon, T.M., Hauton, C., Hayashi, M., Kaieda, H., Leighton, T.G., Sato, T., Sayer, M.D.J., Suzumura, M., Tait, K., Vardy, M.E., White, P.R., Widdicombe, S., 2014. Detection and impacts of leakage from sub-

seafloor deep geological carbon dioxide storage. Nature Climate Change 4(11), 1011-1016.
Boait, F., White, N., Bickle, M., Chadwick, R., Neufeld, J., Huppert, H., 2012. Spatial and temporal evolution of injected CO_2 at the Sleipner Field, North Sea. Journal of Geophysical Research 117, B033309.
Bolster, D., 2014. The fluid mechanics of dissolution trapping in geologic storage of CO_2. Journal of Fluid Mechanics 740, 1-4.
Borgos, H.D., Dahl, G.V., Halvorsen, K.A., Iversen, T., Lygren, M., Nickel, M., Randen, T., Skov, T., Tjostheim, B.A., 2002. SACS2 Final Report by GECO. Schlumberger Stavanger Research, Stavanger, Norway, 1-53.
Boudreau, B.P., Algar, C., Johnson, B.D., Croudace, I., Reed, A., Furukawa, Y., Dorgan, K.M., Jumars, P.A., Grader, A.S., Gardiner, B.S., 2005. Bubble growth and rise in soft sediments. Geology 33, 517-520.
Bradshaw, J., Bachu, S., Bonijoly, D., Burruss, R., Holloway, S., Christensen, N.P., Mathiassen, O.M., 2007. CO_2 storage capacity estimation: issues and development of standards. International Journal of Greenhouse Gas Control 1, 62-68.
Brent, G.F., Allen, D.J., Eichler, B.R., Petrie, J.G., Mann, J.P., Haynes, B.S., 2012. Mineral carbonation as the core of an industrial symbiosis for energy-intensive minerals conversion. Journal of Industrial Ecology 16, 94-104.
Brogi, A., 2011. Variation in fracture patterns in damage zones related to strike-slip faults interfering with pre-existing fractures in sandstone (Calcione area, southern Tuscany, Italy). Journal of Structural Geology 33, 644-661.
Brothers, D.S., Ruppel, C., Kluesner, J., Brink, U., Chaytor, J.D., Hill, J.C., Andrews, B.D., Flores, C., 2014. Seabed fluid expulsion along the upper slope and outer shelf of the US Atlantic continental margin. Geophysical Research Letters 41, 96-101.
Brudy, M., Kjørholt, H., 2001. Stress orientation on the Norwegian continental shelf derived from borehole failures observed in high-resolution borehole imaging logs. Tectonophysics 337, 65-84.
Bui, H., Graham, J., Kumar Singh, S., Snyder, F., Smith, M., 2011. Incorporation of geology with rock physics enables subsalt poststack inversion: A case study in the Gulf of Mexico. Geophysics 76, WB53-WB65.
Bull, J.M., Quinn, R., Dix, J.K., 1998. Reflection coefficient calculation from marine high resolution seismic reflection (Chirp) data and application to an archaeological case study. Marine Geophysical Researches 20, 1-11.
Bünz, S., Plaza-Faverola, A., Hurter, S., Mienert, J., 2014. 4D seismic study of active gas seepage systems on the Vestnesa Ridge, offshore W-Svalbard, EGU General Assembly Conference Abstracts, p. 16026.
Bünz, S., Polyanov, S., Vadakkepuliyambatta, S., Consolaro, C., Mienert, J., 2012. Active gas venting through hydrate-bearing sediments on the Vestnesa Ridge, offshore W-Svalbard. Marine Geology 332, 189-197.
Burnside, N., Naylor, M., 2014. Review and implications of relative permeability of CO_2/brine systems and residual trapping of CO_2. International Journal of Greenhouse Gas Control 23, 1-11.
Cadoret, T., Marion, D., Zinszner, B., 1995. Influence of frequency and fluid distribution on elastic wave velocities in partially saturated limestones. Journal of Geophysical Research: Solid Earth (1978–2012) 100, 9789-9803.
Caldeira, K., Wickett, M.E., 2005. Ocean model predictions of chemistry changes from carbon dioxide emissions to the atmosphere and ocean. Journal of Geophysical Research: Oceans (1978–2012) 110, C09S04.

Cameron, T., Stoker, M., Long, D., 1987. The history of Quaternary sedimentation in the UK sector of the North Sea Basin. Journal of the Geological Society 144, 43-58.
Canadell, J.G., Raupach, M.R., 2008. Managing forests for climate change mitigation. Science 320, 1456-1457.
Carcione, J.M., Picotti, S., 2006. P-wave seismic attenuation by slow-wave diffusion: Effects of inhomogeneous rock properties. Geophysics 71, O1-O8.
Carlsen, I.M., Mjaaland, S., Nyhavn, F., Nakken, E., 2001. SACS2, Monitoring well scenarios. SINTEF Petroleum Research, Trondheim, Norway, 1-43.
Cartwright, J., 2011. Diagenetically induced shear failure of fine-grained sediments and the development of polygonal fault systems. Marine and Petroleum Geology 28, 1593-1610.
Cartwright, J., 2014. Are outcrop studies the key to understanding the origins of polygonal fault systems? Geology 42, 559-560.
Cartwright, J., James, D., Bolton, A., 2003. The genesis of polygonal fault systems: a review. Geological Society, London, Special Publications 216, 223-243.
Cartwright, J., Lonergan, L., 1996. Volumetric contraction during the compaction of mudrocks: A mechanism for the development of regional-scale polygonal fault systems. Basin Research 8, 183-193.
Cartwright, J.A., 1994. Episodic basin-wide fluid expulsion from geopressured shale sequences in the North Sea basin. Geology 22, 447-450.
Cathles, L., Su, Z., Chen, D., 2010. The physics of gas chimney and pockmark formation, with implications for assessment of seafloor hazards and gas sequestration. Marine and Petroleum Geology 27, 82-91.
Cavanagh, A.J., Haszeldine, R.S., 2014. The Sleipner storage site: Capillary flow modeling of a layered CO_2 plume requires fractured shale barriers within the Utsira Formation. International Journal of Greenhouse Gas Control 21, 101-112.
Celia, M.A., Nordbotten, J.M., 2009. Practical modeling approaches for geological storage of carbon dioxide. Ground Water 47, 627-638.
Cevatoglu, M., Bull, J.M., Vardy, M.E., Gernon, T.M., Wright, I.C., Long, D., 2015. Gas migration pathways, controlling mechanisms and changes in sediment acoustic properties observed in a controlled sub-seabed CO_2 release experiment. International Journal of Greenhouse Gas Control 38, 26-43.
Chadwick, A., Arts, R., Bernstone, C., May, F., Thibeau, S., Zweigel, P., 2008. Best practice for the storage of CO_2 in saline aquifers, Observations and guidelines from the SACS and CO2STORE projects. British Geological Survey Keyworth, Nottingham.
Chadwick, A., Arts, R., Eiken, O., Williamson, P., Williams, G., 2006. Geophysical monitoring of the CO_2 plume at Sleipner, North Sea, Advances in the Geological Storage of Carbon Dioxide. NATO Science, IV Earth and Environmental Sciences. Springer, Netherlands, 303-314.
Chadwick, A., Williams, G., Delepine, N., Clochard, V., Labat, K., Sturton, S., Buddensiek, M.-L., Dillen, M., Nickel, M., Lima, A.L., 2010. Quantitative analysis of time-lapse seismic monitoring data at the Sleipner CO_2 storage operation. The Leading Edge 29, 170-177.
Chadwick, R., Arts, R., Eiken, O., 2005. 4D seismic quantification of a growing CO_2 plume at Sleipner, North Sea, in: Dore, A., Vining, B. (Eds.), Petroleum Geology: North-West Europe and Global Perspectives - Proceedings of the 6th Petroleum Geology Conference. . Geological Society of London, London, 1385-1399.
Chadwick, R., Eiken, O., 2013. Offshore CO_2 storage: Sleipner natural gas field beneath the North Sea, in: Gluyas, J., Mathias, S. (Eds.), Geological Storage of Carbon

Dioxide (CO_2): Geoscience, Technologies, Environmental Aspects and Legal Frameworks. Woodhead Publishing, Cambridge, UK, p. 227.
Chadwick, R., Holloway, S., Brook, M., Kirby, G., 2004a. The case for underground CO_2 sequestration in northern Europe. Geological Society, London, Special Publications 233, 17-28.
Chadwick, R., Holloway, S., Kirby, G., Gregersen, U., Johannessen, P., 2000. The Utsira Sand, Central North Sea–an assessment of its potential for regional CO_2 disposal, Proceedings of the 5th International Conference on Greenhouse Gas Control Technologies (GHGT-5), Cairns, Australia, 349-354.
Chadwick, R., Noy, D., 2010. History-matching flow simulations and time-lapse seismic data from the Sleipner CO_2 plume, in: Vining, B., Pickering, S. (Eds.), Petroleum Geology: From Mature basins to New Frontiers - Proceedings of the 7th Petroleum Geology Conference. Geological Society of London, London, 1171-1182.
Chadwick, R., Noy, D., Arts, R., Eiken, O., 2009. Latest time-lapse seismic data from Sleipner yield new insights into CO_2 plume development. Energy Procedia 1, 2103-2110.
Chadwick, R., Williams, G., Williams, J., Noy, D., 2012. Measuring pressure performance of a large saline aquifer during industrial-scale CO_2 injection: The Utsira Sand, Norwegian North Sea. International Journal of Greenhouse Gas Control 10, 374-388.
Chadwick, R., Zweigel, P., Gregersen, U., Kirby, G., Holloway, S., Johannessen, P., 2004b. Geological reservoir characterization of a CO_2 storage site: The Utsira Sand, Sleipner, northern North Sea. Energy 29, 1371-1381.
Chadwick, R.A., Marchant, B.P., Williams, G.A., 2014. CO_2 storage monitoring: leakage detection and measurement in subsurface volumes from 3D seismic data at Sleipner. Energy Procedia 63, 4224-4239.
Chen, D., Wu, S., Wang, X., Lv, F., 2011. Seismic expression of polygonal faults and its impact on fluid flow migration for gas hydrates formation in deep water of the South China Sea. Journal of Geological Research 2011, 1-7.
Chow, A., 2014. Ocean Carbon Sequestration by Direct Injection, in: Esteves, V., Morgado, C. (Eds.), CO_2 Sequestration and Valorization. InTech, p. 470.
Chu, S., Majumdar, A., 2012. Opportunities and challenges for a sustainable energy future. Nature 488, 294-303.
Cunningham, W., Mann, P., 2007. Tectonics of strike-slip restraining and releasing bends. Geological Society, London, Special Publications 290, 1-12.
Dahm, T., 2000. On the shape and velocity of fluid-filled fractures in the Earth. Geophysical Journal International 142, 181-192.
Damen, K., Faaij, A., Turkenburg, W., 2006. Health, safety and environmental risks of underground CO_2 storage-overview of mechanisms and current knowledge. Climatic Change 74, 289-318.
Das, P.K., 2006. Seismic expression of layer bound polygonal fault system: An example from Bass Basin of Australia, Proceedings of the 6th International Conference & Exposition on Petroleum Geophysics, Kolkata, India, 606-614.
De Joussineau, G., Mutlu, O., Aydin, A., Pollard, D.D., 2007. Characterization of strike-slip fault–splay relationships in sandstone. Journal of Structural Geology 29, 1831-1842.
Deegan, C.t., Scull, B.J., 1977. A standard lithostratigraphic nomenclature for the Central and Northern North Sea, Report 77/25, Bulletin 1. HMSO, London.
Den Elzen, M., Meinshausen, M., 2006. Meeting the EU 2^{o}C climate target: global and regional emission implications. Climate Policy 6, 545-564.

Dewar, M., Sellami, N., Chen, B., 2015. Dynamics of rising CO_2 bubble plumes in the QICS field experiment: Part 2–Modelling. International Journal of Greenhouse Gas Control 38, 52-63.
Doney, S.C., Fabry, V.J., Feely, R.A., Kleypas, J.A., 2009. Ocean acidification: the other CO_2 problem. Marine Science 1, 169-192.
Dowdeswell, J., Ottesen, D., 2013. Buried iceberg ploughmarks in the early Quaternary sediments of the central North Sea: A two-million year record of glacial influence from 3D seismic data. Marine Geology 344, 1-9.
Dupré, S., Woodside, J., Foucher, J.-P., De Lange, G., Mascle, J., Boetius, A., Mastalerz, V., Stadnitskaia, A., Ondréas, H., Huguen, C., 2007. Seafloor geological studies above active gas chimneys off Egypt (Central Nile Deep Sea Fan). Deep Sea Research Part I: Oceanographic Research Papers 54, 1146-1172.
Dutta, N., Seriff, A., 1979. On White's model of attenuation in rocks with partial gas saturation. Geophysics 44, 1806-1812.
Ecker, C., Dvorkin, J., Nur, A.M., 2000. Estimating the amount of gas hydrate and free gas from marine seismic data. Geophysics 65, 565-573.
Eichhubl, P., Greene, H., Naehr, T., Maher, N., 2000. Structural control of fluid flow: offshore fluid seepage in the Santa Barbara Basin, California. Journal of Geochemical Exploration 69, 545-549.
Eiken, O., Brevik, I., Arts, R., Lindeberg, E., Fagervik, K., 2000. Seismic monitoring of CO_2 injected into a marine aquifer. SEG Technical Program Expanded Abstracts 2000, 1623-1626.
Eiken, O., Ringrose, P., Hermanrud, C., Nazarian, B., Torp, T.A., Høier, L., 2011. Lessons learned from 14 years of CCS operations: Sleipner, In Salah and Snøhvit. Energy Procedia 4, 5541-5548.
Ennis-King, J., Paterson, L., 2007. Coupling of geochemical reactions and convective mixing in the long-term geological storage of carbon dioxide. International Journal of Greenhouse Gas Control 1, 86-93.
Fall, A., Eichhubl, P., Cumella, S.P., Bodnar, R.J., Laubach, S.E., Becker, S.P., 2012. Testing the basin-centered gas accumulation model using fluid inclusion observations: Southern Piceance Basin, Colorado. AAPG Bulletin 96, 2297-2318.
Feely, R.A., Orr, J., Fabry, V.J., Kleypas, J.A., Sabine, C.L., Langdon, C., 2009. Present and future changes in seawater chemistry due to ocean acidification, in: Mcpherson, B., Sundquist, E. (Eds.), Carbon Sequestration and Its Role in the Global Carbon Cycle. American Geophysical Union, Washington, 175-188.
Fichler, C., Henriksen, S., Rueslaatten, H., Hovland, M., 2005. North Sea Quaternary morphology from seismic and magnetic data: indications for gas hydrates during glaciation? Petroleum Geoscience 11, 331-337.
Foucher, J.-P., Dupré, S., Scalabrin, C., Feseker, T., Harmegnies, F., Nouzé, H., 2010. Changes in seabed morphology, mud temperature and free gas venting at the Håkon Mosby mud volcano, offshore northern Norway, over the time period 2003–2006. Geo-Marine Letters 30, 157-167.
Fu, S., Wilkens, R., Frazer, L., 1996. In situ velocity profiles in gassy sediments: Kiel Bay. Geo-Marine Letters 16, 249-253.
Furre, A., Ringrose, P., Cavanagh, A., Janbu, A., Hagen, S., 2014. Characterisation of a Submarine Glacial Channel and Related Linear Features, EAGE Near Surface Geoscience 2014, First Applied Shallow Marine Geophysics Conference, Athens, Greece.
Furre, A.K., Eiken, O., 2014. Dual sensor streamer technology used in Sleipner CO_2 injection monitoring. Geophysical Prospecting 62(5), 1075-1088.

Galloway, W., Garber, J., Liu, X., Sloan, B., 1993. Sequence stratigraphic and depositional framework of the Cenozoic fill, Central and Northern North Sea Basin, Geological Society, London, Petroleum Geology Conference series, 33-43.
Gardner, T., 2000. An acoustic study of soils that model seabed sediments containing gas bubbles. The Journal of the Acoustical Society of America 107, 163-176.
Gassmann, F., 1951. Elasticity of porous media. Vierteljahrsschrder Naturforschenden Gesselschaft 96, 1-23.
Gay, A., Lopez, M., Cochonat, P., Séranne, M., Levaché, D., Sermondadaz, G., 2006. Isolated seafloor pockmarks linked to BSRs, fluid chimneys, polygonal faults and stacked Oligocene–Miocene turbiditic palaeochannels in the Lower Congo Basin. Marine Geology 226, 25-40.
Geletti, R., Busetti, M., 2011. A double bottom simulating reflector in the western Ross Sea, Antarctica. Journal of Geophysical Research: Solid Earth 116, B04101.
Ghosh, R., Sen, M.K., 2012. Predicting subsurface CO_2 movement: From laboratory to field scale. Geophysics 77, M27-M37.
Ghosh, R., Sen, M.K., Vedanti, N., 2015. Quantitative interpretation of CO_2 plume from Sleipner (North Sea), using post-stack inversion and rock physics modeling. International Journal of Greenhouse Gas Control 32, 147-158.
Gislason, S.R., Oelkers, E.H., 2014. Carbon storage in basalt. Science 344, 373-374.
Glennie, K., 1990. Introduction to the Petroleum Geology of the North Sea. Blackwell Scientific Publications, United States.
Gloaguen, E., Sauvageau, M., Lefebvre, R., 2014. On the importance of using stochastic sesmic inversion in reservoir modelling: an application on a tight oil reservoir, Second EAGE Integrated Reservoir Modelling Conference, Dubai.
Global CCS Institute, 2015. What is CCS? Global Carbon Capture and Storage Institute, Australia.
Gluyas, J., Mathias, S., 2013. Geological storage of carbon dioxide (CO_2): Geoscience, technologies, environmental aspects and legal frameworks. Woodhead Publishing Series in Energy, Cambridge, UK.
Goldberg, D.E., 1989. Genetic algorithms in search, optimization, and machine learning. Addison Wesley Publishing Company, Reading, MA.
Götz, J., Lüth, S., Krawczyk, C.M., Cosma, C., 2014. Zero-Offset VSP monitoring of CO_2 storage: impedance inversion and wedge modelling at the Ketzin pilot site. International Journal of Geophysics 2014, 15.
Goulty, N., 2008. Geomechanics of polygonal fault systems: a review. Petroleum Geoscience 14, 389-397.
Graham, A.G., Stoker, M.S., Lonergan, L., Bradwell, T., Stewart, M.A., 2011. The Pleistocene glaciations of the North Sea basin, in: Ehlers, J., Gibbard, P., Hughes, P. (Eds.), Quaternary glaciations : extent and chronology : a closer look. Elsevier, Oxford, UK, 261-278.
Gregersen, U., Johannessen, P., 2001. The Neogene Utsira Sand and its seal in the Viking Graben area, North Sea Saline Aquifer CO_2 Storage (SACS) project. Geological Survey of Denmark and Greenland, Copenhagen, Denmark, 1-30.
Gregersen, U., Johannessen, P., 2007. Distribution of the Neogene Utsira Sand and the succeeding deposits in the Viking Graben area, North Sea. Marine and Petroleum Geology 24, 591-606.
Gregersen, U., Michelsen, O., Sørensen, J.C., 1997. Stratigraphy and facies distribution of the Utsira Formation and the Pliocene sequences in the northern North Sea. Marine and Petroleum Geology 14, 893-914.

Gregory, A., 1977. Aspects of Rock Physics From Laboratory and Log Data that are Important to Seismic Interpretation: Section 1. Fundamentals of Stratigraphic Interpretation of Seismic Data, in: Payton, C.E. (Ed.), Seismic Stratigraphy-Applications to Hydrocarbon Exploration. American Association of Petroleum Geologists, 15-46.
Greinert, J., Lewis, K., Bialas, J., Pecher, I.A., Rowden, A., Bowden, D., De Batist, M., Linke, P., 2010. Methane seepage along the Hikurangi Margin, New Zealand: Overview of studies in 2006 and 2007 and new evidence from visual, bathymetric and hydroacoustic investigations. Marine Geology 272, 6-25.
Grollimund, B., Zoback, M.D., Wiprut, D.J., Arnesen, L., 2001. Stress orientation, pore pressure and least principal stress in the Norwegian sector of the North Sea. Petroleum Geoscience 7, 173-180.
Grude, S., Landrø, M., White, J., Torsæter, O., 2014. CO_2 saturation and thickness predictions in the Tubåen Fm., Snøhvit field, from analytical solution and time-lapse seismic data. International Journal of Greenhouse Gas Control 29, 248-255.
Guigné, J.Y., Pace, N.G., Chin, V.H., 1989. Dynamic extraction of sediment attenuation from subbottom acoustic data. Journal of Geophysical Research: Solid Earth 94, 5745-5755.
Gunter, W.D., Bachu, S., Benson, S., 2004. The role of hydrogeological and geochemical trapping in sedimentary basins for secure geological storage of carbon dioxide. Geological Society, London, Special Publications 233, 129-145.
Gunter, W.D., Perkins, E.H., McCann, T.J., 1993. Aquifer disposal of CO_2-rich gases: Reaction design for added capacity. Energy Conversion and Management 34, 941-948.
Gutowski, M., Bull, J., Henstock, T., Dix, J., Hogarth, P., Leighton, T., White, P., 2002. Chirp sub-bottom profiler source signature design and field testing. Marine Geophysical Researches 23, 481-492.
Haeckel, M., Wallmann, K., Schmidt, M., Liebetrau, V., Sommer, S., Schroller, D., Schönfeld, J., Karstens, J., Berndt, C., 2013. Fluid expulsion at a 3-km long fracture system in the Northern North Sea-geochemical constraints on the origin of gas and water, AGU Fall Meeting Abstracts, San Francisco.
Hamilton, E.L., 1972. Compressional-wave attenuation in marine sediments. Geophysics 37, 620-646.
Hamilton, E.L., 1987. Acoustic properties of sediments, in: Lara, A., Ranz, C., Carbo, R. (Eds.), Acoustics and Ocean Bottom. CSIC, Madrid, 3-58.
Han, D.-h., Batzle, M.L., 2004. Gassmann's equation and fluid-saturation effects on seismic velocities. Geophysics 69, 398-405.
Hansen, O., Gilding, D., Nazarian, B., Osdal, B., Ringrose, P., Kristoffersen, J.-B., Eiken, O., Hansen, H., 2013. Snøhvit: the history of injecting and storing 1 Mt CO_2 in the Fluvial Tubåen Fm. Energy Procedia 37, 3565-3573.
Hashin, Z., Shtrikman, S., 1963. A variational approach to the theory of the elastic behaviour of multiphase materials. Journal of the Mechanics and Physics of Solids 11, 127-140.
Haszeldine, S., Scott, V., Shackley, S., Gilfillan, S., Mabon, L., Johnson, G., 2014. Sleipner CO_2 securely stored deep beneath seabed, in spite of unexpected Hugin fracture discovery. Scottish Carbon Capture and Storage working paper.
Head, M.J., Riding, J.B., Eidvin, T., Chadwick, R.A., 2004. Palynological and foraminiferal biostratigraphy of (upper Pliocene) Nordland Group mudstones at Sleipner, northern North Sea. Marine and Petroleum Geology 21, 277-297.

Heap, A.D., Nichol, S.L., Brooke, B.P., 2014. Seabed mapping to support geological storage of carbon dioxide in offshore Australia. Continental Shelf Research 83, 108-115.
Heggland, R., 1997. Detection of gas migration from a deep source by the use of exploration 3D seismic data. Marine Geology 137, 41-47.
Henry, P., Lallemant, S., Nakamura, K.-i., Tsunogai, U., Mazzotti, S., Kobayashi, K., 2002. Surface expression of fluid venting at the toe of the Nankai wedge and implications for flow paths. Marine Geology 187, 119-143.
Hermanrud, C., Andresen, T., Eiken, O., Hansen, H., Janbu, A., Lippard, J., Bolås, H.N., Simmenes, T.H., Teige, G.M.G., Østmo, S., 2009. Storage of CO_2 in saline aquifers-Lessons learned from 10 years of injection into the Utsira Formation in the Sleipner area. Energy Procedia 1, 1997-2004.
Hillis, R., Nelson, E., 2005. In situ stresses in the North Sea and their applications: Petroleum geomechanics from exploration to development, Geological Society, London, Petroleum Geology Conference series, 551-564.
Holloway, S., 2005. Underground sequestration of carbon dioxide-a viable greenhouse gas mitigation option. Energy 30, 2318-2333.
Holloway, S., Chadwick, R., Kirby, G., Pearce, J., Gregersen, U., Johannessen, P., Kristensen, L., Zweigel, P., Lothe, A., Arts, R., 2000. Saline Aquifer CO_2 Storage (SACS)–Final report: Work Area 1 (Geology). BGS, Keyworth, UK.
Hornby, B.E., Schwartz, L.M., Hudson, J.A., 1994. Anisotropic effective-medium modeling of the elastic properties of shales. Geophysics 59, 1570-1583.
Howe, J.A., Shimmield, T., Austin, W.E., Longva, O., 2002. Post-glacial depositional environments in a mid-high latitude glacially-overdeepened sea loch, inner Loch Etive, western Scotland. Marine Geology 185, 417-433.
Hurst, A., Cartwright, J., Huuse, M., Jonk, R., Schwab, A., Duranti, D., Cronin, B., 2003. Significance of large-scale sand injectites as long-term fluid conduits: evidence from seismic data. Geofluids 3, 263-274.
Hustoft, S., Mienert, J., Bünz, S., Nouzé, H., 2007. High-resolution 3D-seismic data indicate focussed fluid migration pathways above polygonal fault systems of the mid-Norwegian margin. Marine Geology 245, 89-106.
Huuse, M., Le Heron, D., Dixon, R., Redfern, J., Moscariello, A., Craig, J., 2012. Glaciogenic reservoirs and hydrocarbon systems: an introduction. Geological Society, London, Special Publications 368, 1-28.
Huuse, M., Lykke-Andersen, H., 2000. Overdeepened Quaternary valleys in the eastern Danish North Sea: morphology and origin. Quaternary Science Reviews 19, 1233-1253.
IEA, 2013. Technology Roadmap-Carbon Capture and Storage, Paris, France.
IPCC, 2005. IPCC special report on carbon dioxide capture and storage. Intergovernmental Panel on Climate Change, Working Group III, Geneva, Switzerland, p. 431.
IPCC, 2014. Climate Change 2014: Synthesis Report. Contribution of Working Groups I, II and III to the Fifth Assessment Report of the Intergovernmental Panel on Climate Change, Geneva, Switzerland, p. 151.
Isaksen, D., Tonstad, K., 1989. A revised Cretaceous and Tertiary lithostratigraphic nomenclature for the Norwegian North Sea. Norwegian Petroleum Directorate, p. 59.
Jackson, C., Stoddart, D., 2005. Temporal constraints on the growth and decay of large-scale mobilized mud masses and implications for fluid flow mapping in sedimentary basins. Terra Nova 17, 580-585.

Jacobs, C., 2010. Report of the coring expedition aboard RV Calanus for the QICS Carbon Capture and Storage Project. National Oceanography Centre, Southampton, UK.
Jain, A., Juanes, R., 2009. Preferential mode of gas invasion in sediments: Grain-scale mechanistic model of coupled multiphase fluid flow and sediment mechanics. Journal of Geophysical Research: Solid Earth 114, B08101.
Johnson, B.D., Boudreau, B.P., Gardiner, B.S., Maass, R., 2002. Mechanical response of sediments to bubble growth. Marine Geology 187, 347-363.
Jordt, H., Faleide, J.I., Bjørlykke, K., Ibrahim, M.T., 1995. Cenozoic sequence stratigraphy of the central and northern North Sea Basin: tectonic development, sediment distribution and provenance areas. Marine and Petroleum Geology 12, 845-879.
Karaca, D., Schleicher, T., Hensen, C., Linke, P., Wallmann, K., 2014. Quantification of methane emission from bacterial mat sites at Quepos Slide offshore Costa Rica. International Journal of Earth Sciences 103, 1817-1829.
Karstens, J., Berndt, C., 2015. Seismic chimneys in the Southern Viking Graben-Implications for palaeo fluid migration and overpressure evolution. Earth and Planetary Science Letters 412, 88-100.
Katsman, R., Ostrovsky, I., Makovsky, Y., 2013. Methane bubble growth in fine-grained muddy aquatic sediment: Insight from modeling. Earth and Planetary Science Letters 377, 336-346.
Katzer, J., Moniz, E., Deutch, J., Ansolabehere, S., Beer, J., 2007. The future of coal: an interdisciplinary MIT study. Technical report, Massachusetts Institute of Technology, Cambridge, MA.
Kempf, P., Forwick, M., Laberg, J.S., Vorren, T.O., 2013. Late Weichselian and Holocene sedimentary palaeoenvironment and glacial activity in the high-arctic van Keulenfjorden, Spitsbergen. The Holocene 23, 1607-1618.
Ker, S., Le Gonidec, Y., Marsset, B., Westbrook, G., Gibert, D., Minshull, T., 2014. Fine-scale gas distribution in marine sediments assessed from deep-towed seismic data. Geophysical Journal International 196, 1466-1470.
Kim, G.Y., Kim, D.C., Park, S.C., Lee, G.H., 1999. Chirp (2–7 kHz) echo characters and geotechnical properties of surface sediments in the Ulleung Basin, the East Sea. Geosciences Journal 3, 213-224.
Klein, E., De Lucia, M., Kempka, T., Kühn, M., 2013. Evaluation of long-term mineral trapping at the Ketzin pilot site for CO_2 storage: An integrative approach using geochemical modelling and reservoir simulation. International Journal of Greenhouse Gas Control 19, 720-730.
Koljonen, T., Siikavirta, H., Zevenhoven, R., Savolainen, I., 2004. CO_2 capture, storage and reuse potential in Finland. Energy 29, 1521-1527.
Kongsjorden, H., Kårstad, O., Torp, T.A., 1998. Saline aquifer storage of carbon dioxide in the Sleipner project. Waste Management 17, 303-308.
Korbøl, R., Kaddour, A., 1995. Sleipner West CO_2 disposal-injection of removed CO_2 into the Utsira formation. Energy Conversion and Management 36, 509-512.
Kristensen, T., Huuse, M., 2012. Multistage erosion and infill of buried Pleistocene tunnel valleys and associated seismic velocity effects. Geological Society, London, Special Publications 368, 159-172.
Kristensen, T.B., Huuse, M., Piotrowski, J.A., Clausen, O.R., 2007. A morphometric analysis of tunnel valleys in the eastern North Sea based on 3D seismic data. Journal of Quaternary Science 22, 801-815.

Kurihara, H., Shimode, S., Shirayama, Y., 2004. Sub-lethal effects of elevated concentration of CO_2 on planktonic copepods and sea urchins. Journal of Oceanography 60, 743-750.
Lackner, K.S., Brennan, S., 2009. Envisioning carbon capture and storage: expanded possibilities due to air capture, leakage insurance, and C-14 monitoring. Climatic Change 96, 357-378.
Landschulze, K., Pedersen, R.-B., 2013a. Overburden Integrity for shallow CO_2 Storage in the Central North Sea, ECO2 Second Annual Meeting, Bergen, Norway.
Landschulze, K., Pedersen, R.-B., Tveranger, J., 2014a. Tunnel valleys in the vicinity of the Hugin Fracture-evidence of an eventful geologic history, ECO2 Third Annual Meeting, Salina, Italy.
Landschulze, K., Pedersen, R., 2013b. Caprock integrity for offshore CO_2 storage in the Norwegian North Sea-Seismic investigation of a soft sediment seafloor fracture, AGU Fall Meeting Abstracts, San Francisco.
Landschulze, K., Tveranger, J., Pedersen, R., 2014b. Characterization of Shallow Seal Complexes for CO_2 Storage Sites-Example from the Greater Sleipner Area, EAGE Near Surface Geoscience 2014, First Applied Shallow Marine Geophysics Conference, Athens, Greece.
LeBlanc, L.R., Mayer, L., Rufino, M., Schock, S.G., King, J., 1992. Marine sediment classification using the Chirp sonar. The Journal of the Acoustical Society of America 91, 107-115.
Leighton, T., 2007a. A method for estimating sound speed and the void fraction of bubbles from sub-bottom sonar images of gassy seabeds, ISVR Technical Report. Institute of Sound and Vibration Research, University of Southampton, Southampton, UK, 1-21.
Leighton, T., 2007b. Theory for acoustic propagation in marine sediment containing gas bubbles which may pulsate in a non-stationary nonlinear manner. Geophysical Research Letters 34, L17607.
Leighton, T., Robb, G., 2008. Preliminary mapping of void fractions and sound speeds in gassy marine sediments from subbottom profiles. The Journal of the Acoustical Society of America 124, EL313-EL320.
Leighton, T.G., 1994. The Acoustic Bubble. Academic Press Limited, London.
Levine, J.S., Matter, J.M., Goldberg, D., Lackner, K.S., 2009. Gravitational trapping of carbon dioxide in deep ocean sediments: hydraulic fracturing and mechanical stability. Energy Procedia 1, 3647-3654.
Lichtschlag, A., James, R.H., Stahl, H., Connelly, D., 2015. Effect of a controlled sub-seabed release of CO_2 on the biogeochemistry of shallow marine sediments, their pore waters, and the overlying water column. International Journal of Greenhouse Gas Control 38, 80-92.
Lindeberg, E., Vuillaume, J.-F., Ghaderi, A., 2009. Determination of the CO_2 storage capacity of the Utsira formation. Energy Procedia 1, 2777-2784.
Lister, J.R., 1990. Buoyancy-driven fluid fracture: the effects of material toughness and of low-viscosity precursors. Journal of Fluid Mechanics 210, 263-280.
Liu, N., Liu, L., Qu, X., Yang, H., Wang, L., Zhao, S., 2011. Genesis of authigene carbonate minerals in the Upper Cretaceous reservoir, Honggang Anticline, Songliao Basin: A natural analog for mineral trapping of natural CO_2 storage. Sedimentary Geology 237, 166-178.
Lonergan, L., Cartwright, J., Jolly, R., 1998. The geometry of polygonal fault systems in Tertiary mudrocks of the North Sea. Journal of Structural Geology 20, 529-548.

Lonergan, L., Maidment, S.C., Collier, J.S., 2006. Pleistocene subglacial tunnel valleys in the central North Sea basin: 3-D morphology and evolution. Journal of Quaternary Science 21, 891-903.
Løseth, H., Gading, M., Wensaas, L., 2009. Hydrocarbon leakage interpreted on seismic data. Marine and Petroleum Geology 26, 1304-1319.
Løseth, H., Wensaas, L., Arntsen, B., Hovland, M., 2003. Gas and fluid injection triggering shallow mud mobilization in the Hordaland Group, North Sea. Geological Society, London, Special Publications 216, 139-157.
Lu, J., Wilkinson, M., Haszeldine, R.S., Boyce, A.J., 2011. Carbonate cements in Miller field of the UK North Sea: a natural analog for mineral trapping in CO_2 geological storage. Environmental Earth Sciences 62, 507-517.
Lu, S., McMechan, G.A., 2002. Estimation of gas hydrate and free gas saturation, concentration, and distribution from seismic data. Geophysics 67, 582-593.
Luderer, G., Krey, V., Calvin, K., Merrick, J., Mima, S., Pietzcker, R., Van Vliet, J., Wada, K., 2014. The role of renewable energy in climate stabilization: results from the EMF27 scenarios. Climatic Change 123, 427-441.
Lykke-Andersen, H., Seidenkrantz, M.-S., Knudsen, K., 1993. Quaternary sequences and their relations to the pre-Quaternary in the vicinity of Anholt, Kattegat, Scandinavia. Boreas 22, 291-298.
Maeda, Y., Shitashima, K., Sakamoto, A., 2015. Mapping observations using AUV and numerical simulations of leaked CO_2 diffusion in sub-seabed CO_2 release experiment at Ardmucknish Bay. International Journal of Greenhouse Gas Control 38, 143-152.
Marchetti, C., 1977. On geoengineering and the CO_2 problem. Climatic Change 1, 59-68.
Matter, J.M., Kelemen, P.B., 2009. Permanent storage of carbon dioxide in geological reservoirs by mineral carbonation. Nature Geoscience 2, 837-841.
Mavko, G., Jizba, D., 1991. Estimating grain-scale fluid effects on velocity dispersion in rocks. Geophysics 56, 1940-1949.
Mavko, G., Mukerji, T., 1995. Seismic pore space compressibility and Gassmann's relation. Geophysics 60, 1743-1749.
Mavko, G., Mukerji, T., 1998. Bounds on low-frequency seismic velocities in partially saturated rocks. Geophysics 63, 918-924.
Mavko, G., Mukerji, T., Dvorkin, J., 2009. The Rock Physics Handbook: Tools for seismic analysis of porous media. Cambridge University Press, Cambridge, UK.
Mavko, G.M., Nur, A., 1979. Wave attenuation in partially saturated rocks. Geophysics 44, 161-178.
Mcintyre, K.L., Howe, J.A., 2010. Scottish west coast fjords since the last glaciation: a review. Geological Society, London, Special Publications 344, 305-329.
Meinshausen, M., Meinshausen, N., Hare, W., Raper, S.C., Frieler, K., Knutti, R., Frame, D.J., Allen, M.R., 2009. Greenhouse-gas emission targets for limiting global warming to 2^{o}C. Nature 458, 1158-1162.
Meldahl, P., Heggland, R., Bril, B., de Groot, P., 2001. Identifying faults and gas chimneys using multiattributes and neural networks. The Leading Edge 20, 474-482.
Menand, T., Tait, S.R., 2002. The propagation of a buoyant liquid-filled fissure from a source under constant pressure: an experimental approach. Journal of Geophysical Research 107, 2306.
Miller, H., 2014. Lake bed environments, modern sedimentation and the glacial and post-glacial history of Windermere, UK, Earth Sciences. University of Southampton, Southampton, UK.

Minnaert, M., 1933. XVI. On musical air-bubbles and the sounds of running water. The London, Edinburgh, and Dublin Philosophical Magazine and Journal of Science 16, 235-248.
Minshull, T., Westbrook, G., Marin-Moreno, H., Marsset, B., Ker, S., Sarkar, S., Vardy, M., Henstock, T., 2014. High-Resolution Seismic Definition of the Distribution of Gas in the West Svalbard Margin, AGU Fall Meeting Abstracts, San Francisco.
Miocic, J., Gilfillan, S., McDermott, C., Haszeldine, S., 2014. How secure is subsurface CO_2 storage? Controls on leakage in natural CO_2 reservoirs, EGU General Assembly Conference Abstracts, Vienna, Austria.
Morgan, E.C., Vanneste, M., Lecomte, I., Baise, L.G., Longva, O., McAdoo, B., 2012. Estimation of free gas saturation from seismic reflection surveys by the genetic algorithm inversion of a P-wave attenuation model. Geophysics 77, R175-R187.
Moriarty, P., Honnery, D., 2012. What is the global potential for renewable energy? Renewable and Sustainable Energy Reviews 16, 244-252.
Müller, T.M., Gurevich, B., Lebedev, M., 2010. Seismic wave attenuation and dispersion resulting from wave-induced flow in porous rocks-A review. Geophysics 75, 75A147-175A164.
Muñoz, P., Sellanes, J., Villalobos, K., Zapata-Hernández, G., Mayr, C., Araya, K., 2014. Geochemistry of reduced fluids from shallow cold vents hosting chemosynthetic communities (Comau Fjord, Chilean Patagonia,∼ 42° S). Progress in Oceanography 129, 159-169.
Murphy, W.F., 1984. Acoustic measures of partial gas saturation in tight sandstones. Journal of Geophysical Research: Solid Earth (1978–2012) 89, 11549-11559.
Nicoll, G.D., 2012. Evaluation of the Nordland Group overburden as an effective seal for the Sleipner CO_2 storage site (offshore Norway) using analytical and stochastic modelling techniques, School of Geosciences. University of Edinburgh.
Niu, B., Al-Menhali, A., Krevor, S., 2014. A Study of Residual Carbon Dioxide Trapping in Sandstone. Energy Procedia 63, 5522-5529.
Nooner, S.L., Eiken, O., Hermanrud, C., Sasagawa, G.S., Stenvold, T., Zumberge, M.A., 2007. Constraints on the in situ density of CO_2 within the Utsira formation from time-lapse seafloor gravity measurements. International Journal of Greenhouse Gas Control 1, 198-214.
Nørgaard-Pedersen, N., Austin, W., Howe, J., Shimmield, T., 2006. The Holocene record of Loch Etive, western Scotland: influence of catchment and relative sea level changes. Marine Geology 228, 55-71.
Nunn, J.A., Meulbroek, P., 2002. Kilometer-scale upward migration of hydrocarbons in geopressured sediments by buoyancy-driven propagation of methane-filled fractures. AAPG Bulletin 86, 907-918.
Otsuki, K., Dilov, T., 2005. Evolution of hierarchical self-similar geometry of experimental fault zones: Implications for seismic nucleation and earthquake size. Journal of Geophysical Research: Solid Earth (1978–2012) 110, B03303.
Panda, S., LeBlanc, L.R., Schock, S.G., 1994. Sediment classification based on impedance and attenuation estimation. The Journal of the Acoustical Society of America 96, 3022-3035.
Pandolfi, J.M., Connolly, S.R., Marshall, D.J., Cohen, A.L., 2011. Projecting coral reef futures under global warming and ocean acidification. Science 333, 418-422.
Park, J., Vanneste, M., Bohloli, B., Viken, I., Bjørnarå, T., 2014. In Situ Resistivity of CO_2 Plume at Sleipner from CSEM and Gravity Data, EAGE Near Surface Geoscience 2014, First Applied Shallow Marine Geophysics Conference, Athens, Greece.

Peacock, D., 1991. Displacements and segment linkage in strike-slip fault zones. Journal of Structural Geology 13, 1025-1035.
Pedersen, R., Blomberg, A., Landschulze, K., Baumberger, T., Økland, I., Reigstad, L., Gracias, N., Mørkved, P., Stensland, A., Lilley, M., 2013. Discovery of 3 km long seafloor fracture system in the Central North Sea, AGU Fall Meeting Abstracts, San Francisco.
Petersen, C.J., Bünz, S., Hustoft, S., Mienert, J., Klaeschen, D., 2010. High-resolution P-Cable 3D seismic imaging of gas chimney structures in gas hydrated sediments of an Arctic sediment drift. Marine and Petroleum Geology 27, 1981-1994.
Pinson, L.J., Henstock, T.J., Dix, J.K., Bull, J.M., 2008. Estimating quality factor and mean grain size of sediments from high-resolution marine seismic data. Geophysics 73, G19-G28.
Pires, J., Martins, F., Alvim-Ferraz, M., Simões, M., 2011. Recent developments on carbon capture and storage: An overview. Chemical Engineering Research and Design 89, 1446-1460.
Plaza-Faverola, A., Bünz, S., Mienert, J., 2011. Repeated fluid expulsion through sub-seabed chimneys offshore Norway in response to glacial cycles. Earth and Planetary Science Letters 305, 297-308.
Plaza-Faverola, A., Bünz, S., Mienert, J., 2012. The free gas zone beneath gas hydrate bearing sediments and its link to fluid flow: 3-D seismic imaging offshore mid-Norway. Marine Geology 291, 211-226.
Plaza-Faverola, A., Klaeschen, D., Barnes, P., Pecher, I., Henrys, S., Mountjoy, J., 2012. Evolution of fluid expulsion and concentrated hydrate zones across the southern Hikurangi subduction margin, New Zealand: An analysis from depth migrated seismic data. Geochemistry, Geophysics, Geosystems 13, 1-21.
Praeg, D., 2003. Seismic imaging of mid-Pleistocene tunnel-valleys in the North Sea Basin-high resolution from low frequencies. Journal of Applied Geophysics 53, 273-298.
Qian, J., Wang, X.-J., Wu, S.-G., Wang, Z.-z., Yang, S.-X., 2014. AVO analysis of BSR to assess free gas within fine-grained sediments in the Shenhu area, South China Sea. Marine Geophysical Research 35, 125-140.
Quan, Y., Harris, J.M., 1997. Seismic attenuation tomography using the frequency shift method. Geophysics 62, 895-905.
Queißer, M., Singh, S.C., 2013. Full waveform inversion in the time lapse mode applied to CO_2 storage at Sleipner. Geophysical Prospecting 61, 537-555.
Quinn, R., Bull, J., Dix, J., 1997a. Buried scour marks as indicators of palaeo-current direction at the Mary Rose wreck site. Marine Geology 140, 405-413.
Quinn, R., Bull, J., Dix, J., 1997b. Imaging wooden artefacts using Chirp sources. Archaeological Prospection 4, 25-35.
Quinn, R., Bull, J., Dix, J., 1998. Optimal processing of marine high-resolution seismic reflection (Chirp) data. Marine Geophysical Researches 20, 13-20.
Quintal, B., Steeb, H., Frehner, M., Schmalholz, S.M., 2011. Quasi-static finite element modeling of seismic attenuation and dispersion due to wave-induced fluid flow in poroelastic media. Journal of Geophysical Research: Solid Earth 116, B01201.
Rajan, A., Mienert, J., Bünz, S., 2012. Acoustic evidence for a gas migration and release system in Arctic glaciated continental margins offshore NW-Svalbard. Marine and Petroleum Geology 32, 36-49.
Richardson, M., Briggs, K., 1993. On the use of acoustic impedance values to determine sediment properties. Proceedings of the Institute of Acoustics 15, 15-23.

Riedel, M., Shankar, U., 2012. Combining impedance inversion and seismic similarity for robust gas hydrate concentration assessments–A case study from the Krishna–Godavari basin, East Coast of India. Marine and Petroleum Geology 36, 35-49.
Robb, G., Leighton, T., Humphrey, V., Best, A., Dix, J., Klusek, Z., 2007. Investigating acoustic propagation in gassy marine sediments using a bubbly gel mimic, ISVR Technical Reports. Institute of Sound and Vibration Research, University of Southampton, Southampton, UK, 1-13.
Rollet, N., Logan, G., Ryan, G., Judd, A., Totterdell, J., Glenn, K., Jones, A., Kroh, F., Struckmeyer, H., Kennard, J., 2009. Shallow gas and fluid migration in the northern Arafura Sea (offshore Northern Australia). Marine and Petroleum Geology 26, 129-147.
Rossi, G., Gei, D., Böhm, G., Madrussani, G., Carcione, J.M., 2007. Attenuation tomography: An application to gas-hydrate and free-gas detection. Geophysical Prospecting 55, 655-669.
Sain, R., Mukerji, T., Mavko, G., 2014. How computational rock-physics tools can be used to simulate geologic processes, understand pore-scale heterogeneity, and refine theoretical models. The Leading Edge 33, 324-334.
Sanna, A., Uibu, M., Caramanna, G., Kuusik, R., Maroto-Valer, M., 2014. A review of mineral carbonation technologies to sequester CO_2. Chemical Society Reviews 43, 8049-8080.
Sarkar, S., Berndt, C., Minshull, T.A., Westbrook, G.K., Klaeschen, D., Masson, D.G., Chabert, A., Thatcher, K.E., 2012. Seismic evidence for shallow gas-escape features associated with a retreating gas hydrate zone offshore west Svalbard. Journal of Geophysical Research: Solid Earth (1978–2012) 117, B09102.
Sassen, R., Losh, S., Cathles, L., Roberts, H., Whelan, J., Milkov, A., Sweet, S., DeFreitas, D., 2001. Massive vein-filling gas hydrate: relation to ongoing gas migration from the deep subsurface in the Gulf of Mexico. Marine and Petroleum Geology 18, 551-560.
Schock, S., LeBlanc, L., 1990. Some applications of the Chirp sonar, Oceans, Engineering in the Ocean Environment Conference Proceedings, Washington, 69-75.
Schock, S.G., 2004. A method for estimating the physical and acoustic properties of the sea bed using Chirp sonar data. IEEE Journal of Oceanic Engineering 29, 1200-1217.
Schock, S.G., LeBlanc, L.R., Mayer, L.A., 1989. Chirp subbottom profiler for quantitative sediment analysis. Geophysics 54, 445-450.
Sejrup, H., Larsen, E., Landvik, J., King, E., Haflidason, H., Nesje, A., 2000. Quaternary glaciations in southern Fennoscandia: evidence from southwestern Norway and the northern North Sea region. Quaternary Science Reviews 19, 667-685.
Sellami, N., Dewar, M., Stahl, H., Chen, B., 2015. Dynamics of rising CO_2 bubble plumes in the QICS field experiment: Part 1–The experiment. International Journal of Greenhouse Gas Control 38, 44-51.
Sen, M.K., Stoffa, P.L., 1992. Rapid sampling of model space using genetic algorithms: examples from seismic waveform inversion. Geophysical Journal International 108, 281-292.
Sen, M.K., Stoffa, P.L., 1996. Bayesian inference, Gibbs' sampler and uncertainty estimation in geophysical inversion. Geophysical Prospecting 44, 313-350.
Sha, Z., Liang, J., Zhang, G., Yang, S., Lu, J., Zhang, Z., McConnell, D.R., Humphrey, G., 2015. A seepage gas hydrate system in northern South China Sea: Seismic and well log interpretations. Marine Geology 366, 69-78.
Shaw, B.E., Dieterich, J.H., 2007. Probabilities for jumping fault segment stepovers. Geophysical Research Letters 34, L01307.

Shitashima, K., Maeda, Y., Sakamoto, A., 2015. Detection and monitoring of leaked CO_2 through sediment, water column and atmosphere in a sub-seabed CCS experiment. International Journal of Greenhouse Gas Control 38, 135-142.
Shumway, G., 1960. Sound speed and absorption studies of marine sediments by a resonance method. Geophysics 25, 451-467.
Sivaraj, R., Ravichandran, T., 2011. A review of selection methods in genetic algorithm. International Journal of Engineering Science and Technology 3, 3792-3797.
Slawinski, M.A., 2003. Seismic Waves and Rays in Elastic Media. Elsevier Science Ltd. , Oxford, UK.
Smith, T.M., Sondergeld, C.H., Rai, C.S., 2003. Gassmann fluid substitutions: A tutorial. Geophysics 68, 430-440.
Spence, G., Minshull, T., Fink, C., 1995. Seismic studies of methane gas hydrate, offshore Vancouver Island. Proceedings of the Ocean Drilling Program, Scientific Results 146, 163-174.
Stoffa, P.L., Sen, M.K., 1991. Nonlinear multiparameter optimization using genetic algorithms: Inversion of plane-wave seismograms. Geophysics 56, 1794-1810.
Stuevold, L.M., Faerseth, R.B., Arnesen, L., Cartwright, J., Möller, N., 2003. Polygonal faults in the Ormen Lange field, Møre basin, offshore mid Norway. Geological Society, London, Special Publications 216, 263-281.
Suekane, T., Nobuso, T., Hirai, S., Kiyota, M., 2008. Geological storage of carbon dioxide by residual gas and solubility trapping. International Journal of Greenhouse Gas Control 2, 58-64.
Sun, Q., Wu, S., Cartwright, J., Dong, D., 2012. Shallow gas and focused fluid flow systems in the Pearl River Mouth Basin, northern South China Sea. Marine Geology 315, 1-14.
Sylvester, A.G., 1988. Strike-slip faults. Geological Society of America Bulletin 100, 1666-1703.
Taylor, P., Stahl, H., Vardy, M.E., Bull, J.M., Akhurst, M., Hauton, C., James, R.H., Lichtschlag, A., Long, D., Aleynik, D., 2015. A novel sub-seabed CO_2 release experiment informing monitoring and impact assessment for geological carbon storage. International Journal of Greenhouse Gas Control 38, 3-17.
Telford, W.M., Geldart, L.P., Sheriff, R.E., 1990. Applied Geophysics. Cambridge University Press, Cambridge.
Thibeau, S., Mucha, V., 2011. Have we overestimated saline aquifer CO_2 storage capacities? Oil & Gas Science and Technology 66, 81-92.
Thiel, V., Peckmann, J., Richnow, H.H., Luth, U., Reitner, J., Michaelis, W., 2001. Molecular signals for anaerobic methane oxidation in Black Sea seep carbonates and a microbial mat. Marine Chemistry 73, 97-112.
Tinivella, U., 1999. A method for estimating gas hydrate and free gas concentrations in marine sediments. Bollettino di Geofisica Teorica ed Applicata 40, 19-30.
Tinivella, U., Accaino, F., Camerlenghi, A., 2002. Gas hydrate and free gas distribution from inversion of seismic data on the South Shetland margin (Antarctica). Marine Geophysical Researches 23, 109-123.
Tinivella, U., Carcione, J.M., 2001. Estimation of gas-hydrate concentration and free-gas saturation from log and seismic data. The Leading Edge 20, 200-203.
Tomasini, J., De Santa Ana, H., Johnson, A.H., 2010. Identification of new seismic evidence regarding gas hydrate occurrence and gas migration pathways offshore Uruguay, Proceedings of the AAPG 2010 Annual Convention and Exhibition, New Orleans.

Toms-Stewart, J., Müller, T.M., Gurevich, B., Paterson, L., 2009. Statistical characterization of gas-patch distributions in partially saturated rocks. Geophysics 74, WA51-WA64.
Torp, T.A., Gale, J., 2004. Demonstrating storage of CO_2 in geological reservoirs: The Sleipner and SACS projects. Energy 29, 1361-1369.
Tóth, Z., Spieß, V., Jensen, J., 2014a. Seismo-acoustic signatures of shallow free gas in the Bornholm Basin, Baltic Sea. Continental Shelf Research 88, 228-239.
Tóth, Z., Spiess, V., Mogollón, J.M., Jensen, J.B., 2014b. Estimating the free gas content in Baltic Sea sediments using compressional wave velocity from marine seismic data. Journal of Geophysical Research: Solid Earth 119, 8577-8593.
Tréhu, A.M., Flueh, E.R., 2001. Estimating the thickness of the free gas zone beneath Hydrate Ridge, Oregon continental margin, from seismic velocities and attenuation. Journal of Geophysical Research: Solid Earth 106, 2035-2045.
Upham, P., Roberts, T., 2011. Public perceptions of CCS: Emergent themes in pan-European focus groups and implications for communications. International Journal of Greenhouse Gas Control 5, 1359-1367.
Vardy, M.E., 2015. Deriving shallow-water sediment properties using post-stack acoustic impedance inversion. Near Surface Geophysics 13, 143-154.
Verdon, J.P., Kendall, J.-M., Stork, A.L., Chadwick, R.A., White, D.J., Bissell, R.C., 2013. Comparison of geomechanical deformation induced by megatonne-scale CO_2 storage at Sleipner, Weyburn, and In Salah. Proceedings of the National Academy of Sciences 110, E2762-E2771.
Wagner, C., Gonzalez, A., Agarwal, V., Koesoemadinata, A., Ng, D., Trares, S., Biles, N., Fisher, K., 2012. Quantitative application of poststack acoustic impedance inversion to subsalt reservoir development. The Leading Edge 31, 528-537.
Wagner, S.R., Pennington, W.D., MacBeth, C., 2006. Gas saturation prediction and effect of low frequencies on acoustic impedance images at Foinaven Field. Geophysical prospecting 54, 75-87.
Wang, Z., 2001. Fundamentals of seismic rock physics. Geophysics 66, 398-412.
Warner, M., 1990. Absolute reflection coefficients from deep seismic reflections. Tectonophysics 173, 15-23.
West, J.M., Pearce, J., Bentham, M., Maul, P., 2005. Issue profile: environmental issues and the geological storage of CO_2. European Environment 15, 250-259.
White, J., 1975. Computed seismic speeds and attenuation in rocks with partial gas saturation. Geophysics 40, 224-232.
White, J.C., Williams, G.A., 2014. Utilising spectral decomposition to determine the distribution of injected CO_2 at the Snohvit field, 4th EAGE CO_2 Geological Storage Workshop, Stavanger, Norway.
White, J.C., Williams, G.A., Chadwick, R.A., 2013. Thin Layer Detectability in a Growing CO_2 Plume: testing the Limits of Time-lapse Seismic Resolution. Energy Procedia 37, 4356-4365.
Widess, M., 1973. How thin is a thin bed? Geophysics 38, 1176-1180.
Wilkens, R., Richardson, M., 1998. The influence of gas bubbles on sediment acoustic properties: in situ, laboratory, and theoretical results from Eckernförde Bay, Baltic sea. Continental Shelf Research 18, 1859-1892.
Williams, G., Chadwick, A., 2012. Quantitative seismic analysis of a thin layer of CO_2 in the Sleipner injection plume. Geophysics 77, R245-R256.
Williams, K.L., Jackson, D.R., Thorsos, E.I., Tang, D., Schock, S.G., 2002. Comparison of sound speed and attenuation measured in a sandy sediment to

predictions based on the Biot theory of porous media. IEEE Journal of Oceanic Engineering 27, 413-428.
Winkler, K., Nur, A., 1979. Pore fluids and seismic attenuation in rocks. Geophysical Research Letters 6, 1-4.
Yang, F., Bai, B., Tang, D., Shari, D.-N., David, W., 2010. Characteristics of CO_2 sequestration in saline aquifers. Petroleum Science 7, 83-92.
Yang, J., Davies, R.J., 2013. Gravity-driven faults: Migration pathways for recycling gas after the dissociation of marine gas hydrates. Marine Geology 336, 1-9.
Yilmaz, Ö., 1987. Seismic data processing. Society of Exploration Geophysicists Tulsa, OK.
Yoo, D.G., Kang, N.K., Yi, B.Y., Kim, G.Y., Ryu, B.J., Lee, K., Lee, G.H., Riedel, M., 2013. Occurrence and seismic characteristics of gas hydrate in the Ulleung Basin, East Sea. Marine and Petroleum Geology 47, 236-247.
Zachariasen, J., Sieh, K., 1995. The transfer of slip between two en echelon strike-slip faults: A case study from the 1992 Landers earthquake, southern California. Journal of Geophysical Research: Solid Earth (1978–2012) 100, 15281-15301.
Zevenhoven, R., Fagerlund, J., Songok, J.K., 2011. CO_2 mineral sequestration: developments toward large-scale application. Greenhouse Gases: Science and Technology 1, 48-57.
Zhang, W., Li, Y., Xu, T., Cheng, H., Zheng, Y., Xiong, P., 2009. Long-term variations of CO_2 trapped in different mechanisms in deep saline formations: A case study of the Songliao Basin, China. International Journal of Greenhouse Gas Control 3, 161-180.
Zhang, Z., McConnell, D.R., Han, D.-H., 2012. Rock physics-based seismic trace analysis of unconsolidated sediments containing gas hydrate and free gas in Green Canyon 955, Northern Gulf of Mexico. Marine and Petroleum Geology 34, 119-133.
Zweigel, P., 2000. Seismic anomaly maps in the Neogene, Sleipner area, SINTEF Petroleum Research, Technical Report. 1-9.
Zweigel, P., Arts, R., Lothe, A.E., Lindeberg, E.B., 2004. Reservoir geology of the Utsira Formation at the first industrial-scale underground CO_2 storage site (Sleipner area, North Sea). Geological Society, London, Special Publications 233, 165-180.
Zweigel, P., Hamborg, M., Arts, R., Lothe, A., Sylta, Ø., Tømmerås, A., 2000. Prediction of migration of CO_2 injected into an underground depository: reservoir geology and migration modelling in the Sleipner case (North Sea), 5th International Conference on Greenhouse Gas Control Technologies, Cairns, Australia.